Alma Mater Studiorum – Università di Bologna

DOTTORATO DI RICERCA IN

CHIMICA

Ciclo XXX

Settore Concorsuale: 03/B1

Settore Scientifico Disciplinare:CHIM/03

TITOLO TESI

SMART SURFACES FOR ENVIRONMENTAL REMEDIATION. HIGHLY EFFICIENT PHOTOCALATYTIC NANOCOMPOSITES INCORPORATING METAL OXIDES AND GRAPHENE RELATED MATERIALS.

Presentata da: GLORIA GUIDETTI

Coordinatore Dottorato **Supervisore**

ALDO RODA **MARCO MONTALTI**

Esame finale anno 2018

ABSTRACT

SMART SURFACES FOR ENVIRONMENTAL REMEDIATION. HIGHLY EFFICIENT PHOTOCALATYTIC NANOCOMPOSITES INCORPORATING METAL OXIDES AND GRAPHENE RELATED MATERIALS.

GLORIA GUIDETTI

After the first "commitment period" of the Kyoto Protocol on 25 September 2015, the United Nations General Assembly identified air pollution as a global health priority of the 2030 Agenda for Sustainable Development [1]. The global air pollution impact on human health was quantified in 2016, when World Health Organization estimated that up to date one out of every nine deaths was related to outdoor /indoor air pollution[2]. As a consequence the World's population expressed the need to have Healthier Cities and the design of new technologies to eliminate air pollutants [e.g. nitrogen oxides (NOx) and organics] by using natural sunlight, and their integration into smart cities became the centre of an ever increasing research[3]. Photocatalysts based on TiO_2 are already on the market[4] and embedded in commercial products, such as cement[5]. However, they work only with the UV light $\lambda<380nm$ [6], with a significant drop of performance in the visible[7]. In this work I enhanced and extend the TiO_2 spectral activity by creating hybrid photocatalysts with organics (e.g perylenes), or graphene and related materials (GRM-PCs). We test the photocatalytic activity by monitoring the dye degradation (rhodamine B, (RhB)) caused by GRM-PCs after a fixed irradiation time with respect to pristine TiO_2. We embed graphene, MoS_2,

WS_2 and red phosphorous (RP) into TiO_2. GRM-PCs based on TiO_2 mixed with exfoliated graphite (TiO_2-Gr) or with RP show ~90% higher photocatalytic activity, in terms of dye degradation, than pristine TiO_2, after 20 min UV-Vis irradiation. Tests in the visible range ($400<\lambda<800$ nm) show that RP is ideal for indoor applications, with a~800% improvement of photocatalytic activity with respect to TiO_2, after 40 min visible light irradiation ($5mW/cm^2$). The photocatalytic activity of TiO_2-Gr is tested after mixing in an industrial concrete matrix, resulting in an increment of dye degradation of 50%. These data underpin the potential of GRM-PCs for smart surfaces. In a city such as Milan, covering 15% of visible urban surfaces with TiO_2-based cement photocatalysts would enable a reduction in pollution~50%. An efficient dispersion of the new cementitious coatings I have developed will allow to reach an abatement of the pollution of 90% with 2.5% surface covering. Furthermore the improved performance of TiO_2- Perylene photocatalysts in the visible range will extend the applications also in conditions where commercial TiO_2 do not perform well, such as in low sunlight (seasonal variations, north-located countries) and for indoor application, since the TiO_2-Perylene based photocatalysts can be activated also by visible light.

[1] U. N. A., Resolut. Adopt. by Gen. Assem. 25 Sept. 2015, 2015
[2]http://www.who.int/mediacentre/news/releases/ 2016/air-pollutionestimates/en/.
[3] H. Tong, et al. Adv. Mater., 24, 229 (2012)
[4]http://www.ti-line.net/
[5]http://www.italcementigroup.com/ITA/Ricerca+e+Innovazione/Prodotti+Innovativi/TX+Active/
[6] M. R. Hoffmann et al. Chem. Rev., 95, 69 (1995)
[7] R. Asahi et al. Science, 293, 269, (2001)

SMART SURFACES FOR ENVIRONMENTAL REMEDIATION. HIGHLY EFFICIENT PHOTOCALATYTIC NANOCOMPOSITES INCORPORATING METAL OXIDES AND GRAPHENE RELATED MATERIALS.

2.3.1. Kinetic photocatalytic tests of: TiO_2:Gr 10:1
2.3.2. Scanning Transmission Electron Microscopy (STEM): TiO_2:Gr 10:1
2.3.3. High-resolution powder X-Ray diffraction (HRPXRD) measurements: TiO_2:Gr 10:1
2.3.4. Raman spectroscopy TiO_2:Gr 10:1
2.3.5. Photophysical characterization: TiO_2:Gr 10:1
2.3.6. Problem in the interpretation of the mechanism of photocatalysis
2.3.7. Broadband TA spectroscopy: TiO_2:Gr 10:1
2.3.8. **Concluding remarks on Section 2.3:** the most performing material: TiO_2:Gr 10:1. Final interpretation of the photocatalytic mechanism in TiO_2/Gr PCs

2.4. Characterization of other composites: TiO_2:TMDCs/RP
2.4.1. Kinetic photocatalytic tests by means of fluorescence
2.4.1.1. Procedure and results
2.4.2. Absorption measurements
2.4.3. Scanning Electron Microscopy (SEM)
2.4.4. What happens during the sonication to the starting materials? HR-PXRD measurements on:
2.4.4.1. TiO_2 starting material
2.4.4.2. MoS_2 and WS_2starting material
2.4.4.3. TiO2/TMDCs nanocomposites
2.4.5. Raman spectroscopy
2.4.6. Surface area analysis: Brunauer–Emmett–Teller (BET) measurements
2.4.7. **Concluding remarks on Section 2.4:** characterization of the composites TiO_2:TMDCs/RP

2.5. Colloidal TiO_2 with Perylene
2.5.1. Synthetic pathway: Colloidal TiO_2- NPs and commercial Perylene.
2.5.2. Dynamic Light Scattering (DLS) characterization of colloidal modified TiO_2- NPs
2.5.3. Absorption measurements
2.5.4. Kinetic Photocatalytic tests
2.5.5. Photophysical characterization
2.5.5.1. Fluorescence quantum yield
2.5.5.2. Emission measurements

1. INTRODUCTION: PHOTOCATALYSTS FOR ENVIRONMENTAL REMEDIATION.

1.1. Environmental Pollution Outdoor and Indoor

Environmental pollution, especially toxic gases and organics in air and water, caused by anthropic activities, severely threaten ecological balance and human health[1]–[3]. Up to now the Environmental Protection Agency (EPA) identified classes of Hazardous Air Pollutants compounds, of organic and inorganic origin, and revised the national air quality standards for these substances[4]. The main organic pollutants are benzene derivatives (e.g. 1,2,4-trichlorobenzene, Nitrobenzene), polycyclic aromatic hydrocarbons (IPA; e.g. Chrysene, Anthracene, Benzo(ghi) perylene,. Pyrene, etc.). The main inorganic pollutants are: sulphur dioxide (SO_2), oxides of nitrogen (NO_X), carbon monoxide (CO), ozone, particular matter (PM) (with a diameter less than 10 millionths of a meter) and lead. For instance one of the parameters to monitor the air quality is the estimation of the $PM_{2.5}$, which includes also pollutants such as sulphate, nitrates and black carbon. Because of $PM_{2.5}$ diameter, this substance penetrate deep into the lungs and in the cardiovascular system, posing the greatest risks to human health. At local urban level, major polluters are blast-fuels vehicles, industries, thermoelectric power plants, fuels for domestic heating, combustion of waste, especially if unsuitable dust-abatement and fumigation systems are implemented.

Figure. 1 Graphic scheme of the world situation concerning the WHO guideline on the air pollution. More than 80% of people living in urban areas that monitor air pollution in 2016 are exposed to air quality levels that exceed the World Health Organization (WHO) limits.[5]

Cities are in fact the places where the sources of imbalance for the environment are most concentrated, with direct consequences also on the health of citizens. As shown in Figure 1, the result is that more than 80% of people living in urban areas that monitor air pollution in 2016 are exposed to air quality levels that exceed the World Health Organization (WHO) limits[5]

The 98% of cities in low- and middle income countries with more than 100000 inhabitants do not meet WHO air quality guidelines [5] for annual mean of particulate matter with a diameter of less than 2.5 micrometres (PM2.5), as it is possible to see from the map in Figure 2. WHO guideline limits for annual mean of $PM_{2.5}$ are 10 µg/m^3 annual mean.

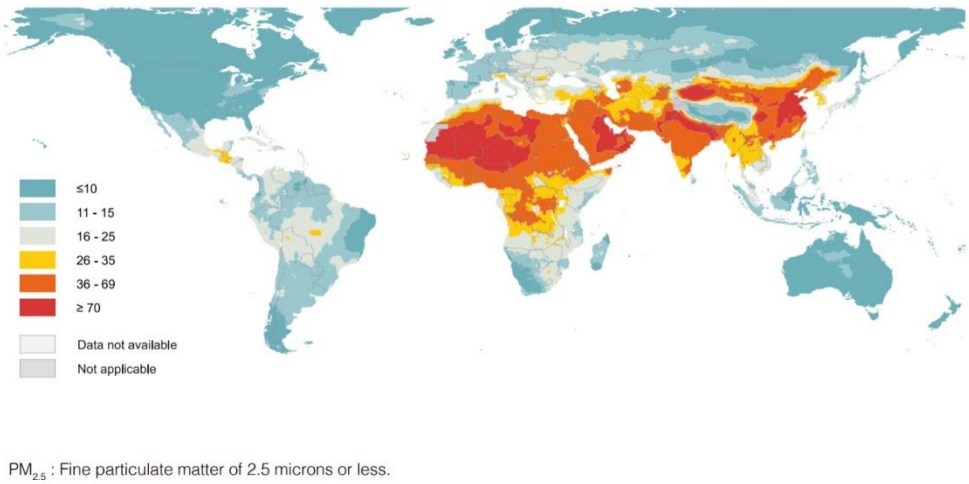

Figure. 2 Global map of modelled annual median concentration of PM2.5, in µg/m^3 (2016)[5].

Out of the conventional outdoor air pollution the WHO according to the EPA identified the problem of the **indoor** air pollution. Indoor air pollution is caused by the incomplete combustion of fuel in low-efficiency stoves and lamps used for cooking, space heating and lighting [6].

Consequences of the outdoor/indoor air pollution can be seen public health and the environment from climate change. In 2012, because of **outdoor air pollution**, almost 94% of deaths worldwide are due to non communicable diseases in adults, such as cardiovascular diseases (stroke and ischaemic heart disease), chronic obstructive pulmonary disease and lung cancers. The remaining deaths occur in children under five years of age due to acute lower respiratory infections (Figure 3).These health issues kills around 3 million people each year.

For the year 2012, the **indoor air pollution** was responsible of 4.3 million premature deaths worldwide, mostly in low- and middle income countries (LMICs) where there is a lack of access to clean or modern energy services[6]. The overall situation was evaluated in 2016, when WHO estimated that up to date **one out of every nine deaths was related to outdoor /indoor air pollution**[2]**,** while at least **1.8 billion people have used a contaminated drinking-water source**[3]**.**

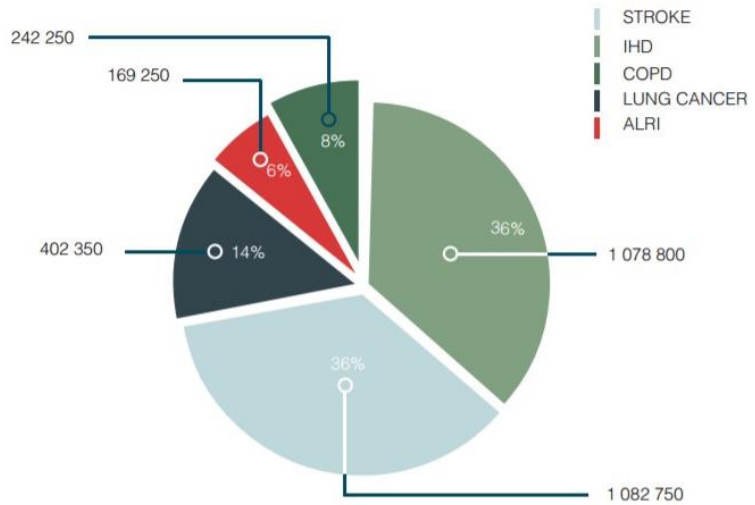

Figure. 3 Deaths attributable to AMBIENT AIR POLLUTION in 2012. Percentage represents percentage of total AAP burden. AAP: ambient air pollution; ALRI: acute lower respiratory disease; COPD: chronicobstructive pulmonary disease; IHD: Hischemic Heart Disease

Figure. 4scheme of the 17 Sustainable Development Goals (SDGs) of the 2030 Agenda for Sustainable Development[7].

On 25 September 2015, the United Nations General Assembly identified **air pollution as a global health priority in the 17 Sustainable Development Goals (SDGs) of the 2030 Agenda for Sustainable Development**[7], that on 1 January 2016 officially came into force (Goals 3,6,14),Figure 4. In November 2016[8], also the European Commission (EC) outlined its strategic approach towards the implementation of the 2030 Agenda, including the Sustainable Development Goals [7]. They provide concrete objectives for the next 15 years, focussed inter alia on:

1. human dignity,
2. regional and global stability,
3. healthier planet,
4. fair and resilient societies,
5. prosperous economies.

These decision reinforced the European Union (UE) objectives for 2020 and 2030 (H2020 and H3030 respectively) already adopted by EC in 2013 in the Clean Air Policy Package[9].

1.2. Semiconductors photocatalysts →TiO_2

All the above mentioned actions from UN and UE sides showed the need to have Healthier and Smarter Cities for the future World's population [5]–[9]. For air pollution remediation, the **environmental contaminants** (e.g. NO, NO_2, SO_2, suspended organic particulate, volatile organic compounds, aromatic hydrocarbons, etc.) **must be turned into harmless compounds** [10]**.**The design of new technologies to eliminate air pollutants **by using natural sunlight photocatalytic reactions**[11]**,** and their integration into smart cities is at the centre of an ever increasing research [12]. This can be done exploiting photocatalysts (PCs) able to absorb light and produce reactive holes and electrons that degrade the pollutants via redox processes. The rate at which the target molecules undergo photo-degradation, per absorbed photons and per unit time, is defined as the **photocatalytic quantum efficiency (PQE)**. Since the photocatalytic degradation uses solar energy and chemicals (the photocatalyst) which are not consumed in the process [11], [13], this technology is a promising, inexpensive and environmentally friendly solution for pollution abatement. Thus the important parameters in the choice of a photocatalyst with a good PQE are that:

1. The PCs **excitation energy ΔE** (the photon energy required in order to produce reactive electrons and holes) should match the natural solar light spectrum
2. The PCs **photogeneration yield** (**PY):** the number of photons that manage to produces reactive e-h pairs with respect of the photons that irradiate the system) has to be close to 1.
3. The **energy of the reactive electron/holes** has to reach the activation energy of the photodegradation starting reaction, expressed with respect of the energy of a normal hydrogen electrode (**E_{NHE}**), to perform photocatalytic reactions.
4. The **lifetime** (τ) of the **reactive e**/h has to be as long as possible in order to perform photocatalytic reaction. The recombination of the photo-generated e-h pairs causes a decrease of the PQE.

The use of semiconductors as PCs is a very convenient way to perform photocatalysis since they meet the above mentioned criteria. In order to reach the **ΔE**, the photon should overcome the semiconductor Energy bandgap (Eg, eV) of that is the energy required to promote one electron from

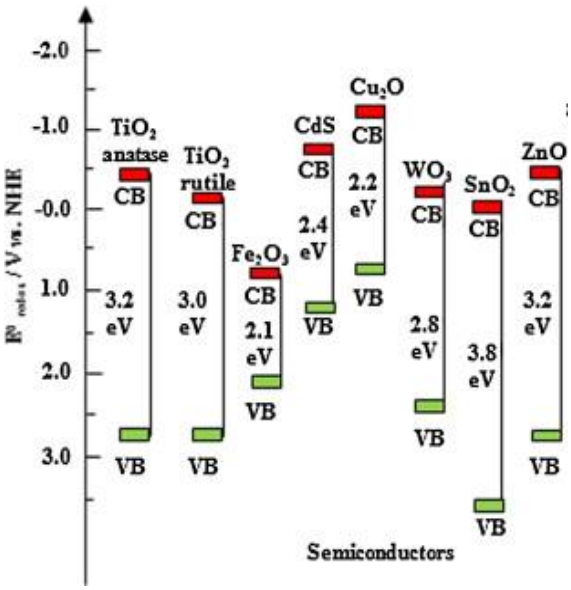

the valence band (VB) to the conduction band (CB), and leaving a hole in the VB. The Eg of lots of semiconductors (e.g. metal-oxides, metal-sulphides, metal-nitrides) lies within the energy spectral content of the sunlight from 3.55 to 0.62 eV (most of the power lies between 350 and 2000 nm)[14], as it is possible to notice from Figure 5 [15].

Figure. 5 Band gap of some photocatalysts with respect to the redox potential of different chemical species[15]

Furthermore, semiconductors have an electronic structure composed by a filled valence band (VB) and an empty conduction band (CB), so then there is a very efficient **photogeneration yield** [16]. Lastly the generation of reactive oxygen species [17] (ROS), (e.g. $OH^{\cdot}$, $O_2^{-\cdot}$), was identified as one of the main photodegradation mechanism of organic pollutants. The ROS reactions take place starting from the water and oxygen already present in the environment. So that the $\mathbf{E}_{NHE}$ of the following reactions has to be taken into account in the evaluation of a possible PCs[18]:

$$H_2O + h^+ (VB) \rightarrow OH^{\cdot} + H^+ \qquad \mathbf{E°_{NHE} \approx 2.27\ V} \qquad (Eq1)$$

$$O_2 + e^- (CB) \rightarrow O_2^{-\cdot} \qquad \mathbf{E°_{NHE} \approx -0.28\ V} \qquad (Eq2)$$

As it is possible to see from Figure 6 not all the PCs manage that have the Energy of the CB ($\mathbf{E_{CB}}$) above the $\mathbf{E}_{NHE}$ required for the $O_2^{-\cdot}$ production (Eq. 1), and neither the Energy of the VB ($\mathbf{E_{VB}}$) under the $\mathbf{E}_{NHE}$ required for the $OH^{\cdot}$ generation. In a basic environment, where there is an high concentration of $[OH^-]$ the generation of ROS is favoured since another reaction occur:

$$OH^- + h^+ (VB) \rightarrow OH^{\cdot} \qquad \mathbf{E°_{NHE} \approx 1.9\ V} \qquad (Eq3)$$

This reaction (Eq.3) is really important since it is located at a less positive potential than Eq. 1, so the photogenerated holes, that meet OH^- species, are more able to produce $OH^{\cdot}$ with respect of the one that meet H_2O.

Between all the semiconductor PCs is it possible to notice two classes (metal oxides, MX and Quantum dots, QD) which have demonstrated they efficiency in degrading a wide range of ambiguous refractory organics into readily biodegradable compounds, and eventually mineralized them to innocuous carbon dioxide and water [19].

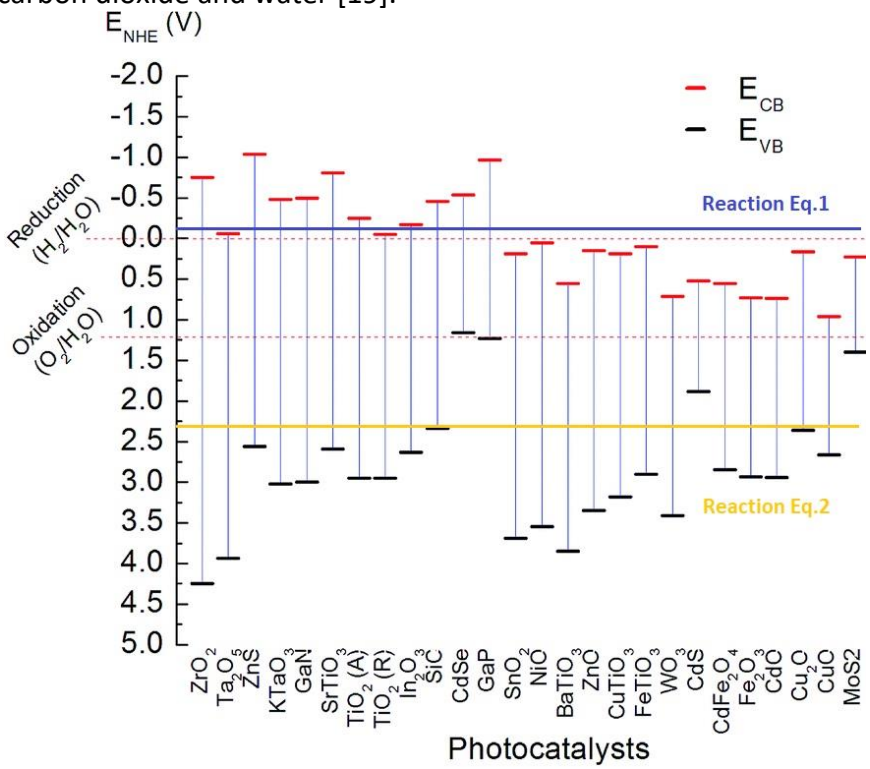

Figure. 6 CB and VB E_{NHE} of metal oxides and semiconductor photocatalysts [20] *and their position with respect of Eq.1 and Eq.2.*

The advantages in using MX (e.g. TiO_2, ZnO, FeO_3, WO_3, Fe_2O_3) with respect of QD(e.g. CdS, GaP, ZnS) is that MX in general remain stable after the repeated catalytic cycles, whereas Cds or GaP are degraded along to produce toxic products[21]. Amongst the oxide semiconductor photocatalysts (such as ZnO, FeO_3, WO_3 [20]), titanium dioxide nanoparticles (TiO_2-NPs),in its anatase form (A), have been widely used for a range of applications, including self-cleaning [20]and surfaces sterilization [22], air [23] and water [24]purification. For the above mentioned reasons I decided to **focus** my attention **on TiO_2-NPs as semiconductor PCs.**

1.2.1. Photocatalytic reactions of TiO_2

As described in the section above, PCs as are able to absorb light and produce reactive holes(h) and electrons (e) in valence and conduction bands respectively (Eq4)[25]. In particular TiO_2 has a band gap (Eg) ≈3.25 eV[10]), and, as a result, can be activated as PC only with the UV part of the solar spectrum[26]

$TiO_2 + hv(UV) \rightarrow TiO_2(e^-(CB) + h^+(VB))$ *(Eq4)*

These reactive carriers can degrade directly via redox processes the pollutants(X) that gets in contact with the surface of PCs (Eq.5-6) [26].

$S + h^+ \rightarrow$ *oxidation products* *(Eq5)*

$S + e^- \rightarrow$ *reduction products* *(Eq6)*

Otherwise e/h can react with H_2O (Eq7) and O_2 (Eq8) and generate reactive oxygen species (Eq7-11)[17] (ROS) (e.g. $O_2^{-\cdot}$; $HOO^{\cdot}$; $OH^{\cdot}$ that with several redox steps brig contaminants to be degraded (Eq12)[26].

$H_2O + h^+(VB) \rightarrow OH^{\cdot} + H^+$ *(Eq7)*

$O_2 + e^-(CB) \rightarrow O_2^{-\cdot}$ *(Eq8)*

$O_2^{-\cdot} + H^+ \rightleftarrows HOO^{\cdot}$ *(Eq9)*

$2HOO^{\cdot} \rightarrow H_2O_2 + O_2$ *(Eq10)*

$H_2O_2 \rightarrow 2OH^{\cdot}$ *(Eq11)*

$S + OH^{\cdot} \rightarrow H_2O + S$ *(degradation intermediates)* *(Eq12)*[25]

All the above mentioned reaction occurs in the proximity of the TiO_2 surface, and bring the pollutants to be degraded after several reaction steps, Figure 7.

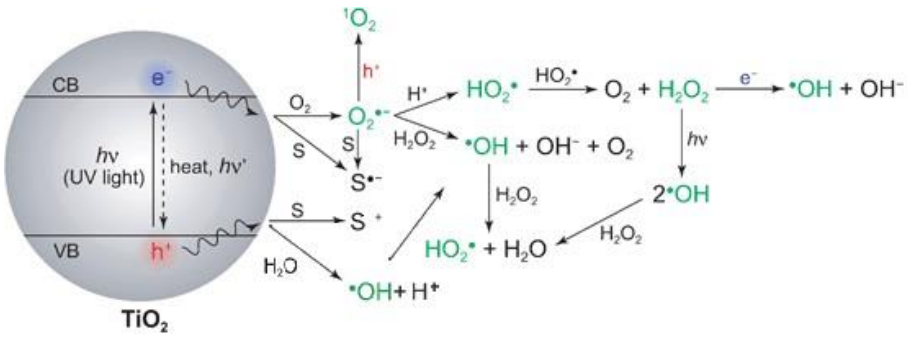

Figure. 7 Photo- reactions above the absorption of a photon (hv) in a semiconductor PCs, and the generation of ROS and the direct degradation and S.

1.2.2. Anatase TiO_2-NPs Pros and cons

TiO_2-NPs, in its anatase form (A), have been widely used for a range of applications[20], [22]–[24]. Anatase is the most active allotropic form [27]. among the various ones available, either natural (rutile(R) and brookite) or artificial (TiO_2–B, TiO_2–H)[26]. Even if both R and A belongs to a tetragonal crystallographic form, A is thermodynamically less stable than R and A formation is kinetically favoured at lower temperature (<600°C)[28]. This lower temperature could explain higher surface area, and a higher surface density of active sites for adsorption and for catalysis. Anatase has a larger band gap than rutile TiO_2 (~3.0 for R and ~3.2 for A)[15].The evidence of the different reactivity are reported, the anatase (101) crystallographic surface exhibits a higher photocatalytic activity than all investigated rutile surfaces [29]. These results explain why the TiO_2 in its A form is preferred in the production of photocatalysis. From now on the discussion will be focused on TiO_2-NPs (A).

The motivations of the wide use of the TiO_2-NPs are based on its the **pros** of:

1. stability in water[21];
2. non-toxicity[10];
3. low cost (1.9K USD/Ton at 2016 prices[30]);
4. good photocatalytic performances[15], [16], [18]

On the other hand, the **cons** of the use of the TiO_2 are that:

1. **High and narrow range of ΔE**, and **low PY with respect of** the photon energies available from **the solar spectrum**→it can be activated as PC only with the UV part of the solar spectrum hv<3.2eV (380nm). For this reason the TiO_2-based PCs are not active, and used, in indoor conditions where the UV component of the solar light is not present[31]. This is a drawback also for outdoor applications since the UV light is just ∼4% of the total solar radiation resulting in the ∼96% waste of useful energy to perform the photodegradation processes[28], [32];
2. **Low τ** (High e/h pair recombination) and consequently **low PQE**→the 90%[33] of sunlight that manage to activate TiO_2-NPs is lost because the recombination of the photo-generated electron-hole pairs. Hence, a key problem in the application of TiO_2-NPs in surfaces for pollutants degradation in outdoor applications, is to increase the efficacy of the PC to tackle and partially compensate its limited activity.

1.3. Concluding remarks on Chapter 1

How to solve TiO_2 drawbacks?

The purpose of this work

The **PQE** of a PCs can be **enhanced** playing on the modifications of the **ΔE**, the **PY**, the E_{CB} / E_{VB}. and the τ of e/h pair as explained in the section 1.2. In order to solve TiO_2-NPs cons, these PCs can be **modified** in order to broaden the photoresponse of TiO_2 catalyst for solar spectrum, and bring it to have a lower edge of ΔE (modification of the Eg) [19], [34]–[36]. This can be done with a direct modification of TiO_2 nanostructure [34], [35] during the synthesis by using: **noble metals or metal ions incorporation** [37]; **transition metals** [38] **and non-metals doping**[32], Figure 8. Furthermore in order to slow down the recombination of the photo-generated e-h pairs a possible modification can be the functionalization with compounds able to accept electron/holes (such as carbon nanomaterials). This is expected to slow down the charges recombination in the semiconductor, leading to an increase of the PQE and of the photocatalytic activity of TiO_2. For this reason in the recent years, the integration of TiO_2 with **carbon nanomaterials** (such as nanotubes[39], carbon dots[40], graphene oxide[41], reduced graphene oxide[42] has been studied from the scientific community. Another Type of TiO_2 modification can be the use of **organic (e.g. perylenes)** [43]–[45]**or inorganic (e.g. MoS_2**[46]**, WS_2**[47], QD) **dyed sensitizers** [48]. This type of modification plays a role in the enhancement of the PY. In general the sensitizer has a very good and broad ΔE, but it does not manage to perform photocatalytic reaction alone. So the excited sensitizer under solar illumination can provide additional electrons to the CB of TiO_2 for enhancing the formation of electron–hole pairs and the PQE.

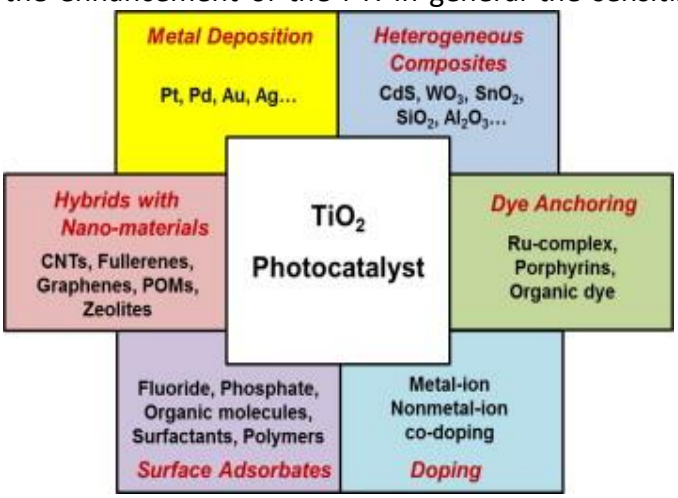

Figure. 8 Various modification methods of TiO_2 photocatalyst [35]

In this work is reported the developments of a new generation of photocatalysts, TiO_2-based (Chapter 2) or different semiconductors PCs nanocomposite able to photodegrade pollutants, more efficient than the already existing TiO_2 based photocatalyst. The effort was devoted to the design of PCs able to overcome TiO_2 drawbacks and ideally convert, with the highest PQE efficiency, all the photon energy of the entire solar spectrum in a long living e/h pair for the photodegradation of air pollutants and PCs real market application into photocatalytic cementitious surfaces(chapter 3). The properties of this new generation photocatalysts were also applied exploited in perovskite solar cells (chapter 3).

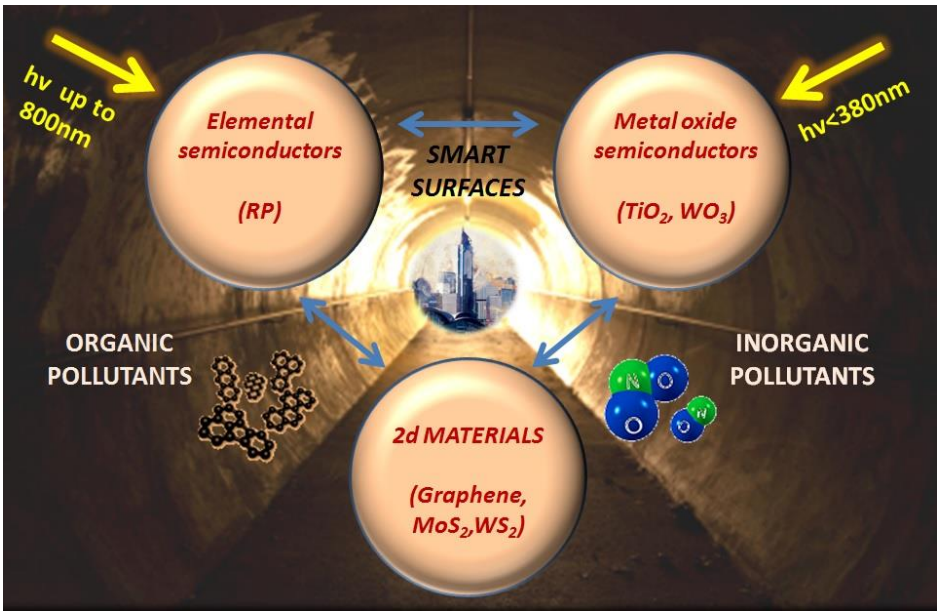

Figure. 9 Scheme of the photocatalytic nanocomposites composition in photodegradation of volatile pollutants.

Since the real application of these a new generation of photocatalysts can be reached using an industrial approach, the focus of this work is on the modification of commercial powder of TiO_2, by using graphene (but also transition metal dicalcogenides(TMDC) or Red phosphorus (RP)). Another approach is the modification of colloidal TiO_2, whose can be easily synthesized in large volume, with organic sensitizers (e.g. Perylene)(chapter 2). All the components used to enhance TiO_2 performances (e.g. Graphene and perylenes) were studied in different way to have a overall knowledge of the above mentioned systems (chapter 4,5).

1.4. Bibliography chapter 1

[1] "No Title," *http://www.who.int/topics/en*.

[2] "No Title," *http://www.who.int/mediacentre/news/releases/ 2016/air-pollution-estimates/en/.*

[3] "No Title," *https//www.unicef.org/publications/files/ Progress_on_Drinking_Water_Sanitation_and_ Hyg.*

[4] "No Title," *https://www.epa.gov/clean-air-act-overview/air-pollution-current-and-future-challenges*.

[5] "No Title," *http://www.who.int/phe/health_topics/outdoorair/databases/cities/en/*.

[6] WHO, "No Title," *Indoor air Qual. Guidel. Househ. fuel Combust.*, 2014.

[7] . U. N. A., "No Title," *Resolut. Adopt. by Gen. Assem. 25 Sept. 2015*, 2015.

[8] "No Title," *http://www.un.org/en/ga/search/view_doc.asp?symbol=A/RES/70/1&Lang=E*.

[9] "No Title," *http://ec.europa.eu/environment/air/clean_air/index.htm*.

[10] M. R. Hoffmann, S. T. Martin, W. Choi, and D. W. Bahnemann, "Environmental applications of semiconductor photocatalysis," *Chem. Rev.*, vol. 95, no. 1, pp. 69–96, 1995.

[11] H. Tong, S. Ouyang, Y. Bi, N. Umezawa, M. Oshikiri, and J. Ye, "Nano-photocatalytic materials: possibilities and challenges," *Adv. Mater.*, vol. 24, no. 2, pp. 229–251, 2012.

[12] M. Fleisch and D. Bahnemann, "Photocatalitically Active Concrete: How Innovative Construction Materials Can Contribute to the Degradation of Dangerous Air Pollutants," *Beton- Und Stahlbetonbau*, vol. 112, pp. 47–53, 2017.

[13] Q. Zhang *et al.*, "Achieving significantly enhanced visible-light photocatalytic efficiency using a polyelectrolyte: the composites of exfoliated titania nanosheets, graphene, and poly(diallyl-dimethyl-ammonium chloride)," *Nanoscale*, vol. 7, no. 33, pp. 14002–14009, 2015.

[14] J. V Gómez, F. E. Sandnes, and B. Fernández, "Sunlight intensity based global positioning system for near-surface underwater sensors," *Sensors*, vol. 12, no. 2, pp. 1930–1949, 2012.

[15] O. Ola and M. M. Maroto-Valer, "Review of material design and reactor engineering on TiO 2 photocatalysis for CO 2 reduction," *J. Photochem. Photobiol. C Photochem. Rev.*, vol. 24, pp. 16–42, 2015.

[16] A. Mills and S. Le Hunte, “An overview of semiconductor photocatalysis,” *J. Photochem. Photobiol. A Chem.*, vol. 108, no. 1, pp. 1–35, 1997.

[17] T. Hirakawa and Y. Nosaka, “Properties of O2•-and OH• formed in TiO2 aqueous suspensions by photocatalytic reaction and the influence of H2O2 and some ions,” *Langmuir*, vol. 18, no. 8, pp. 3247–3254, 2002.

[18] A. Fujishima, T. N. Rao, and D. A. Tryk, “Titanium dioxide photocatalysis,” *J. Photochem. Photobiol. C Photochem. Rev.*, vol. 1, no. 1, pp. 1–21, 2000.

[19] M. N. Chong, B. Jin, C. W. K. Chow, and C. Saint, “Recent developments in photocatalytic water treatment technology: a review,” *Water Res.*, vol. 44, no. 10, pp. 2997–3027, 2010.

[20] Y. Lai *et al.*, “Recent Advances in TiO2-Based Nanostructured Surfaces with Controllable Wettability and Adhesion,” *Small*, vol. 12, no. 16, pp. 2203–2224, 2016.

[21] T. Xia *et al.*, “Comparison of the abilities of ambient and manufactured nanoparticles to induce cellular toxicity according to an oxidative stress paradigm,” *Nano Lett.*, vol. 6, no. 8, pp. 1794–1807, 2006.

[22] S. Nishimoto and B. Bhushan, “Bioinspired self-cleaning surfaces with superhydrophobicity, superoleophobicity, and superhydrophilicity,” *Rsc Adv.*, vol. 3, no. 3, pp. 671–690, 2013.

[23] A. H. Mamaghani, F. Haghighat, and C.-S. Lee, “Photocatalytic oxidation technology for indoor environment air purification: The state-of-the-art,” *Appl. Catal. B Environ.*, vol. 203, pp. 247–269, 2017.

[24] C. Yu, W. Zhou, H. Liu, Y. Liu, and D. D. Dionysiou, “Design and fabrication of microsphere photocatalysts for environmental purification and energy conversion,” *Chem. Eng. J.*, vol. 287, pp. 117–129, 2016.

[25] A. Ajmal, I. Majeed, R. N. Malik, H. Idriss, and M. A. Nadeem, “Principles and mechanisms of photocatalytic dye degradation on TiO 2 based photocatalysts: a comparative overview,” *Rsc Adv.*, vol. 4, no. 70, pp. 37003–37026, 2014.

[26] A. L. Linsebigler, G. Lu, and J. T. Yates Jr, “Photocatalysis on TiO2 surfaces: principles, mechanisms, and selected results,” *Chem. Rev.*, vol. 95, no. 3, pp. 735–758, 1995.

[27] M. D. Hernández-Alonso, F. Fresno, S. Suárez, and J. M. Coronado, “Development of alternative photocatalysts to TiO 2: challenges and opportunities,” *Energy Environ. Sci.*, vol. 2, no. 12, pp. 1231–1257, 2009.

[28] X. Chen and S. S. Mao, “Titanium dioxide nanomaterials: synthesis, properties, modifications, and applications,” *Chem. Rev*, vol. 107, no. 7, pp. 2891–2959, 2007.

[29] A. Y. Ahmed, T. A. Kandiel, T. Oekermann, and D. Bahnemann, “Photocatalytic activities of different well-defined single crystal TiO2 surfaces: anatase versus

rutile," *J. Phys. Chem. Lett.*, vol. 2, no. 19, pp. 2461–2465, 2011.

[30] http://www.cnchemicals.com/Press/88893-CCM:%20TiO2%20price%20in%20China%20still%20booming%20in%20December%202016.html., "No Title."

[31] C. Tuchinda, S. Srivannaboon, and H. W. Lim, "Photoprotection by window glass, automobile glass, and sunglasses," *J. Am. Acad. Dermatol.*, vol. 54, no. 5, pp. 845–854, 2006.

[32] A. Fujishima, X. Zhang, and D. A. Tryk, "TiO2 photocatalysis and related surface phenomena," *Surf. Sci. Rep.*, vol. 63, no. 12, pp. 515–582, 2008.

[33] N. Serpone, D. Lawless, and R. Khairutdinov, "Size effects on the photophysical properties of colloidal anatase TiO2 particles: size quantization versus direct transitions in this indirect semiconductor?," *J. Phys. Chem.*, vol. 99, no. 45, pp. 16646–16654, 1995.

[34] C. Y. Wang, C. Y. Liu, and T. Shen, "Surface modification of semiconductor photocatalyst," *Chem. J. CHINESE Univ.*, vol. 19, no. 12, pp. 2013–2019, 1998.

[35] H. Park, Y. Park, W. Kim, and W. Choi, "Surface modification of TiO2 photocatalyst for environmental applications," *J. Photochem. Photobiol. C Photochem. Rev.*, vol. 15, no. Supplement C, pp. 1–20, 2013.

[36] S. M. Gupta and M. Tripathi, "A review of TiO2 nanoparticles," *Chinese Sci. Bull.*, vol. 56, no. 16, p. 1639, 2011.

[37] M. Ni, M. K. H. Leung, D. Y. C. Leung, and K. Sumathy, "A review and recent developments in photocatalytic water-splitting using TiO2 for hydrogen production," *Renew. Sustain. Energy Rev.*, vol. 11, no. 3, pp. 401–425, 2007.

[38] M. I. Litter, "Heterogeneous photocatalysis: transition metal ions in photocatalytic systems," *Appl. Catal. B Environ.*, vol. 23, no. 2, pp. 89–114, 1999.

[39] K. Dai, T. Peng, D. Ke, and B. Wei, "Photocatalytic hydrogen generation using a nanocomposite of multi-walled carbon nanotubes and TiO2 nanoparticles under visible light irradiation," *Nanotechnology*, vol. 20, no. 12, p. 125603, 2009.

[40] M. Sun, X. Ma, X. Chen, Y. Sun, X. Cui, and Y. Lin, "A nanocomposite of carbon quantum dots and TiO 2 nanotube arrays: enhancing photoelectrochemical and photocatalytic properties," *Rsc Adv.*, vol. 4, no. 3, pp. 1120–1127, 2014.

[41] K. R. Reddy, M. Hassan, and V. G. Gomes, "Hybrid nanostructures based on titanium dioxide for enhanced photocatalysis," *Appl. Catal. A Gen.*, vol. 489, pp. 1–16, 2015.

[42] L. Han, P. Wang, and S. Dong, "Progress in graphene-based photoactive nanocomposites as a promising class of photocatalyst," *Nanoscale*, vol. 4, no. 19, pp. 5814–5825, 2012.

[43] S. Ferrere and B. A. Gregg, “New perylenes for dye sensitization of TiO2,” *NEW J. Chem.*, vol. 26, no. 9, pp. 1155–1160, 2002.

[44] S. Wang *et al.*, “Dye sensitization of nanocrystalline TiO2 by perylene derivatives,” *Synth. Met.*, vol. 128, no. 3, pp. 299–304, 2002.

[45] L. I. Hernández *et al.*, “Spectral Characteristics and Photosensitization of TiO2 Nanoparticles in Reverse Micelles by Perylenes,” *J. Phys. Chem. B*, vol. 117, no. 16, pp. 4568–4581, Apr. 2013.

[46] W. Zhou *et al.*, “Synthesis of Few-Layer MoS2 Nanosheet-Coated TiO2 Nanobelt Heterostructures for Enhanced Photocatalytic Activities,” *SMALL*, vol. 9, no. 1, pp. 140–147, 2013.

[47] W. K. Ho, J. C. Yu, J. Lin, J. G. Yu, and P. S. Li, “Preparation and photocatalytic behavior of MoS2 and WS2 nanocluster sensitized TiO2,” *LANGMUIR*, vol. 20, no. 14, pp. 5865–5869, 2004.

[48] K. Vinodgopal and P. V Kamat, “Photochemistry on surfaces: photodegradation of 1, 3-diphenylisobenzofuran over metal oxide particles,” *J. Phys. Chem.*, vol. 96, no. 12, pp. 5053–5059, 1992.

2. STUDY OF NEW PHOTOCATALYTIC MATERIALS

2.1. How to test the photocatalytic activity against environmental pollutants: dyes and lights

How can we can test photoactive nanocomposites? Pollution is everywhere even if it's not visible. In order to evaluate the photocatalytic activity of the PCs we need to have molecules that can mimic the behaviour of the molecular pollutants that gets in contact with the PCs, but in the mean time they can be also easily detectable in order to monitor their degradation. In this study the photocatalytic activity is investigated by following the photo-degradation of a molecular non azo-dye, Xanthene (Rhodamine B; RhB), or a Thiazine (Metylene Blue; MB) as model compound for an organic pollutant, since their molecular structures are close to that of the environmental contaminants used in industry and agriculture[1]. Their degradation can be easily quantified by using simple analytical technique such as UV-Vis and fluorescence spectroscopy. The photocatalytic experiments are performed in order to simulate the degradation of pollutants in outdoor conditions as well as indoor.

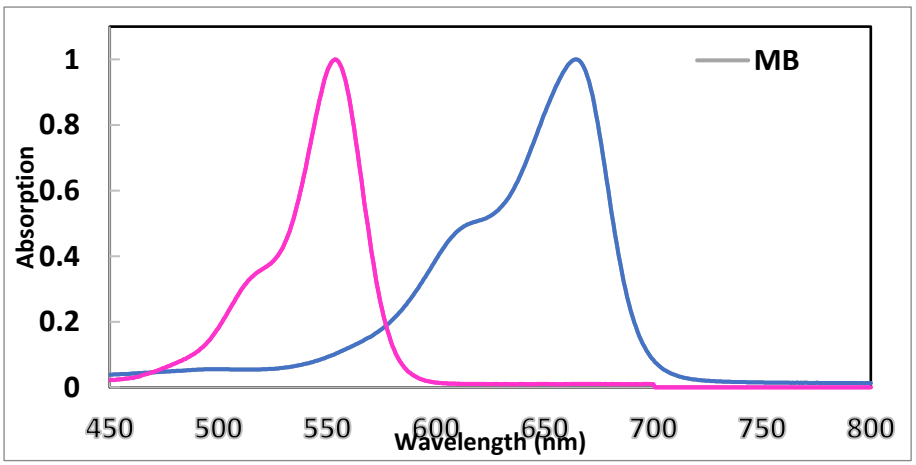

Figure. 1 Absorption spectra of MB and RhB in the Vis range 450-800nm

The difference in those two applications is the type of light, and consequently the energy of the photons, that is normally present in these two conditions. In indoor conditions the UV component of the solar light is not present[2], since: firstly the illumination from bulbs is in the range of 400-800 nm, and second part of the UV component of the natural sunlight is catted off from the windows of the houses. So that in order to simulate the performance of the PCs in those two conditions we used two different light sources with different irradiation wavelengths. The choice of the molecular compound to evaluate the photocatalytic activity of the PCs under UV and Vis light is crucial since the use of particular irradiation wavelength can activate the molecular dye with a subsequent sensitization of the TiO_2. In fact the light assisted degradation process involves the initial excitation of the surface adsorbed dye followed by the charge injection to the conduction band of the semiconductor. This process bring to the production of additional reactive electrons in the CB of TiO_2 and a consequent enhancing theTiO_2 degradation mechanism. The evaluation of this effect can be estimated by the ΔE and the energies E_{NHV} of the LUMO (Lowest unoccupied molecular orbital) and HOMO(highest occupied molecular orbital) levels of the dyes with respect of the E_{NHV} of the CB and VB of TiO_2. Figure 1 reports the absorption spectra of the RhB and MB, which reflects more or less the ΔE of a semiconductor. Both MB and RhB absorb in the Vis range, so they can in principle sensitize the TiO_2. But if we look at the position of the HOMO and LUMO the situation is different. Unlike RhB, the MB cannot work as the photo-sensitizer on TiO_2 due to the unmatched band position between dyes and TiO_2(A)[3]. Because of all the considered parameters tests the Outdoor conditions were tested

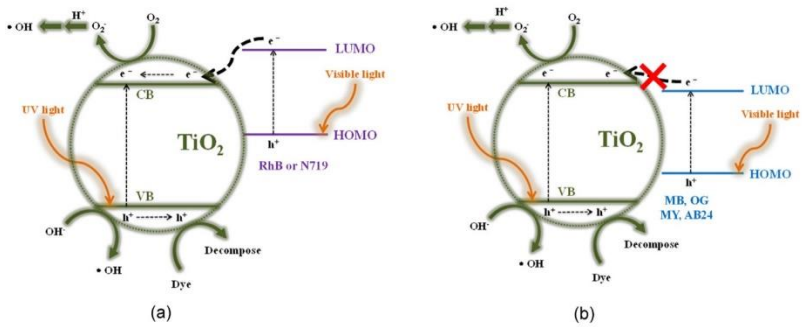

Figure. 2 Schematic mechanisms illustrate (a) matched and (b) unmatched band position between LUMO of dyes and CB of A-TiO_2. The enhanced photo-sensitizing current and the generation of highly oxidative species on the A-TiO_2 surface are expected to occur via mechanism (a) [3]

Because of all the considered parameters tests the **Outdoor Conditions** were tested with a UV/VIS mercury lamp, with RhB (Figure 3). The photoreactivity is investigated after photoexcitation of the TiO_2 by exposing each sample to a UV Mercury lamp (RadiumSanoluxHRC300-280E27) which emits in the UVA/UVB range (280-400nm). The lamp has irradiance I (W/m2),defined as emitted power per unit area, equal to I = 3 W/m2 in the UVA (280-315nm) and to I = 13.6 W/m2 in the UVB (315nm-400nm), at 0.5m from the irradiation source. Taking into account these parameters and placing our sample 35 cm from the lamp, we evaluate a power of 0.15 mW/cm^2 in the UVA/UVB range on the surface of the solution.

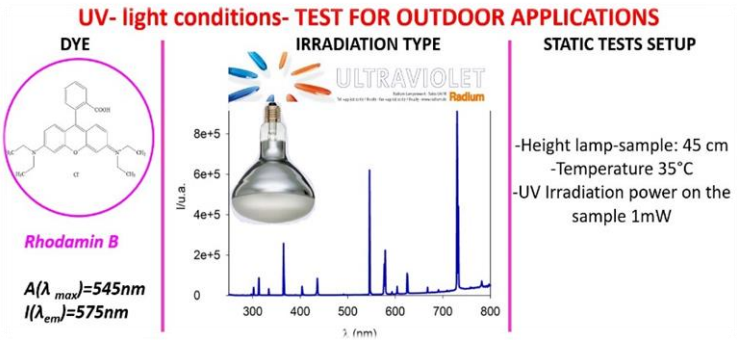

Figure. 3 Conditions and materials used to perform photocatalytic tests in outdoor conditions: (left) dye used, (center) spectra of the irradiation lamp, (right) set up conditions for the irradiation.

The **Indoor Conditions** were tested with a VIS LED light (400-800nm), with MB (Figure 4). The lamp is a 200W (Warm White 2700-3500k) Solla LED Flood Light. Taking into consideration the irradiation parameters, the lamp was putted at an height of 20 cm obtaining a power of 0.7mW/cm^2 on the surface of the samples.

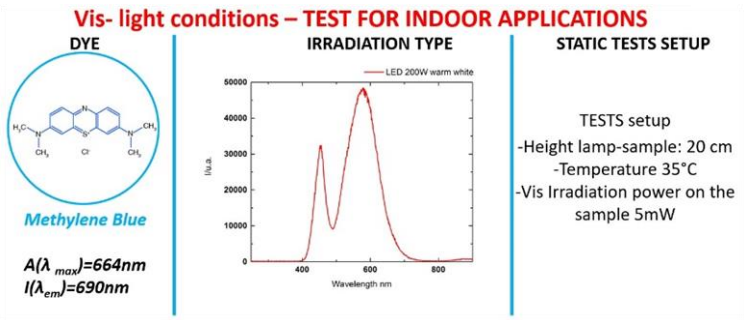

Figure. 4 Conditions and materials used to perform photocatalytic tests in indoor conditions: (left) dye used, (centre) spectra of the irradiation lamp, (right) set up condition of the irradiation.

2.1.1. Photocatalytic tests

This test follows the same procedures reported to characterize other TiO_2-carbon composites[4], [5]. TiO_2-based PCs are dispersed in an aqueous solution. In order to allow a correct comparison of the samples to understand the effect of the dopants on the PQE of TiO_2, the amount of the catalyst used in each experiment is chosen to guarantee the same quantity of TiO_2 (2mg/ml) inside each suspension. Considering the affinity of graphitic flakes, 2d materials and porous nanoparticles for polycyclic aromatic and cationic compounds like MB or RhB, the suspensions are left in the dark for 40 minutes, in order to attain adsorption-desorption equilibrium between the solid PCs and the dye. Actually, it has been recently shown [6] that, when RhB is physically adsorbed onto graphene flakes, there is a ground state interaction that brings to a decrement in the intensity of the UV/Vis absorption and of the emission of the dye. Since this interaction is just with the graphene surface, after a certain period of time, saturation occurs and the concentration of free RhB stops decreasing [7]. As well as **the adsorption** phenomenon happens with graphene, there can be an adsorption effect with the other materials that are present in the newly synthesized nanocomposites. Than it is important to determine the fraction of dye that remains free inside the solution. This information is necessary to discriminate whether the change in the dye concentration under irradiation is exclusively due to a photoreaction or to adsorption. The concentration CD (mol L^{-1}) of free RhB/MB present in solution after incubation in the dark is derived from the UV/Vis absorption spectra (λmax RhB=554nm, λmax MB=554nm). Then, the percentage Ads of dyes adsorbed on the composites is calculated starting from the initial concentration C0 (mol·L^{-1}) of the used dye, as follows (Eq 13):

$$Ads = \left[\frac{(C_0 - C_D)}{C_0}\right] * 100$$

The **photoreactivity** in indoor /outdoor is investigated after photoexcitation of the PCs by exposing each sample to the irradiation of the Vis or UV lamp respectively. Then the suspensions are irradiated for a fix time (t) and the collected volumes are centrifuged, diluted and analysed with the same procedure explained for the determination of CD, detecting the concentration C(t) of RhB/MB not degraded after the time interval t from the

beginning of the irradiation. The percentage of dye photodegraded, P(t) is calculated as [8] (Eq 14):

$$P(t) = \left[\frac{(C_D - C_I)}{C_0}\right] * 100$$

Using this approach, the photocatalytic activity is assessed independently of the possible adsorption of the dye onto the surface of the photoactive materials, since the concentration of the dye after pre-equilibration is taken as a reference.

In order to test a range of different type of photocatalyst we set a **preliminary photocatalytic test**, and then, for the most promising PCs further photocatalytic characterization in terms of kinetic photocatalytic tests. The advantage of this test is that it:

- Uses a **law quantity** of materials in terms of PCS powders and dyes
- **Is fast** since the optimization of the irradiation conditions allowed us to irradiate the samples for tens of minutes(Figure
- Allows to analyse up to **multiple samples simultaneously**, since the position of the lamp allows to irradiate with the same power an homogeneous space to place the samples.

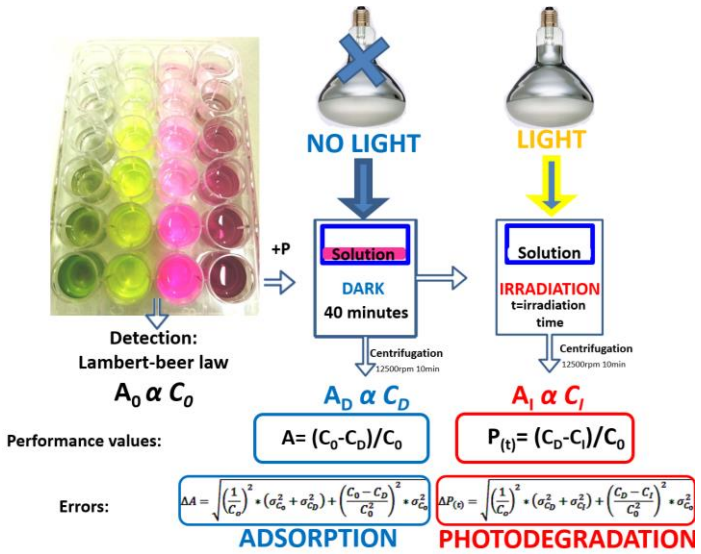

Figure. 5 Scheme of the photocatalytic procedure in order to obtain Absorption and Photocatalytic activity of the synthesized PCs

The procedure is the following (see figure 5, 6):

1. 500µl of the photocatalyst mixture with TiO_2 content (2mg/ml) and 200µl of dye solution ($1 \cdot 10^{-4}$ M) are loaded in the well plates of a Multiwell Plates Platform (dia. 1.55cm).
2. The platform is left in the dark for 40 min in order to allow the formation of the adsorption equilibrium, and detect the adsorption value for each PCs.
3. The platform is irradiated with the given lamp for indoor or outdoor tests (see Figure 3,4) for a fix period of time
4. The solution is centrifuged at 12500 rpm for 10 min, to remove the photocatalyst and stop the photocatalytic reaction. The upper 0.5ml of each centrifuged sample is collected and then diluted with water (1:6 ratio) to reach the 3ml volume of analysis of a standard cuvette for a UV/Vis spectrophotometer.
5. UV-VIS absorption spectra were recorded at 25°C by means of Cary 300 UV-Vis spectrophotometer (Agilent Technologies).
6. The absorption values are then correlate to the concentration of the dye through the Lambert- Beer Law (Figure 6): A0 is proportional to C0, AD to CD and AI to CI.
7. The elaboration of the data allows the estimation of the %P and % Ads and the overall evaluation of the photocatalytic activity of the samples that is an estimation of the PQE of the PCs(see Eq 13 and 14).

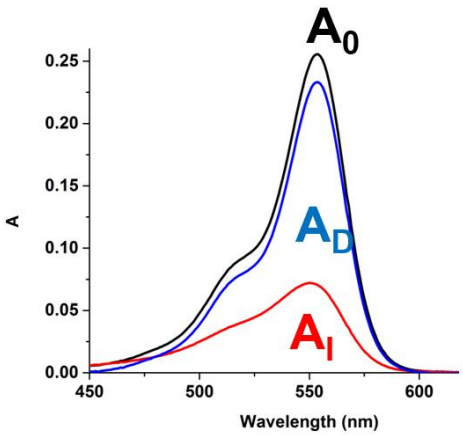

Figure. 6 Example of the absorption value of RhB dye during a photocatalytic test. A0 is the absorption of the pristine solution of RhB, Ad is the absorption of the RhB solution after the incubation in the dark with the photocatalyst, and AI is the absorption after 10 minutes irradiation of the system. In every case the absorption value is proportional to the amount of RhB left inside of the solution.

2.2. Commercial TiO_2 with Graphene/2d materials/ semiconductor via bath sonication

In this section is reported the preparation of a TiO_2/GRMs doped photocatalyst. The preparation involves a sonication-assisted exfoliation of graphite/2d materials or semiconductors in bulky powder form, in presence of TiO_2-NPs, using commercial starting materials available in large scale. This synthetic process is necessary to :

1. Promote the physical interaction between TiO_2 and GRMs and, as a consequence, allow the energy transfer between the two subunit, after the photo-excitation of the system;
2. Exfoliate the GRMs, since the exfoliation process brings a size quantization effect that can affect the EA, Eg and E_{NHV} of CB and VB gap of the TiO_2 sensitizer.

2.2.1. Focus on Graphene as TiO_2 sensitizer

As explained in the previous sections, the recombination of the photo-generated e-h pairs in the TiO_2 structure as well as its limited solar spectrum absorption cause a decrease of the PQE. The integration of TiO_2 with carbon nanomaterials, such as nanotubes[9], carbon dots[10], graphene oxide[11], reduced graphene oxide[12] has been pursued to enhance its PQE. The effectiveness of incorporation of carbon based materials in improving TiO_2's PQE, is documented in a number of studies [4], [5], [11]–[44]. Between all the carbon nanomaterials, **graphene** is a carbon sheet only one atom thick made of sp^2 carbon, and it is the prototype of two-dimensional materials[45] that can be obtained through exfoliation of graphite. Exfoliate graphite means overcome the forces of π-π stacking within the flake graphite and produce a 2d honeycomb structured material: graphene. The optical absorption coefficient of a single layer graphene is ≈2.3% in visible light, furthermore the absorption is in a broad spectral range, from UV to IR and THz. Graphene is a conductor (Eg= 0 eV) since it has an high thermal conductivity κ (∼2000 to 5300 W m^{-1} K^{-1} and can withstand high current densities (million times higher than copper). Facing these properties, the functionalization of TiO_2 with

graphene, that is able to: i)accept electron/holes slowing down the charges recombination in the semiconductor; ii) sensitize it with different irradiation wavelength; would lead an increment of the photocatalytic activity of TiO_2.

2.2.2. Focus on 2d materials (MoS_2,WS_2) and semiconductors (RP) as TiO_2 sensitizer

During the past 20 years TMDCs, in particular molybdenum and tungsten dichalcogenides, have been extensively studied because of their tuneable electronic structure that makes them attractive for a variety of applications[46]–[48]. These materials can in principle act as sensitizers in the same way of graphene. However, the CB energy levels of bulk **MoS_2 and WS_2** are less negative than that of TiO_2. This means that TiO_2 is not able to accept electrons from these potential sensitizers[49]. Because of the effect of quantum confinement, the redox potentials as well as the band gaps of MoS_2 and WS_2 nanoclusters can be increased significantly. This tuning of the properties can be reached with a physical modification, in terms of thickness and lateral size of the bulk powders. In fact TMDs are layered materials with strong in-plane bonding and weak out-of-plane interactions and this allows their exfoliation into two-dimensional layers of single unit cell thickness[47]. The few-layered dichalcogenides, obtained either through exfoliation of bulk materials or bottom-up syntheses are direct-gap semiconductors, whose bandgap energy, varies between compounds depending on their composition, structure and dimensionality, see figure 7. Furthermore their characteristics influence the carrier type and they can behave as n- or p-type semiconductors [48]. Evidence of the interaction between TiO_2 and TMDCs in the enhancement of the photocatalytic activity were recently reported by Li et all[49].

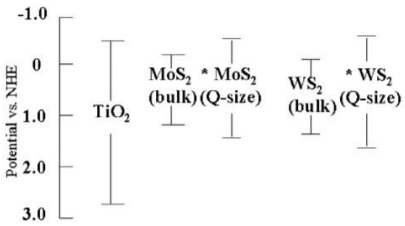

Figure. 7 Energy levels of the conduction and valence band edges vs normal hydrogen electrode (NHE) for pure TiO_2, WS_2, and MoS_2 with various sizes at pH 7. (Asterisk indicates band gap increase due to the quantum-sized effect.)[49]

Regarding elementalsemiconductors as TiO_2 sensitizers, we selected **RP** as the best candidate of our study since it has: visible light absorption (1.4<Eg<2eV), low cost, low toxicity. If modified with imperfections and disordering, RP surface can have a better Vis light adsorption ability with respect of the Bare RP, and a narrower band gap (1.42 eV), indicating its potential excellent Vis light-driven photocatalytic activity. The production of ROS from O_2 and OH^- (or H_2O) requires respectively an E_0 ($O_2/O_2^{\bullet-}$) = −0.33 eV vs NHE and E_0 (OH^- or H_2O /OH°) = between 2.8 and 1.9 eV vs NHE. Taking into consideration that the RP bands, CB and VB, are at E_{NHE}=+0.8 eV and E_{NHE} −0.62 eV respectively, the process of ROS production from O_2 is favoured, on the other hand the one from OH^- (or H_2O) is forbidden[50], see figure 8. For this reason the coupling of the surface treated RP with TiO_2 can be beneficial, since the matching of the energy level of CB and VB with the one of TiO_2, can bring to an efficient energy transfer and the production of ROS from both O_2 and OH^- (or H_2O)[51].

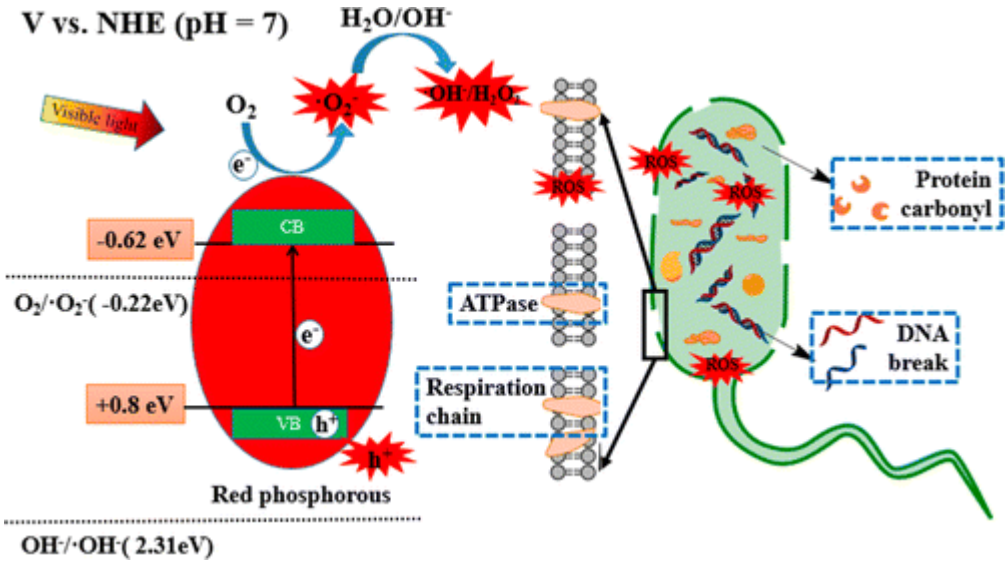

Figure. 8 Illustration summarizing the proposed bactericidal mechanism of red phosphorus under visible light: Red phosphorus quickly generate ROSs; ROSs subsequently inhibits bacterial surface metabolism [50].

2.2.3. Green synthesis of TiO_2-GRMs/RP doped PCs

Liquid-phase exfoliation (LPE) of graphite and 2d materials is a common procedure to obtain exfoliated materials with enhanced and tuneable optical and electronic properties[45], [48], [52]–[56]. Because of the hydrophobic properties of GRM it is not possible to obtain stable solution of exfoliated GRM directly in water. In fact usually LPE is performed by using surfactants or dispersant molecules[45], [52], [53] that can be hazardous or not conform to the principles of the green chemistry. In this study **the TiO_2-NPs are directly used to exfoliate graphite flakes/MoS_2/WS_2 in water** and produce the photocatalytic composite with the aid of a bath sonication –cavitation forces[53]. Regarding RP based compounds a pre-treatment of the RP powders with a miclofluidizer was done in order to obtain a modified **RP (m-RP)** with an higher rate of visible-absorbing defects on the RP structure. A for typical synthesis of PCs we used 2 mg/ml aqueous dispersion of TiO_2-NPs adding a certain weight amount of raw GRMS or m-RP, and we sonicated the samples for 4 (or 8) hours (Fisherbrand FB 15069, Ultrasonic frequency 37kHz, Ultrasonic peak 3200W) at 40°C. The exfoliation is performed in Millipore ultrapure water (resistivity 18.2 MΩ·cm at 25°C). Different TiO_2: dopant mass ratios w/w are used: 1:1 (e.g.in TiO_2Gr1:1), 10:1 (e.g.in TiO_2Gr10:1) and 100:1 (e.g.in TiO_2Gr100:1). Above, the list of the starting materials:

- TiO_2-NPs in the anatase form from HOMBIKAT AHP 200, Sachtleben Chemie GmbH (purity of the crystalline anatase phase ≥94%w/w, average surface area equals 193m^2/g)
- Natural graphite flakes from Sigma-Aldrich with particle size 100 mesh (≥75% minimum)
- MoS_2 powder (Aldrich) Particle size: ≈ 6 µm (max 40 µm).
- WS_2 powder (Aldrich, purity 99%) Particle size: 2 µm
- RP powder (Aldrich, purity 97%)

The sonicated solution are then dried in a oven at 80°C overnight. The collected powder are then dispersed again, with the aid of a mild 10 min sonication, in a water solution at fix TiO_2 concentration of 2mg/ml. Then the photocatalytic tests were performed as described in the previous sections. All

the doping materials, were tested performing tests with the doping concentration of the final PCs.

2.2.3.1. Influence of the sonication time on photocatalytic activity

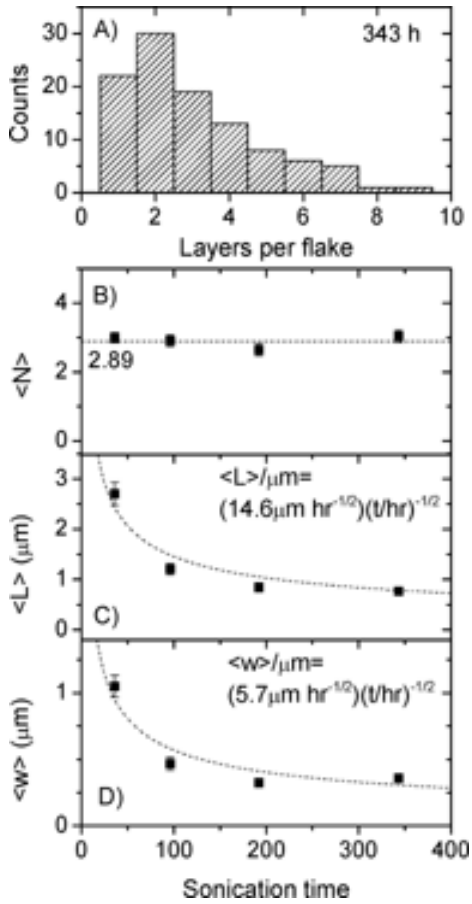

Is it well known that the process of sonication influences the exfoliation rate and the lateral size of the GRMs. This is due to the intrinsic mechanism of the ultrasonic synthetic pathways. This synthesis implies the use of an ultrasonic reactor that emits into the liquid high power and high frequency (20kHz) sound waves [57]. The compression of these waves in a non-compressible liquid creates micro-cavity bubbles in the liquid itself. These bubbles collapse violently creating enormous instantaneous pressures and temperatures.

Figure. 9 A) Histogram showing the number of layers per flake measured for the 343-h sonication times. B) Mean number of layers per flake. C,D) Mean length and width of flakes, respectively. Note that both flake length and width scale well with the inverse square root of time (t−1/2) [58].

The ultrasonic power intensity and density in a sonication bath is highly dependant on the amount of liquid the bath and the shapes and sizes of the objects placed within it. For this reason we decided to use the same bath sonication apparatus (Fisherbrand FB 15069, Ultrasonic frequency 37kHz, Ultrasonic peak 3200W) sonicating the same quantity of material (200ml

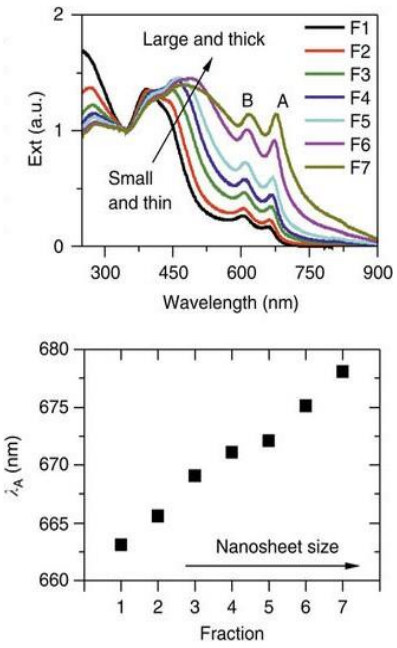

solution). In general, it was reported that higher sonication time bring more exfoliated materials with lower lateral size, and in particular in the case of graphite exfoliation, both flake length and width scale well with the inverse square root of sonication time ($t^{-1/2}$), as it is possible to see from Figure 9 [58]. On the other hand increasing the sonication time means also an higher rate of structural defects and a shift in the absorption spectrum through the UV range, e.g. Figure 10 [59].

Figure. 10 MoS_2 size-dependent extinction spectra. (up) Extinction spectra of the fractions normalized to the local minimum at 345 nm. The positions of the A- and B-excitons are marked. (down) Peak position (wavelength) of the A-exciton, λ A, as a function of fraction number[59].

Furthermore in graphene a lower conductivity and electron mobility brought by the presence of oxygen defects on graphene surface. Just to evaluate the influence of the sonication time on the photocatalytic activity of the PCs were produced with a fix weight composition of the PCs (TiO_2:doping =10:1) and the sonication process was carried on for 4 or 8 hours, see Table 1.

Table 1 Table reports the weight composition and the treatment of the PCs. In this stage, just to compare the effect of the sonication on the photocatalytic activity of the PCs, we prepared two batches of sample with 10:1 ratio and we sonicated them for 4 or 8 hours.

	Methods		% Content w/ w total				
Samples	**Preparation**	**Time**	**TiO_2**	**Graphite**	**MoS_2**	**WS_2**	**RP**
TiO_2	**Bath sonication**	**4 h or 8 h**	**100**				
Graphite				**100**			
TiO_2:Gr_2 10:1			**90**	**10**			
MoS_2					**100**		
TiO_2:MoS_2 10:1			**90**		**10**		
WS_2						**100**	
TiO_2:WS_2 10:1			**90**			**10**	
RP							**100**
TiO_2:RP 10:1			**90**				**10**

All the TiO_2 based samples showed a positive photocatalytic behaviour after 10 minutes irradiation time compared to the bare TiO_2. The photocatalytic activity, reported in the 2nd and 4th line of Table 2, of the samples obtained with 4h sonication time are really close to the one obtained after 8h sonication. In the case of the composite with Gr and MoS_2, the %P decreased when the sonication was increased of 4 hours. To sum up, results shows that **longer sonication time, but 4 hours, doesn't seem to affect the photocatalytic activity of the PCs.** All the doping materials, tested in doping concentration, didn't display a photocatalytic activity but RP (P=5%).

Table 2 Adsorption and photocatalytic activity of TiO_2 based samples, 10 min UV irradiation, (4 or 8 hours sonication time)

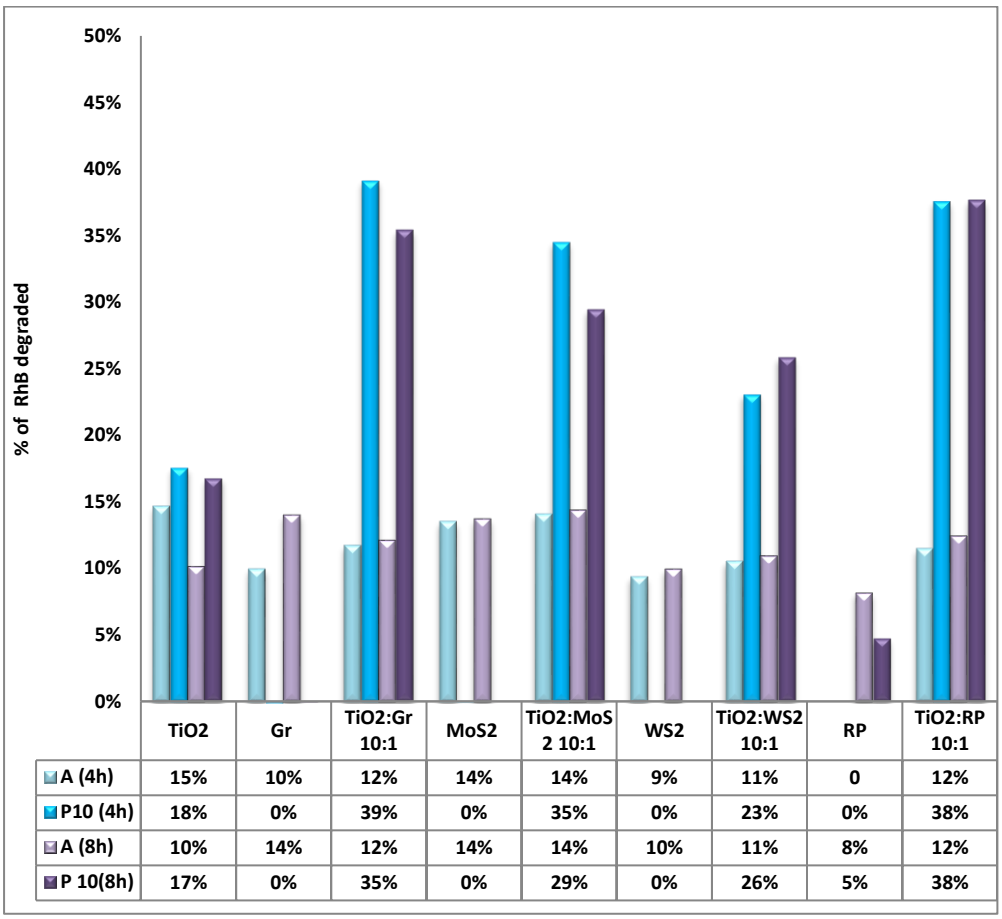

	TiO2	Gr	TiO2:Gr 10:1	MoS2	TiO2:MoS2 10:1	WS2	TiO2:WS2 10:1	RP	TiO2:RP 10:1
A (4h)	15%	10%	12%	14%	14%	9%	11%	0	12%
P10 (4h)	18%	0%	39%	0%	35%	0%	23%	0%	38%
A (8h)	10%	14%	12%	14%	14%	10%	11%	8%	12%
P 10(8h)	17%	0%	35%	0%	29%	0%	26%	5%	38%

2.2.3.2. Influence of the irradiation time on photocatalytic activity: kinetic behaviour

The most promising samples, see Table 2, were analysed not only after 10 min irradiation time, but also after 20 min to assess the kinetic photocatalytic activity. This preliminary kinetic measurement is necessary since the doping of TiO_2 can influence the carrier density, their lifetime and their reactivity toward the production of ROS and the dye degradation. On the other hands, the presence of a dopant can be beneficial in a first stage, but then affect the long-term stability of the PCs. It is known that the type of the dye as well the type of the irradiation setup influence the kinetic behaviour[60] The selection of 10 and 20 minutes irradiation time was performed by doing a preliminary experiment of complete discoloration of the RhB solution with TiO_2 in our set up conditions.

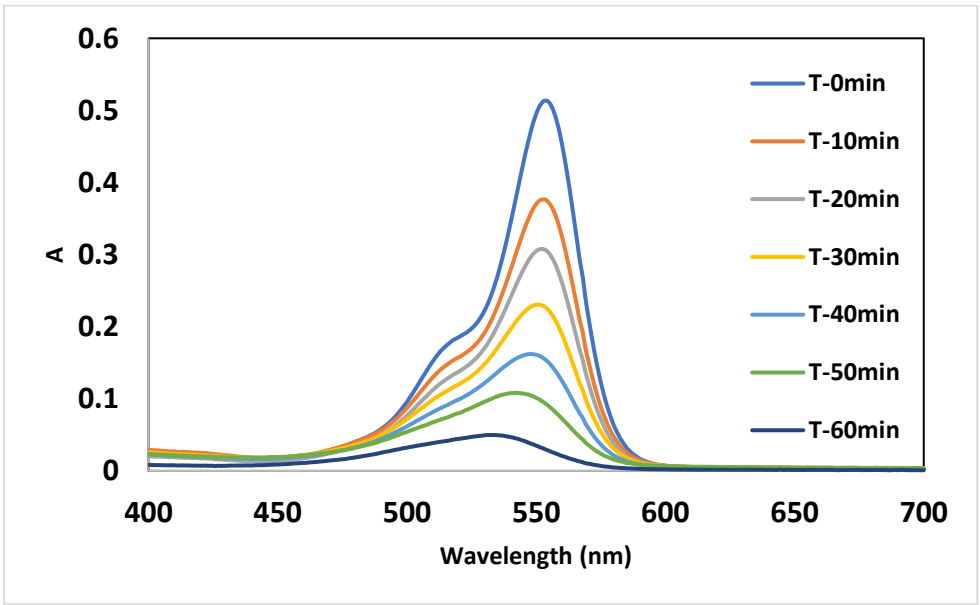

Figure. 11 Absorbance spectra of RhB solution after increasing irradiation times: 0, 10, 20, 30, 40, 50, 60 min; in presence of TiO_2. As it is possible to see a complete discoloration of the solution is reached after 60 min irradiation in the condition of: volume of the sample, surface exposed, irradiance power, dye and photocatalyst concentration.

As it is possible to see from Figure 11, a nearly complete discoloration of the solution is reached after 60 min irradiation. After 10 minutes irradiation nearly the 20% of RhB was degraded, and after 20 min the 40%. Since we

Figure. 12 Picture of the 4h sonication photocatalyst TiO_2:X (10:1); where X is (from right to left): WS_2, RP, MoS_2, Gr and the last is the bare TiO_2.

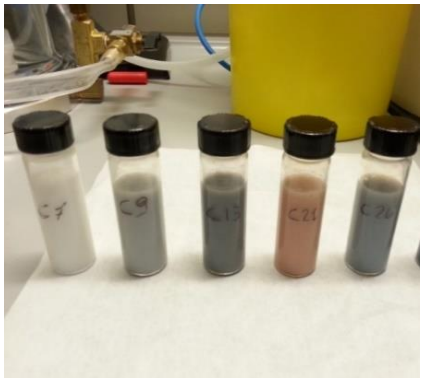

expect an enhancement of the TiO_2 performances brought by the presence of dopants, we selected these irradiation time in order to appreciate the increment in the photocatalytic activity with respect of the non-doped system. Longer irradiation time would have brought a flattening of the results toward the 100% of degradation. then, we selected the samples with 10:1 ratio of materials and 4 hour of sonication, see Figure 11, in order to have a preliminary feedback on the kinetic behaviour of the newly synthesized PCs.

Table 3 Adsorption and photocatalytic activity of TiO_2 based samples (ratio10:1, sonication 4h) after 0, 10, 20 min UV irradiation

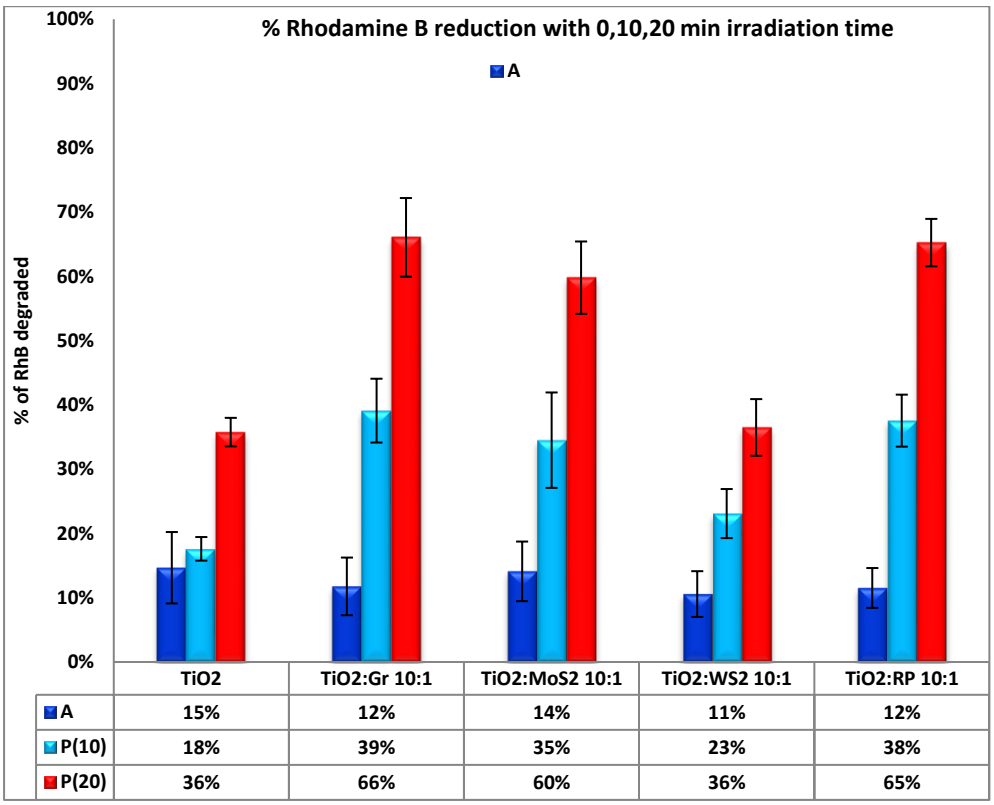

	TiO2	TiO2:Gr 10:1	TiO2:MoS2 10:1	TiO2:WS2 10:1	TiO2:RP 10:1
A	15%	12%	14%	11%	12%
P(10)	18%	39%	35%	23%	38%
P(20)	36%	66%	60%	36%	65%

Table 3 shows the results of the tests. As it is possible to see in the case of the WS_2 compound we observe a flattening of the photocatalytic activity after 10 min irradiation since the P(20) value is more or less equal with respect of the reference. In the case of Gr, MoS_2 and RP doping the P(20) of the PCs keep on being better with respect of the bare TiO_2. In order to see whether there is a difference in the kinetic constant of the PCs we calculated the increment %ΔP(t) in the photocatalytic activity with respect of the TiO_2 reference after t= 10 or 20 minutes irradiation time with the following equation (Eq.15):

$$\%\Delta P(t) = 100 - \left(\frac{P(t)_{TiO2\ doped}}{P(t)_{TiO2}} * 100\right)$$

Results shows that there is an initial %ΔP(10) in the photocatalytic activity that is higher in the case of the presence of Gr and RP (~110-115). This means that the effect of the MoS_2 on the initial kinetic constant of the TiO_2 is lower with respect of the other dopants(but WS_2). On the other hand if we compare the normalized increment in the photocatalytic activity between 10 and 20 min defined as the difference between the photocatalytic activity at two different delay time normalized with the average value (Eq.16):

$$\%\Delta P(\Delta t) = \left(P(t_2) - P(t_1) \Big/ \overline{P(t_{1,2})} * 100\right)$$

Table 4 Increment of the photocatalytic activity after 10 minutes and 20 minutes irradiation with respect of titania. In the last column normalized increment in the photocatalytic activity between 10 and 20 min irradiation.

Samples	$\%\Delta P(10)$	$\%\Delta P(20)$	$\%\Delta P(10-20)$
TiO2	0	0	
TiO_2:Gr 10:1	**116**	**83**	**-33.2**
TiO_2:MoS_2 10:1	**94**	**67**	**-33.5**
TiO_2:WS_2 10:1	27	0	-
TiO_2:RP 10:1	**111**	**81**	**-31**

It is possible to see from Table 4, that in this second stage the constant seems to be the same for all the photocatalytic samples, since the %ΔP(20-10) is the same for all the samples. It is possible to conclude that there is **an influence on the fastest kinetic constant of the photocatalytic process that is higher in the case of RP and Gr**, and slightly lower for MoS_2. This discrepancy in the kinetic constant reach a flattening after 20 minutes irradiation. This means that the slower kinetic constant is the same for Gr, RP and MoS_2. By the way

it has to be noticed that the absolute value in case of MoS_2 sample keep on being lower with respect of the RP or GR compounds. **The WS_2 sample showed a inactivation for longer irradiation time.**

2.2.3.3. Influence of TiO_2 doping on photocatalytic activity with UV and Vis light conditions

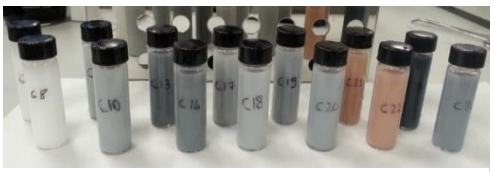

Figure. 13 Picture of the 4h sonication photocatalyst. In the first line the 100:1 samples, in the second line the 1:1 ones.

Each composition was synthesized in the ratio TiO_2: dopant =10:1, 100:1 and 1:1, see figure 13. All the composition were sonicated for 4 hours and the suspension were dried in the oven at 80°C overnight following the standard procedure.

Table 5 Adsorption and photocatalytic activity of TiO_2 based samples (ratio100:1,10:1,1:1)with sonication 4h and 20 min UV irradiation.

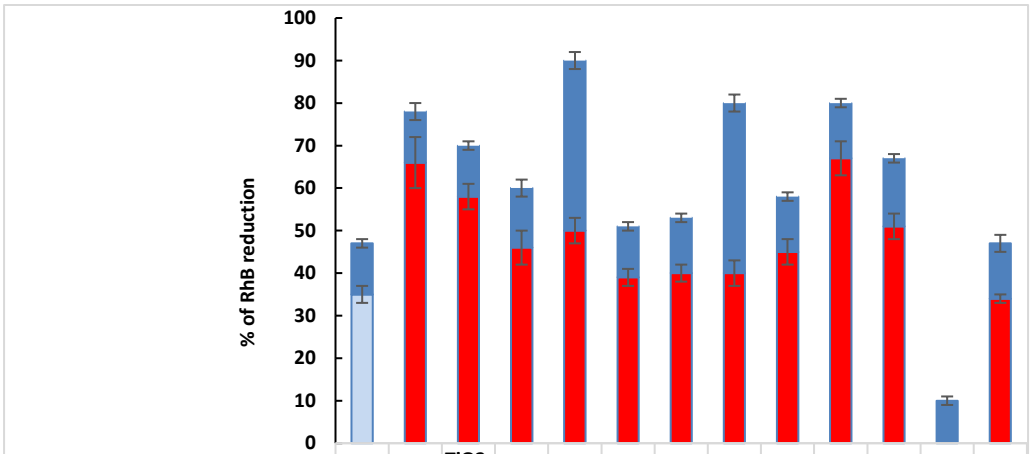

	TiO2	TiO2: Gr 10:1	TiO2: MoS2 100:1	TiO2: MoS2 10:1	TiO2: MoS2 1:1	TiO2: WS2 100:1	TiO2: WS2 10:1	TiO2: WS2 1:1	TiO2: RP 100:1	TiO2: RP 10:1	TiO2: RP 1:1	RP (0.2 mg/ml)	M-RP (0.2 mg/ml)
P(20) % increment (TiO2 ref.)	0	89	66	51	43	11	9	14	29	91	46	0	0
A %	12	12	12	14	40	12	13	40	13	13	16	10	13
P (20min) %	35	66	58	46	50	39	40	40	45	67	51	0	34

Since the photocatalytic activity of the RP at doping level was positive, we keeped on with the characterization of the commercial RP and the microfluidized one (m-RP), in the concentration of 0.2 mg/ml. Table 5 shows the results for the photocatalytic tests with UV light. Table 6 the results obtained with Visible light conditions(Figure 3), methylene blue (λ max: 664 nm) and 30 min irradiation time.

Table 6 Adsorption and photocatalytic activity of TiO_2 based samples (ratio100:1,10:1,1:1)with sonication 4h and 30 min Vis irradiation

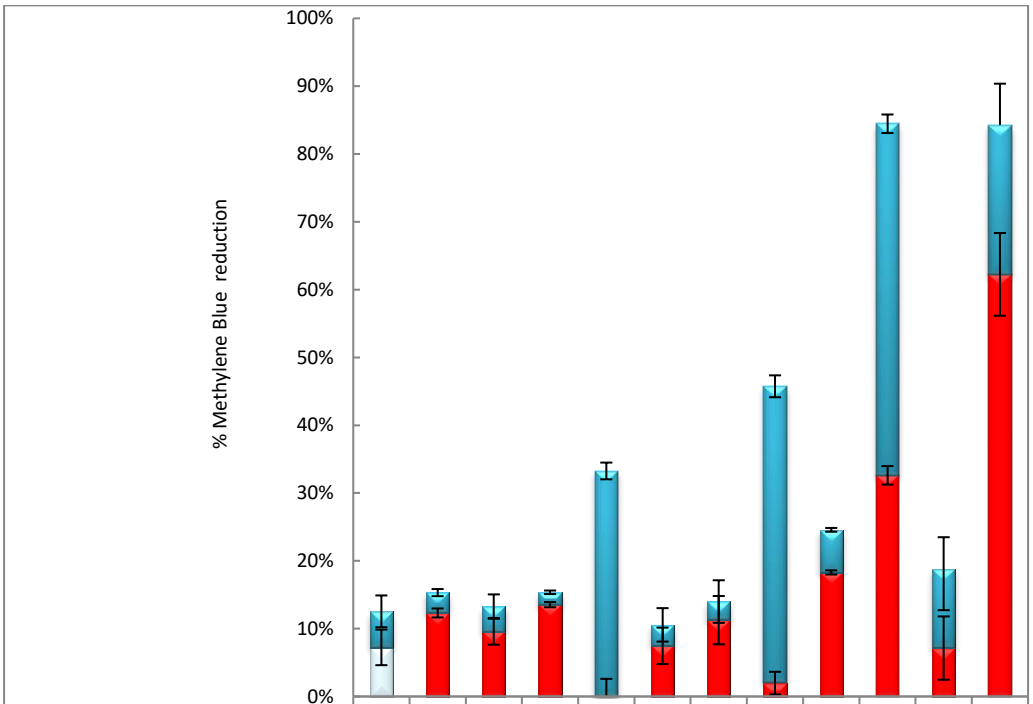

	TiO2	TiO2: Gr 10:1	TiO2: MoS2 10:1	TiO2: MoS2 100:1	TiO2: MoS2 1:1	TiO2: WS2 10:1	TiO2: WS2 100:1	TiO2: WS2 1:1	TiO2: RP 10:1	TiO2: RP 1:1	RP 0.2mg/ml	M-RP 0.2mg/ml
Pvis(30) % increment (TiO2 ref.)	0	70	32	87	0	3	55	0	153	350	0	760
%A	5%	3%	4%	2%	33%	3%	3%	44%	6%	52%	12%	22%
%Pvis(30)	7%	12%	10%	14%	0%	7%	11%	2%	18%	33%	7%	62%

Just to have a better visualization and comment on the results, the data were express as increment with respect of the TiO_2, calculated as shown in Equation 15

2.2.4. Concluding remarks on Section 2.2: best parameters for synthetic pathway

Table 7 Adsorption and increment of the photocatalytic performances of the PCs synthetized with different doping amount of GRMs/RP.

Results

UV light

Samples (ratio in w:w)	% Adsorption of RhB in dark	%ΔP (20) UV light (TiO2 ref.)
TiO_2	12	0
TiO_2:Gr 10:1	12	89
TiO_2:MoS_2 100:1	12	66
TiO_2:MoS_2 10:1	14	51
TiO_2:MoS_2 1:1	40	43
TiO_2:WS_2 100:1	12	11
TiO_2:WS_2 10:1	11	9
TiO_2:WS_2 1:1	40	14
TiO_2:RP 100:1	13	29
TiO_2:RP 10:1	13	91
TiO_2:RP 1:1	16	46
RP (0.2mg/ml)	10	0
M-RP (0.2mg/ml)	13	0

Vis light

Samples (ratio in w:w)	% Adsorption of MB in dark	%ΔP (30) Vis light (TiO2 ref.)
TiO_2	5	0
TiO_2:Gr 10:1	3	70
TiO_2:MoS_2 100:1	2	87
TiO_2:MoS_2 10:1	4	32
TiO_2:MoS_2 1:1	33	0
TiO_2:WS_2 100:1	3	55
TiO_2:WS_2 10:1	3	3
TiO_2:WS_2 1:1	44	0
TiO_2:RP 10:1	6	153
TiO_2:RP 1:1	52	350
RP (0.2mg/ml)	12	0
M-RP (0.2mg/ml)	22	760

As reported longer sonication time, but 4 hours, doesn't seem to affect the photocatalytic activity of the PCs. So all the composites were synthetized with 4 h sonication time. As reported in Table 7, an increment in the photocatalytic activity under UV light with respect of TiO_2 was observed in all the doping ranges and doping type. In particular results for TiO_2:MoS_2 showed that for higher doping the absorbance of the dye on the top of the photocatalyst increased with the weight amount of MoS_2, (from +12% to +40% going from the composites 100:1 to the 1:1 ratios). On the other hand the **photocatalytic activity under UV light decreased with the increment of MoS_2 ratio going from +66% to +43%.** In the case of WS_2 doped compounds we observed the same behaviour with the adsorption value that was observed for the MoS_2 compounds. In contrast with the previous system, the

increment of **the UV photocatalytic activity for WS_2 samples was not so high floating around +9-14%**.In the case of **RP** based compounds while the adsorption keep on being constant, **the photocatalytic activity seems to have a paraboloid trend reaching the 91% of increment** with the weight composition 10:1. The **indoor tests** showed an adsorption behaviour with MB, a **Vis light** driven photocatalytic activity for **MoS_2** samples that followed the same trend displayed with UV light test, going from a value of +**87% for TiO_2:MoS_2 100:1** to a complete inactivity for the PCs obtained with TiO_2:MoS_2 1:1. For WS_2 photocatalysts the trend was exactly the same with respect of the one observed for MoS_2, but with lower values (+55% for TiO_2:WS_2 100:1). RP composites showed an increment in Ads as well as in the P with the best performance for the compounds **TiO_2:RP 1:1 of +350%**. We also tested the bare commercial RP and the **m-RP** at doping level. What we observed was a unexpected photocatalytic activity in the case of the processed RP with an increment of **+750. In the following section 2.2 is reported a full characterization of the compound TiO_2:Gr 10:1 that is one of the most promising samples both in UV and Vis light showing an %ΔP(20)UV of + 89 an a %ΔP(30)Vis of +70%.**

Figure. 14 Powders of TiO_2 and graphite starting materials,TiO_2 suspension(left), TiO_2:Graphene 10:1 liquid suspension(centre), black Graphene suspension (right).

2.3. Characterization of the most performing material: TiO_2:Gr 10:1

The compound TiO_2:Gr 10:1 is one of the most promising PCs both in UV and Vis light showing an %ΔP(20)UV of + 89 an a %ΔP(30)Vis of +70%. In order to understand wat was going on during the sonication process as well as the interaction between graphite/graphene and TiO_2 we did a full characterization of the nanocomposite. First, we did a **full kinetic study of photocatalytic activity** by measuring the rate of degradation Rhodamine B in water under 1mW UV-light irradiation. With respect to the commercial TiO_2, used as starting material for the preparation of the composites, an increase of up to 100% of the degradation rate constant is observed. Then **the exfoliation process was studied by** high-resolution powder X-Ray diffraction **(HRPXRD)** measurements with synchrotron radiation, **Raman**, Scanning electron spectroscopy **(SEM)** and transmission electron microscopy **(TEM)** in order to investigate the effect of both sonication time and concentration of graphite starting material TiO_2-NPs. In the end, **the mechanism** for the enhanced photocatalytic activity, the e-h pairs generation and its effect on PQE, **are investigated by ultrafast TA spectroscopy** with sub-200 fs time resolution and broad spectral coverage (430-1400 nm). With this aim, we compare the decays of photo-generated e-h pairs in TiO_2/Gr with those of the pristine TiO_2. We observe that in the nanocomposite, thanks to the electronic interaction between TiO_2 and the exfoliated graphite, the excited TiO_2-NPs inject electrons into the carbon structures. The corresponding increased efficiency in the photo-production ofreactivespeciesintheTiO$_2$/Gr nanocomposites explain the improvement of the photocatalytic performances with respect to the bare TiO_2-NPs. Two different TiO_2-Graphite mass ratios are used: 1:1 in TiO_2Gr1:1 and 10:1 in TiO_2-Gr10:1.

2.3.1. Kinetic photocatalytic tests of: TiO_2:Gr 10:1

As already explained in the previous section, in order to allow a correct comparison of the samples to understand the effect of the flakes on the PQE of TiO_2, the amount of the catalyst used in each experiment is chosen to guarantee the same quantity of TiO_2 (2mg/ml) inside each suspension. In fact, for instance the weight of graphite inside of TiO_2-Gr10:1 and TiO_2-Gr1:1 is different. We test 10 ml mixture comprising 2.86%ml of an aqueous solution of RhB (0.05mg/ml, $1 \cdot 10^{-4}$M), 2.14% ml H_2O and 50% suspension of photocatalyst (with the same amount of TiO_2 2mg/ml). Considering the affinity of graphitic flakes, due to the π-π stacking of their aromatic systems, for polycyclic aromatic and cationic compounds like RhB, the suspensions are magnetically stirred for 40 min in the dark, in order to attain adsorption-desorption equilibrium between the solid nanocomposite and the dye. Actually, it has been recently shown[6] that, when RhB is physically adsorbed onto graphene flakes, there is a ground state interaction that brings to a decrement in the intensity of the UV/Vis absorption and of the emission of the dye. Since this interaction is just with the graphene surface, after a certain period of time, saturation occurs and the concentration of free RhB stops decreasing[7]. As already explained, it is important to determine the fraction of RhB that remains free inside the solution, since this information is necessary to discriminate whether the change in the dye concentration under irradiation is exclusively due to a photoreaction or to adsorption. To obtain the adsorption value, after the stirring in the dark, 0.75ml of the RhB nanocomposites suspension is taken from each sample and centrifuged at 9000 rpm for 10 min at T=25°C in order to separate the nanocomposite from RhB solution. The upper 0.5ml of each centrifuged sample is collected and then diluted with water (1:6 ratio) to reach the 3-ml volume of analysis of a standard cuvette for a UV/Vis spectrophotometer. The concentration CD (mol L−1) of free RhB present in solution after incubation in the dark is derived from the UV/Vis absorption spectra (λmax=554nm). Then, the percentage Ads of RhB adsorbed on the composites is calculated using the Eq 13. The photoreactivity is investigated after photoexcitation of the TiO_2 by exposing each sample to a UV Mercury lamp (RadiumSanoluxHRC300-280E27) with a power of 1 mW in the UVA/UVB range on the surface of the solution. The

suspensions are irradiated for 60 minutes, sampling 0.75ml of solution every time interval t of 10 min. The collected volumes are centrifuged, diluted and analysed with the same procedure explained for the determination of CD, detecting the concentration C(t) of RhB not degraded after the time interval t from the beginning of the irradiation. The percentage of RhB photodegraded, P(t) is calculated using the Eq. 14.

Table 8 Percentage of photodegradation (P), after 20 min and 40 min irradiation time, and the percentage of adsorption (Ads) of RhB on the surface of the composite after incubation in the dark

	TiO_2	TiO_2-Gr10:1	TiO_2-Gr1:1
P(20min)	38%	51%	45%
P(40min)	66%	83%	64%
Ads	5%	5%	35%

Table 8 reports the P(t) values of the photocatalysts after 20 or 40 min irradiation and the PCs adsorption in dark. For TiO_2-Gr10:1 photocatalyst after 20 min irradiation and after 40 min (Table 8, column 1-2) is it possible to notice an increment of the photocatalytic activity with respect of the reference sample. For TiO_2-Gr1:1, instead, the increment of P(t) is lower (Table8, column 1 and 3) at 40 minutes and nearly zero after 40 min with respect of titania reference.. Furthermore, the adsorption of RhB in TiO_2-Gr1:1 is no longer negligible and goes from 5% (TiO_2-Gr10:1) to 35%(TiO_2-Gr1:1). Our findings are in agreement with previous studies[4], [32], [35], [61] which investigated the adsorption and the photocatalytic activity of similar TiO_2-Gr samples, with different weight addition ratios of graphite. In all these works, especially in the one by Zhang et al.[35], higher weight ratio of graphene (more than 10% w/w of graphene with respect to TiO_2) is associated with a decrease of the photocatalytic activity and an enhanced adsorption of pollutants. Furthermore, the increment in the adsorption of RhB in the case of TiO_2-Gr1:1, Table 8, with respect of TiO_2-Gr10:1 could also affect the long term photocatalytic activity of the nanocomposite, since it was reported that the adsorption of organic molecules on graphene decreases the photocatalytic performance over five reaction cycles with the same photocatalytic powder[62]. Taking into consideration the results discussed above, the composite TiO_2-Gr10:1 is identified as the most promising photocatalytic compound since it gives the highest value of P(t) with the

lowest adsorption of RhB compared with the other samples. We characterize the photo-degradation kinetic of the nanocomposites, reported in Fig. 15.

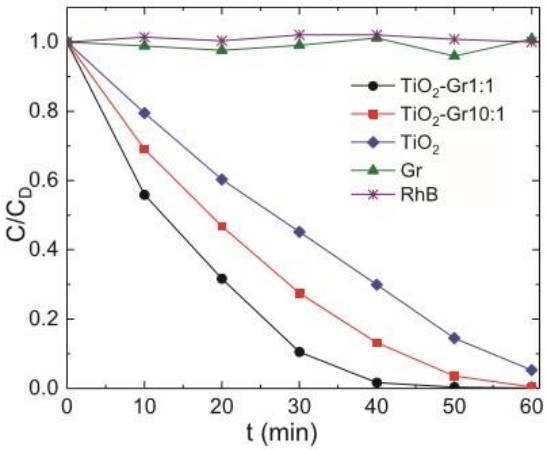

Figure. 15 Photocatalytic degradation of RhB under UV light irradiation for various compositions of TiO_2-Gr composites along with pure TiO_2.

The trends indicate that the dye's degradation temporal profile is a pseudo-zero-order reaction that is a combination of zero-order and a first-order kinetics. In zero-order kinetic reactions, the rate of the process is independent of the reactant concentration and the RhB concentration decreases linearly with time, as it can be seen at t= 0,10,20,30 min in Fig. 15. On the other hand, in a first order reaction, the concentration of the dye is proportional to the rate of the photo-degradation process, as it is at t= 30,40,50,60 min in Fig.15. A pseudo-zero-order kinetics, commonly occurs in the case of heterogeneous catalysis, and it has been previously observed in organic dye photocatalysis, as summarized in the Ref.[60]. In fact, in the case of a solid photocatalyst, the reaction occurs only in the proximity of the catalyst's surface, that becomes saturated at a given dye concentration. Further increase of dye's concentration cannot cause additional changes to the system, such that the reaction rate is independent of concentration of RhB and it depends only on the ability of the catalyst to degrade the dye. In order to compare the different kinetics, the initial points are fitted to a zero-order model[63] Eq.17:

$$C(t)/C_D = 1 - kt$$

where k(min^{-1}) is the kinetic constant of the process and t (min) is the reaction time.

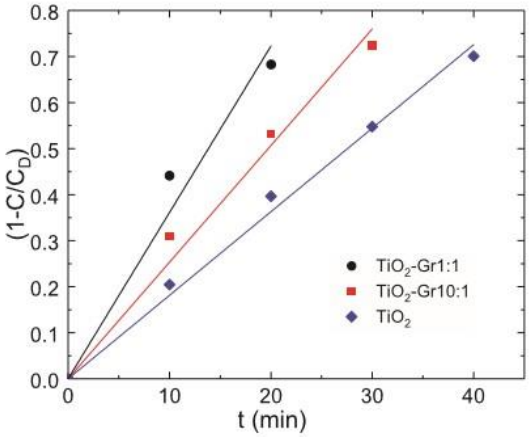

Figure. 16 Zero order photodegradation kinetics of photodegradation of RhB, given as (1-C/CD) as a function of time, for the TiO_2, TiO_2-Gr10:1 and TiO_2-Gr1:1 samples. Lines represent the interpolation fitting of the experimental points.

Table 9 Kinetic constants and linear regression coefficients (R2) for the fitting lines reported in Fig.16

	TiO_2	TiO_2-Gr10:1	TiO_2-Gr1:1
k(min^{-1})	0.018	0.025	0.036
R^2	0.99	0.98	0.97

Fig.16 shows the experimental P(t) and the best fits with the parameters in Table 9. For pristine TiO_2, we get k∼0.018 min^{-1}, while for TiO_2-Gr10:1, k is ∼0.025 min^{-1} and for TiO_2-Gr1:1, k is ∼0.036 min^{-1}. In this case, the higher k for TiO_2-Gr1:1 with respect to TiO_2-Gr10:1 is due to a combination of both photocatalysis and adsorption, that brings a higher concentration of dye in proximity of the photoactive surface of the nanocomposite. In this case, the dye adsorption seems to be beneficial for the system, but as a side effect, the adsorption may affect the overall long term stability of the nanocomposite. The generation of reactive oxygen species[64] (ROS) was identified as the photodegradation mechanism of organic pollutants and RhB[65]. The presence of flakes may result in a higher ROS generation, due to the electron transfer from TiO_2 to the flakes, allowing a more stable charge separation in TiO_2, and a higher production rate of ROS. The first step of the photo-electrochemical reaction is the photo-excitation of e-h pairs in TiO_2-NPs by absorption of UV photons with energy exceeding the TiO_2 gap. The conversion

of the absorbed light into chemical energy (i.e. the potential energy of undergoing a specific chemical reaction, e.g. the ROS generation) depends on the competition between charge recombination, either radiative or non-radiative, and the separation of the photo-excited charges required to initiate the oxidative (reductive) pathways[64]. Accordingly, the enhancement of photocatalytic activity may be traced back into modifications of relaxation channels of the photoexcited e-h in TiO_2, induced by the graphitic flakes

2.3.2. Scanning Transmission Electron Microscopy (STEM): TiO_2:Gr 10:1

The characterization of the morphology of TiO_2-Gr10:1, is investigated by scanning electron microscopy (SEM,Quanta3D, FEI Company). The results are obtained by the group of Nico Sommerjik (Eindhoven University). Figure 17 a shows the presence of graphitic flakes covered by a compact layer of TiO_2-NPs. From the higher magnification image, Fig.17 b, the edges of the flakes decorated by the NP agglomerates are visible. The lateral size of the flakes is measured by Scanning Transmission Electron Microscopy (STEM, Magellan 400L FEI) depositing ~ 20µl of the TiO_2-Gr10:1 dispersion on a holey carbon copper grid (300 mesh).

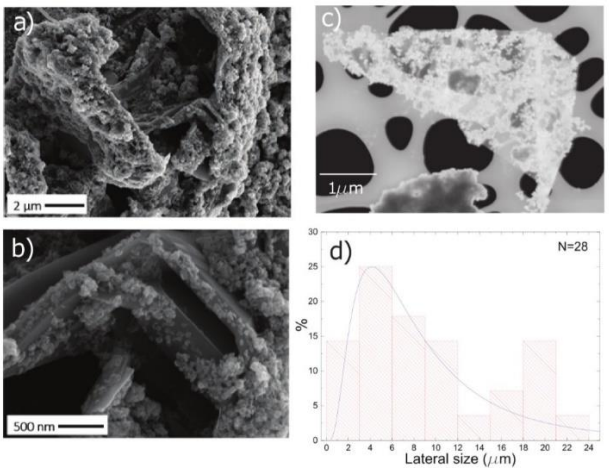

Figure. 17 a) SEM images of TiO_2-Gr 10:1 composite b) Higher magnification image of figure a) showing the flakes decorated with the NPs c)Representative STEM image of a flake of the TiO_2-Gr10:1 d) Distribution of the flakes lateral size measured by STEM

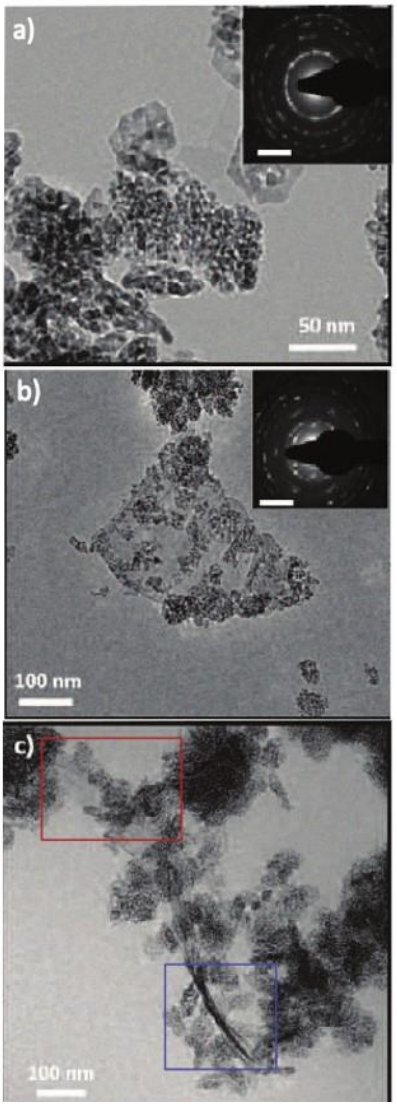

Figure. 18 a) Dry TEM images of TiO_2 NPs, inset diffraction pattern of the NPs b)Dry TEM of the graphite flake covered by the NPs, inset corresponding diffraction pattern c) Cryo-TEM image of TiO_2-Gr10:1 in suspension state with TiO_2-NPs decorating the surface of the flakes (red rectangle) and the edges (blue rectangle). The scale bar in the inset in a,b is 1nm

Analysing the isolated flakes, of which a representative one is shown in Fig.17 d, an average lateral size of∼5 µm is estimated, see Fig. 1 d. TEM image (TEM,Tecnai T20 FEI) in Fig.18 a, shows clusters of TiO_2-NPs, as confirmed by the diffraction pattern (inset Fig.18 a) of∼50nm with a particle size of∼5-10nm. In Fig.18 b, a graphite flake decorated by the NPs is visible with the corresponding diffraction pattern (inset Fig.2 b) of both graphite, bright spots, and the TiO_2-NPs, hollow rings. To exclude that the TiO_2-NPs adhesion to the flakes is simply due to the drying of the TiO_2-Gr10:1 suspension, we perform Cryo-TEM (CRyoTitan FEI) experiments. This technique allows to investigate the morphology of TiO_2-Gr10:1 nanocomposites as present inside the liquid state. 20 µl of suspension of the TiO_2-Gr10:1 is deposited on a holey carbon grid (Quantifoil R2/2 200mesh), then the sample is loaded into the chamber of a machine called Vitrobot (FEI VitrobotTM Mark III) that maintains 100% humidity and a temperature of 4°C. Inside the chamber there are two blotting papers on either side of the sample, they close on the grid and leave a very thin layer of the suspension in the order of hundreds of nm[66]. At the end the sample is plunged into liquid ethane at 183.3 °C, this temperature avoids the formation of ice crystals, creating a vitreous ice (amorphous solid form of water). Fig.18 c confirmsthatTiO_2-NPs are adhering to the flakes, both on the surface (red rectangle) and at the edges (blue rectangle) already in the liquid state.

2.3.3. High-resolution powder X-Ray diffraction (HRPXRD) measurements: TiO_2:Gr 10:1

In order to study the process of graphite exfoliation brought by the sonication of TiO_2 NPs as well as the influence of the liquid-phase we perform HR-PXRD measurements in Technion University with the aid of professor Boaz Pokroy. This is done on samples of TiO_2-Gr prepared varying the sonication time (5 and 30 min) and the concentration of the TiO_2-NPs (TiO_2-Gr1:1 and TiO_2-Gr10:1 ratios). Powdered samples are loaded into 1 mm diameter boro silicate glass capillaries and powder diffraction patterns are collected at ambient temperature with an incident X-ray wavelength of 0.319902 Å. Full width at half maximum (FWHM) of the{002} graphite diffraction peak are deduced by the Rietveld refinement method[67]. That was done by using the General Structure Analysis System (GSAS) program and EXPGUI interface (a graphical user interface for GSAS)[68], [69].

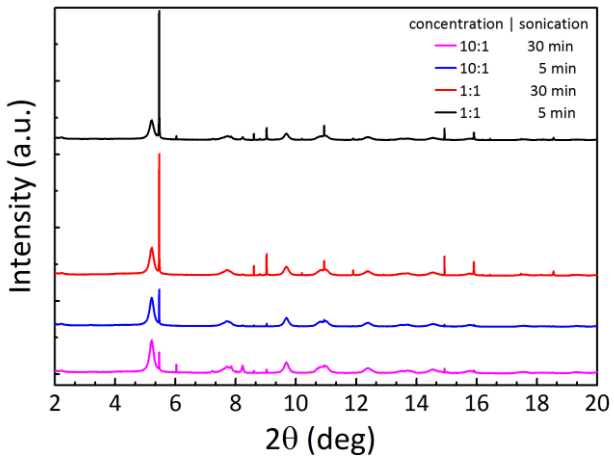

Figure. 19 HR-PXRD diffraction profiles of the 1:1 and 10:1 TiO_2/Gr composites sonicated for 5 and 30 min. The data confirm the presence of the two crystalline phases of TiO_2 (anatase) and graphite

The XRD patterns collected from the above described samples, Fig.19, confirms the presence of the two major crystalline phases of TiO_2 anatase (The Joint Committee on Powder Diffraction Standards, JCPDS 21-1272) and graphite (JCPDS 75-2078)[70].

The samples exhibit basal reflection shifted toward higher d spacings values d(002=3.357 Å), Figure 20, than pristine graphite (JCPDS 75-2078, d002=3.347 Å).This may suggesting that TiO_2-NPs assisted exfoliation increases the inter-planar spacing of the resulting graphitic flakes. Moreover, the {002} diffraction peak of the sample TiO_2-Gr10:1 sonicated for 30 min exhibits the lowest intensity (974 counts) while the highest is recorded for the sample TiO_2-Gr1:1 sonicated for 5 min (3520 counts) (Fig.4a). This suggests that increasing the sonication time and TiO_2-NPs concentration reduces graphitic crystallinity and decreases the number of planes oriented along {002} direction[70]. In addition, as both concentration of TiO_2-NPs and sonication time increase, the 002 reflection broadens (Fig.20a) and the corresponding FWHM increases (Fig.20 b).

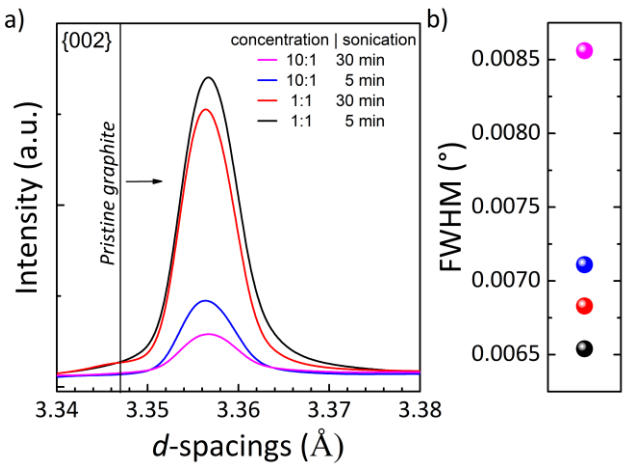

Figure. 20 a) The {002} graphite reflection and b) its FWHM value for different TiO2/Gr composites, sonicated for 30 min and 5 min. TiO2-Gr composites demonstrates the most pronounced drop (pink line) and broadening of the{002}graphite reflection (pink square).

The broadened FWHM is due to smaller crystallites[70], [71]. The samples sonicated during 5 and 30 min demonstrate a decrease in crystallite size from 255 to 195 nm, respectively. Displayed structural changes of the graphite phase within TiO_2-Gr composites such as progressive decrease in intensity of the{002}graphite peak and its significant broadening are indicative of the decreased graphitic nature of the samples, most likely, achieved, as a result of TiO_2 NPs assisted exfoliation[68], [72].

2.3.4. Raman spectroscopy TiO_2:Gr 10:1

With the aid of Prof. A. C. Ferrari's group (Cambridge University) we performed Raman spectroscopy to analyse the TiO_2-Gr10:1 composite as well as the starting graphite. For both samples 60µl of aqueous solution are deposited by drop cast onto a glass substrate 1cmx1cm, due to overlapping of the TiO_2 Anatase peaks with the Silicon substrate, then heated at 100°C for 20 min, to ensure water evaporation. Raman spectra are acquired at 514.5 nm using a Renishaw InVia spectrometer equipped with a 50x objective. The power on the sample is kept below 1mW to avoid any possible damage. The spectral resolution is∼1cm−1. A statistical analysis is performed as follows: the substrate is divided into 4 regions ∼500x500 µm^2 and in each 5 points are acquired. A representative spectrum of the starting graphite (red line) and of TiO_2-Gr10:1 (blue line) are shown in Figure 21 . The peaks at 144, 397, 518 and 639 cm−1 are the Eg, B1g, A1g and Eg of anatase phase of TiO2[73]. According to the q vector relaxation model (QVRM) in ref.[74] is possible to derive the crystallite size of the TiO_2-NPs considering the position Pos (Eg@144cm−1) and the FWHM(Eg@144cm−1). For the sample analysed the Pos(Eg@144cm−1) is ∼147cm−1 with its FWHM of ∼20cm−1, from the model these values correspond to a crystallite size between 5-10 nm.

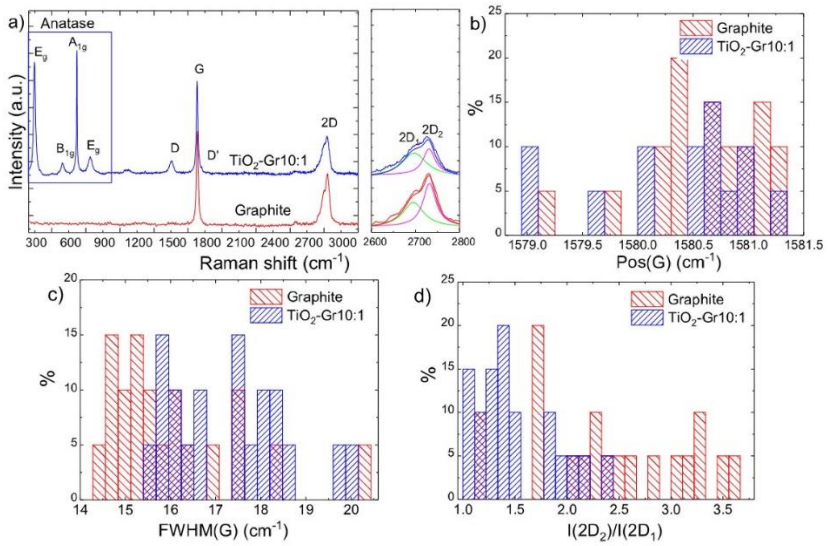

Figure. 21 a) Representative Raman spectra at 514.5 nm for graphite (red curve) and TiO2-Gr (blue curve), (b,c,d) Distribution of (b) Pos(G), (c) FWHM(G) and (d) I(2D2)/I(2D1).

Figure 21 b, c show no significant difference between Pos(G) and FWHM(G) of graphite and of TiO2-Gr10:1 composite. The 2D band line shape for the composite still resembles the one of graphite with two components (2D1, 2D2) but their intensity ratio I(2D2)/I(2D1) is reduced from 2.4 to ∼1.4, value corresponding to the one of ∼ 6-8 layers, Fig.5 d. This indicates that the flakes are undergoing exfoliation, as also confirmed by XRD, see Figure21 a,b. I(D)/I(G) ratio for the starting graphite is ∼0.1 and the one of the TiO2- Gr10:1 ∼0.17 corresponding to a sp2 cluster dimension of respectively 0.45nm and 0.26nm. The halve of the cluster dimension implies a reduction of the flakes size responsible for the arising of the D band.

2.3.5. Photophysical characterization: TiO_2:Gr 10:1

Then we investigate the photo-physical properties of the samples by UV-visible (UV- Vis) diffuse reflectance spectrometry. This technique can give information about the absorption spectrum of a solid sample and it is currently used for the determination of the bandgap of TiO_2-NPs[75]. In fact, in case of a powder, the incident light is almost completely scattered and it is necessary to use diffuse reflectance instead of transmission spectroscopy to characterize the sample. In general, a solid sample can have a specular reflection or a diffuse reflection. The diffuse reflection is dependent on some physical parameters that have to be taken into consideration during the preparation of the powders[76] such as: the particle size, the refractive index and the packing. The particle size of the samples that we want to compare has to be in the same order of magnitude, since a size reduction causes reduction of the diffuse reflection from the surface [77]. The refractive index has to be comparable, since the higher the refractive index, the higher is the specular reflection from the sample[78]. On the other hand, this effect can be avoided dispersing the sample in a non-absorbing medium with a low refractive index, e.g. NaCl, which is commonly used to characterize carbon-based samples[79]. Finally, the packing is important, because in order to have a high diffuse reflection signal and avoid the light transmission, the sample has to be sufficiently thick (in our case higher than 3mm)[80], [81]. Taking into account all these parameters, the diffuse reflectance of the samples can

be measured and linked to the absorption coefficient through the Kubelka-Munk (KM) function[80] F(R). For a thick sample(3mm) [81], [82], unaffected by the light transmission, F(R) can be written as[83] (Eq 18):

$$F(R) = {(1-R)^2}/{2R} = {K}/{s} = {2.303\ \varepsilon c}/{s}$$

where R (arbitrary units) is the absolute reflectance, K (cm^{-1}) is the absorption coefficient, s (cm^{-1}) is the scattering coefficient, ε is the absorptivity ($M^{-1}{\cdot}cm^{-1}$) and c(M) is the concentration of the sample. In order to fulfill all the above-mentioned conditions [76] the spectra are recorded on samples dispersed in NaCl. The diffuse reflectance measurements are performed with a Perkin Elmer Lambda45 UV-Vis spectrophotometer equipped with a Harricks praying mantis diffuse reflectance accessory. For each TiO2-Gr sample an amount of 10 mg is mixed with 500 mg of NaCl. We use a quartz cuvette with 0.5 cm optical path. The reflectance background of NaCl (the reference) is taken as baseline for each measurement. Since the samples are dispersed into in a non-absorbing matrix (NaCl), s in Eq(1) can be assumed to be the one of the NaCl, and it is constant for all the samples. As a consequence, F(R) is proportional only to K.

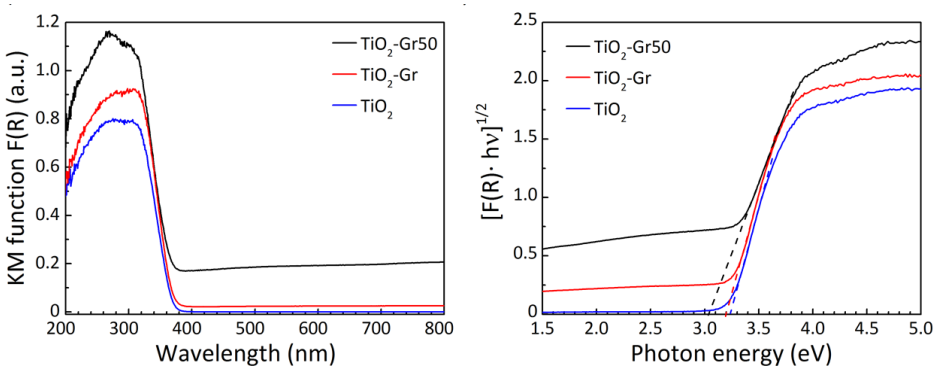

Figure. 22 a) UV-Vis diffuse reflectance spectra F(R) elaborated and normalized with Kubelka-Munk (KM), b) Tauc plot of the modified KM function. Dotted line shows the linear extrapolation of the E_{gap}.

The spectra of pristine TiO_2, TiO_2-Gr10:1 and TiO_2-Gr1:1 composites are reported in Figure 22. An electronic transition from the valence band to the conduction band of TiO_2 can be seen around 340-360nm in all the samples, as expected for anatase based nanocomposite[75], [78]. The presence of exfoliated graphite can be noticed in the samples TiO_2-Gr10:1 and TiO_2-Gr1:1

because of the value F(R) in the range from 400 to 800nm. Being linked to K, F(R) can be used to evaluate the absorption for the calculation of the energy band gap of the composites[84] Figure 22 b reports the Tauc equation[85] which is commonly used to estimate the optical bandgap of semiconductors: $[F(R)\cdot hv]1/2$ vs. hv, where hv is the photon energy. The obtained bandgap, which is 3.25eV for the pristine TiO_2, decreases in the presence of exfoliated graphite to 3.20 and 3.02eV for TiO_2-Gr10:1 and TiO_2 -Gr1:1, respectively. This modification could be expected, since it was already shown in similar systems with TiO_2 and reduced graphene oxide[86]–[88]. Extinction spectra in liquid phase are obtained by using a reduced optical path of ~ 180µm with respect of the 1 cm path conventionally used in spectrophotometers. UV-VIS absorption spectra in the liquid phase are recorded at 25°C with a Cary300 UV-Vis spectrophotometer (Agilent Technologies).

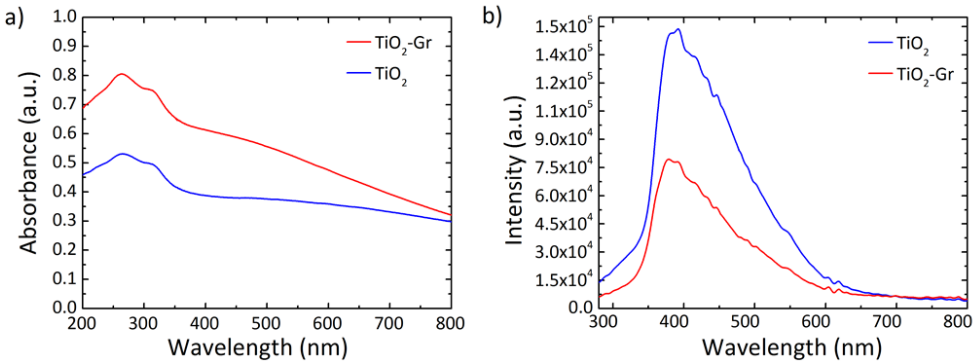

Figure. 23a) Extinction spectra in the liquid phase obtained by using two quartz slides corresponding to a thickness of the solution≈180µm, b) Emission spectra obtained using a front phase geometry with a scan angle of 90o, and 266nm excitation wavelength.

Figure 23 a shows two bands in the UV region at 250 and 320nm, that are characteristic of the TiO_2-NPs[89]. The photoluminescence (PL) spectra of pristine TiO_2 and TiO_2-Gr10:1 in the liquid phase, following excitation at 266 nm (~4.7 eV), are reported in Figure 23. While the shape of the spectra is similar, the quenching of the PL intensity in TiO_2-Gr10:1 points to an electronic interaction between the excited TiO_2 and the exfoliated graphite, preventing radiative recombination of the photogenerated e-h pairs

2.3.6. Problem in the interpretation of the mechanism of photocatalysis

The e-h pairs generation and evolution in TiO_2/carbon nanocomposites like TiO_2/reduced graphene oxide (RGO)[86], [90], [91] and TiO_2/graphene quantum dots (GQD)[92], have been experimentally investigated by means of transient absorption (TA) spectroscopy. The TA measurements outlined the possibility of electron transfer both from RGO/GQD to TiO_2 and vice versa. Going into details, Williams et al.[92] identified, in TiO_2/GQD composite, an ultrafast electron injection, from the GQDs to the TiO_2's conduction band, with a time constant of < 15 fs, after the photoexcitation of the GQDs at 2.4 eV, well-below the TiO_2's energy gap (~3.2 eV). Similarly, Wang et al.[90] reported a charge transfer in TiO2/RGO from RGO to TiO2 upon exciting RGO at 2.75 eV, still below the TiO_2 bandgap. In $Ti_{0.91}O_2$/RGO nanocomposites, Manga et al.[91] reported that the mechanism of e-h pairs generation and their dynamics after photoexcitation below the $Ti_{0.91}O_2$'s bandgap, are driven by the absorption of visible light from the RGO nanosheets and the subsequent injection of the photoexcited electrons into the conduction band (d-orbitals) of $Ti_{0.91}O_2$. On the other hand, in $Ti_{0.91}O_2$/RGO composites with 0,1 wt% of RGO, Morais et al[86] demonstrated that exciting both TiO_2 and RGO with 3.5 eV photons, the RGO sheets can act as electron acceptors and cause the decrease of the charge recombination rate in the TiO_2. As proposed by the authors, this process can explain the observed enhancement of the PQE and of the photocatalytic activity of the nanocomposite. The charge transfer is deduced from TA measurements that indicate an increment in lifetime and yield of both the photo-generated holes and electrons, which, however, were not quantified. No measurements is reported of the charge separation dynamics in the TiO_2/RGO nanocomposite, which was studied in a temporal range (from $1x10^{-6}$ to 1 second) that is much longer than the timescale for electron/hole separation and migration (from 0 to $1x10^{-6}$ seconds). The charge transfer processes were investigated also theoretically by computational simulations performed by Long et al.[93] predicting that electron and energy transfer in graphene/TiO_2 composites can proceed in both directions, depending on the energy of the excited electron. Despite the above mentioned literature, a detailed understanding of the mechanisms responsible for the increased PQE in TiO_2/carbon nanocomposites is still

missing. Beside the number of reports of the improved photocatalytic efficiency, no clear evidence for the specific role of the structure of the carbon-based material is reported. Furthermore, up to now, no studies have addressed the correlation between the addition of pristine, liquid-exfoliated graphene (without any oxidation /reduction process)[45], [52], [53] and the improvement of the PQE and of the generation of e-h reactive species in TiO_2 nanostructures.

2.3.7. Broadband TA spectroscopy: TiO_2:Gr 10:1

In order to identify of e-h reactive species in TiO_2 nanostructures, we perform a comparative study of charge-carriers dynamics in pristine TiO_2 and TiO_2-Gr 10:1. We use broadband TA spectroscopy with sub-200-fs time-resolution. We excite the samples with UV pulses centred at 266 nm (~4.7 eV), well-above the electronic band gap of TiO_2, and we measure the transient differential transmission (ΔT/T) over a broad spectral region spanning from the near-infrared (NIR) to the visible (430-1400nm range). The pump-probe setup starts with an amplified Ti:sapphire laser (Coherent, Libra), delivering 100-fs, 500-μJ pulses at 800nm and 1kHz repetition rate. The pump pulse centred at 266 nm is generated by frequency tripling the laser output and it is modulated with a chopper at 500 Hz. The broadband probe pulse is obtained by white light continuum generation in a sapphire (for the visible) or YAG (for the infrared) plate and its spectrum is detected by an optical multichannel analyser. The parallel linearly polarized pump and probe pulses are focused on the sample in a non-collinear geometry with spot sizes of 180 and 80μm, respectively. The pump power is 1.6 mW corresponding to an incident fluence of ~3 mJ/cm^2 (~1016 photons cm^{-2}). The measured signal is the delay-dependent differential transmission spectrum, defined as (Eq 19)

$$\Delta T/_{T(\lambda,\tau)} = {}^{T_{on}(\lambda,\tau)}/_{T_{off}(\lambda)} - 1$$

where T_{on} and T_{off} are the probe spectra transmitted through the excited and the unexcited sample, respectively, λ is the probe wavelength and τ the pump-probe delay. The time delay is tuned by varying the optical path of the

pump pulse with a motorized translation stage and the temporal resolution of the apparatus is of the order of 180 fs.

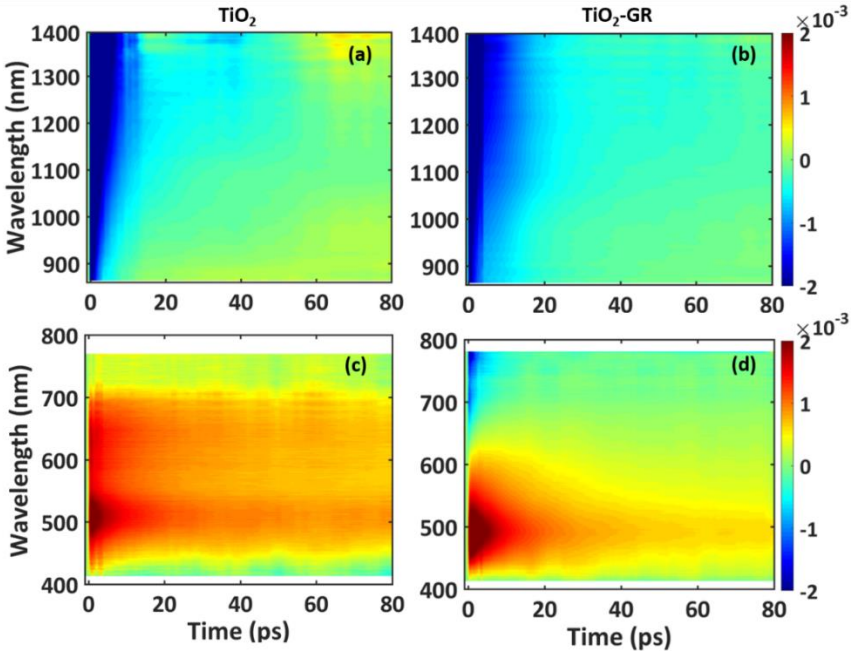

Figure. 24 Transient Absorption measurements. ΔT/T maps as a function of probe wavelength and pump-probe delay of pure TiO_2 in the NIR (a) and in the visible range (c); ΔT/T maps of the TiO_2-Gr10:1 nanocomposite in the NIR (b) and visible range (d).

The measured ΔT/T (λ,τ) maps of pristine TiO_2 and TiO_2-Gr10:1, as a function of the probe wavelength λ and the pump-probe delay τ, are reported in Figure 24. We start by discussing the TA maps in the NIR, Figure 24 a,b, where the TiO_2 exhibits a broad photo-induced absorption (PA, ΔT/T <0) band from 870 to 1400nm. We assign this PA to the intraband transitions of the photo-excited free electrons from the conduction band (CB) edge, as already observed for anatase TiO_2-NPs[94]–[97] An additional source of PA in the NIR comes from the transition of trapped electrons to the CB[98]. A large variety of trapping states is expected in TiO_2[99], with energy distribution dependent on sample preparation; according to[99] and references within, the contribution of trapped electrons to the PA signal should dominate over the free-electron absorption in the range 870-1150nm. In the NIR both monolayer[100] and multilayer graphene[101] show a positive ΔT/T signal, corresponding to photo-bleaching (PB) due to Pauli blocking[100], [101]from the hot electron distribution in the CB. Since the TA spectrum of TiO_2-Gr10:1

in the NIR consists of a PA band, its optical response is dominated by TiO2 due both to the higher intensity of the transient signal from TiO_2 and to the higher concentration of TiO_2 with respect to graphene flakes. The TA maps of TiO_2Gr10:1 and TiO_2 in NIR differ for their time decay, as shown in Figure 25a.

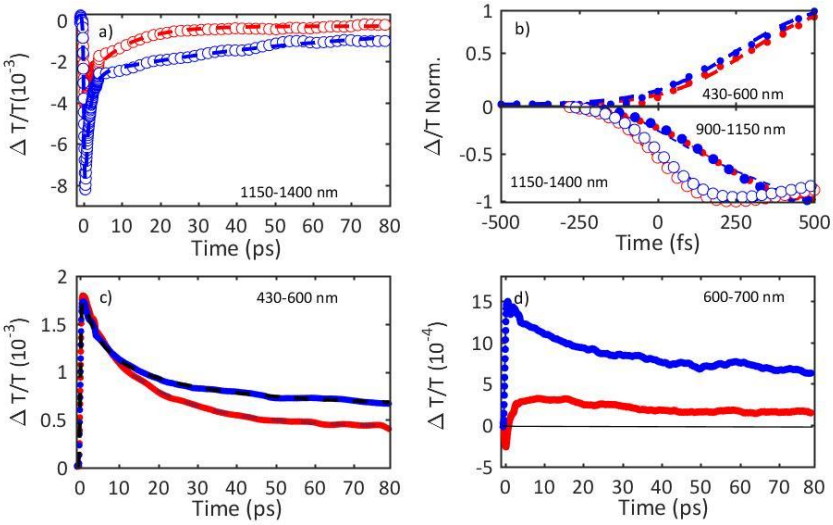

Figure. 25 Integrated dynamics for fixed wavelength ranges. a,c,d) Relaxation dynamics of TiO_2 (blue dots) and TiO_2-Gr10:1 (red dots) together with the best fit function (dot lines). b) Normalized signal build up for the different transient transmission bands: SE in the range 430-600nm, PA in the range 1150nm-1400nm (open dots) and 900-1150nm (full dots).

The portion of the PA band in the range 1150-1400 nm can be attributed to free electrons, as confirmed by the instantaneous (i.e. resolution limited) formation in Figure 25 b and by the monotonic increase of the signal with probe wavelength. For pure TiO_2, this PA relaxes following a bi-exponential decay with time constants $\tau1TiO_2/PA$ = 500fs,$\tau2TiO_2/PA$ = 45ps. Conversely, in the presence of the exfoliated graphite flakes, the relaxation dynamics is best fitted by a three-exponential decay with time constants $\tau1G/PA$ = 500fs,$\tau2G/PA$ = 4ps,$\tau3G/PA$ = 20ps. In both TiO_2 and TiO_2-Gr10:1, the first sub-ps decay component is associated to the trapping of free electrons[102]–[104]. The appearance of an additional decay channel and the overall shortening of the PA bands lifetime can be explained by ultrafast charge transfer from TiO_2 to the graphite flakes, which act as electron scavengers. Interestingly, the dynamics of the PA in the range 870-1150nm, mainly related to absorption from trapped electrons[102], appears almost unperturbed by the presence of exfoliated graphite, suggesting that the electron transfer

mostly involves free electrons. In both samples, this PA band shows a build-up with a 400-500fs time constant (Figure 25 b, related to the process of electron trapping (which was found to occur with ∼200 fs time constant in other studies[105]). This rise matches the sub-ps decay component (indicated as τ1 TiO_2/PA, τ1 G/PA) of the PA in the range 1150-1400nm, observed in both TiO_2 and TiO_2-Gr10:1, which we attribute to free-electrons trapping. Further evidences of electron transfer from TiO_2 to flakes can be found in the out-of-equilibrium optical response in the visible range, Figure24 c, d. In the TiO_2 sample we observe an increase in transmission ((ΔT/T) >0) in the visible which, considering the vanishing ground state absorption in this spectral range, can be assigned to stimulated emission (SE), i.e. amplification of the probe beam due to optical gain. We identify two overlapping SE bands: the first one, in the range 430-600nm, due to the recombination of free electrons with trapped holes, and, the second, in the range 600-700nm, due to recombination of trapped electrons with free holes. In TiO_2-Gr10:1 the second, red shifted SE band is strongly quenched and a residual component appears only few ps after excitation (Figure 25 d). The SE band in the range 430-600nm, related to trapped holes recombination, instead, can be observed in both samples, but in the TiO_2-Gr10:1 it decreases faster to equilibrium (Figure 25 c). This band is not formed instantaneously, but as ingle exponential build up with 400-500 fs time constant is observed, possibly due to hole trapping, see Figure 25 b. The SE relaxation dynamics can be fitted in both samples by a bi-exponential decay on top of a long lasting component related to the emission on the ns timescale[97]. In pristine TiO_2, we get τ1 TiO_2/SE = 5ps, τ2 TiO_2/SE = 45ps, while in TiO_2-Gr10:1 we obtain τ1 G/SE = 4ps,τ2 G/SE = 20ps (Fig. 11 c). While τ1 TiO_2/SE could depend on the lifetime of the trapped holes, the other three relaxation components τ2 TiO_2/SE, τ1 G/SE and τ2 G/SE, match quite closely those observed for the PA decay in the NIR (equal to τ2 TiO_2/PA, τ2 G/PA, τ3 G/PA). This indicates that the SE band at 430-600nm and the PA band at 1150-1400nm decay with similar dynamics. These components can be associated to the population dynamics of free electrons, whose lifetime, in the TiO_2-Gr10:1 nanocomposite, is limited by the charge transfer to graphitic flakes which thus occurs on a time-scale of 4-20ps. Previous ultrafast spectroscopy studies [104], [105] on Pt loaded TiO_2 NPs suggested a similar electron transfer time of several ps. In our case, electron transfer to the graphitic flakes increases the trapped holes lifetime, because it inhibits one of the recombination channels, thus enhancing the oxidative photocatalytic reactivity of the composite at the surface.

2.3.8. Concluding remarks on Section 2.3: the most performing material TiO_2:Gr 10:1. Final interpretation of the photocatalytic mechanism in TiO_2/Gr PCs

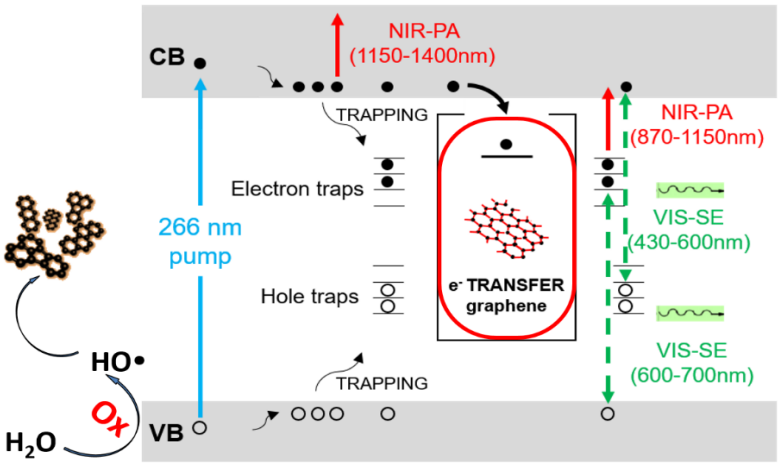

Figure.26 Schematic illustration of different optical transitions contributing to the observed transient absorptions signal of TiO_2 and TiO_2-Gr10:1 nanocomposites

This section presented the full characterization of TiO_2/Gr nanocomposites that in the first preliminary photocatalytic tests displayed an enhanced photocatalytic activity with respect to the bare commercial TiO_2-NPs. These composites are produced via liquid phase exfoliation of graphite in presence of TiO_2-NPs, without surfactants which could prevent the energy transfer between TiO_2 and graphite flakes. The nanocomposites morphology is characterized by a combination of SEM,TEM and the structure is studied by XRD and Raman spectroscopy revealing a strong interaction between TiO_2 and the carbon atoms. The enhanced photocatalytic activity is monitored for two different concentration of TiO_2 and graphite, and an ideal mass ratio of 10:1 %w/w is identified. We observe that the experimental photo-degradation kinetics of the nanocomposites consists of a combination of zero-order and first order processes. Finally, a comparative study by ultrafast TA of the transient optical properties, demonstrates that the increase in the photocatalytic activity of the nanocomposites is due to the electron transfer from TiO_2 to the graphite flakes, which occurs within the first picoseconds of the relaxation dynamics. Figure 26 summarizes the photoexcitation scenario of TiO_2 and TiO_2-Gr10:1 samples, including the different charge relaxation pathways.

2.4. Characterization of other composites: TiO_2:TMDCs/RP

Results of dye degradation in indoor (Vis) as well as outdoor(UV) obtained with TiO_2:TMDCs/RP showed in most of the case a positive trend. in order to have more knowledge in terms of time dependency of photocatalytic activity (kinetic behaviour), photophysics (UV/Vis absorption and Raman spectra) and morphology (HRXRD and SEM). In this section is reported a full characterization of the TiO_2:X (X=MoS_2, WS_2, RP) with doping ratio 100:1 10:1 1:1 w/w with respect of TiO2.PCs

2.4.1. Kinetic photocatalytic tests by means of fluorescence

The kinetics of photocatalytic degradation of pollutants of all the compounds were investigated by means of fluorescence spectroscopy. The advantage of using this technique is that the irradiation of the PCs and the detection of dyes degradation can be performed simultaneously. In the previous kinetic photocatalytic test, showed in section 2.3.1, the degradation was measured by taking an aliquot of the solution, after a defined period of irradiation time, and by measuring the RhB left by means of absorption spectra.

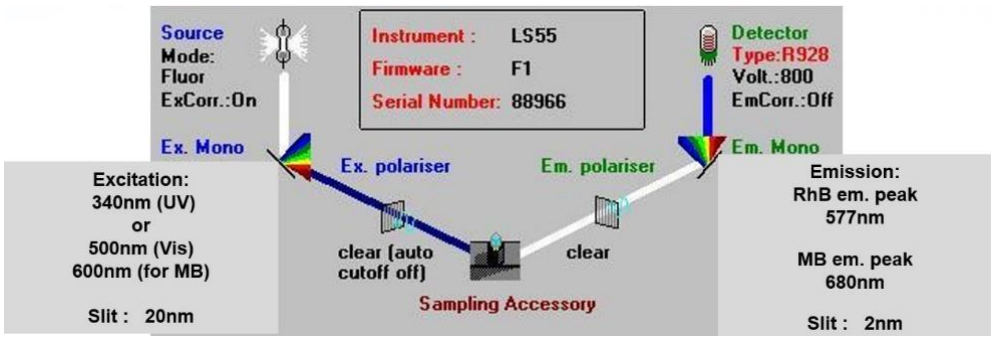

Figure. 27 scheme of a fluorimeter and parameters to perform and detect indoor (Vis) and outdoor (UV) kinetic tests.

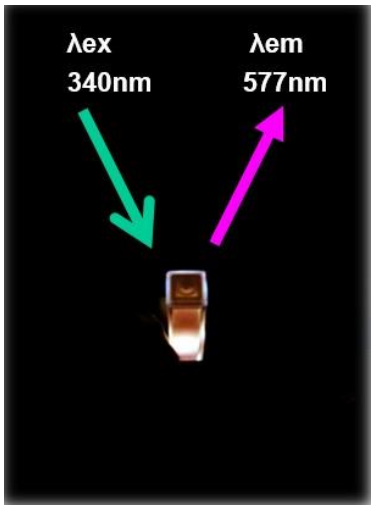

Figure. 28 PCS and RhB solution inside of the fluorimeter during an experiment of kinetic photodegradation of RhB. The irradiation wavelength is 340nm and the detection is in the peak of fluorescence of the dye.

It is not trivial to irradiate and measure the absorption of the dye during irradiation of the sample since the UV/Vis absorption needs a range of wavelength to probe the samples that does not manage to activate efficiently the PCs. With a fluorescence measurement, the measurements are performed inside a fluorimeter, as shown in Figure 27,28. Here the simultaneous excitation end detection is possible since the intrinsic geometry of the fluorescence measurement allows to use an excitation beam that is perpendicular to the detection of the fluorescence emission. Exploiting an:

1. single wavelength excitation able to activate the PCs and to excite the dyes.
2. a multi-wavelength detection of the dyes fluorescence signal that is (in our experimental conditions) proportional to the amount of dye left inside of the solution.

As a matter of fact the photodegradation process involves the formation of several radicals on the MB/RhB aromatic molecular structure that bring to the disruption of their molecular structure as well as of their aromatic system [8]. Even a small modification of the molecular structure bring to a modification or a quenching of the fluorescence signal of MB/RhB as well as for their characteristic absorption spectra.

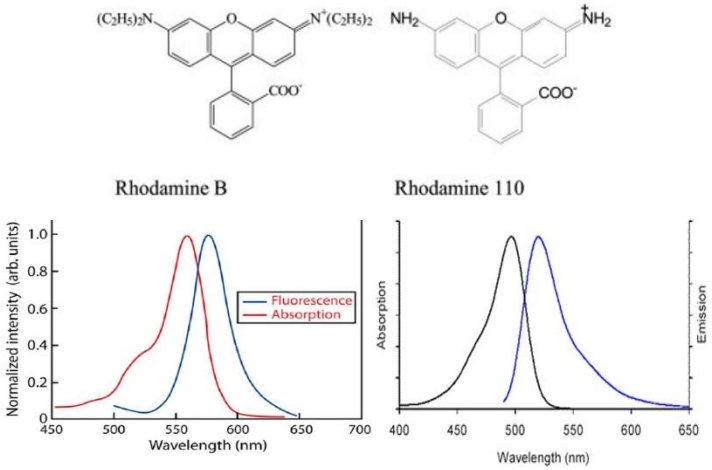

Figure. 29 Molecular structure, absorption and emission spectra of RhB, on the left side, and de-ethylated RhB (or Rh110) on the right side

As it is possible to see from Figure 29, the RhB de-ethylation bring to the formation of the RhB 110. This molecule has a blue –shift of both absorption and emission with respect of the normal RhB. The de-ethylated product is one of the possible reaction product of the photocatalytic photodegradation of the RhB. In fact most of the N-de-ethylation processes were taken place by the formation of nitrogen centered radical during the destruction of RhB dye chromophore structure. The photocatalytic degradation of RhB by the photogenerated active species such as °OH and hole could attack the central carbon of RhB to decolorize the dye and further degraded via N-de-ethylation process[8].

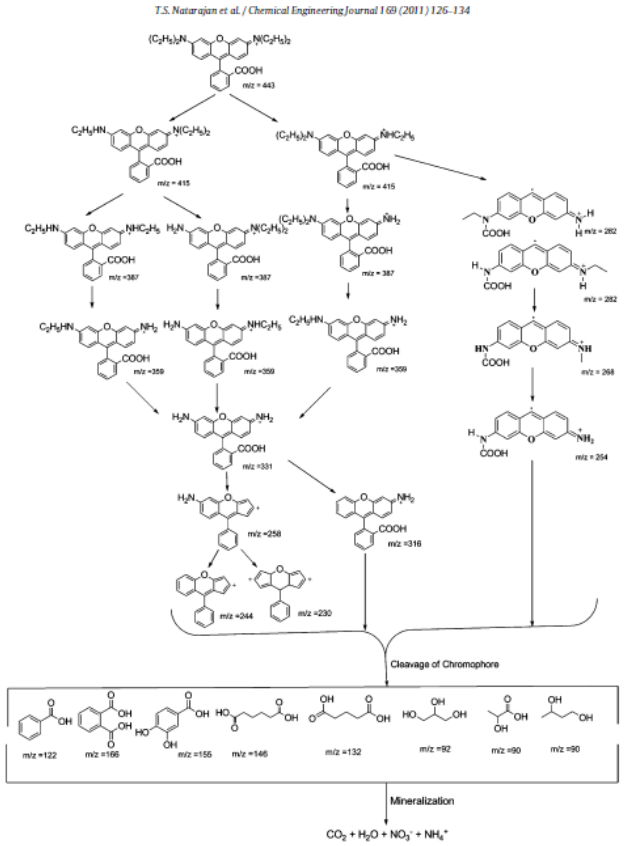

Figure. 30 mechanism of RhB degradation pathway[8]*. As it is possible to see the degradation bring to the disruption of the aromatic system of RhB dye that is the one responsible of its fluorescence signal.*

The same spectral effect can be observed in the case of methylene Blue for Vis photodegradation kinetic measurements. After all this consideration it is understandable that is it possible to monitor the kinetic behaviour of the PCs upon light irradiation by a simultaneous monitoring of the fading of dye's fluorescence upon excitation of both dye and photocatalyst. In order to perform an outdoor kinetic photodegradation test RhB dye is used, and the system is constantly

irradiated with a single wavelength light 340 nm, used for exciting both the photocatalyst and, to a less extent, the dye. The fluorescence signal of RhB is detected collecting continuously the emission intensity at 577nm, see Figure 27, 28. The Vis indoor kinetic photodegradation test is performed both with RhB and MB dye with a single excitation wavelength of 500 and 600 nm respectively. The fluorescence signals are detected collecting continuously the emission intensity at 577nm or 680nm, see Figure 28. For the analysis of TiO_2-GRMs/RP samples only RhB dye was tested.

2.4.1.1. Procedure and results

All the examined compounds in this section are the ones that in UV or Vis photocatalytic tests displayed a positive behaviour, see Table 7. In this section it was not possible to perform the analysis of the 1:1 ratio samples since the measurement of the absorption as well of the kinetic photocativity is strictly dependent on the scattering of the solution, and, due to the presence of high amount of doping material, it was not possible to use the solutions as prepared. Furthermore the procedure we used for sample preparatopm (and first proposed by Serpone and coworkers [106])brought to the precipitation of all the PCS powder, so we carried on the analysis of the other promising samples. The selected ones were: TiO_2: WS_2/MoS_2/Gr in the ratio 10:1 and TiO_2: WS_2/MoS_2/RP in the ratio 100:1. As mentioned, all the powders are treated with the procedure of Serpone et all [106]. A 6ml water dispersion of each PCs compound 2mg/mL (TiO_2 weight reference) is sonicated for 45 minutes, after addition of 60 µL HCl 1M. Immediately after the sonication, the dispersion is centrifuged at 20°C with 2000 RPM for 10 minutes. This centrifugation process bring to the sedimentation of the aggregates that would have prevented the correct analysis of the solution because of the scattering effects[107]. The final concentration of the dispersion was estimated to be almost 1mg/mL [106]. The kinetic test is performed on centrifuged PCs solutions, with a further dilution in order to have a TiO_2 concentration of 0.2 mg/mL. Then an RhB was added to the solution in order to have a final concentration of 1×10^{-6}M. the kinetic test is performed irradiating the system either in the UV (340 nm) or in the visible (500 nm) and recording the fluorescence spectrum in sequential cycles. The experimental parameters are reported in Table 10:

Table 10 Kinetic analysis experimental parameters.

Parameters	Photodegradation kinetic UV test	Photodegradation kinetic Vis test
λexc (nm)	340	500
Excitation slit (nm)	20	20
λem (nm)	450-700	520-700
Emission slit (nm)	2	1
Cycles	40	120
Scan speed (nm/s)	0.1	0.1
Stirring speed (RPM)	500	500

Then, to compare the behaviour of the different materials, the fluorescence intensity at a 585nm emission wavelength is plotted and analysed as a function of irradiation time.

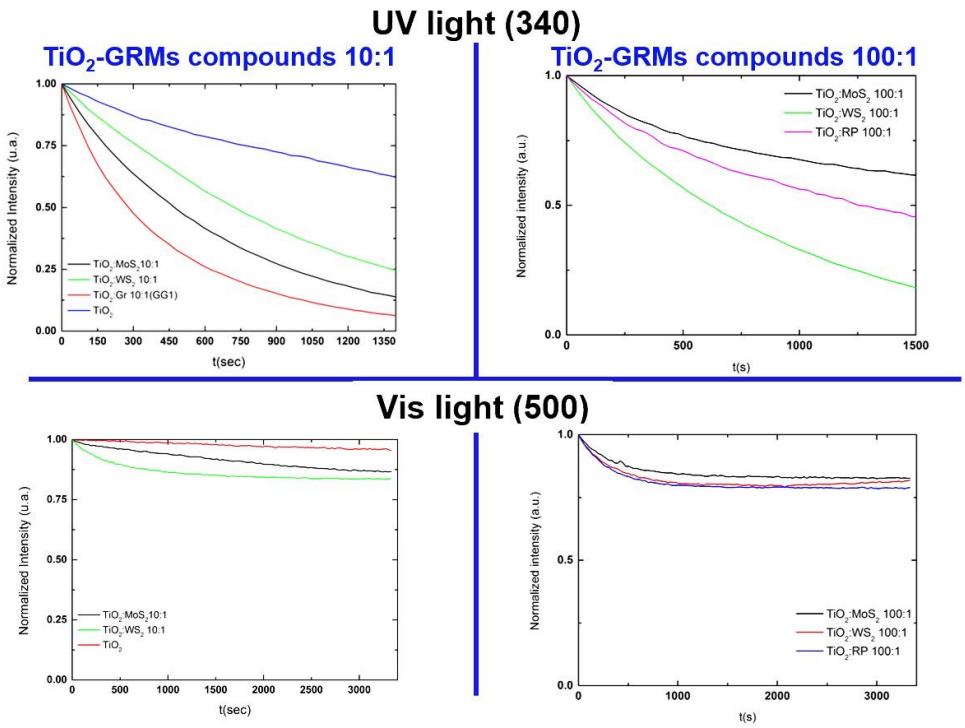

Figure. 31 Normalized plot of the RhB fluorescence intensity signal at 577 nm during irradiation time (3500sec = 60 minutes). On the left column the samples with 10:1 ratio, in the second column the samples 100:1. In the first line kinetic test in UV conditions, in the second line kinetic tests in Vis light conditions.

The set of **samples with 10:1** ratio shows that the most active photocatalyst with 340 nm irradiation light is TiO_2:Gr, followed by TiO_2:MoS_2 and TiO_2:WS_2. That could be also deducible from the preliminary **UV** photocatalytic tests previousely discussed, since the increment with respect of the reference sample was the **higher in the case of Gr doping(%ΔP=+89), followed by MoS_2 (%ΔP=+51) and WS_2(%ΔP=+9)**. Furthermore it is possible to note that the degradation process of rhodamine B is more or less linear in the case of TiO_2. The doped PCs show initial linearity of the process, that then deviates. This deviation implies that more than one process as well as more than one kinetic constant is involved, and the photodegradation process in the case of the presence of dopants, follows a different pathway with respect of the one of the reference. So a higher activity, and a modification of the degradation kinetic, of TiO_2:Gr 10:1 and TiO_2:MoS_2 with respect of TiO_2:WS_2 can be due to a higher interaction between TiO_2 and the dopants as well as an higher exfoliation of the layered material. A stronger interaction between the components of the PCs can bring a change in the absorption spectra. These aspects will be investigated in the following section. In the case of a **Vis light 500nm** and **10:1 samples**, is it possible to note that the WS_2 seems to be the most promising one since the drop of fluorescence is higher with respect of GR and MoS_2. However it has to be noticed that the shape of this curve after a while reaches a plateau. This seems that after a certain period of time the overall activity of the sample is affected. On the other hand the **linearity of the MoS_2 and Gr curve made us to predict, with some mathematical extrapolation process, that with longer irradiation time the performances of these samples would have outmatch the one of WS_2.** The kinetic tests with UV light of the 100:1 samples display and anomalous behaviour in the case of MoS_2. As a matter of fact this sample was one of the most promising in UV static photocatalytic test with a %ΔP=+66.Since this sample was synthesized again, we tough about a contamination of this batch of samples. Due to the overlap of the curve it is not possible to note any discrepancy in the kinetic photocatalytic behaviour of the 100:1 samples.

2.4.2. Absorption measurements

Extinction spectra in liquid phase are obtained by using solutions containing 0.2 mg/mL (referring to TiO_2 weight content). Absorption spectra are

obtained by using standard 1 cm optical path cuvette conventionally used in spectrophotometers. UV-VIS absorption spectra in the liquid phase are recorded at 25°C with a Cary300 UV-Vis spectrophotometer (Agilent Technologies). The absorption range was 250 nm – 800 nm with a scan rate of 480 nm/min .All the PCS, selected as explained in the previous section 2.3.1, were processed with the procedure proposed by Serpone explained in the previous section. In order to prepare the samples it was assumed that after the centrifugation the amount of titania left inside of the suspension was the same on every samples and equal to 1mg/ml. Figure32 a shows the absorption spectra collected for the 10:1 samples. Is it possible to note that the spectra are different in intensity in the region of adsorption of TiO_2, between 200-350nm. Since the TiO_2 starting material is a commercial product, this can be due different final concentrations after the centrifugation process maybe brought by different particle aggregation that led to different concentration with the same centrifugation time. However it is important to observe the shape of the spectrum which displays the typical shape of peak of TiO_2 with two bands in the UV region at 250 and 320nm, that are characteristic of the TiO_2-NPs[89]. **It has to be noticed that the intensity ratio of the 250 and 320 bands of each spectrum is higher in the case of photocatalysts with higher photocatalytic activity**. Further investigation has to be done in order to address this phenomena.

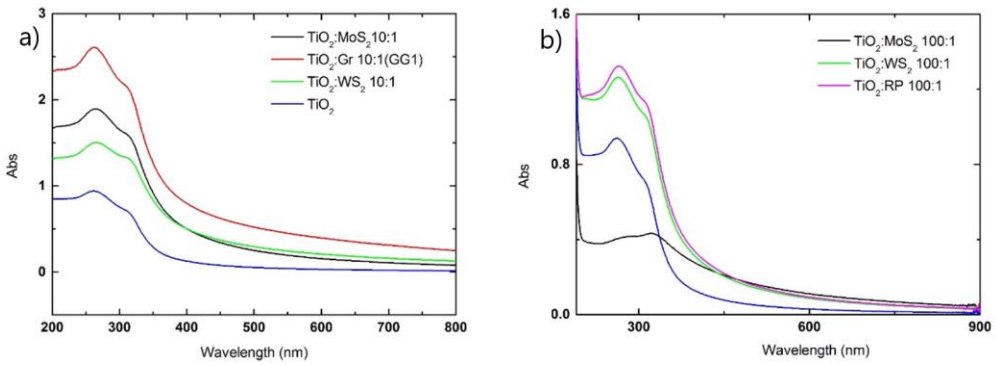

Figure. 32 a) Absorption spectra of TiO_2-Graphene 10 :1, TiO_2-MoS_2 10 :1 and TiO_2-WS_2 10 :1, b) Absorption spectra of TiO_2-MoS_2 100 :1 TiO_2-RP 100 :1, and TiO_2-WS_2 100 :1; compared to TiO_2 spectrum(blue line).

In the sample TiO_2-Graphene 10:1, the presence of graphene is highlighted by the different band slope at almost 300 nm, that it is typical of the exfoliated graphite [108]. On the other end for the TMDCs doped PCs no characteristic

peak of the exfoliated material between 600 and 700nm as it can be seen in see Figure 10. This can be due to an insufficient concentration of the exfoliated material, an inefficient exfoliation or a complete coverage of the flakes. Figure 32 b shows 100:1 samples. TiO_2-MoS_2 100:1 and TiO_2-RP 100:1 absorption display the typical band shape of TiO_2, while TiO_2-MoS_2 100:1 has an unusual peak. Probably due to a contamination of the sample.

2.4.3. Scanning Electron Microscopy (SEM)

In order to evaluate the effect of sonication on the commercial Tio2, Scanning Electron Microscopy (SEM, Magellan 400L FEI) images are collected by depositing ~ 20µl of the TiO2 dispersion on a holey carbon copper grid (300 mesh).

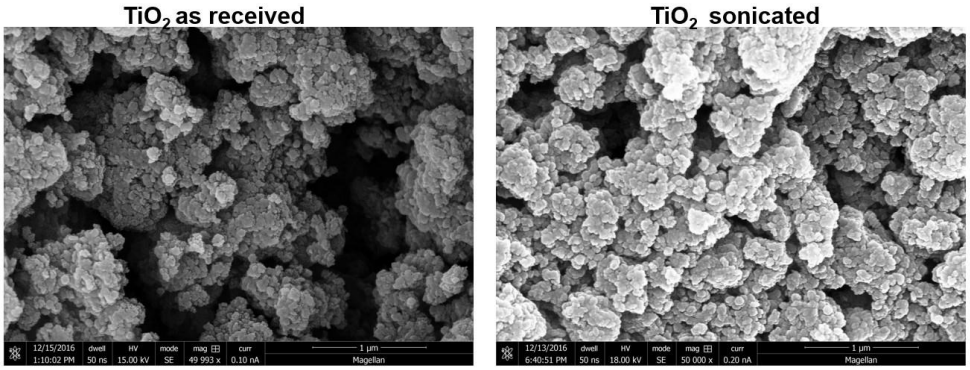

Figure. 33 SEM images of the bare commercial TiO2 as received, and the TiO2 after the sonication in water media and drying.

As it is possible to see from Figure 33 the external morphology of the samples doesn't seems to be affected by the sonication. The only difference that can be noticed is that the sonicated sample is more homogeneous with respect of the unsonicated. This means that the sonication process bring to the disruption of macroscopic aggregates, but does not affect the overall morphology of the starting material. Figure 34 shows the SEM analysis of MoS_2 and WS_2. As it is possible to see in MoS_2 the typical triangular shape of the exfoliated material[109] is present in the 100:1 sample. On the other hand the 1:1 sample does not display the typical triangular appearance of the

exfoliated material. The same effect was noticed in the WS_2 samples where both the 100:1 and 1:1 ratio of doping showed that the appearance of the WS_2 flakes inside of the final material is still hexagonal as the bulk one, and not triangular as expected[110]. The 10:1 samples showed situation that confirmed the exfoliation in case of Molybdenum samples.

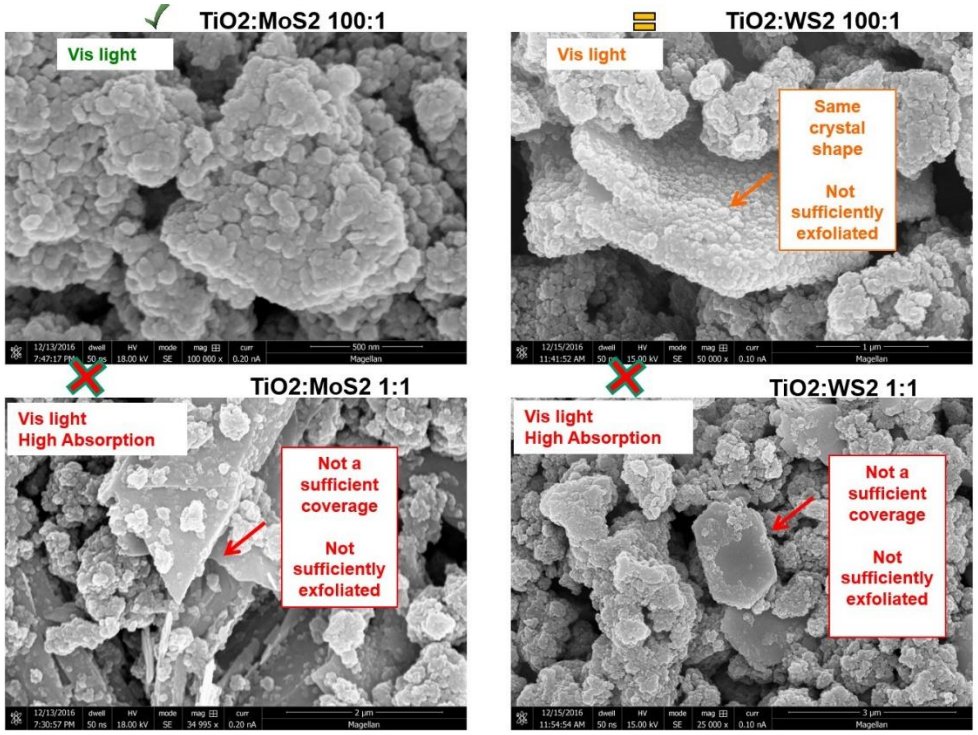

Figure. 34 Sem images of the samples: TiO_2-MoS_2 100:1, TiO_2-MoS_2 1:1, TiO_2-WS_2 100:1 and TiO_2-WS_2 1:1

It is possible to conclude from SEM image that MoS_2 and WS_2 samples have a different behaviour during the sonication. **MoS_2 samples displayed an exfoliation in case of 10:1 and 100:1 ratio.** Higher doping level are not beneficial since the quantity of TiO_2 does not manage to exfoliate as well as cover the flakes. This is also confirmed by absorption and photocatalytic tests reported in Table 8. On the other hand the **WS_2 samples** does not display a sufficient exfoliation **keep on being more like the bulk starting material**. This is confirmed by the poor photocatalytic enhancement of the photocatalysis, see Table 8, as well as a strong absorption. RP compounds, Figure 35, don't have a crystal structure since RP is in its amorphous form. So we compared the microfluidized processed and the unprocessed samples. What is possible

to notice is that in the case of TiO_2-m-RP the titania coverage of RP powders is higher with respect of the unprocessed material. This stronger interaction can be due to the presence of more defects on the RP surfaces.

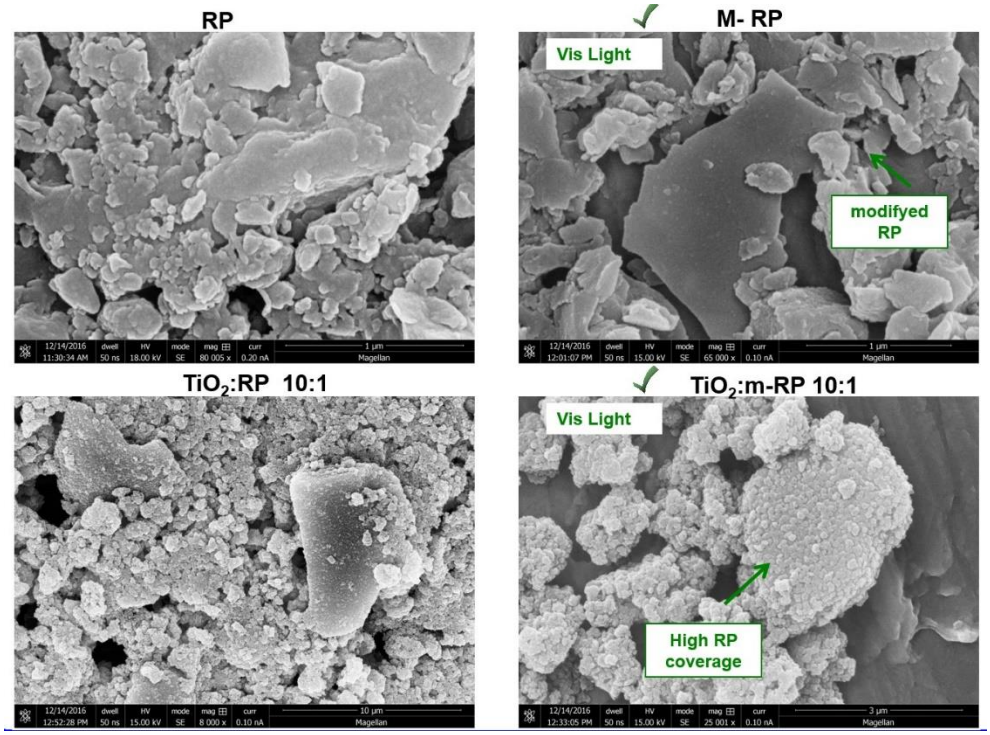

Figure. 35 SEM images of the RP based samples. It is possible to notice the difference in the interaction between titania nanoparticles and the RP in the case of microfluidized samples.

2.4.4. What happens during the sonication to the starting materials? HR-PXRD measurements

2.4.4.1. TiO_2 starting material

In order to study what was going on during the sonication of TiO_2 NPs as well as the influence of the water on the crystal structure of TiO_2, phase we perform HR-PXRD measurements in Technion University with the aid of professor Boaz Pokroy. XRD measurements were performed on powdered samples that are loaded into 1 mm diameter boro silicate glass capillaries and powder diffraction patterns are collected at ambient temperature with an incident X-ray wavelength of 0.319902 Å.

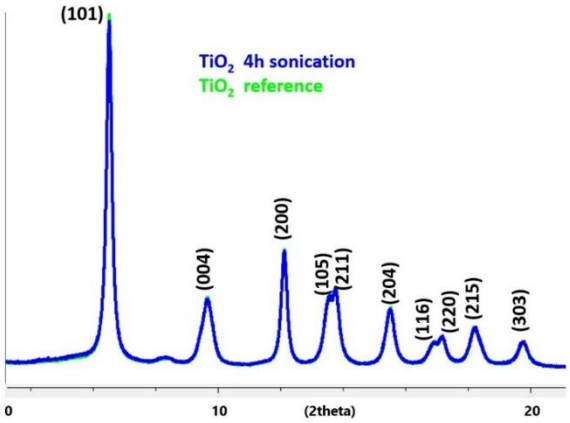

Figure. 36 HR-PXRD diffraction profiles of the sonicated and unsonicated TiO_2. Data confirm the presence of the crystalline phases of TiO_2 (anatase)

The XRD patterns collected from the sonicated and unsonicated commercial TiO_2 starting material, Figure 37. As it is possible to see we observed a complete overlap of the crystalline profile of the two samples. Furthermore the shape of the observed spectra reveals the presence of the major crystalline phase of TiO_2 anatase (The Joint Committee on Powder Diffraction

Standards, JCPDS 21-1272). **It is possible to conclude that sonication has no effect on the structure of TiO_2.**

2.4.4.2. MoS_2 and WS_2 starting material

Then the most promising novel photocatalysts and corresponding reference materials were measured at high resolution powder diffraction beamline. Regarding the dopants we measured: - MoS_2 raw material, MoS_2 after 4h sonication; - WS_2 raw material, WS_2 after 4h sonication. **Since RP is in its amorphous form, the XRD pattern was not collected.**

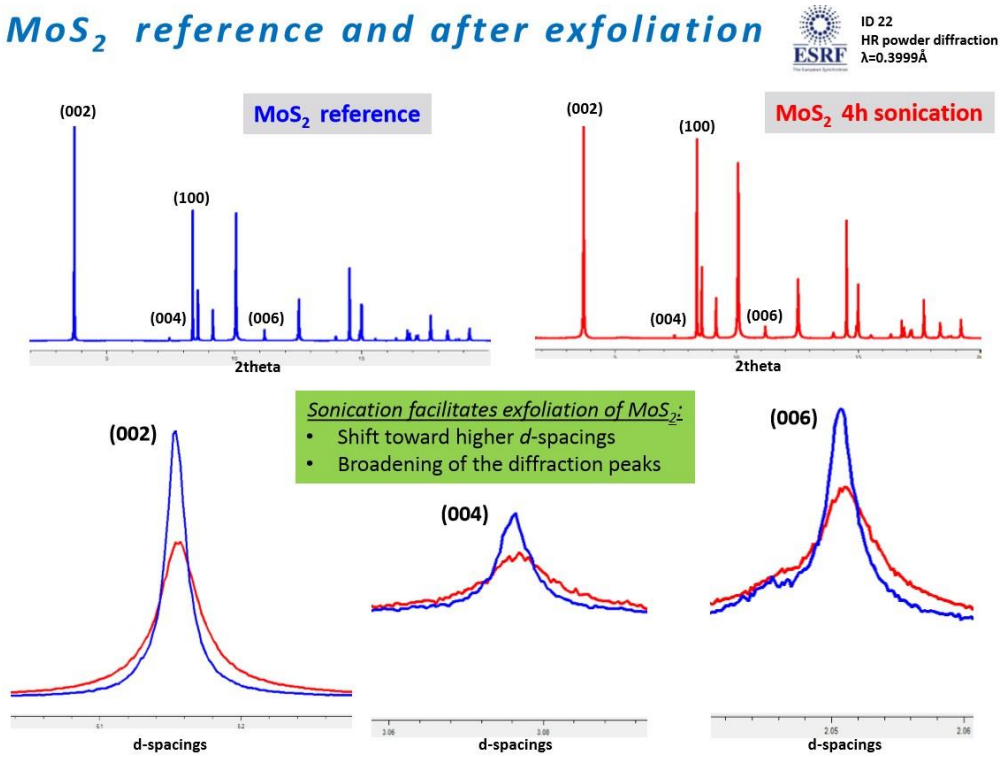

Figure. 37 (First raw)HR-PXRD diffraction profiles of MoS_2 reference and MoS_2 sonicated for 4h. (Second raw) (Second raw) comparison between the d- spacing of the sonicated and unsonicated sample.

Regarding the MoS_2 reference samples, the XRD patterns collected, Figure 37, confirms the presence of the {002}, {004},{100}, {006} reflections of MoS_2 crystal phase [111], [112]. All the above mentioned basal diffraction peak of the sample MoS_2 sonicated for 4h exhibit the lowest intensity while the highest is recorded for the unsonicated sample. This suggests that increasing the sonication process reduces MoS_2 crystallite size of the raw powders and decreases the number of planes oriented along {002}, {004} and {006} directions.

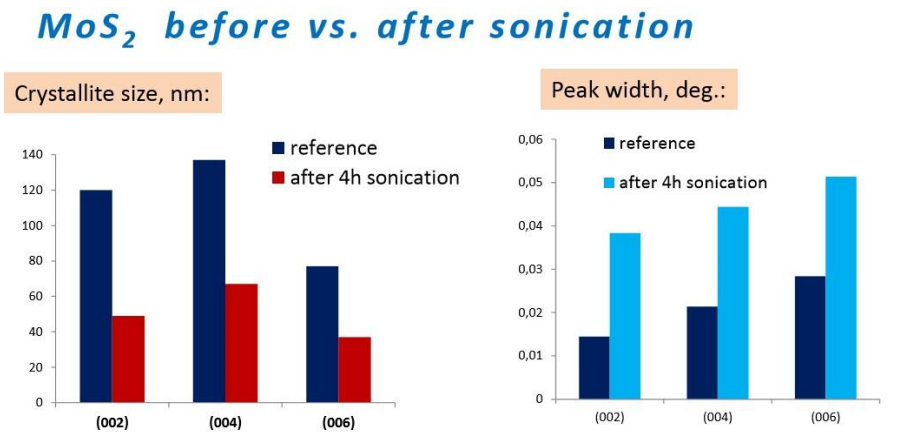

d-spacings, Å :

	(002)	(004)	(006)
reference	6.13262	3.06631	2.04421
after 4h sonication	6.15496	3.07748	2.05165
d-spacings increase, %	2.2	1.1	0.7

Lattice parameters, Å:

	a	c
reference	3.16216	12.30662
after 4h sonication	3.16238	12.30977
distortion	7.0E-05	2.6E-04

Figure. 38 Result of the spectra analysis: crystallite size, d- spacing, peak width and lattice parameters of the sonicated and unsonicated MoS_2

The confirmation of these preliminary considerations on crystallite size was done by the application of Rietveld refinement method[67] by which the full width at half maximum (FWHM) of the diffraction peaks are deduced. The Rietveld refinement method was done by using the General Structure Analysis System (GSAS) program and EXPGUI interface (a graphical user interface for GSAS). It is possible to notice that the FWHM of the above mentioned reflections {002}, {004} and {006}, increases with the sonication time, see “Pack width” section in Figure 38. The broadened FWHM is due to smaller crystallites, see “Crystallite size” section in Figure 38[70], [71].

Furthermore the analysis of the {002}, {004}, {006} showed that the sonication bring the basal reflection to be shifted toward higher d spacing value of 2.2%, 1.1% and 0.7% respectively, see “d-spacing” section in Figure 38, than pristine MoS_2. In addiction the exfoliation was confirmed by a partial distortion of the fundamental lattice of MoS_2 along a and c directions, that is diagnostic of its exfoliation [112] see “Lattice parameters” section in Figure 38. From the comparison between the MoS_2 raw material and MoS_2 after 4h sonication is it possible to notice that there is: a shift toward higher d- spacing, a drop of intensity and ta broadening of the {002}, {004}, {006} characteristic peak of the MoS_2. **Is it possible to conclude that in case of MoS_2 the sonication significantly facilitates exfoliation of the raw materials.**

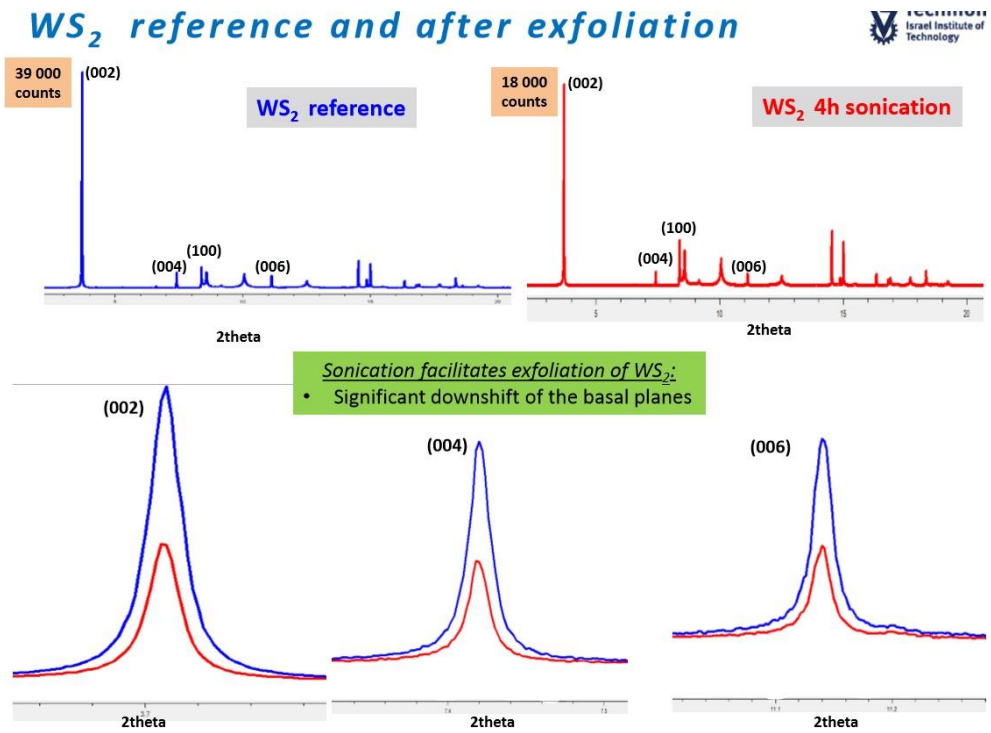

Figure. 39(First raw)HR-PXRD diffraction profiles of WS_2 reference and WS_2 sonicated for 4h. (Second raw) (Second raw) comparison between the d- spacing of the sonicated and unsonicated sample.

The comparison between the XRD patterns collected for the WS_2 raw material and WS_2 after 4h sonication reveals that there is not a significant difference between the two samples[113], [114]. No broadening of the characteristic peak and no shift in the d- spacing. The only difference that can be noticed,

Figure 39 Second raw, is that there is a drop of the intensity of the characteristic diffraction signals. This means a smaller crystallite size. **It is possible to conclude that in case of WS_2 sonication bring just the reduction of the crystallite size, but no exfoliation.** This result confirms the ones obtained with SEM and photocatalytic tests.

2.4.4.3. TiO_2/TMDCs nanocomposites

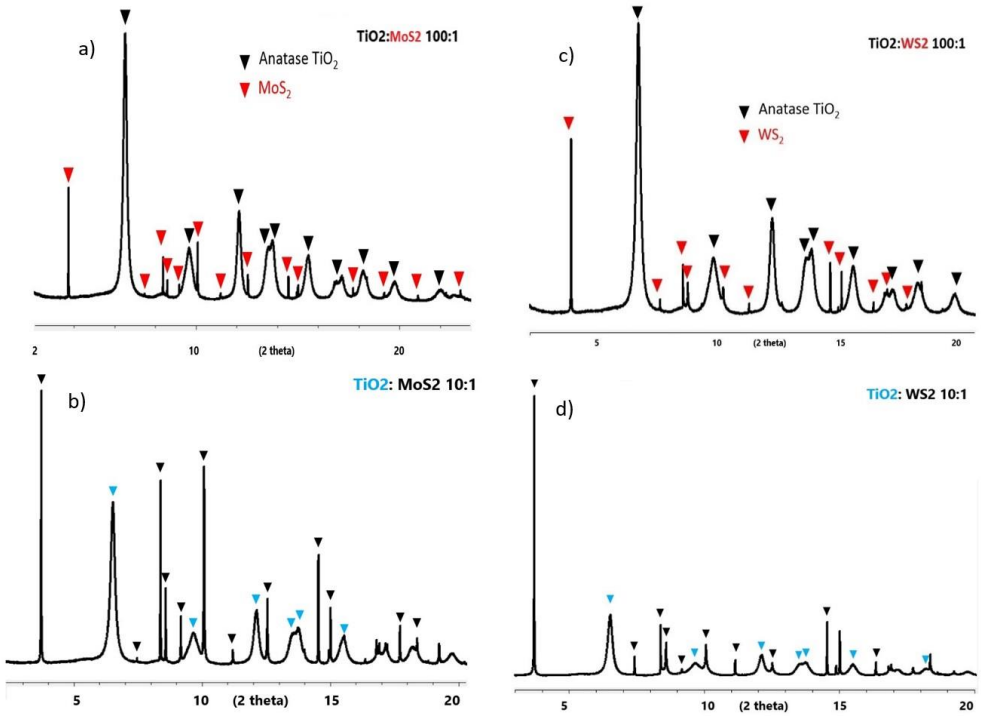

Figure. 40 HR-PXRD diffraction profiles of: a) TiO_2:MoS_2 100:1 b) TiO_2:MoS_2 10:1 c) TiO_2:WS_2 100:1 d) TiO_2:WS_2 10:1

After the analysis of the reference materials, the most promising photocatalysts, TiO_2:MoS_2 10:1 and 100:1, TiO_2:WS_2 10:1 and 100:1, were measured at high resolution powder diffraction beamline. The XRD data confirmed that every compound contains two pure phases: anatase TiO_2 and MoS_2/WS_2 respectively, see Figure 40.

Full Rietveld refinement of data, performed as explained for the raw materials, was done. In the case of MoS_2 raw material it is possible to notice that after sonication the d-spacing increase and significant decrease in the crystallites size along out-of-plane directions. When MoS_2 is in PCs compounds the results demonstrates that the d-spacings increase along (002), (004), (006), with respect of the unsonicated Mos_2, see Figure 41. However no peak broadening so as no decrease in the crystallite size after sonication in the presence of TiO_2. This means **that TiO_2 allows the MoS_2 exfoliation, since we have an higher d-spacing with respect of the reference, but it also protect the MOS_2 from the reduction of the crystallite size brought by the sonication process.**

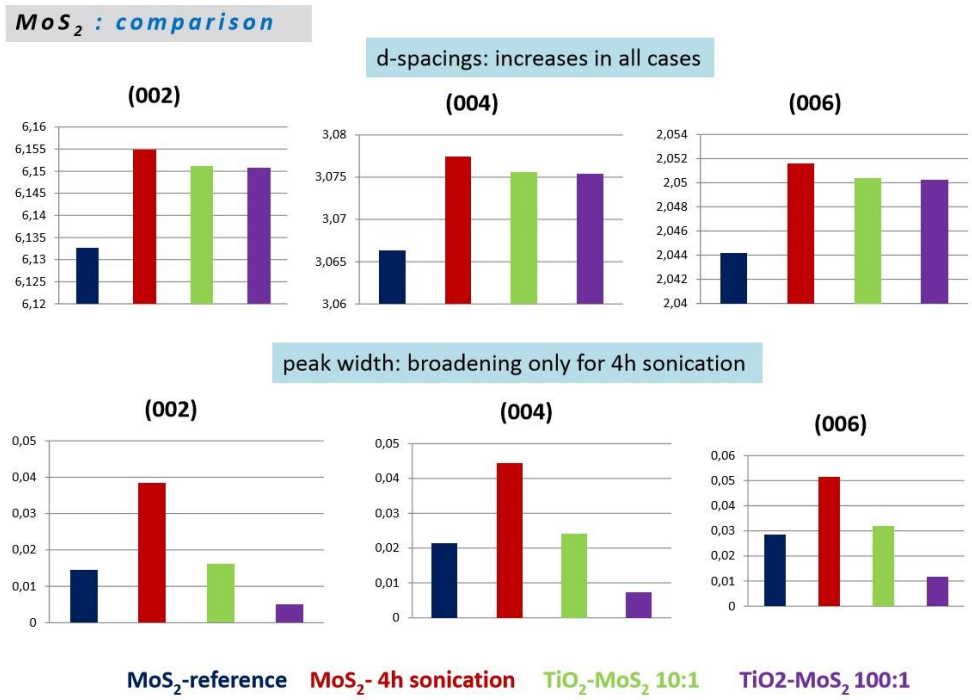

Figure. 41 Result of the spectra analysis. A comparison of d- spacing and peak width of the sonicated and unsonicated MoS_2 reference and in the presence of TiO2 with 10:1 and 100:1 weight ratios.

On the other hand, full Rietveld refinement of data and detailed structural XRD analysis of the WS_2 compounds demonstrate that for the raw material we have a slight increase in the d-spacings after 4h sonication. However if we compare the result with the TiO_2: WS_2 photocatalyst it is possible to see from

Figure 42 that there is no considerable changes in the structure and microstructure after sonication in the presence of TiO_2 since there is no significant change in the peak width. A comparison to reference WS_2 after 4 h sonication with respect of the sonication in presence of titania shows that: there is no change in grain size, the crystallite are less disordered (higher d-spacing), and crystals are more oriented along (002) direction. **This means that in case of WS_2, sonication slightly affect the bulk material and sonication in presence of titania has no effect at all on the modification of the bulk starting material.**

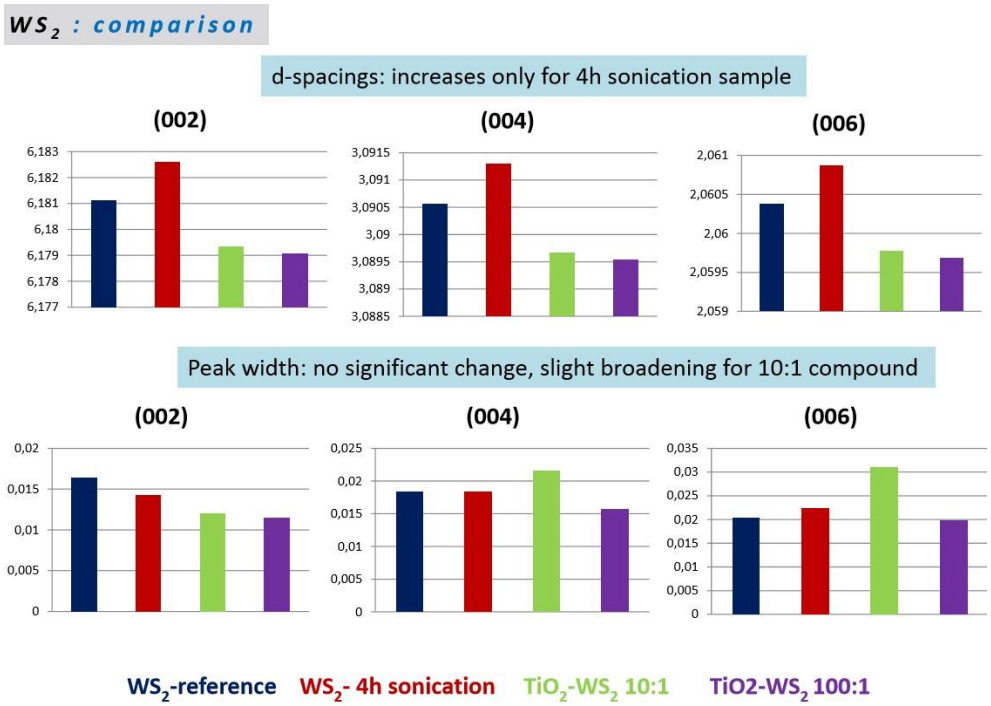

Figure. 42 Result of the spectra analysis. A comparison of d- spacing and peak width of the sonicated and unsonicated WS_2 reference and in the presence of TiO_2 with 10:1 and 100:1 weight ratios.

2.4.5. Raman spectroscopy

Raman spectrum was collected for the 10:1 ratio samples. This selection was made since SEM images of the 1:1 samples displayed an insufficient exfoliation of the bulk doping material, and on the other hand, the high quantity of titania nanoparticles in the 100:1 ratio PCs made impossible the analysis of the TMDC/RP doping.

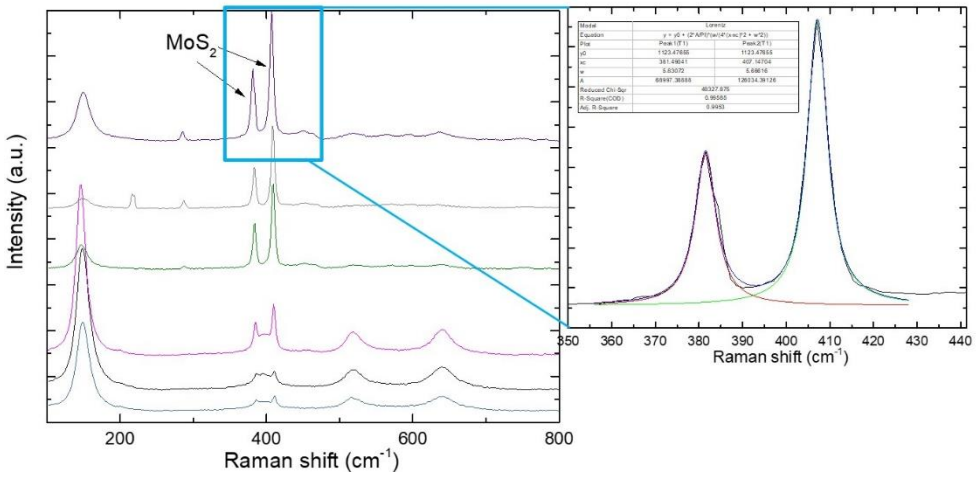

Figure. 43 Raman spectra at 514.5 nm for TiO_2:MoS_2 10:1

Raman spectra are acquired at 514.5 nm using a Renishaw InVia spectrometer equipped with a 50x objective. The power on the sample is kept below 1mW to avoid any possible damage. For all the samples 60µl of aqueous solution are deposited by drop cast onto a glass substrate 1cmx1cm, due to overlapping of the TiO_2 Anatase peaks with the Silicon substrate, then heated at 100°C for 20 min, to ensure water evaporation. Raman results displayed some interesting feature about the composites, that though are of difficult analysis due to the presence of titania nanoparticles. **TiO_2: WS_2 photocatalyst samples seems to be not well exfoliated.** Regarding TiO_2: MoS_2 it is possible to observe an evidence of the MoS_2 flakes embedded in TiO_2 matrix, see Figure 43. The peaks at 144, 397, 518 and 639 cm−1 are the Eg, B1g, A1g and Eg of anatase phase of TiO_2[73]. According to the q vector relaxation model (QVRM) in ref.[74] is possible to derive the crystallite size of the TiO_2-NPs considering the position Pos (Eg@144cm−1) and the FWHM(Eg@144cm−1). For the sample analyzed the Pos(Eg@144cm−1) is ∼147cm−1 with its FWHM

of ~20cm−1, from the model these values correspond to a crystallite size between 5-10 nm. A detailed analysis of the MoS_2 Raman peak [111] reveals that in **the sample the TiO_2:MoS_2 10:1 the molybdenum flakes are in an exfoliation degree between 6 and 20 layers per flake**[112]**.** These results confirm the one obtained in the previous sections.

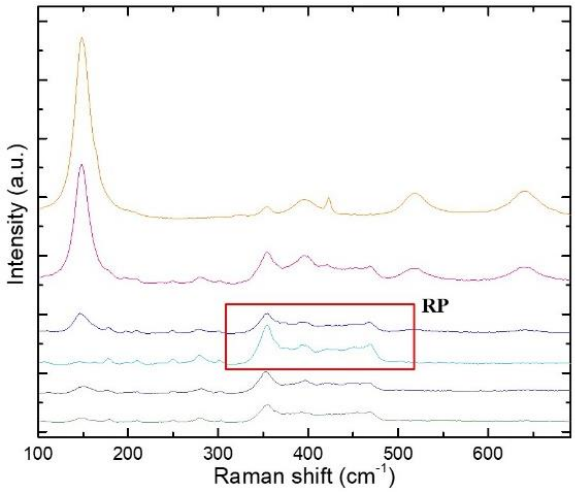

Figure. 44 Raman spectra at 514.5 nm for TiO_2:RP 10:1 with RP not microfluidized. RP shows the characteristic Raman modes of the bulk RP.

Raman spectrum of the TiO_2:RP 10:1 (RP not microfluidized) compound reveals that there are three bands from 300 to 500cm^{-1}.These bands can be assigned to the B^1, A^1, and E^1modes of red P. In particular, the peak at around 349 cm^{-1} can be assigned to the B1 mode, the peak at around 392 cm^{-1} can be assigned to the A1 mode symmetric stretch motion and the peak around 458 cm^{-1} can be assigned to the E1 mode[115]. **The photoactive bare m-RP showed an enhancement of the E1 degenerative mode**, Figure 45. Further investigation has to be done in order to clarify the nature and the role of this spectral mode in photocatalysis.

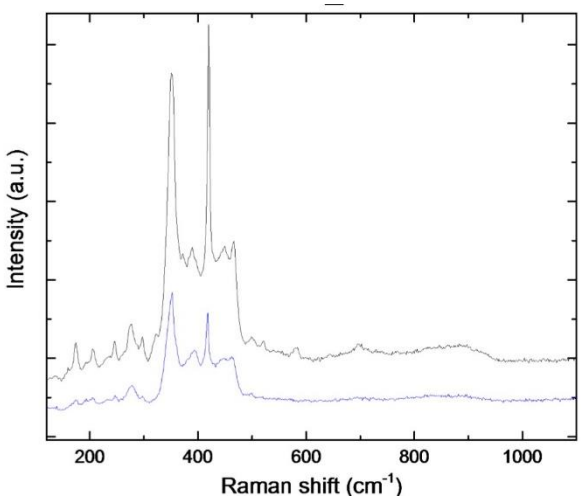

Figure. 45 Raman spectra at 514.5 nm for microfluidized RP. The comparison with the RP not microfluidized (Fig 44) shows a discrepancy in the characteristic Raman modes of the bulk RP.

2.4.6. Surface area analysis: Brunauer–Emmett–Teller (BET) measurements

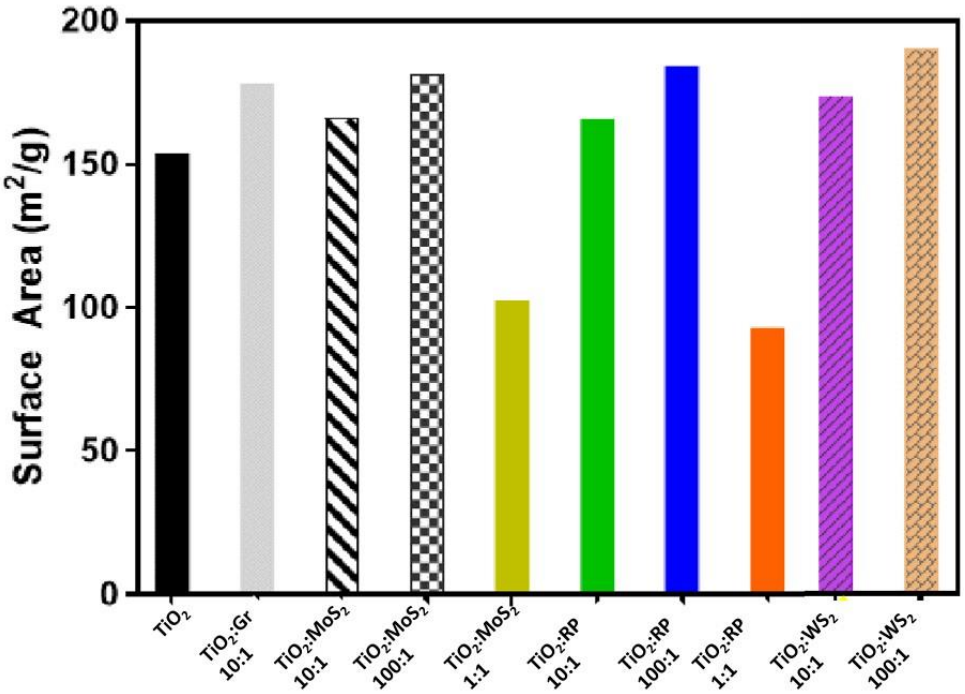

Figure. 46 Surface area of the synthesized photocatalysts. It is possible to notice that lower doping level bring to higher surface area with respect of the TiO_2 reference.

There are many parameters that can influence on photocatalytic performance of TiO_2 based photocatalyst. The morphological parameters of TiO_2 -NPs are: the size, specific surface area, pore volume, pore structure, crystalline phase and the exposed surface facets[116]. In particular some reports strictly correlate the surface area with the photocatalytic activity since the photocatalytic degradation process as well as the ROS production happens on the surface of the titania NPs[117]. In order to see whether there can be any correlation between the photocatalytic activity and the BET value of the PCs surface area was measured. BET measurement is a technique based on adsorption isotherms of gases (typically N_2) that permits to calculate the surface area of the adsorbent. Figure 46 shows that doping of TiO_2 with Graphene, TMDs and Red Phosphorous confers to the system a higher surface

area per gram. In general for all the analysed sample is it possible to notice that the 1:1 samples have a lower surface area with respect of the bare TiO_2. The 10:1 ratio PCs have an higher surface area compared with the one of TiO_2, and the highest value is obtained with the 100:1 sample. This is due to the fact that lower amount of doping bring to a higher yield of exfoliation of the material. As a matter of facts XRD analysis of the sonicated dopants reveals that the crystallite size as well as the exfoliation increase during the sonication process.

Table 11 BET values and photocatalytic results for all the samples.

Sample	%A RhB	%A MB	%P(20) UV/Vis light	%P Vis light	BET (m^2/g)
TiO_2	12	5	35	7	153.94
GG1	12	3	66	12	178.215
TiO_2:MoS_2 100:1	12	2	58	14	181.043
TiO_2:MoS_2 10:1	14	4	53	10	165.976
TiO_2:MoS_2 1:1	40	33	50	0	102.681
TiO_2:RP 100:1	13	3	45	15	184.198
TiO_2:RP 10:1	13	6	67	18	165.719
TiO_2:RP 1:1	16	52	51	33	92.866
TiO_2:WS_2 100:1	12	3	39	11	192.00
TiO_2:WS_2 10:1	13	44	40	7	170.00

Table 11 report the summary of the photocatalytic tests and the BET measurements. In the case of molybdenum doped compound there is a clear evidence that lower doping level of dopants bring to higher surface area and higher photocatalytic activity. On the other hand, for RP and WS_2 compound there is no correlation between the surface area and the photocatalytic activity of the sample. **These consideration confirm the fact that it is not just the effect of the surface area to influence the photocatalytic activity of the PCs, but the performance are strictly correlate to the type of doping material as well as the interaction with light and TiO_2.**

2.4.7. Concluding remarks on Section 2.4: characterization of the composites TiO_2:TMDCs/RP

Preliminary photocatalytic tests on the samples with 10:1 ratio showed an increment that was the higher in the case of Gr doping(%ΔP=+89), followed by MoS_2 (%ΔP=+51) and WS_2(%ΔP=+9). Kinetic photocatalytic tests by means of fluorescence at excitation wavelength at 340nm showed the same trend. So the better photocatalytic result showed in the preliminary tests keep on being conserved during all the degradation pathway. The kinetic photocatalytic tests by means of fluorescence at excitation wavelength at 500 nm showed a linearity of the MoS_2 and Gr curve. This made us to predict, with some mathematical extrapolation process, that with longer irradiation time the performances of these samples would have outmatch the one of WS_2.
Absorption measurements showed that the intensity ratio of the 250 and 320 bands of each spectrum is higher in the case of photocatalysts with higher photocatalytic activity. Furthermore SEM measurements enlighten the fact that MoS_2 samples displayed an exfoliation in case of 10:1 and 100:1 ratio, whereas WS_2 samples does not display a sufficient exfoliation keeping on being more like the bulk starting material. From HR-PXRD measurements was possible to investigate the changes in the structure of the starting materials. For TiO_2 starting material it was possible to conclude that sonication has no effect on the structure of TiO_2. For MoS_2 and WS_2starting material it is possible to conclude that in case of MoS_2 the sonication significantly facilitates exfoliation of the raw materials but in case of WS_2 sonication bring just the reduction of the crystallite size, but no exfoliation. In the composites TiO_2/TMDCs nanocomposites HR-PXRD measurements showed that TiO_2 allows the MoS_2 exfoliation, since we observed an higher d-spacing with respect of the reference, but it also protect the MOS_2 from the reduction of the crystallite size brought by the sonication process. Surface area analysis(BET) measurements confirm the fact that it is not just the effect of the surface area to influence the photocatalytic activity of the PCs, but the performance are strictly correlate to the type of doping material as well as the interaction with light and TiO_2.

2.5. Colloidal TiO_2 with Perylene

As explained in the previous sections, in order to obtain an enhancement of the photocatalytic performance of TiO_2-NPs we need to design a system that involves an energy transfer between a photo-responsive (or conducting) sub-unit and the TiO_2 that then is the responsible of the photocatalytic effect. An alternative to the 2d material for titania modification can be the insertion of molecular organic dye as sensitizers. In general, highly efficient dye sensitizers must meet the following requirements: (1) strong physical/chemical adsorption capacity, high light-absorption efficiency, and a wide range of absorption spectrum regions; (2) long lifetime of excited states and high quantum yield; and (3) matching band structure of the TiO_2 to decrease energy loss during the process of electron transfer. Because of these peculiar requirements, during the past decade, much attention has been paid to design the right organic molecule for the modification of TiO_2, with the objective not to influence TiO_2-NPs charge separation lifetime, as showed in the case of TiO_2-Gr 10:1, but rather to extend TiO_2-NPs photoresponse to visible light[118]–[121]. In particular several studies focussed on the sensitization of mesoporous films and colloidal suspensions with dye molecules in the form of the dye-sensitized solar cells (DSSC) in order to improve the efficiency of photoelectrochemical devices[119]. The first successful attempt in the production of DSSC was made by Grätzel and co-workers with high surface area titanium dioxide nanocrystalline particles sensitized by ruthenium bipyridyl complexes [122]–[124]. With these devices Grätzel reported a visible light conversion efficiencies of 10% [125], and this results attract lots of attention on ruthenium bipyridyl complexes as TiO_2 sensitizers[126]. However, the investigation and development of other dye−semiconductor systems are essential to furthering our fundamental understanding of the sensitization - electron injection process toward titania NPs. The dye is typically adsorbed on the surface of the semiconductor particles and acts as an electron donor, injecting electrons from its excited state(s) into the conduction band of the semiconductor under visible light irradiation. In particular in order to understand the carrier (e/h) dynamics, upon photon irradiation, transient measurements in the femtosecond time scale were performed [126]–[129]. These study outlined the importance of having a LUMO of the dye that is less negative than the conduction band of the TiO_2-NPs, in order to compete with the mechanism of self-relaxation of

the molecular dye. Furthermore the HOMO of the sensitizer has to be over the CB of TiO_2 in order to allow a fast and efficient electron transfer. dye molecules. A requirement of the system is that the dye has to be adsorbed on the semiconductor surface by an electrostatic, hydrophobic, or chemical interaction. For these reason these type of dyes were reported by the scientific: riboflavin, xanthene dyes(e.g. RhB) and porphyrin by colloidal TiO_2[118], but also oxazines, erythrosin B, eosin, chlorophyilin, phthalccyanines[130], squaraine[131] and perylenes[121], [126], [129], [132], [133].

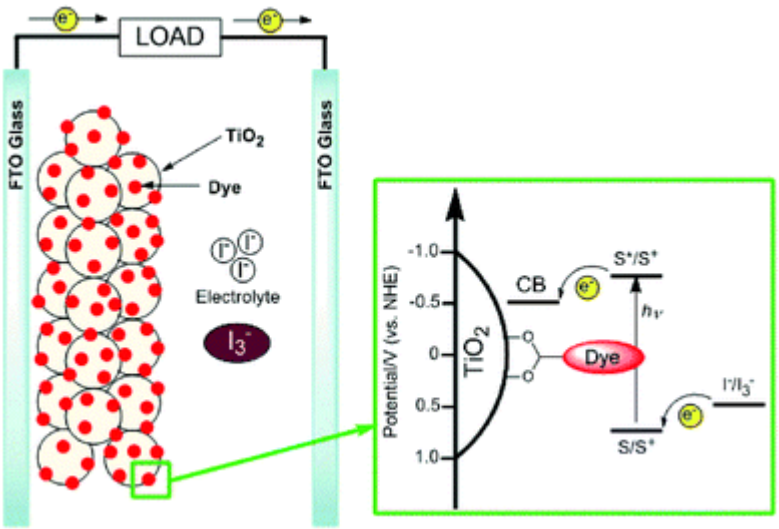

Figure. 47 Construction and operation of a DSSC.[129]

As expected the performance of the sensitization were found to be different with different dyes. In some cases, an electron is transferred from the HOMO of an adsorbed molecule to the valence band of the photoexcited semiconductor. In this case, the molecule (often a pollutant) is photodegraded (photo-oxidized), as it happens in the case of RhB discussed in the previous sections. Thus a series of charge-transfer reactions can be induced. The surface charge-transfer process had been confirmed and studied by transient absorption spectroscopy as well as with fluorescence quenching and photocatalytic activity(toward the sensitizer as well as with respect of other molecules). Among all the above mentioned sensitizers, perylene derivatives were found to be a promising candidates due to their thermal and chemical stability, low cost and good light-harvesting

ability[129]. Furthermore Perylene has a fast electron injection in TiO_2 , ~ 190-210 fs [134], [135], and a slower back electron transfer of the electron injected into the semiconductor NP with the dye radical cation(e.g. recombination time for perylenes: 14 μs - 30 ms[135]) compared to other dye sensitizers (e.g. recombination time for squaraine dye : 2.7 ns[136]) . In addition, the high absorbance in the visible ($\varepsilon \sim 10^5$ M^{-1} cm^{-1}) range (absorption at 450–750 nm) and emission from a singlet state with high quantum yield. Further clarification on perylenes properties will be given in the dedicated chapter 5. One particular feature of great interest in designing perylenes as sensitizers is the ability to impart charge transfer absorption characteristics by inducing perturbation of HOMO and LUMO distribution with electron-donating group on the perylene bay[129], with respect of the perylene modification in its extremities. Among all the type of perylenes, perylene imides have been an object of research for 100 years as key n-type semiconductors in the field of organic electronics, but there has been very few studies of the perylene-sensitized TiO_2 composite used to photocatalytically degrade pollutants [137]–[139]. For all the above mentioned reason for our synthesis we selected PBI (N,N'-Bis(2,5-di-tertbutylphenil)-3,4,9,10-perylenedicarboximide) to obtain a sensitization of the TiO_2 photocatalyst in the Visible range of light, in order to investigate whether this type of PBI sensitization, that is really promising for DSSC [121], [132], [133], might be suitable for photocatalysis. In literature we found system for photocatalysis obtained by the modification of commercial TiO_2[137], [138] (tested with the degradation of methylene orange or aliphatic alchools) or an hydrothermal synthesis of TiO_2 with a direct coupling of the perylene[139] (tested with the degradation of RhB). Up to now no studies regarding photocatalysis with colloidal TiO_2 were developed. The advantage in the use of semiconductor particles of colloidal dimensions is that they are sufficiently small to yield transparent solutions, allowing direct analysis of electron transfer by fluorescence quenching technique[118], [140]. The synthetic pathway has to take into consideration the effects of:

1. the interfacial couplings, since studies reports that in general the sensitization of TiO_2 has better results in case of the physical/chemical coupling of the dye with TiO_2 sub-unit [118], [130],
2. the chemical environment, since perylene and perylenes derivatives, in polar solvents, tend to do a π-π stacking forming aggregates that can tune their photophysical properties.

Wei et all reported a system based on perylenetetracarboxylic acid diimide (PTCDI) and commercial TiO_2 where a free aggregation of Perylene on TiO_2 surface occours. They found that self-assembly of PTCDI has been reconstructed on P25 NP via arrangement of short-range π–π stacking, and that structure is important in order to achieve an high photocatalytic activity. They claim that this self-assembled PTCDI exhibited a novel stacking mode in the existence of P25 NP and favoured effective charge transfer with less charge recombination in PTCDI self-assembly[137].

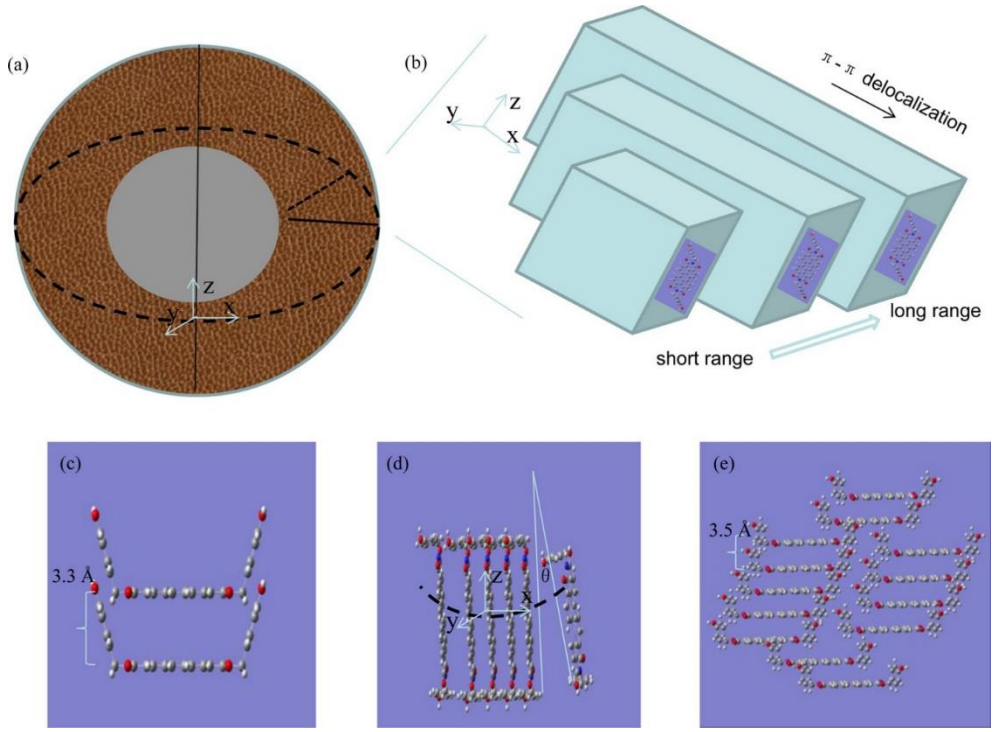

Figure. 48 Rearrangement stacking mode of PTCDI self-assembly of PTCDI/P25 hybrid in the X, Y, and Z directions, with the X axis as the π–π stacking direction, the Y axis as the edge-to-edge stacking direction, and the Z axis as the side-chain interaction direction. (a) 3D PTCDI/P25 core–shell model. (b) Stacking model along the Y axis. (c) Optimal conformation of the isolated molecule obtained from DFT calculations at the B3LYP/6-31G level. (d) π–π stacking model at the same radius, with the disordered structure displayed with the dihedral angle (ϑ) between two PTCDI molecules. (e) Staggered π–π stacking mode, which fabricates the short-range structure*[137].

For all the above mentioned reasons we developed a system based on colloidal TiO_2 NPs with perylene bisimide(PBI) derivative, that interacts with the TiO_2 subunit by physical adsorption of PBI in the form of aggregates.

2.5.1. Synthetic pathway: Colloidal TiO_2- NPs and commercial Perylene

Colloidal TiO_2 nanoparticles were synthesized in water solution by means of two non-ionic surfactants: Triton™ X100 (TX) and Pluronic® F127 (Plur), purchased from Sigma-Aldrich, following an industrial patented protocol [141]. Titanium tetraisopropoxide (TTIP, ≥97.0%,Sigma-Aldrich), has been chosen as a TiO_2 precursor. Triton™ X-100 or Pluronic® F127 (10% w/w) and concentrated HCl (1,4mL) were placed in a 500 mL round bottom flask with 250 mL of Millipore ultrapure water (resistivity 18.2 MΩ·cm at 25°C). The solution was heated up at 50 °C and stirred for almost 30 minutes. Then 1,5% w/w of TTIP was added very rapidly. A white precipitate was immediately noticed. After 24h stirring at 50° a semi transparent colloidal solution of TiO_2-NPs (15 mg/ml) was collected. The modification with PBI, from Sigma Aldrich, was done by adding 200 µL of PBI (1 mg/mL in THF) to a 2 mL solution of TX or Plur-TiO_2 previously synthesized. The solutions were stirred in dark for almost 2 hours, obtaining the samples: TX-TiO_2 _PBI and Plur-TiO_2_PBI.

2.5.2. Dynamic Light Scattering (DLS) characterization of colloidal modified TiO_2- NPs

Dispersions 0.2 mg/mL of TX-TiO_2 and Plur-TiO_2 were examined with Dynamic Light Scattering (DLS). TX-TiO_2 and Plur-TiO_2 were filtered with a 0.2 µm filter, in order to avoid precipitates or other impurities during the analysis. Table 12 reports the Z-Average and the PDI (Polydispersity index) values are reported. The Z-Average parameter is overall average size based on a specific fit of the scattering intensity on to the raw correlation function data. The fitting is also called cumulate method and can be thought of as force-fitting the result to a simple Gaussian distribution where the z-average is the mean and the PDI is related to the width of this simple distribution. Generally speaking, the Z-Average value gives information about the medium particles size present in the solution and PDI indicates the size dispersion in solution. The more the PDI is small, the more the sample has size uniformity.

Table 12 Dls data obtained by the analysis of TiO_2 colloidal suspensions with different solvents.

Sample	Z-Average (nm)	PDI
TX-TiO_2	35	0.351
Plur-TiO_2	33	0.237

The obtained, Table 12, **results clearly show that the dimension of the synthesized TiO_2 obtained by the surfactants-assisted method are in the consistent and in the nanometres region (average diameter of 33-35nm).**

2.5.3. Absorption measurements

Absorption spectra of the PBI doped and the bare TX-TiO_2 and Plur-TiO_2 solutions were collected with a concentration of 0.4 mg/mL. Two other solutions were also taken as references: Plur_PBI and TX_PBI in order to collect the absorption spectra of PBI in this form of aggregate. These solution were analysed with the same doping concentration of PBI with respect to the others, TX-TiO_2 _PBI and Plur-TiO_2_PBI, but without titania. The absorption range was 350 nm – 800 nm with a scan speed 480 nm/min.

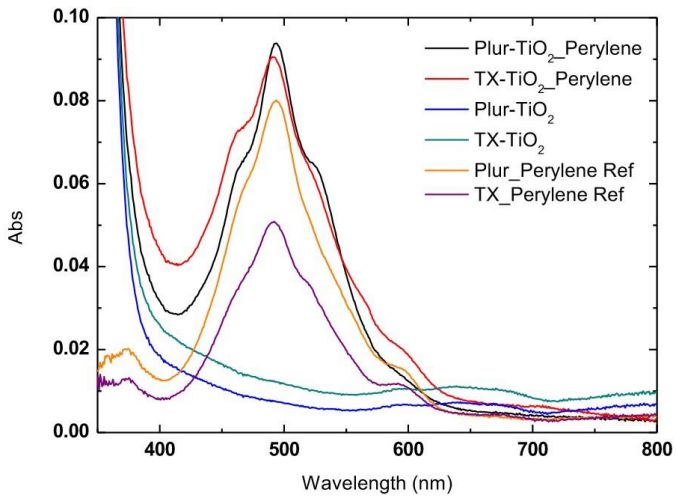

Figure. 49 Absorption spectra of Plur-TiO_2_PBI, TX-TiO_2_PBI, Plur-TiO_2, TX-TiO_2, Plur _PBI and TX _PBI

All the spectra show the characteristic band of PBI with a maximum at 500 nm. PBI band structure is more defined in the samples Plur-TiO_2_PBI and TX-TiO_2_PBI with respect to the reference samples in which TiO_2 is not present. This is probably due to an interaction between PBI and the surfactants that is stronger in the samples without TiO_2. The collected absorption spectra do not display scattering due to larger PBI aggregates. In fact, aggregation caused by π-π stacking is very frequent in perylene dyes solutions, mainly at high concentration[137].

2.5.4. Kinetic Photocatalytic tests

As explained in the Section 2.4.1, two different kinetic analysis for each compound were carried on, irradiating the system either in the UV (340 nm) or in the visible (500 nm) and recording the fluorescence spectrum of RhB in 70 sequential cycles on the 450-700 and 520-700nm ranges respectively.

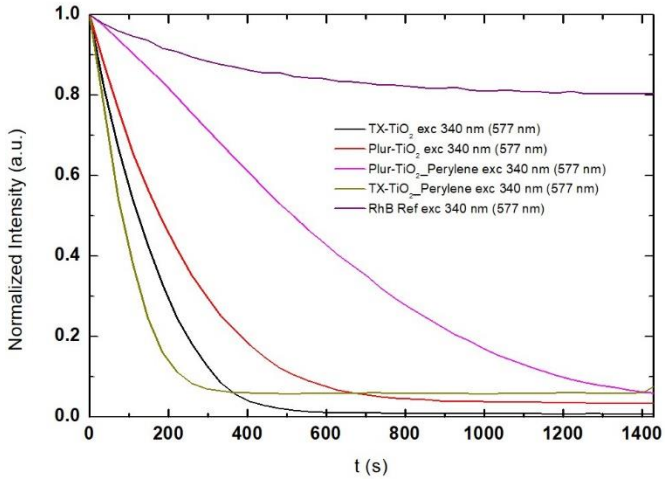

Figure. 50 Normalized fluorescence intensity at 577nm of RhB with all the PCS and reference samples during irradiation at excitation wavelength 340 nm.

Then, to compare the behaviour of the kinetic of different materials, the fluorescence intensity at a selected emission wavelength were fitted as a function of time. The kinetic law and the background theory were already explained in the Section 2.3.1 and 2.4.1. The following parameters were

calculated in the graphs with the normalized intensity following the kinetic equation Eq.17:

- For the analysis with λexc = 340 nm, the initial kinetic constant, k (t=0s) and the %P after 600 s (10 minutes) and 1400 s (≈ 23 minutes).

- For the analysis with λexc = 500 nm, the initial kinetic constant, k (t=0s) the %P after 600 s (10 min), 1500 s (25 min) and 3000 s (50 min).

Table 13 Summary of the kinetic parameters: k, %P (600 sec), %P (1500sec) calculated on the normalized fluorescence intensity at 577nm of RhB with all the PCS and reference samples during irradiation at excitation wavelength 340 nm.

λ_{exc} = 340 nm	**k (t = 0 s)**	**% P after 600s**	**%P after 1400s**
TX-TiO_2	- 0.0041	99	99
TX-TiO_2_PBI	- 0.0054	94	94
Plur-TiO_2	- 0.0030	92	97
Plur-TiO_2_PBI	- 0.0009	56	94
RhB Reference	- 0.0005	16	19

The obtained results displayed in Table 13 lead to the considerations that all the photocatalysts degrade all the RhB dye after almost 600 seconds (20 minutes), hence they all have good efficiencies. This means that, **as expected, the activity of TiO_2 nanoparticles with UV light is not enhanced by the PBI**. Furthermore comparing the %P after 600 and 1400 sec it is possible to note that the most active photocatalysts are TX-TiO_2, TX-TiO_2_PBI. With these TX based colloidal system the RhB degradation is faster at the beginning of the analysis with respect of the Pluronic based ones. A relevant difference between the two used surfactants is present. In particular, **TiO_2 nanoparticles with Triton™ X-100 show better performances compared to the TiO_2 nanoparticles stabilized by Pluronic F127.** In addition, if we compare the % P of the two surfactants after 600 and 1400 seconds, and the trend of the curve (Figure 50), is it possible to notice that in the case of Pluronic surfactant the kinetic trend tends to be more linear and close to a zero order kinetic model. Therefore, it is clear that there is an effect of the surfactant on the system. This was also deducible from the absorption spectra reported in Figure 49. Photodegradation kinetic profiles of all the composites **upon Vis 500** nm irradiation are collected. In this situation, **the excitation wavelength was optimal for the excitation of the PBI.** Hence, a better performance for PBI samples is expected.

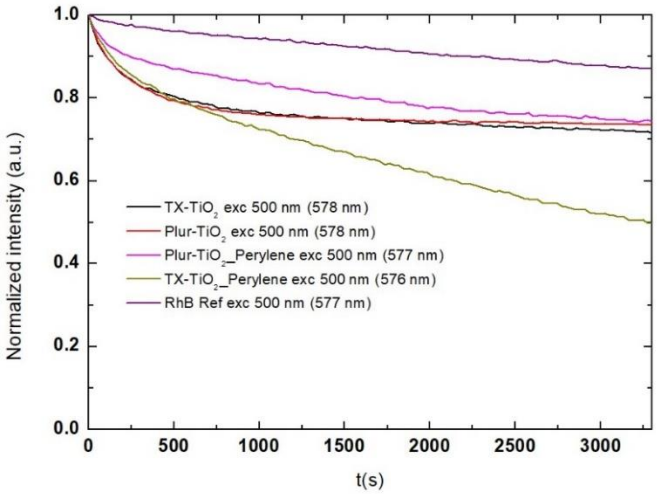

Figure. 51 Normalized fluorescence intensity at 577nm of RhB with all the PCS and reference samples during irradiation at excitation wavelength 500 nm.

From Figure 51 it is possible to notice that the samples containing perylene and titania are the one that in the long term bring to the complete decolouration of the solution since the slope of the trend tends to decrease with the increment of the irradiation time. On the other hand, the bare TiO_2 samples with both Pluronic and TX after a while reach a plateau. Table 14 confirm these preliminary results.

Table 14 Summary of the kinetic parameters: k, %P (600 sec), %P (1500sec), %P (3000sec) calculated on the normalized fluorescence intensity at 577nm of RhB with all the PCS and reference samples during irradiation at excitation wavelength 340 nm.

λ_{exc} = 500 nm	**k (t = 0 s)**	**% P after 600s**	**% P after 1500s**	**% P after 3000s**
TX-TiO_2	- 0.0010	21	25	28
TX-TiO_2_PBI	- 0.0008	20	33	48
Plur-TiO_2	- 0.0010	22	25	26
Plur-TiO_2_PBI	- 0.0007	14	20	25
RhB Reference	- 0.0002	4	8	12

Despite of the fact that initially the kinetic constant value of both TX-TiO_2 and Plur-TiO_2 is lower with respect of the perylene doped ones, the %P of the **bare TiO_2 is constant between 20 and 28 %**. In the case of Plur-TiO_2_PBI this %P value starts with 14% and after 300 seconds it rose at 25% with a constant growing trend. **The best performance is obtained in the case of TX-TiO_2_PBI**,

where from an initial %P 600 of 20, **after 3000 sec a photodegradation of 48% is obtained**

2.5.5. Photophysical characterization

2.5.5.1. Fluorescence quantum yield

Fluorescence quantum yields of PBI of the most promising photocatalysts TX_PBI, TX-TiO_2_PBI(see Table 14) were calculated, using Fluorescein as standard[142]. In particular, absorption spectra and emission spectra (λexc= 470 nm) of Fluorescein reference in aqueous solution with NaOH 10^{-2}M, TX_PBI, TX-TiO_2_PBI in aqueous solution were collected. Fluorescence quantum yields were calculated with this formula[142] (Eq 20):

$$\Phi = \Phi_r \frac{I}{I_r} \frac{A_r}{A} \frac{n^2}{n_r^2}$$

Where ϕ is the quantum yield; I is the integrated area of emission spectrum; A is the absorbance at the excitation wavelength and n is refractive index of the solvent The parameters with the subscript "r" are referred to Fluorescein whose quantum yield is 0.92-0.95 in these conditions[142].

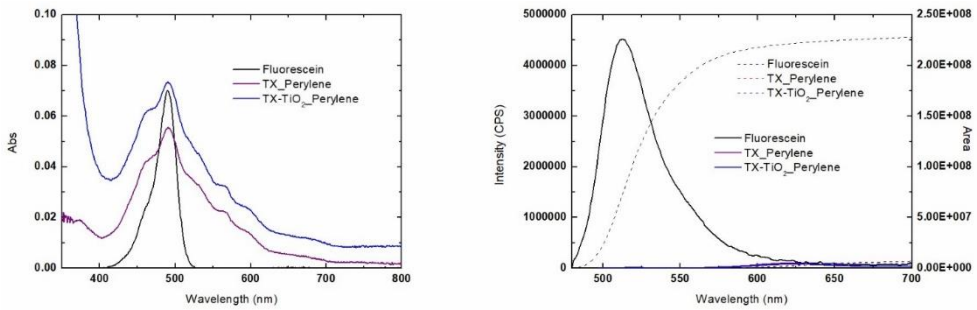

Figure. 52 (left) Absorption spectra of Fluorescein, TX_PBI, TX-TiO_2_PBI and TX-TiO_2-G_PBI. (Right) Integrated emission spectra for the determination of quantum yields.

Quantum yields in the case of TX_PBI was 2.0% and for TX-TiO_2_PBI was 1.2%. This is a very promising result, because it means that 40% of excited dyes in TX-TiO_2_PBI does not have a mechanism of relaxation through

emission of a photon. Probably this means that the 40% of the exited molecules interact with TiO_2 for its sensitization. This result is in line with the photocatalytic performances observed in the previous section, that shows the TX-TiO_2_PBI to be the best sample in terms of photocatalytic activity in visible light.

2.5.5.2. Emission measurements

PBI emission spectra for different excitation wavelength were collected in the samples TX_PBI, TX-TiO_2_PBI to give the emission maps. The parameters were: λexc (nm) 400-600nm and λem (nm) 480-800.

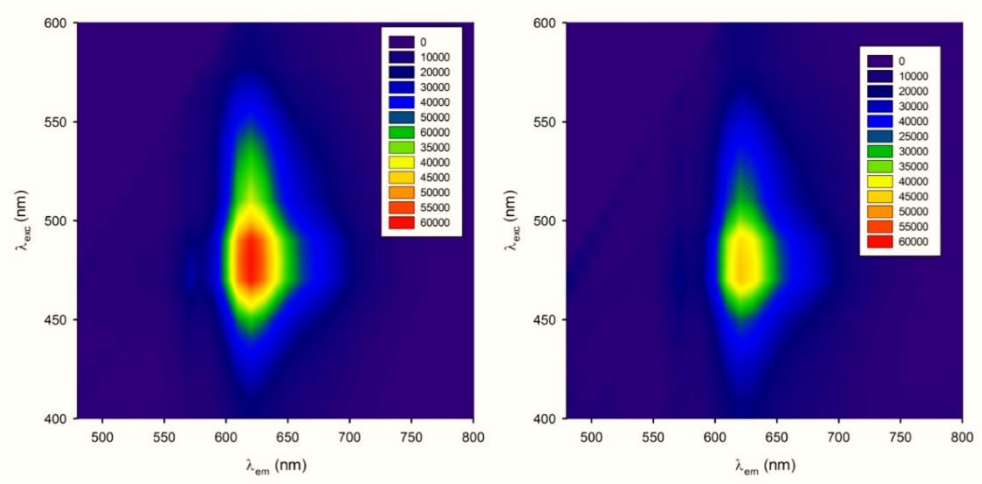

Figure. 53 (left)TX_PBI emission map, (right) TX-TiO_2_PBI emission map λexc (nm) 400-600nm and λem (nm) 480-800

From these maps, it can be noticed that, for all the excitation wavelengths, there is always the formation of a peak at almost 620-630 nm in the emission spectra, for all the samples. Instead, in samples TX_PBI and TX-TiO_2_PBI another emission peak at ≈ 570 nm is present for excitation wavelength up to almost 470 nm.

2.5.5.3. Time Resolved Emission Spectra (TRES)

PBI emission decays for different emission wavelengths were collected in the samples TX_PBI, TX-TiO_2_PBI. Time Resolved Emission Spectra (TRES) were performed with a diode laser exciting at 408 nm and probing the emission in the range of 550 to 750nm (steps 10 nm).

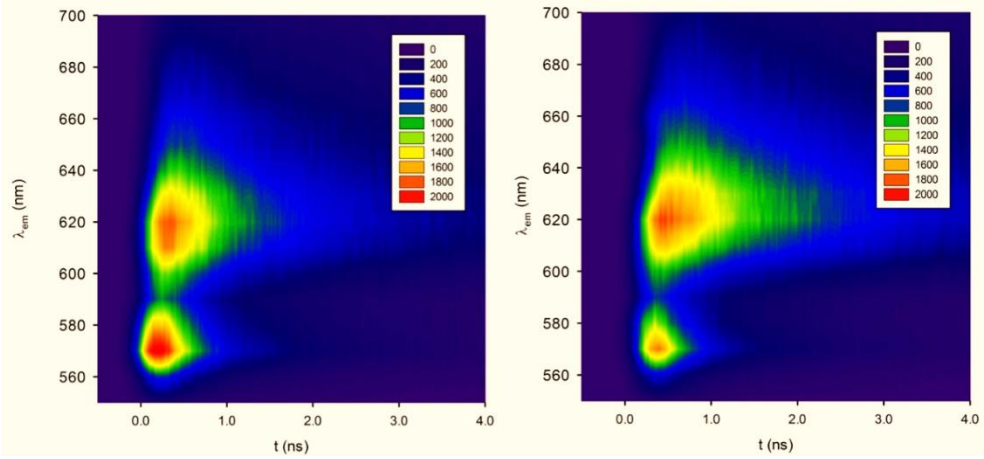

Figure. 54 Emission lifetime decay of (left)TX_PBI and (right)TX-TiO_2_PBI.

These graphs show three phenomena:

1- The two present emission peaks at ≈ 570 nm and ≈ 620 nm do not appear at the same time. In fact, immediately after the laser impulse the peak at 570 nm forms while the other peak appears with a little delay. This means that there is the formation of the first peak which then seems to be converted to the second one. This effect is more pronounced in TX_PBI than in the other samples. In fact, in TX-TiO_2_PBI the delay of the second peak with respect to the first is smaller, denoting a faster conversion.

2- While **the decay of the peak at 570 nm is quite fast, the decay of the peak at 620 nm is slower. In particular, in samples TX-TiO_2_PBI** this decay is largely slower than in TX_PBI. This can be due to a **slower charge recombination in the formers with respect to the latter**.

3- Mainly in TX-TiO_2_PBI, another less intense peak appears at almost 640 nm. Further investigations needs to be done.

2.5.6. Concluding remarks on Section 2.5: colloidal TiO_2 sensitized with Perylene

TX-TiO_2 _PBI and Plur-TiO_2_PBI were successfully synthesized. DLS measurements reveals that the synthesized TiO_2 obtained by the surfactants-assisted method are consistent and in the nanometres region (average diameter of 33-35nm). Photocatalytic tests showed that upon excitation at 340nm, as expected, the activity of TiO_2 nanoparticles with UV light is not enhanced by the PBI. In general TiO_2 nanoparticles with Triton™ X-100 show better performances compared to the TiO_2 nanoparticles stabilized by Pluronic F127. With Vis light excitation the best performance is obtained in the case of TX-TiO_2_Perylene, where from an initial %P 600 of 20, after 3000 sec a photodegradation of 48% is obtained. Fluorescence quantum yields of PBI of the most promising photocatalysts TX_PBI, TX-TiO_2_PBI showed that quantum yields in the case of TX_PBI was 2.0% and for TX-TiO_2_PBI was 1.2%. Probably this means that the 40% of the exited PBI molecules interact with TiO_2 for its sensitization. Emission lifetime maps displayed in samples TX-TiO_2_PBI that the decay at 620 nm is largely slower than in TX_PBI. This can be due to a slower charge recombination in the formers with respect to the latter, that is an additional parameter that can explain the enhancement in the photocatalytic activity of TX-TiO_2_PBI

2.6. Bibliography chapter 2

[1] R. Jain, M. Mathur, S. Sikarwar, and A. Mittal, "Removal of the hazardous dye rhodamine B through photocatalytic and adsorption treatments," *J. Environ. Manage.*, vol. 85, no. 4, pp. 956–964, 2007.

[2] C. Tuchinda, S. Srivannaboon, and H. W. Lim, "Photoprotection by window glass, automobile glass, and sunglasses," *J. Am. Acad. Dermatol.*, vol. 54, no. 5, pp. 845–854, 2006.

[3] Y.-C. Hsiao, T.-F. Wu, Y.-S. Wang, C.-C. Hu, and C. Huang, "Evaluating the sensitizing effect on the photocatalytic decoloration of dyes using anatase-TiO 2," *Appl. Catal. B Environ.*, vol. 148, pp. 250–257, 2014.

[4] N. Zhang, Y. Zhang, and Y.-J. Xu, "Recent progress on graphene-based photocatalysts: current status and future perspectives," *Nanoscale*, vol. 4, no. 19, pp. 5792–5813, 2012.

[5] Y. Liang, H. Wang, H. S. Casalongue, Z. Chen, and H. Dai, "TiO2 Nanocrystals Grown on Graphene as Advanced Photocatalytic Hybrid Materials," *Nano Res.*, vol. 3, no. 10, pp. 701–705, 2010.

[6] G. Guidetti, A. Cantelli, R. Mazzaro, L. Ortolani, V. Morandi, and M. Montalti, "Tracking graphene by fluorescence imaging: a tool for detecting multiple populations of graphene in solution," *Nanoscale*, vol. 8, no. 16, pp. 8505–8511, 2016.

[7] P. Kar *et al.*, "Facile synthesis of reduced graphene oxide--gold nanohybrid for potential use in industrial waste-water treatment," *Sci. Technol. Adv. Mater.*, vol. 17, no. 1, pp. 375–386, 2016.

[8] T. S. Natarajan, M. Thomas, K. Natarajan, H. C. Bajaj, and R. J. Tayade, "Study on UV-LED/TiO 2 process for degradation of Rhodamine B dye," *Chem. Eng. J.*, vol. 169, no. 1, pp. 126–134, 2011.

[9] K. Dai, T. Peng, D. Ke, and B. Wei, "Photocatalytic hydrogen generation using a nanocomposite of multi-walled carbon nanotubes and TiO2 nanoparticles under visible light irradiation," *Nanotechnology*, vol. 20, no. 12, p. 125603, 2009.

[10] M. Sun, X. Ma, X. Chen, Y. Sun, X. Cui, and Y. Lin, "A nanocomposite of carbon quantum dots and TiO 2 nanotube arrays: enhancing photoelectrochemical and photocatalytic properties," *Rsc Adv.*, vol. 4, no. 3, pp. 1120–1127, 2014.

[11] K. R. Reddy, M. Hassan, and V. G. Gomes, "Hybrid nanostructures based on titanium dioxide for enhanced photocatalysis," *Appl. Catal. A Gen.*, vol. 489, pp. 1–16, 2015.

[12] L. Han, P. Wang, and S. Dong, "Progress in graphene-based photoactive nanocomposites as a promising class of photocatalyst," *Nanoscale*, vol. 4, no. 19,

pp. 5814–5825, 2012.

[13] R. Leary and A. Westwood, “Carbonaceous nanomaterials for the enhancement of TiO2 photocatalysis,” *Carbon N. Y.*, vol. 49, no. 3, pp. 741–772, 2011.

[14] W. Tu, Y. Zhou, and Z. Zou, “Versatile Graphene-Promoting Photocatalytic Performance of Semiconductors: Basic Principles, Synthesis, Solar Energy Conversion, and Environmental Applications,” *Adv. Funct. Mater.*, vol. 23, no. 40, pp. 4996–5008, 2013.

[15] P. Wang *et al.*, “Dye-Sensitization-Induced Visible-Light Reduction of Graphene Oxide for the Enhanced TiO2 Photocatalytic Performance,” *ACS Appl. Mater. Interfaces*, vol. 5, no. 8, pp. 2924–2929, 2013.

[16] N. Zhang, M.-Q. Yang, S. Liu, Y. Sun, and Y.-J. Xu, “Waltzing with the Versatile Platform of Graphene to Synthesize Composite Photocatalysts,” *Chem. Rev.*, vol. 115, no. 18, pp. 10307–10377, 2015.

[17] C. Chen *et al.*, “Synthesis of Visible-Light Responsive Graphene Oxide/TiO2 Composites with p/n Heterojunction,” *ACS Nano*, vol. 4, no. 11, pp. 6425–6432, 2010.

[18] J. Du *et al.*, “Hierarchically Ordered Macro-Mesoporous TiO2-Graphene Composite Films: Improved Mass Transfer, Reduced Charge Recombination, and Their Enhanced Photocatalytic Activities,” *ACS Nano*, vol. 5, no. 1, pp. 590–596, 2011.

[19] J. Guo *et al.*, “Sonochemical synthesis of TiO2 nanoparticles on graphene for use as photocatalyst,” *Ultrason. Sonochem.*, vol. 18, no. 5, pp. 1082–1090, 2011.

[20] C. H. Kim, B.-H. Kim, and K. S. Yang, “TiO2 nanoparticles loaded on graphene/carbon composite nanofibers by electrospinning for increased photocatalysis,” *Carbon N. Y.*, vol. 50, no. 7, pp. 2472–2481, 2012.

[21] I. Y. Kim *et al.*, “A Strong Electronic Coupling between Graphene Nanosheets and Layered Titanate Nanoplates: A Soft-Chemical Route to Highly Porous Nanocomposites with Improved Photocatalytic Activity,” *Small*, vol. 8, no. 7, pp. 1038–1048, 2012.

[22] N. Li, G. Liu, C. Zhen, F. Li, L. Zhang, and H.-M. Cheng, “Battery Performance and Photocatalytic Activity of Mesoporous Anatase TiO2 Nanospheres/Graphene Composites by Template-Free Self-Assembly,” *Adv. Funct. Mater.*, vol. 21, no. 9, pp. 1717–1722, 2011.

[23] Y. T. Liang, B. K. Vijayan, K. A. Gray, and M. C. Hersam, “Minimizing Graphene Defects Enhances Titania Nanocomposite-Based Photocatalytic Reduction of CO2 for Improved Solar Fuel Production,” *Nano Lett.*, vol. 11, no. 7, pp. 2865–2870, 2011.

[24] Y. T. Liang, B. K. Vijayan, O. Lyandres, K. A. Gray, and M. C. Hersam, “Effect of

Dimensionality on the Photocatalytic Behavior of Carbon-Titania Nanosheet Composites: Charge Transfer at Nanomaterial Interfaces," *J. Phys. Chem. Lett.*, vol. 3, no. 13, pp. 1760–1765, 2012.

[25] J. Liu, Z. Wang, L. Liu, and W. Chen, "Reduced graphene oxide as capturer of dyes and electrons during photocatalysis: surface wrapping and capture promoted efficiency," *Phys. Chem. Chem. Phys.*, vol. 13, no. 29, pp. 13216–13221, 2011.

[26] S. Liu, H. Sun, S. Liu, and S. Wang, "Graphene facilitated visible light photodegradation of methylene blue over titanium dioxide photocatalysts," *Chem. Eng. J.*, vol. 214, pp. 298–303, 2013.

[27] X. Pan, Y. Zhao, S. Liu, C. L. Korzeniewski, S. Wang, and Z. Fan, "Comparing Graphene-TiO2 Nanowire and Graphene-TiO2 Nanoparticle Composite Photocatalysts," *ACS Appl. Mater. Interfaces*, vol. 4, no. 8, pp. 3944–3950, 2012.

[28] L. M. Pastrana-Martinez *et al.*, "Advanced nanostructured photocatalysts based on reduced graphene oxide-TiO2 composites for degradation of diphenhydramine pharmaceutical and methyl orange dye," *Appl. Catal. B-Environmental*, vol. 123, pp. 241–256, 2012.

[29] M. S. A. S. Shah, A. R. Park, K. Zhang, J. H. Park, and P. J. Yoo, "Green Synthesis of Biphasic TiO2-Reduced Graphene Oxide Nanocomposites with Highly Enhanced Photocatalytic Activity," *ACS Appl. Mater. Interfaces*, vol. 4, no. 8, pp. 3893–3901, 2012.

[30] J. Shen, M. Shi, B. Yan, H. Ma, N. Li, and M. Ye, "Ionic liquid-assisted one-step hydrothermal synthesis of TiO2-reduced graphene oxide composites," *Nano Res.*, vol. 4, no. 8, pp. 795–806, 2011.

[31] N.-P. Thuy-Duong *et al.*, "The role of graphene oxide content on the adsorption-enhanced photocatalysis of titanium dioxide/graphene oxide composites," *Chem. Eng. J.*, vol. 170, no. 1, pp. 226–232, 2011.

[32] Y. Wang, R. Shi, J. Lin, and Y. Zhu, "Significant photocatalytic enhancement in methylene blue degradation of TiO2 photocatalysts via graphene-like carbon in situ hybridization," *Appl. Catal. B-Environmental*, vol. 100, no. 1–2, pp. 179–183, 2010.

[33] G. Williams, B. Seger, and P. V Kamat, "TiO2-graphene nanocomposites. UV-assisted photocatalytic reduction of graphene oxide," *ACS Nano*, vol. 2, no. 7, pp. 1487–1491, 2008.

[34] N. Yang *et al.*, "Photocatalytic Properties of Graphdiyne and Graphene Modified TiO2: From Theory to Experiment," *ACS Nano*, vol. 7, no. 2, pp. 1504–1512, 2013.

[35] H. Zhang, X. Lv, Y. Li, Y. Wang, and J. Li, "P25-Graphene Composite as a High Performance Photocatalyst," *ACS Nano*, vol. 4, no. 1, pp. 380–386, 2010.

[36] J. Zhang, Z. Xiong, and X. S. Zhao, "Graphene-metal-oxide composites for the

degradation of dyes under visible light irradiation," *J. Mater. Chem.*, vol. 21, no. 11, pp. 3634–3640, 2011.

[37] L.-W. Zhang, H.-B. Fu, and Y.-F. Zhu, "Efficient TiO2 photocatalysts from surface hybridization of TiO2 particles with graphite-like carbon," *Adv. Funct. Mater.*, vol. 18, no. 15, pp. 2180–2189, 2008.

[38] P. Zhang *et al.*, "TiO2@carbon core/shell nanofibers: Controllable preparation and enhanced visible photocatalytic properties," *Nanoscale*, vol. 3, no. 7, pp. 2943–2949, 2011.

[39] Y. Zhang, Z.-R. Tang, X. Fu, and Y.-J. Xu, "TiO2-Graphene Nanocomposites for Gas-Phase Photocatalytic Degradation of Volatile Aromatic Pollutant: Is TiO2-Graphene Truly Different from Other TiO2-Carbon Composite Materials?," *ACS Nano*, vol. 4, no. 12, pp. 7303–7314, 2010.

[40] Y. Zhang, Z.-R. Tang, X. Fu, and Y.-J. Xu, "Engineering the Unique 2D Mat of Graphene to Achieve Graphene-TiO2 Nanocomposite for Photocatalytic Selective Transformation: What Advantage does Graphene Have over Its Forebear Carbon Nanotube?," *ACS Nano*, vol. 5, no. 9, pp. 7426–7435, 2011.

[41] Y. Zhang, N. Zhang, Z.-R. Tang, and Y.-J. Xu, "Improving the photocatalytic performance of graphene-TiO2 nanocomposites via a combined strategy of decreasing defects of graphene and increasing interfacial contact," *Phys. Chem. Chem. Phys.*, vol. 14, no. 25, pp. 9167–9175, 2012.

[42] D. Zhao, G. Sheng, C. Chen, and X. Wang, "Enhanced photocatalytic degradation of methylene blue under visible irradiation on graphene@TiO2 dyade structure," *Appl. Catal. B-Environmental*, vol. 111, pp. 303–308, 2012.

[43] N. Yang, J. Zhai, D. Wang, Y. Chen, and L. Jiang, "Two-dimensional graphene bridges enhanced photoinduced charge transport in dye-sensitized solar cells," *ACS Nano*, vol. 4, no. 2, pp. 887–894, 2010.

[44] T.-F. Yeh, J. Cihlář, C.-Y. Chang, C. Cheng, and H. Teng, "Roles of graphene oxide in photocatalytic water splitting," *Mater. Today*, vol. 16, no. 3, pp. 78–84, 2013.

[45] A. C. Ferrari *et al.*, "Science and technology roadmap for graphene{,} related two-dimensional crystals{,} and hybrid systems," *Nanoscale*, vol. 7, no. 11, pp. 4598–4810, 2015.

[46] M. Chhowalla, H. S. Shin, G. Eda, L.-J. Li, K. P. Loh, and H. Zhang, "The chemistry of two-dimensional layered transition metal dichalcogenide nanosheets," *Nat. Chem.*, vol. 5, no. 4, pp. 263–275, Apr. 2013.

[47] J. N. Coleman *et al.*, "Two-Dimensional Nanosheets Produced by Liquid Exfoliation of Layered Materials," *Science (80-.).*, vol. 331, no. 6017, pp. 568–571, Feb. 2011.

[48] Q. H. Wang, K. Kalantar-Zadeh, A. Kis, J. N. Coleman, and M. S. Strano, "Electronics

and optoelectronics of two-dimensional transition metal dichalcogenides," *Nat. Nanotechnol.*, vol. 7, no. 11, pp. 699–712, Nov. 2012.

[49] W. K. Ho, J. C. Yu, J. Lin, J. G. Yu, and P. S. Li, "Preparation and photocatalytic behavior of MoS2 and WS2 nanocluster sensitized TiO2," *LANGMUIR*, vol. 20, no. 14, pp. 5865–5869, 2004.

[50] D. Xia, Z. Shen, G. Huang, W. Wang, J. C. Yu, and P. K. Wong, "Red Phosphorus: An Earth-Abundant Elemental Photocatalyst for ``Green{''} Bacterial Inactivation under Visible Light," *Environ. Sci. Technol.*, vol. 49, no. 10, pp. 6264–6273, 2015.

[51] S. A. Ansari and M. H. Cho, "Highly Visible Light Responsive, Narrow Band gap TiO2 Nanoparticles Modified by Elemental Red Phosphorus for Photocatalysis and Photoelectrochemical Applications," *Sci. Rep.*, vol. 6, 2016.

[52] Y. Hernandez *et al.*, "High-yield production of graphene by liquid-phase exfoliation of graphite.," *Nat. Nanotechnol.*, vol. 3, no. 9, pp. 563–8, Sep. 2008.

[53] F. Bonaccorso, A. Lombardo, T. Hasan, Z. Sun, L. Colombo, and A. C. Ferrari, "Production and processing of graphene and 2d crystals," *Mater. Today*, vol. 15, no. 12, pp. 564–589, 2012.

[54] M. Xu, T. Liang, M. Shi, and H. Chen, "Graphene-Like Two-Dimensional Materials," *Chem. Rev.*, vol. 113, no. 5, pp. 3766–3798, 2013.

[55] H. S. S. R. Matte *et al.*, "MoS2 and WS2 Analogues of Graphene," *Angew. CHEMIE-INTERNATIONAL Ed.*, vol. 49, no. 24, pp. 4059–4062, 2010.

[56] G. Cunningham *et al.*, "Solvent Exfoliation of Transition Metal Dichalcogenides: Dispersibility of Exfoliated Nanosheets Varies Only Weakly between Compounds," *ACS Nano*, vol. 6, no. 4, pp. 3468–3480, Apr. 2012.

[57] "No Title," *Evol. sonciation microvcavity bubbles http//www.epigentek.com/ Cat. [online; accessed 12-february-2017].*

[58] U. Khan, A. O'Neill, M. Lotya, S. De, and J. N. Coleman, "High-Concentration Solvent Exfoliation of Graphene," *Small*, vol. 6, no. 7, pp. 864–871, 2010.

[59] C. Backes *et al.*, "Edge and confinement effects allow in situ measurement of size and thickness of liquid-exfoliated nanosheets," *Nat. Commun.*, vol. 5, p. ncomms5576, 2014.

[60] K. Rajeshwar *et al.*, "Heterogeneous photocatalytic treatment of organic dyes in air and aqueous media," *J. Photochem. Photobiol. C Photochem. Rev.*, vol. 9, no. 4, pp. 171–192, 2008.

[61] P. Zhu, A. S. Nair, S. Peng, S. Yang, and S. Ramakrishna, "Facile Fabrication of TiO2-Graphene Composite with Enhanced Photovoltaic and Photocatalytic Properties by Electrospinning," *ACS Appl. Mater. Interfaces*, vol. 4, no. 2, pp. 581–585, 2012.

[62] Y. Zhu, Y. Wang, W. Yao, R. Zong, and Y. Zhu, “New insights into the relationship between photocatalytic activity and TiO2-GR composites,” *RSC Adv.*, vol. 5, no. 37, pp. 29201–29208, 2015.

[63] Y. Li, S. Sun, M. Ma, Y. Ouyang, and W. Yan, “Kinetic study and model of the photocatalytic degradation of rhodamine B (RhB) by a TiO 2-coated activated carbon catalyst: effects of initial RhB content, light intensity and TiO 2 content in the catalyst,” *Chem. Eng. J.*, vol. 142, no. 2, pp. 147–155, 2008.

[64] T. Hirakawa and Y. Nosaka, “Properties of O2•-and OH• formed in TiO2 aqueous suspensions by photocatalytic reaction and the influence of H2O2 and some ions,” *Langmuir*, vol. 18, no. 8, pp. 3247–3254, 2002.

[65] Y. Gao, X. Pu, D. Zhang, G. Ding, X. Shao, and J. Ma, “Combustion synthesis of graphene oxide-TiO2 hybrid materials for photodegradation of methyl orange,” *Carbon N. Y.*, vol. 50, no. 11, pp. 4093–4101, 2012.

[66] “No Title.” .

[67] R. A. Young, *The rietveld method*, vol. 5. International union of crystallography, 1993.

[68] O. Tanaike and M. Inagaki, “Ternary intercalation compounds of carbon materials having a low graphitization degree with alkali metals,” *Carbon N. Y.*, vol. 35, no. 6, pp. 831–836, 1997.

[69] A. N. Fitch, “The high resolution powder diffraction beam line at ESRF,” *J. Res. Natl. Inst. Stand. Technol.*, vol. 109, no. 1, pp. 133–142, 2004.

[70] B. H. Toby, “EXPGUI, a graphical user interface for GSAS,” *J. Appl. Crystallogr.*, vol. 34, pp. 210–213, 2001.

[71] C. E. Holcombe, “USAEC Oak Ridge Y-12 Plant,” *Rep. Y 1887*, 1973.

[72] T. Fukunaga, K. Nagano, U. Mizutani, H. Wakayama, and Y. Fukushima, “Structural change of graphite subjected to mechanical milling,” *J. Non. Cryst. Solids*, vol. 232, pp. 416–420, 1998.

[73] T. Ohsaka, F. Izumi, and Y. Fujiki, “Raman spectrum of anatase, TiO2,” *J. Raman Spectrosc.*, vol. 7, no. 6, pp. 321–324, 1978.

[74] V. Swamy, A. Kuznetsov, L. S. Dubrovinsky, R. A. Caruso, D. G. Shchukin, and B. C. Muddle, “Finite-size and pressure effects on the Raman spectrum of nanocrystalline anatase Ti O 2,” *Phys. Rev. B*, vol. 71, no. 18, p. 184302, 2005.

[75] K. M. Reddy, S. V Manorama, and A. R. Reddy, “Bandgap studies on anatase titanium dioxide nanoparticles,” *Mater. Chem. Phys.*, vol. 78, no. 1, pp. 239–245, 2003.

[76] S. D. Jackson and J. S. J. Hargreaves, “Metal Oxide Catalysis,” *Met. Oxide Catal.*, vol.

1, pp. 60–62, 2008.

[77] J. L. Ilari, H. Martens, and T. Isaksson, “Determination of Particle Size in Powders by Scatter Correction in Diffuse Near-Infrared Reflectance,” *Appl. Spectrosc.*, vol. 42, no. 5, pp. 722–728, 1988.

[78] A. B. Murphy, “Band-gap determination from diffuse reflectance measurements of semiconductor films, and application to photoelectrochemical water-splitting,” *Sol. Energy Mater. Sol. Cells*, vol. 91, no. 14, pp. 1326–1337, 2007.

[79] J. M. Olinger and P. R. Griffiths, “Effects of Sample Dilution and Particle Size/Morphology on Diffuse Reflection Spectra of Carbohydrate Systems in the Near- and Mid-Infrared. Part I: Single Analytes,” *Appl. Spectrosc.*, vol. 47, no. 6, pp. 687–694, 1993.

[80] P. Kubelka and F. Munk, “An article on optics of paint layers,” *Z. Tech. Phys*, vol. 12, no. 593–601, 1931.

[81] G. Kortüm, *Reflectance spectroscopy: principles, methods, applications*. Springer Science & Business Media, 2012.

[82] J. Workman Jr and A. Springsteen, *Applied spectroscopy: a compact reference for practitioners*. Academic Press, 1998.

[83] A. A. Christy, O. M. Kvalheim, and R. A. Velapoldi, “Quantitative analysis in diffuse reflectance spectrometry: A modified Kubelka-Munk equation,” *Vib. Spectrosc.*, vol. 9, no. 1, pp. 19–27, 1995.

[84] X.-Y. Liu, H.-W. Zheng, Z.-L. Zhang, X.-S. Liu, R.-Q. Wan, and W.-F. Zhang, “Effect of energy level matching on the enhancement of photovoltaic response about oxide/Zn2SnO4 composites,” *J. Mater. Chem.*, vol. 21, no. 12, pp. 4108–4116, 2011.

[85] J. Tauc, “Optical properties and electronic structure of amorphous Ge and Si,” *Mater. Res. Bull.*, vol. 3, no. 1, pp. 37–46, 1968.

[86] A. Morais, C. Longo, J. R. Araujo, M. Barroso, J. R. Durrant, and A. F. Nogueira, “Nanocrystalline anatase TiO2/reduced graphene oxide composite films as photoanodes for photoelectrochemical water splitting studies: the role of reduced graphene oxide,” *Phys. Chem. Chem. Phys.*, vol. 18, no. 4, pp. 2608–2616, 2016.

[87] D. Chen, L. Zou, S. Li, and F. Zheng, “Nanospherical like reduced graphene oxide decorated TiO2 nanoparticles: an advanced catalyst for the hydrogen evolution reaction,” *Sci. Rep.*, vol. 6, p. 20335, 2016.

[88] L.-L. Tan, W.-J. Ong, S.-P. Chai, and A. R. Mohamed, “Reduced graphene oxide-TiO2 nanocomposite as a promising visible-light-active photocatalyst for the conversion of carbon dioxide,” *Nanoscale Res. Lett.*, vol. 8, no. 1, p. 465, Nov. 2013.

[89] D. Gu, Y. Lu, and B. Yang, “Facile preparation of micro–mesoporous carbon-doped TiO 2 photocatalysts with anatase crystalline walls under template-free condition,”

Chem. Commun., no. 21, pp. 2453–2455, 2008.

[90] P. Wang *et al.*, "Photoinduced Electron Transfer Pathways in Hydrogen-Evolving Reduced Graphene Oxide-Boosted Hybrid Nano-Bio Catalyst," *ACS Nano*, vol. 8, no. 8, pp. 7995–8002, 2014.

[91] K. K. Manga, Y. Zhou, Y. Yan, and K. P. Loh, "Multilayer Hybrid Films Consisting of Alternating Graphene and Titania Nanosheets with Ultrafast Electron Transfer and Photoconversion Properties," *Adv. Funct. Mater.*, vol. 19, no. 22, pp. 3638–3643, 2009.

[92] K. J. Williams, C. A. Nelson, X. Yan, L.-S. Li, and X. Zhu, "Hot Electron Injection from Graphene Quantum Dots to TiO2," *ACS Nano*, vol. 7, no. 2, pp. 1388–1394, 2013.

[93] R. Long, N. J. English, and O. V Prezhdo, "Photo-induced Charge Separation across the Graphene–TiO2 Interface Is Faster than Energy Losses: A Time-Domain ab Initio Analysis," *J. Am. Chem. Soc.*, vol. 134, no. 34, pp. 14238–14248, 2012.

[94] S. H. Szczepankiewicz, J. A. Moss, and M. R. Hoffmann, "Slow Surface Charge Trapping Kinetics on Irradiated TiO2," *J. Phys. Chem. B*, vol. 106, no. 11, pp. 2922–2927, 2002.

[95] T. Yoshihara *et al.*, "Identification of Reactive Species in Photoexcited Nanocrystalline TiO2 Films by Wide-Wavelength-Range (400−2500 nm) Transient Absorption Spectroscopy," *J. Phys. Chem. B*, vol. 108, no. 12, pp. 3817–3823, 2004.

[96] A. Yamakata, T. Ishibashi, and H. Onishi, "Time-resolved infrared absorption spectroscopy of photogenerated electrons in platinized TiO2 particles," *Chem. Phys. Lett.*, vol. 333, no. 3–4, pp. 271–277, 2001.

[97] A. Yamakata, T. Ishibashi, and H. Onishi, "Water- and Oxygen-Induced Decay Kinetics of Photogenerated Electrons in TiO2 and Pt/TiO2: A Time-Resolved Infrared Absorption Study," *J. Phys. Chem. B*, vol. 105, no. 30, pp. 7258–7262, 2001.

[98] F. J. Knorr, C. C. Mercado, and J. L. McHale, "Trap-State Distributions and Carrier Transport in Pure and Mixed-Phase TiO2: Influence of Contacting Solvent and Interphasial Electron Transfer," *J. Phys. Chem. C*, vol. 112, no. 33, pp. 12786–12794, 2008.

[99] J. Schneider *et al.*, "Understanding TiO2 photocatalysis: mechanisms and materials," *Chem. Rev.*, vol. 114, no. 19, pp. 9919–9986, 2014.

[100] M. Breusing *et al.*, "Ultrafast nonequilibrium carrier dynamics in a single graphene layer," *Phys. Rev. B*, vol. 83, no. 15, p. 153410, 2011.

[101] D. Sun *et al.*, "Ultrafast Relaxation of Excited Dirac Fermions in Epitaxial Graphene Using Optical Differential Transmission Spectroscopy," *Phys. Rev. Lett.*, vol. 101, no. 15, p. 157402, 2008.

[102] Y. Tamaki *et al.*, "Trapping dynamics of electrons and holes in a nanocrystalline TiO2

film revealed by femtosecond visible/near-infrared transient absorption spectroscopy," *Comptes Rendus Chim.*, vol. 9, no. 2, pp. 268–274, 2006.

[103] K. Iwata *et al.*, "Carrier Dynamics in TiO2 and Pt/TiO2 Powders Observed by Femtosecond Time-Resolved Near-Infrared Spectroscopy at a Spectral Region of 0.9− 1.5 μm with the Direct Absorption Method," *J. Phys. Chem. B*, vol. 108, no. 52, pp. 20233–20239, 2004.

[104] Y. Tamaki, A. Furube, M. Murai, K. Hara, R. Katoh, and M. Tachiya, "Dynamics of efficient electron-hole separation in TiO2 nanoparticles revealed by femtosecond transient absorption spectroscopy under the weak-excitation condition," *Phys. Chem. Chem. Phys.*, vol. 9, no. 12, pp. 1453–1460, 2007.

[105] A. Furube, T. Asahi, H. Masuhara, H. Yamashita, and M. Anpo, "Direct observation of a picosecond charge separation process in photoexcited platinum-loaded TiO 2 particles by femtosecond diffuse reflectance spectroscopy," *Chem. Phys. Lett.*, vol. 336, no. 5, pp. 424–430, 2001.

[106] N. Serpone, "Relative photonic efficiencies and quantum yields in heterogeneous photocatalysis," *J. Photochem. Photobiol. A Chem.*, vol. 104, no. 1–3, pp. 1–12, 1997.

[107] A. Salinaro, A. V Emeline, J. Zhao, H. Hidaka, V. K. Ryabchuk, and N. Serpone, "Terminology, relative photonic efficiencies and quantum yields in heterogeneous photocatalysis. Part II: Experimental determination of quantum yields," *Pure Appl. Chem.*, vol. 71, no. 2, pp. 321–335, 1999.

[108] L. Guardia, J. I. Paredes, R. Rozada, S. Villar-Rodil, A. Martínez-Alonso, and J. M. D. Tascón, "Production of aqueous dispersions of inorganic graphene analogues by exfoliation and stabilization with non-ionic surfactants," *Rsc Adv.*, vol. 4, no. 27, pp. 14115–14127, 2014.

[109] G. Eda, H. Yamaguchi, D. Voiry, T. Fujita, M. Chen, and M. Chhowalla, "Photoluminescence from Chemically Exfoliated MoS2," *NANO Lett.*, vol. 11, no. 12, pp. 5111–5116, 2011.

[110] S.-H. Su *et al.*, "Controllable synthesis of band-gap-tunable and monolayer transition-metal dichalcogenide alloys," *Front. Energy Res.*, vol. 2, p. 27, 2014.

[111] C. Lee, H. Yan, L. E. Brus, T. F. Heinz, J. Hone, and S. Ryu, "Anomalous Lattice Vibrations of Single- and Few-Layer MoS2," *ACS Nano*, vol. 4, no. 5, pp. 2695–2700, 2010.

[112] H. Li *et al.*, "From Bulk to Monolayer MoS2: Evolution of Raman Scattering," *Adv. Funct. Mater.*, vol. 22, no. 7, pp. 1385–1390, Apr. 2012.

[113] A. Molina-Sanchez and L. Wirtz, "Phonons in single-layer and few-layer MoS2 and WS2," *Phys. Rev. B*, vol. 84, no. 15, 2011.

[114] A. Berkdemir *et al.*, “Identification of individual and few layers of WS2 using Raman Spectroscopy,” *Sci. Rep.*, vol. 3, Apr. 2013.

[115] E. N. Rissi, E. Soignard, K. A. McKiernan, C. J. Benmore, and J. L. Yarger, “Pressure-induced crystallization of amorphous red phosphorus,” *Solid State Commun.*, vol. 152, no. 5, pp. 390–394, 2012.

[116] A. Fujishima, X. Zhang, and D. A. Tryk, “TiO2 photocatalysis and related surface phenomena,” *Surf. Sci. Rep.*, vol. 63, no. 12, pp. 515–582, 2008.

[117] B. Liu *et al.*, “Mesoporous TiO2 Core–Shell Spheres Composed of Nanocrystals with Exposed High-Energy Facets: Facile Synthesis and Formation Mechanism,” *Langmuir*, vol. 27, no. 13, pp. 8500–8508, Jul. 2011.

[118] A. Kathiravan and R. Renganathan, “Effect of anchoring group on the photosensitization of colloidal TiO2 nanoparticles with porphyrins,” *J. Colloid Interface Sci.*, vol. 331, no. 2, pp. 401–407, Mar. 2009.

[119] D. Friedrich and M. Kunst, “Influence of dye-adsorption on charge carrier kinetics in TiO2 colloidal systems,” *NANO ENERGY*, vol. 1, no. 2, pp. 303–308, Mar. 2012.

[120] K. Kitazume, Y. Chen, M. Itou, Y. Araki, S. Uchida, and O. Ito, “Photoinduced electron-transfer processes between phthalocyanines and perylene derivatives,” *J. Porphyr. Phthalocyanines*, vol. 10, no. 9–10, pp. 1190–1196, 2006.

[121] C. Li *et al.*, “An Improved Perylene Sensitizer for Solar Cell Applications,” *ChemSusChem*, vol. 1, no. 7, pp. 615–618, 2008.

[122] B. O’regan and M. Grätzel, “A low-cost, high-efficiency solar cell based on dye-sensitized colloidal TiO 2 films,” *Nature*, vol. 353, no. 6346, pp. 737–740, 1991.

[123] A. Hagfeldt and M. Graetzel, “Light-induced redox reactions in nanocrystalline systems,” *Chem. Rev.*, vol. 95, no. 1, pp. 49–68, 1995.

[124] N. Vlachopoulos, P. Liska, J. Augustynski, and M. Grätzel, “Very efficient visible light energy harvesting and conversion by spectral sensitization of high surface area polycrystalline titanium dioxide films,” *J. Am. Chem. Soc.*, vol. 110, no. 4, pp. 1216–1220, 1988.

[125] M. K. Nazeeruddin *et al.*, “Conversion of light to electricity by cis-X2bis (2, 2’-bipyridyl-4, 4’-dicarboxylate) ruthenium (II) charge-transfer sensitizers (X= Cl-, Br-, I-, CN-, and SCN-) on nanocrystalline titanium dioxide electrodes,” *J. Am. Chem. Soc.*, vol. 115, no. 14, pp. 6382–6390, 1993.

[126] K. Tennakone, P. K. M. Bandaranayake, P. V. V Jayaweera, A. Konno, and G. Kumara, “Dye-sensitized composite semiconductor nanostructures,” *Phys. E-LOW-DIMENSIONAL Syst. NANOSTRUCTURES*, vol. 14, no. 1–2, pp. 190–196, Apr. 2002.

[127] Y. Liu, J. I. Dadap, D. Zimdars, and K. B. Eisenthal, “Study of interfacial charge-transfer complex on TiO2 particles in aqueous suspension by second-harmonic

generation," *J. Phys. Chem. B*, vol. 103, no. 13, pp. 2480–2486, Apr. 1999.

[128] J. E. EVANS, K. W. SPRINGER, and J. Z. ZHANG, "FEMTOSECOND STUDIES OF INTERPARTICLE ELECTRON-TRANSFER IN A COUPLED CDS-TIO2 COLLOIDAL SYSTEM," *J. Chem. Phys.*, vol. 101, no. 7, pp. 6222–6225, 1994.

[129] S. Mathew and H. Imahori, "Tunable, strongly-donating perylene photosensitizers for dye-sensitized solar cells," *J. Mater. Chem.*, vol. 21, no. 20, pp. 7166–7174, 2011.

[130] C. Divya, B. Janarthanan, and J. Chandrasekaran, "Review on Recent Advances in Titanium Dye Oxide Nanoparticles for Dye Sensitized Solar Cell Applications," 2017.

[131] C. Y. Wang, C. Y. Liu, W. Q. Wang, and T. Shen, "Photochemical events during the photosensitization of colloidal TiO2 particles by a squaraine dye," *J. Photochem. Photobiol. A-CHEMISTRY*, vol. 109, no. 2, pp. 159–164, 1997.

[132] Y. Shibano, T. Umeyama, Y. Matano, and H. Imahori, "Electron-donating perylene tetracarboxylic acids for dye-sensitized solar cells," *Org. Lett.*, vol. 9, no. 10, pp. 1971–1974, 2007.

[133] C. Li and H. Wonneberger, "Perylene Imides for Organic Photovoltaics: Yesterday, Today, and Tomorrow," *Adv. Mater.*, vol. 24, no. 5, SI, pp. 613–636, Feb. 2012.

[134] B. Burfeindt, T. Hannappel, W. Storck, and F. Willig, "Measurement of Temperature-Independent Femtosecond Interfacial Electron Transfer from an Anchored Molecular Electron Donor to a Semiconductor as Acceptor," *J. Phys. Chem.*, vol. 100, no. 41, pp. 16463–16465, Jan. 1996.

[135] L. I. Hernández *et al.*, "Spectral Characteristics and Photosensitization of TiO2 Nanoparticles in Reverse Micelles by Perylenes," *J. Phys. Chem. B*, vol. 117, no. 16, pp. 4568–4581, Apr. 2013.

[136] P. V Kamat, S. Das, K. George Thomas, and M. V George, "Ultrafast photochemical events associated with the photosensitization properties of a squaraine dye," *Chem. Phys. Lett.*, vol. 178, no. 1, pp. 75–79, 1991.

[137] W. Wei, D. Liu, Z. Wei, and Y. Zhu, "Short-Range pi-pi Stacking Assembly on P25 TiO2 Nanoparticles for Enhanced Visible-Light Photocatalysis," *ACS Catal.*, vol. 7, no. 1, pp. 652–663, 2017.

[138] C. Guarisco *et al.*, "Visible-light driven oxidation of gaseous aliphatic alcohols to the corresponding carbonyls via TiO2 sensitized by a perylene derivative," *Environ. Sci. Pollut. Res.*, vol. 21, no. 19, pp. 11135–11141, 2014.

[139] S. Jing, Z. FengWei, Z. Tong, and L. Jia, "Photocatalytic degradation of rhodamine B by dye-sensitized TiO2 under visible-light irradiation," *Sci. CHINA-CHEMISTRY*, vol. 54, no. 1, pp. 167–172, 2011.

[140] N. Serpone, D. Lawless, and R. Khairutdinov, "Size effects on the photophysical properties of colloidal anatase TiO2 particles: size quantization versus direct

transitions in this indirect semiconductor?," *J. Phys. Chem.*, vol. 99, no. 45, pp. 16646–16654, 1995.

[141] G. Baldi, M. Bitossi, and A. Barzanti, "Method for the preparation of aqueous dispersions of TiO2 in the form of nanoparticles, and dispersions obtainable with this method." Google Patents, 30-Apr-2013.

[142] L. Moggi, A. Juris, and M. T. Gandolfi, "Manuale del fotochimico." Bononia University Press, Bologna, 2006.

3. REAL APPLICATIONS OF PHOTOCATALYTIC NANOCOMPOSITES

3.1. Application in smart surfaces: TiO_2:Gr nanocomposites in concrete

The photocatalyst products are to a large extent used in the construction sector: construction accounts for ~90% of the market[1]. It is projected to grow with a Compound Annual Growth Rate (CAGR)of 13% from nearly $1.4 billion in 2015 to $2.6 billion in 2020[1]. Titanium dioxide, mainly in the form of anatase nanoparticle (TiO_2-NP), has a wide application as photocatalyst (PC) for cementitious materials[2]–[15]. These applications of TiO_2-based PCs to cementitious materials are mainly aimed to achieve two goals: self – cleaning effect of cementitious surfaces [16]–[19] and the degradation of environmental contaminants[9], [14], [15], [20]. As regard, self-cleaning property it tackles the problem of the preservation of the original appearance of the surface of the building, mainly of the architectural concretes, over time and it is much appreciated especially for buildings located in polluted environments such as urban areas [16]–[19], [21] . The depolluting action of photocatalytic cement surfaces has the purpose to turn into harmless compounds the environmental contaminants (e.g. NO, NO_2, SO_2, suspended organic particulate, volatile organic compounds, aromatic hydrocarbons, etc.) and prevent heir accumulation[2], [4], [13], [22]–[24] according to the European Union (EU) environmental regulations directives (e.g., 2008/50/EC). TiO_2-NPs have the advantages of stability in water, non-toxicity[25], [26] , low cost (1.9K USD/Ton at 2016 prices[27]) and has a wide application as photocatalyst for cementitious materials because of its good compatibility with the inorganic matrix. TiO_2 has a band gap (ΔE) ≈3.25 eV[26]), and, as a result, can be activated as PC only with the UV part of the solar spectrum[28]. For this reason the TiO_2-based PCs-incorporated in cement based materials are not active, and used, in indoor conditions where the UV component of the solar light is not present[29]. This is a drawback also for outdoor

applications since the UV light is just ∼4% of the total solar radiation resulting in the ∼96% waste of useful energy to perform the photodegradation processes[30], [31]. Furthermore the 90%[32] of sunlight that manage to activate TiO_2-NPs is lost because the recombination of the photo-generated electron-hole pairs. Hence, a key problem in the application of TiO_2-NPs in cementitious material for outdoor structures and buildings, is to increase the efficacy of the PC to tackle and partially compensate its limited activity. It has to be considered that the possibility to degrade air contaminants by photocatalytic cementitious surfaces in real conditions is also limited by the continuous refresh of the polluted air entering in contact with the photocatalytic surface[33] and by the variable sunlight intensity over year and over latitude[34]. Clouds are a further factor affecting the intensity of sunlight on Earth. Even on a clear day about a quarter of the potential radiation is lost by light cloud increasing to half with thicker cloud and arriving to more than ninety percent under a dark thundery sky. Is it possible to find patent application with photocatalytic compositions, especially useful as paints, renders and plasters, provided with a high photocatalytic power, preferably with a mixture of anatase TiO_2 and rutile TiO_2 (International Patent Application Publication No. WO 2009/013338)[35]. Other Patents e.g International Patent Application Publication No. WO 2009/080647[36] describes a photocatalytic composite comprising a titanium dioxide supported on metakaolin with a photocatalytic activity of the composition that is higher than 80% in term of degree of NOx oxidation. **Hence, a key problem to solve in the application of photocatalysis in cementitious material for outdoor structures and buildings, is to increase the efficacy of the photocatalyst (particularly TiO_2-based) to tackle and partially compensate for its limited activity in real conditions caused by the continuous refresh of the polluted air entering in contact with the photocatalytic surface and by the variable sunlight intensity over year and over latitude.** In the previous chapter of this work we identified graphene as the most promising material for TiO_2 modification. Up to now there are just few works regarding the application of TiO_2/carbon nanomaterials in cement[37], that can turn in to future market product[38], [39] as the TiO_2-cement photocatalyst already is[7].

3.1.1. Industrial scale up of TiO_2-Gr nanocomposites

As said, there are already coatings/paints and cements on the market that make use of TiO_2 for photocatalytic self-cleaning and air purification. However, the performance is currently not good enough to allow a broad uptake of the technology for the current price tag. The cost of a cement with some peculiar functionalities is 1 Euro/kg. In order to transform a façade of a 5-storey building into a photocatalytic surface a cost of 100€ extra is needed[40]. Flooring in photocatalytic blocks charges on average between 10 - 20% more than normal paving[40]. A problem for a successful integration of new technologies in this particular market is the very high **price sensitivity and the large quantity of material needed**. The insertion of a small quantity of graphene can in principle enhance the performance of the bare commercial titanium dioxide, as shown in the previous section, maintaining the same performance of a already commercialized cement lowering the TiO_2 content, and, as a consequence, the cost of concrete. However the price of Graphene has to be considered. So we decided to use graphite flakes or partially exfoliated graphite as starting materials for all the compound tested in the cementitious matrix. The issue was to find the more convenient way to promote the interaction between TiO_2 and graphene and in the mean-time exfoliate graphite. The most promising techniques that matched the requirements were:

-Bath sonication[41]–[43];

-Ball milling[44]–[46];

-Shear exfoliation[47], [48];

Regarding the Bath sonication technique, the process was already explained in the section related to the composite TiO_2: Gr 10:1. The other synthetic pathways will be explained in the following sections.

3.1.1.1. Industrial production via Ball milling

First, in order to obtain carbon modified –TiO_2 photocatalytic products by ball-milling we thought to the possibility of exfoliating graphite in presence of TiO_2, to promote some interaction able to improve the photocatalytic activity of TiO_2, chosen as reference.

Figure. 1 Pulverisette 6 ball mill apparatus

Figure 1 show the Pulverisette 6 used for the process, with one grinding bowl having planetary movement. Test were performed in dry conditions with a grinding aid for the exfoliation of graphite, Melamine (M), and adding also TiO_2 directly in the Zirconium jar, to try to take advantage of its interaction with graphite/graphene during graphite exfoliation by the impact forces generated in the grinding process. As starting materials we selected: Titanium dioxide (AHP200 from Sachtleben Chemie with average surface area of 160-240 m2/g and anatase purity>90%; Gaphite flakes (from Sigma Aldrich) with an average dimension of +100 mesh; Melamine (from Alfa Aesar) with a purity of >99%. Melamine was introduced in the ball mill to promote graphite exfoliation according to literature [44], [46].In exemplary procedures, the photocatalysts **MCG06** and **MCG06S** were prepared as follows[38].

A composition (15g) of the ingredients were processed for MCG06 and MCG06S in the ratio **TiO2: melamine: graphite flakes 1:1:1 w/w/w**. The Ball milling apparatus was equipped with a Zircomiun jar (250ml) containing Zirconium balls ranging from 5 to 20 mm (n°10 of ϕ5mm+n°15 of ϕ10mm+n°6 of ϕ20mm). The composition was next milled in a planetary mill for enough long time and rotational speed to forecast partial graphite exfoliation, 1 cycle- at 150 rpm for 45 minutes[44]. Only for S samples the photocatalyst (7 g) was then mixed with 2-propanol (100 ml) for 10 min. The dispersion was there after sonicated for 4 hours and was then dried at 60°C.The product was then milled in a centrifugal mill at 150 rpm for 45 minutes.

3.1.1.2. Industrial production via shear exfoliation

Figure. 2 Laboratory blender used to obtain shear exfoliation forces necessary to produce PCs.

High-shear mixing was demonstrated to be a scalable alternative to sonication for the exfoliation of layered crystals such as graphite[48]. Shear exfoliation can produce large quantities of defect-free, unoxidized graphene. Though this exfoliation mechanism is lighter with respect of bath sonication and ball milling. Since that, a partially pre-exfoliated graphite (G2Nan paste purchased by Nanesa), see Table1, needs to be used as starting material. The TiO_2 source was the same used for the ball milling and the bath sonication samples, and in addiction a non ionic surfactant, as Pluronic P123(purchased by BASF), and a ionic one, as SILIPON RN 6031, were proofed to stabilize the liquid suspension during the exfoliation process. Pluronic P123 is a bi-functional block copolymer surfactant terminating in primary hydroxyl groups, in the scientific literature[49] proved to be effective in the process of exfoliation of graphite[50]. SILIPON RN 6031 is an air-entraining agent used as believed aid

to the process of mechanical exfoliation of graphite[42], to promote the distancing among the layers of graphite products (stable in solution) by the Coulomb repulsion among sheets covered by surfactant. Photocatalytic preliminary tests of the powders obtained with and without the surfactants showed that either ionic and non-ionic surfactant negatively affect the photocatalytic performances of the PCs. Then their use was abandoned.

Table 1 Data sheet of G2Nan paste purchased by Nanesa

Properties G2Nan paste	Values
Appearance (colour)	Black
Appearance (form)	Paste
Carbon content (%)	>98
Bulk Density (g/cm^3)	0.042-0.020
Specific surface area(m^2/g)	>20
Average particle lateral size µm	5-50

The photocatalysts of the series **LAGi (i=2,5,10)** were prepared adding G2Nan paste (4% dry graphene like matter) and TiO2 powder to water to produce an aqueous slurry. The TiO_2:G2Nan ratio as in Table2 below, show the photocatalyst obtained by "blender method".

Table 2 Description of the photocatalysts of the series LAGi (i=2,5,10) obtained with the blender method

Photocatalyst	TiO_2/G2Nan(w/w) dry matter
LAG2	50:1
LAG5	20:1
LAG10	10:1
LAG10S	10:1

The slurry was then mixed in the laboratory blender at 11000 rpm for 40 min. The product was dried at 60°C. The obtained powder was mixed for 20 seconds by the laboratory blender. For the S sample the dispersion was next sonicated for 4 hours in 2-propanol, the product was dried at 60°C, and was finally mixed for 20 seconds by the laboratory blender.

Figure. 3 Photocatalyst in powder form before (LAG10 on the left) and after sonication treatment(LAG10-S on the right)

3.1.2. Photocatalytic reduction of inorganic pollutants: tests with NOx

The photocatalytic activity of TiO_2 photocatalyst incorporated cement based materials evaluated by NOx abatement adopting the recirculation procedure. The gas flow method is compared using the apparatus reported in the Italian standard UNI 11247. The UNI EN 11247 standard describes a method aimed at assessing the index of photocatalytic abatement due to the action of inorganic materials. The sample to be investigated was collocated inside a reaction chamber (3 litres) containing the already mentioned Mercury lamp Radium Sanolux HRC 300-280 E27 UV-lamp, with an irradiance (I) both in UVA (280nm- 315nm; I=3W/m2 at 0.5m) and UVB (315nm- 400nm; I=13.6W/m2 at 0.5m). In the UV (λ<400 nm) irradiance spectrum the main component is the 365 nm line signal brought by the presence of mercury inside of the lamp (according the standard UNI 11247 irradiance integrated at λ <350 nm is forecast to be 10% lower than the irradiance integrated between 350 and 400 nm). The irradiation system provides for an average irradiance (in UV-A band) of (20±1) W/m^2 on the specimen surface (64cm^2) during the test. In the

standardized continuous flow procedure according to UNI 11247, that is a "dynamic" continuous flow method, the flow of polluted air containing 0.55ppm of NOx (of which NO_2=0.15ppm and NO=0.4ppm) was constant (1.5 litre/min).

Figure. 4 Instrument used for the NOx abatement test

The first phase of the test was in dark conditions and it was necessary to equalize the adsorption processes and to achieve a constant gas flow and NOx concentration (CB). During this first phase in dark conditions, the concentration of the gas entering and leaving the reactor is constantly measured. When the concentration of the outlet gas from the reactor is stable, the second phase of the test starts the lamp is switched on. At this stage, the system is allowed to balance for a certain time to reach an equilibrium gas concentration (CL). In the "gas recirculation" procedure, that is a "static" method, a certain volume of air is compelled to recirculate during the experiment with no air exchange over time. As in the gas flow procedure CB and CL are registered in the dark and light phases respectively. The difference between the NOx concentration measured in the dark and the light phase allows to calculate the Ac index of the photocatalytic abatement since the illumination activates the photocatalytic reactions, which lead to the degradation of the NOx.The photocatalytic abatement A_C is (Eq 21):

$$A_C = 100 * \frac{(C_{B-}C_L)}{C_B} * \frac{I_N}{I} * \frac{S_N}{S}$$

A_C = photocatalytic adimensional abatement index under test conditions (%).
C_B = NOX concentration at the reactor's exit in dark conditions (ppb).
C_L = NOX concentration at the reactor's exit under radiation (ppb).
I = average irradiance as measured and corrected (W m^{-2}).
I_N = nominal irradiance (20 W m^{-2}).
S = surface area of the specimen as measured (cm^2).
S_N = nominal surface area of the specimen (64 cm^2).
For all the tests carried out, the surface of the samples S was 61 cm^2.

3.1.3. Photocatalytic reduction of inorganic pollutants: tests with NOx on powders

The UNI 11247 standard was developed for testing hardened materials such as mortars, not powders. Nevertheless due the high number of the experimental photocatalysts synthesized in the work and considering the high relative quantities of powder necessary for the preparation of the mortar samples, a preliminary photocatalytic characterization of the photocatalysts in powder form was necessary. This characterization permitted the identification of the best samples for the assessment in mortar, preparatory to achieve the aim of the project. To apply the standard test to powder samples we had to tackle the problem of the possible alteration or removal of the surface of the specimen by the gas flow in the reaction chamber. For this reason it was necessary to set up a method for the realization of a powder-film, compact and able to remain intact during the test. To compare the results, the TiO_2 weight was kept constant in the preparation of the experimental photocatalyst, in particular, 0,5 g of TiO_2 were used. Only some samples were prepared with higher TiO_2 amounts to verify its influence on the photocatalytic activity. The preparation of the powder samples occurred in three phases:

- mixing the composite with 2-propanol (20ml);
- bath sonication of the mixture for 10 min;
- drying at room temperature.

Using this methodology it was possible to prepare an inorganic very thin deposit of the photocatalyst on the bottom of a Petri glass, approx. ϕ=8.8 mm (area =61 mm^2).For the bath sonication a BANDELIN SONOREX (frequency of

35 kHz and power 80/320 W) was used. The next drying process allowed the formation of a homogeneous and continuous deposit, ready for the measurement of Ac.

Figure. 5 Film of LAG10 powder samples

Table 3 Results of photocatalytic activity on powder samples with NOx abatement. The prefix LA indicates samples prepared via technical blender; in particular:A symbol indicates anatase; G indicates Nanesa graphene;F the Sigma Aldrich graphite flakes the different number indicates the percentage of graphene.The prefix MCG indicates samples prepared via ball milling.For both preparations, S symbol indicates an additional sonication treatment (for four hours) of the powder.

	Test on Powders					
Graphite	Code	TiO_2 weight [g]	Average Ac	Dev. std.	Increase Ac%	
-	A	0,5	32,0	0,8	reference	1° batch
-	A	1,5				
Sigma	MCG06	1,5	49,1	0,3	53	
G2nan	LAG10	0,55	54,6	4,3	69	
-	A	0,5	28,8	3	reference	2° batch
-	A	1,5				
Sigma	MCG06-S	1,5	47,0	2,8	63	
G2nan	LAG10-S	0,55	52,2	2,0	81	
G2nan	G	0	1,0	1,7	-	
G2nan	LAG2	0,5	42,3	1,7	31	
G2nan	LAG5	0,5	48,8	1,2	51	
Sigma	F	0	1,0	0,2	-	
Sigma	TiO2:Gr10:1	0,5	54,0		68,8	

Results of the NOx abetment on powders are reported in the Table 3. In the first part of the table (in orange) the results of two series of batches of the same powders are shown; in the second one (in green) the results of the

powders more active as photocatalytic activity. In order to compare different samples, it seemed more convenient to consider the increment of the experimental powder compared to the reference sample, exclusively prepared with the commercial TiO_2 Hombikat 200 (AHP), instead of the absolute value of the photocatalytic abatement. For the samples of 1st and 2nd batch, it is possible to note an increment of A_C, compared to the reference samples, higher than 50%. These samples were selected for the preparation of the relevant mortars. In order to sum up the reduction of inorganic pollutants: tests with NOx on powders :

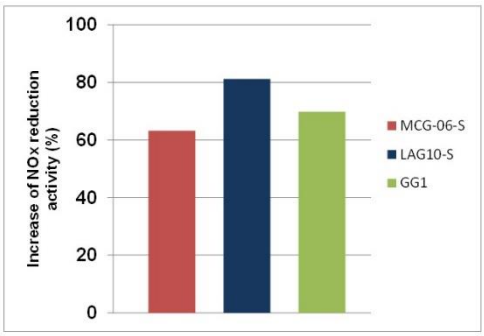

Figure. 6 Increment in NOx abatement brought by the modification of the TiO2 with graphene

- **LAG10-S and MCG-06-S**, obtained after sonication treatment gave the better photocatalytic activity in powder form . arriving approx. **up to Ac=+80%** (sample LAG10-S) with respect of TiO_2. The unsonicated samples LAG10 and MCG-06 shower a lower performances with respect of the sonicated ones, see Figure 6.

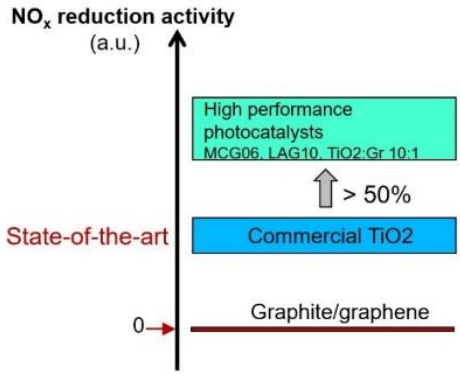

Figure. 7 Scheme of the performance reached with respect of the state of the art with commercial TiO_2 embedded in cement matrix

The preparation of the photocatalyst **TiO_2:Gr 10:1** by sonication has an effect in the abetment of the NOx contaminants that is **+68%** higher with respect of the bare titania. **With the current state of the art technology of titania an increment of more then 50% in nitrous oxides abatement is reached with graphene doping of TiO_2 nanocomposites**, as it possible to see from Figure 7.

3.1.4. Photocatalytic tests with RhB on powders: industrial scale up of the test

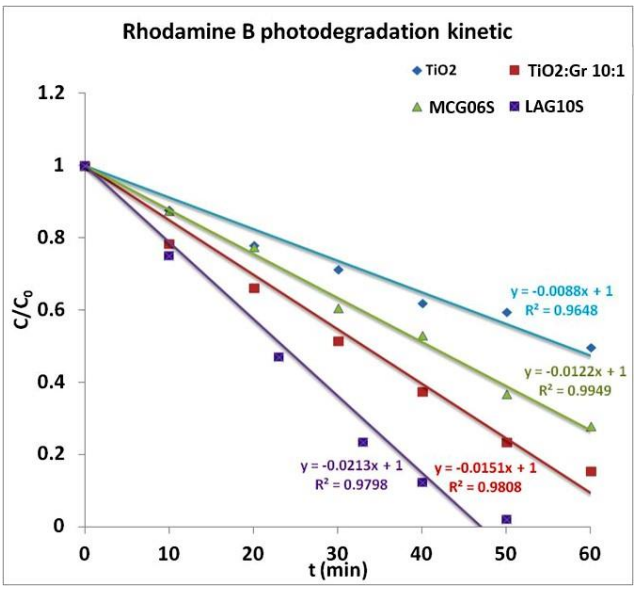

Figure. 8 Photocatalytic degradation of RhB given as C/CD as a function of time, for the TiO_2(AHP200), LAG10S , TiO_2:Gr 10:1 and MCG06S samples. Lines represents the interpolation fitting of the experimental points.

The procedure for the photocatalytic test on organic pollutants is the scale up of the procedure followed in case of the characterization of the TiO_2:Gr 10:1 reported in the previous chapter. Solutions of with the following composition were analysed inside of a Becker Pyrex, 400ml(diameter=8cm, height of the solution tested =3.5cm c.a.) : 28.6ml of an aqueous solution of Rhodamine B (RhB) (0.05mg / ml;1 * 10^{-4}M), 21,4 ml ultrapure H_2O purified with milliQ system and 50ml of photocatalyst water solution pre-sonicated with a bath sonicator for 5 min. As in the other photocatalytic tests, the weight amount of photocatalyst was calculated in order to have the same amount of TiO_2 (2mg / ml) inside of the photocatalyst water solution. Before irradiation, the suspensions were magnetically stirred (3000 rpm) in the dark for 40 minutes to reach the adsorption–desorption equilibrium. After that, an aliquot of 5ml was sampled from each solution and the RhB concentration detected was taken as degradation kinetic starting point (CD). The solution was irradiated for 60 minutes, sampling 5 ml of solution every 10 minutes. Each aliquot was centrifuged a (9000rpm;time: 10 min; T = 25°C) and the upper 0.5 ml of each sample were then diluted with water (1: 6 ratio)to be analysed. The irradiation setup was the following: Mercury lamp Radium Sanolux HRC 300-280 E27 UV-lamp, with an irradiance (I) both in UVA (280nm- 315nm;

I=3W/m2 at 0.5m) and UVB (315nm- 400nm; I=13.6W/m2 at 0.5m). The Pyrex Becker was located at 35 cm from the irradiation source. The detection of RhB left in the solution after a given irradiation time (C) was estimated using by means of UV-VIS absorption spectra recorded at 25°C with a Cary 300 UV-Vis spectrophotometer (Agilent Technologies). The data of maximum absorbance at 554nm were corrected for the absorbance of 650nm.The results, reported in Figure 8, demonstrated that the decomposition of dye could be assigned to a zero order kinetics model. That is the one showed in section 2.3.1 Eq 17:

$$C(t)/C_D = 1 - kt$$

where k is the apparent rate constant of RhB photodegradation. Figure 8 shows the fitting of the experimental points For the pure TiO_2(AHP200), the obtained k value is estimated to be 0.0088 min-1, while for the composites MCG06S k is 0.0122 min-1, TiO_2:Gr 10:1 is 0.0151 min-1 and for LAG10S k is 0.0213 min-1. This means that the composites **MCG06S, TiO_2:Gr 10:1 and LAG10S fasten the photodegradation** of rhodamine B respectively **of 1.39, 1.72 and 2.42 times** comparing of the pure TiO_2(AHP200).

3.1.5. Preparation of photocatalytic cementitious and lime surfaces

Figure. 9 Appearance of a cement photocatalytic paste before the hardening.

The fresh cementitious mixture is mortar prepared according to the procedure described in the standard UNI EN 196-1 and replacing part of the cement with the photocatalyst, as it is possible to see from Figure 9.

Figure. 10 hardening process of the photocatalytic mortar Petri capsule at room temperature and 90% relative humidity

The fresh mortar was poured into the lid of a Petri capsule and maintained in a conditioned room at 20°C and 90% relative humidity (RH) for 7 days, see Figure 10. Then the sample was left at 20°C and 60% RH for all the time before the measurement. The fresh cementitious mixture is mortar prepared with hydraulic lime i.pro chaux pure NHL5 (instead of white cement i.design Italbianco 52.5R) according to the procedure described in the standard UNI EN 196-1 and replacing part of the hydraulic lime with the photocatalyst, as shown in the Table 4.

Table 4 Components and weight ratios of a standard mortar sample.

Component	Name	Composition	Note
White cement	i.design Italbianco 52.5R	1 part (comprising TiO_2)	
Hydraulic lime	i.pro chaux pure NHL5	1 part (comprising TiO_2)	As alternative binder
TiO_2	Hombikat AHP200	1.5%, 3% by weight of cement	
MHE cellulose	Tylose MH15000 YP4	0.36% by weight of cement	Only in some mixtures
Sand	According to EN196	3 parts	
Water/cement	Town water supply	0.5	

3.1.6. Characterization of Photocatalytic cementitious surfaces: micro-Raman, HR-SEM and EDS quantitative measurements.

In order to assess the actual distribution of the Photocatalysts inside of the cementitious matrix as well as the conservation of the pristine PCs as inserted before the mixing, surface analysis with **micro-Raman, HR-SEM and Energy-dispersive X-ray spectroscopy(EDS) quantitative analysis.**
Micro Raman analysis performed on the LAG10S and MCG06S incorporated cement, Figure 11, and lime pastes (ca. 1mm thickness) confirm the presence of the photocatalyst on the surface of the sample.

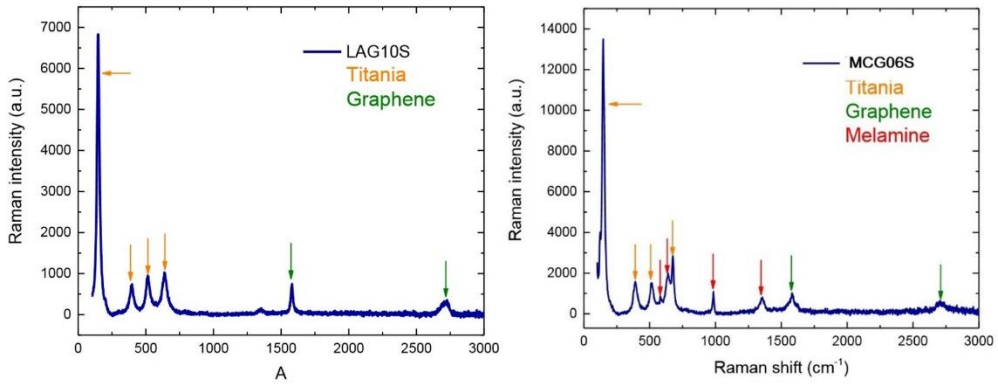

Figure. 11 Raman spectrum of graphene edge, carried on cement mortar for LAG10S and MCG06S

High Resolution Scanning Electron Microscope (HR-SEM) images of LAG10S and MCG06S powders clearly show the presence of Titania interacting with graphene Figure 12.

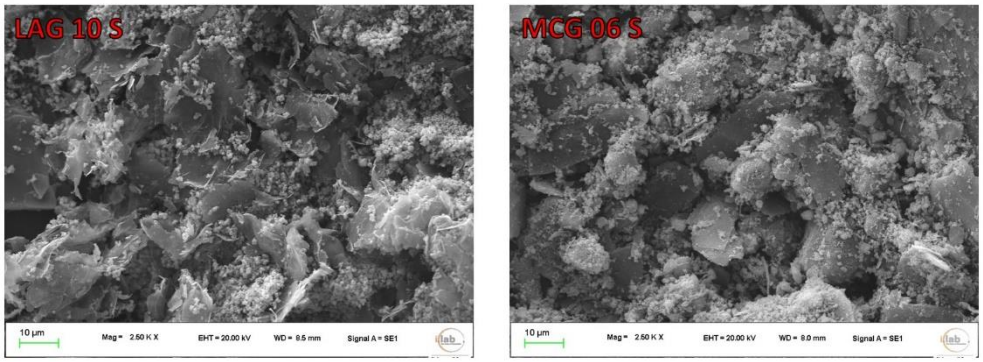

Figure. 12 SEM images of the photocatalysts of LAG10S and MCG06S. It is possible to notice that the actual distribution of titania on the top of graphene is better in the case of LAG10S sample.

Then in order to understand why the sample LAG10 S was the most performing one, HR-SEM images of MCG06 and LAG10S incorporated cement and lime samples are taken . The acquisition was also performed in the phase contrast mode, Figure 13. This analysis reveals the presence of graphene areas on the surface of the samples. That graphene areas are clearly observed utilizing in-lens detector due to their different distinctive morphology as compared to the cement matrix, Figure 13.

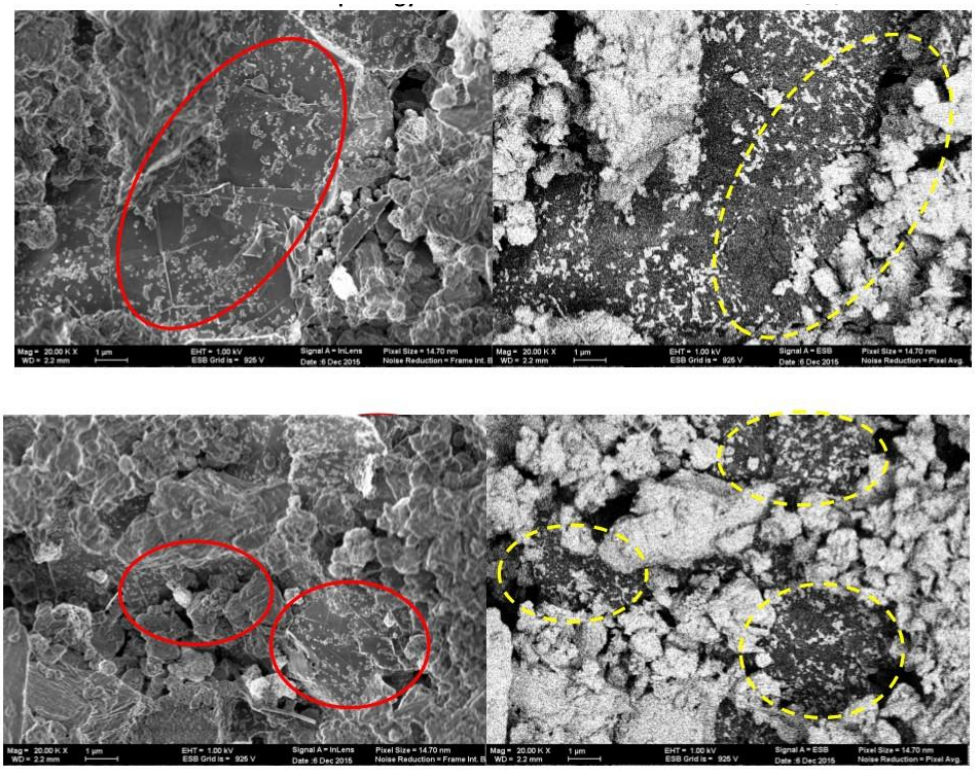

Figure. 13 Images obtained by In lens (left panels) and energy selective backscattered detector (EsB; right panels), First raw is the LAG10S sample in cement matrix. Second raw is the MCG06S sample in cement matrix. It is possible to notice the compositional contrast between graphene (darker area; designated by arrows) and cement matrix.

Moreover, employing the energy selective backscattered (EsB) detector allowed observation of the compositional contrast between graphene and cement matrix. Dark regions derived from the lower matrix both morphologically and their Z contrast atomic number of graphene as compared to the cement matrix confirm its presence within the samples. The same is visible within the lime matrix, Figure 14.

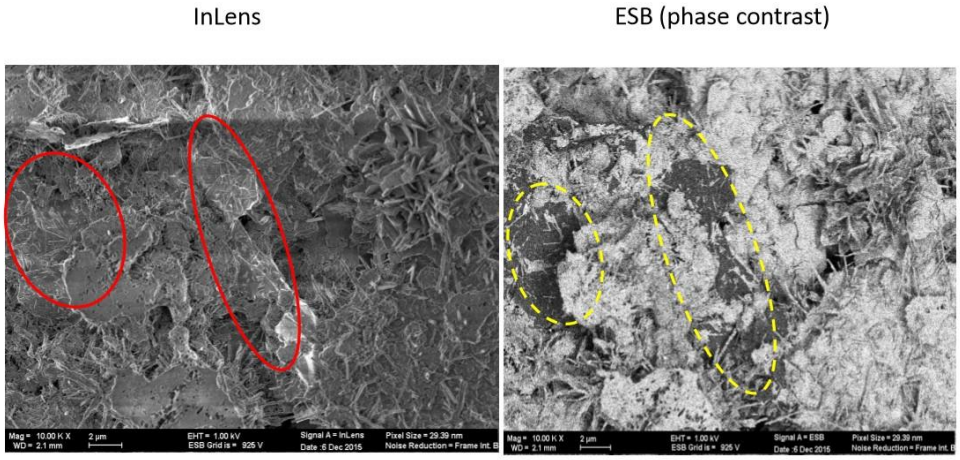

Figure. 14 images obtained by In lens (left panel) and energy selective backscattered detector (EsB; right panel), demonstrating the morphology of LAG10S incorporated hydrated lime sample (left panel), and compositional contrast between graphene (darker area; designated by arrows) and hydrated lime matrix (right panel).

EDS quantitative analysis on cementitious matrix incorporating TiO_2 reference, LAG10S and MCG06 was performed. This is an analytical technique used for the elemental analysis or chemical mapping of a sample, in order to quantify the elements of interest on the analysed surfaces, Figure 15 (left).

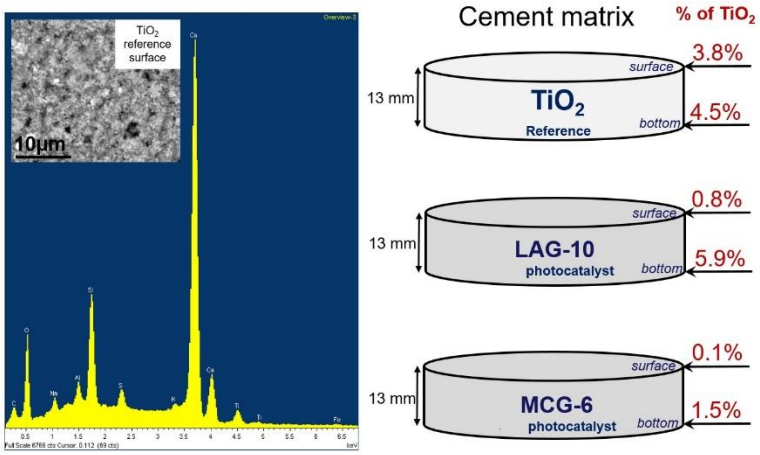

Figure. 15(left) EDS spectra on cementitious matrix incorporating TiO_2 reference, inset: Portion of the sample mapped with EDS. (right) distribution in terms of upper-lower TiO_2 concentration(%) visualized utilizing Cameo+ function in different cementitious samples.

Results showed that photocatalysts incorporating graphene demonstrate unexpected distribution in terms of Δ upper-lower TiO_2 concentration visualized utilizing Cameo+ function. In fact the % of TiO_2 present on the top of the reference sample is 3.8% with respect of the 0.8% and 0.1% of LAG10S and MCG06S. this effect can be due to a different settling or migration of the photocatalyst during the hardening phase of the concrete. In order to avoid this problem we decided to move from 13mm to 1mm thick samples, Figure 16.

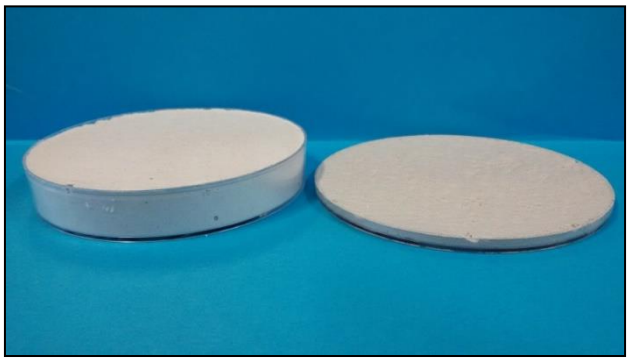

Figure. 16. (right) Cementitious sample of 13 mm thickness with anisotropic concentration of the graphene based PCs, and the 1mm thick homogeneous sample.

3.1.7. Photocatalytic reduction of inorganic pollutants by photocatalytic surfaces: tests with NOx

Test of NOx abatement are performed on TiO_2 reference and the chosen photocatalysts: LAG10, LAG10S, MCG06, MCG06S and TiO_2:Gr 10 1 in mortars All the photocatalysts are incorporated in a cementitious matrix Italcementi Italbianco 52.5R and hydraulic lime. The insertion of cellulose as additive to the cementitious matrix was evaluated in order to enhance the dispersion of the PCs and avoid the settling effect noticed from EDS measurements results discussed in the previous section.

Table 5 Results obtained using cement binder

Mortar sample name	Samples compositions		RAc (%) (Ac sample/Ac reference)
	Photocatalyzer 3%TiO_2	Binder	
AI3	TiO_2	Italbianco 52.5R	1.00
GI	G2Nan		0.00
LAG2I	LAG2		1.11
LAG5I	LAG5		1.14
LAG10I	LAG10		1.17
LAG10SI	LAG10S		1.23
AI1.5	TiO_2		1.00
FI1.5	Graphite Flakes (milled)		0.00
MCG06MI	MCG06 (+cellulose)		1.18
MCG06SI	MCG06S		1.21
AI	TiO_2		1.00
GG1I	TiO_2:Gr 10:1		1.13

Table 6 Results obtained using hydraulic lime binder

Mortar sample	Samples compositions		RAc (%) (Ac sample/Ac reference)
	Photocatalyzer 3% TiO_2	Photocatalyzer 3% TiO_2	
AC3	TiO_2	Hydraulic lime	1.0
LAG10MC	LAG10 (+cellulose)		1.15
LAG10SC	LAG10S		1.42
LAG10SMC	LAG10S (+cellulose)		1.40
MCG06MC	MCG06 (+cellulose)		1.08
MCG06SC	MCG06S		1.22
MCG06SMC	MCG06S (+cellulose)		1.46
AC	TiO_2		1.00
GG1C	TiO_2:Gr 10:1		1.14

Hereafter some remarks concerning the activity of the photocatalytic mortars reported in Table 5 and 6:

- the mortar containing the hydraulic lime as binder shows the higher Ac % increase; about 40% for the better photocatalysts;
- the mortar containing the Italbianco binder shows an Ac increase, of about 20% Ac increase with the most performing photocatalyst LAG10S, but the absolute values of abatement are lower than those obtained with the same LAG10S in hydraulic lime.
- the formulation of the mortar with cellulose increases the photocatalyst dispersity, and as a consequence in the case of MCG06 sample enhance also its photocatalytic performance;
- the sonication treatment performed on the powder in a bath for four hours improves the efficiency of the photocatalysts, especially in the lime matrix, as it is possible to notice comparing the LAG10/LAG10S (+15% and +42% respectively) and MCG06/MCG06S (+22 and +46%)

3.1.8. Self-cleaning test: Photocatalytic tests with RhB on photocatalytic cementitious and lime surfaces

In exemplary procedures, the self-cleaning performances of hardened hydraulic lime-based samples (3 mm thickness) doped with the different photocatalysts were investigated, in real-time, under continuous light irradiation according to the following procedure. the photoactive samples were stained with a dye solution. After drying, the stains on the samples surfaces were observed with a colour camera during the irradiation with a light source. The images were acquired on a PC and processed to calculate the fraction of light adsorbed by the stain during the irradiation. Staining process: in exemplary procedures, a volume of 0.050 ml of an ethanol solution of Rhodamine B (0.25g/L) was dropped on the top of the surface of the photoactive sample. Self-cleaning tests were performed on dried samples (30 minutes after dye solution deposition at 25 °C, atmospheric pressure). Photodegradation test: in exemplary procedures, the set-up used for the photodegration test consisted in an irradiation lamp, a sample holder, and a Cmos Colour Camera equipped with a 14 mm objective. In exemplary procedures, all the measurements were performed in the same conditions in

particular as follows. The sample was kept horizontal with the active face upward. The lamp (Mercury lamp Radium Sanolux HRC 300-280 E27 lamp) was positioned on the top of the sample at 40 cm from its surface. The emission cone of the lamp was directed downward with the axis of the emission cone vertical and directed toward the rhodamine stains. The camera was positioned at 45 cm at an angle of 10° with respect to the lamp axis. The camera was oriented to point at the intersection of the lamp emission axis with the sample surface. The stain image was focused manually. The acquisition parameters of the camera were set manually and kept unchanged during all the experiments. After the samples were positioned under the irradiation lamp the discoloration was monitored acquiring images (one frame every 20 seconds) of the sample under continuous irradiation at 25 °C for 24 h. For the quantitative analysis, the images were recorded and processed to calculate the average intensity per pixel (I) across the stained region. In particular, the average intensity (I) was measured in the same sample area and with the same irradiation set up, before staining (I_0) and after staining, as a function the time, during irradiation time (I_t). Absorbance due to the stain was measured as (Eq. 21):

$$A_t = \log \frac{I_0}{I_t}$$

Images acquisition and processing was performed with the softwares IC Capture 2.3 and ImageJ.

3.1.8.1. Results for lime coatings

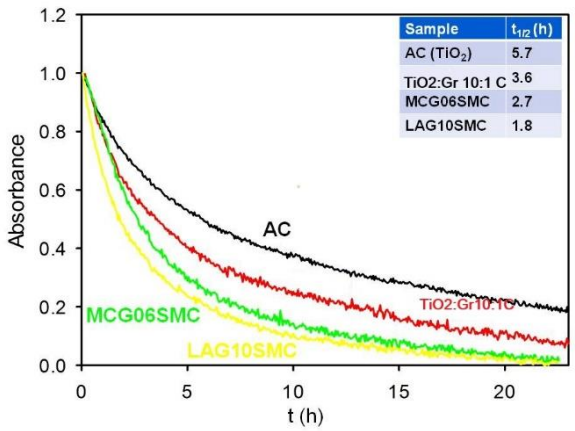

Figure. 17 Graphs demonstrating the photodegradation of Rhodamine B on the top of lime coatings made with photocatalytic additives: AC (TiO_2 reference), TiO_2:Gr 10:1, MCG06S and LAG10S (as described below) as a function of irradiation time. Inset presents a table reporting the different times in which Rhodamine B adsorption is half of the initial starting value.

In particular, the absorbance At was measured as a function of time for the different photo-catalysts. The photodegradation rate of rhodamine on the top surface was greatly influenced by the nature of the photocatalytic additive. Specifically, as a quantitative parameter of the rate of photodegradation, the half-time t1/2, defined as the irradiation time after which the value of absorbance At is equal to the half of the initial absorbance value A0, is calculated. According to this parameter, the hydraulic lime (C) samples MCG06SMC and LAG10SMC showed a faster photodegradation kinetics with respect to the control sample AC incorporating only the TiO_2, Figure 17. In particular **the half time t1/2 was reduced by a factor of: 1.60 (for TiO_2:Gr 10:1), 2.11 (for MCG06SMC) and 3.17 (for LAG10SMC)** with respect to the control sample AC incorporating only the TiO2. Table 7 below presents the results for real-time photodegradation (self-cleaning) tests with hydraulic lime binder.

Table 7 results for real-time photodegradation (self-cleaning) tests with hydraulic lime binder

Mortar sample	**Photocatalyzer**	**Binder**	$R_{t_{1/2}}$ ($t_{1/2\ sample}$/ $t_{1/2\ reference}$)
AC	TiO_2	Hydraulic lime	1.00
TiO_2:Gr 10:1C	TiO_2:Gr 10:1		1.60
MCG06SMC	MCG06S		2.11
LAG10SMC	LAG10S		3.17

3.1.8.2. Results for cementitious coatings.

The effect of the photocatalysts is shown in Figure 18. Within the first 5 hours of irradiation, the LAG10SMI and MCG06SMI showed a faster photodegradation of Rhodamine B respect to the reference AI (TiO_2). In particular, after 1 hour of irradiation the absorbance of rhodamine B on the top of cementitious **TiO_2:Gr 10:1I, MCG06SMI and LAG10SMI is reduced by a factor of 1.10 in respect to the reference** AI.

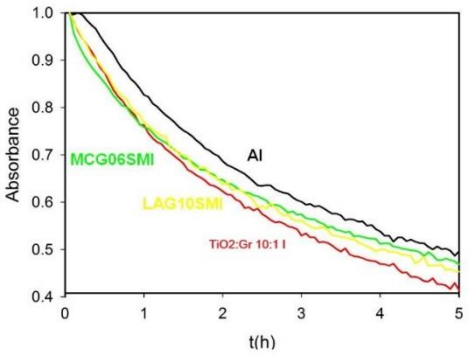

Figure. 18 presents graphs demonstrating the photodegradation of Rhodamine B, while focusing on the first 5-hour irradiation time of the Rhodamine B photodegradation on the top of cementitious coatings made with photocatalytic additives: TiO_2(AHP200), TiO_2:Gr 10:1 I, MCG06S and LAG10S (as described below), showing that the presence of graphene inside the photocatalyst fastens the initial photodegradation of pollutants

3.1.9. Concluding remarks on Section 3.1: photocatalysts embedded in cementitious matrix

1. LAG10S and MCG06S, obtained after sonication treatment gave the better photocatalytic activity in powder form, arriving approx. up to Ac=80% (sample LAG10S).
2. The preparation of the photocatalyst prolonging the sonication time was positive permitting to get Ac% higher than 20% in cementitious matrix.
3. In the powder, Ac does not seem to be influenced by the amount of photocatalyst but it could depend on the amount of the photocatalyst present on the surface of the mortars.
4. In cementitious and lime matrix, the use of cellulose permitted to greatly improve the homogeneity of the mortar samples.
5. With the experimental photocatalyst, Ac % in mortar containing cement grow up to about 20%.
6. With the experimental photocatalyst LAG10S and MCG06S (+cellulose), Ac % in mortar containing lime matrix grow up to about 40%.
7. Increases of Ac % with catalyst in powder form were confirmed by corresponding increases in mortar containing the catalyst even if with a lower value.
8. These data are confirmed by the self cleaning tests, that showed in lime matrix that the half time t1/2 of RhB was reduced by a factor of: 1.60 (for TiO_2:Gr 10:1), 2.11 (for MCG06SMC) and 3.17 (for LAG10SMC).

3.2. Application on Photovoltaics: Pervskite solar cells (PSC) with TiO_2:graphene nanocomposites

In collaboration with the University of Tor Vergata (Rome), we tried to build photovoltaic cells based on the combination of TiO_2/G with hybrid perovskites (P). Perovskites demonstrated strong potentialities for optoelectronic applications, due to their specific electronic and optical properties. They are indeed associated with larges degrees of freedom regarding the variations of materials and crystal structures, leading to 3D, 2D, or 1D materials with tenable bandgap, thus well adapted for solar energy conversion. Hybrid perovskite materials were used as alternative photo-sensitizer on nanocrystalline TiO_2, and what we tried to do was to replace the standard TiO_2 in PV solar cells with a TiO_2- Gr nanocomposite. The photoconversion efficiency of PV is dependent on: charge generation (formation of excitons), charge separation (electrons/holes separation) and charge extraction/transport (the removal of electrons and holes from the photo-absorber to an external circuit or to another active surface). The use of graphene in the those device is desirable due to its inherent nature to extract and transport charges from photon-absorbing semiconductors that should enhance the photoconversion efficiency of the device. An Example of this effect brought by the presence of graphene in perovskite solar cell was reported by Palma et all, where they introduced Reduced Graphene Oxide (RGO) applied as Hole Transporting Material[51].

In this study we tried to use graphene as a electron scavenger from Perovskite as well as from TiO_2 nanostructure toward the transmission of this carrier to the anode. The structure of the PSC that we produced is shown in Figure 19, and it is composed of a:

- Fluorine-doped Tin Oxide (FTO) transparent conductive layer on glass,
- compact c-TiO_2 layer (80 nm),
- 300 nm mesoporous nc-TiO_2 layer (that is the one that we are going to modify)
- $CH_3NH_3PbI_3$ perovskite,
- Spiro-OMeTAD HTM, doped with TBP and Li-TFSI
- gold counter-electrode.

The synthesis of four different nc-TiO_2 doped compounds was done by using two different kind of graphene source (EG=elecrochemical exfoliated

graphene; FG= graphite flakes) with two different doping levels. The TiO_2 source was the diluted Dyesol paste that is the usual starting material for the TiO_2 deposition in PV cells.

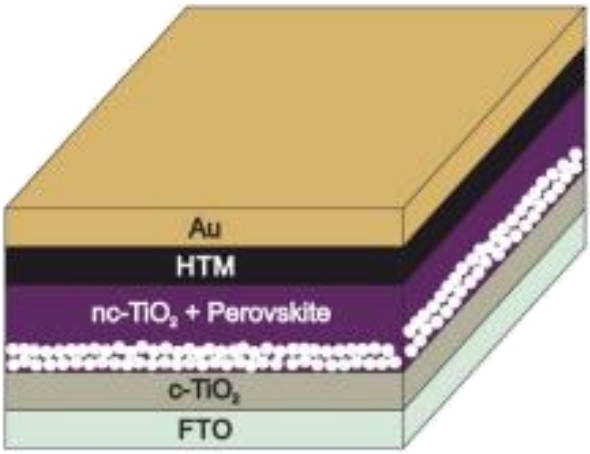

Figure. 19 Scheme of the PSC [51].*In this work we substitute the nc-TiO_2 with TiO_2-Gr.*

3.2.1. Photocatalysts TiO_2: Gr as PV components

As explained, the synthesis of four different nc-TiO_2 doped compounds was done by using two different kind of graphene source (EG=electrochemical exfoliated graphene; FG= graphite flakes). The FG were purchased from Sigma Aldrich. The EG graphene was obtained by Professor's Xinliang Feng group of Technische Universität Dresden, Germany. The synthesis was performed through the exfoliation in H_2SO_4 to create some defects and make easier for TiO_2 particles to attach to the surface. EG has a typical powder conductivity of around 15 S/cm and 80 S/cm for a freeze dried and conventionally dried sample @5 MPa, respectively. The typical characterization data is the following (measured on the samples after dispersion/sonication in DMF):

- Typical Sheet Size: 5-10 µm
- Oxygen content: ~7.5 at.% (C/O-ratio: 12.3)
- Raman ID/IG-ratio: ~0.4

- Sheet resistance: 4.8 kΩ/□
- Solubility: ~1mg/ml in DMF (stable >2 weeks)
- Typical composition: 1-Layer: 25%, 2-Layer: 35%, 3-Layer: 23%, 4-Layer: 12% (and 5%larger)

Regarding the synthesis of different nc-TiO_2 doped we used two doping level of graphene source 0.5 mg/ml and 2.5mg/ml, by the insertion of the doping amount in a TiO_2 paste (purchased by Dyesol) and diluted in a ratio 1:5 w/w with ethanol. The obtained samples have the composition as described in Table 8.

NAME	EG (mg/ml)	FG(mg/ml)
EG1	0.5	
EG2	2.5	
FG1		0.5
FG2		2.5

Table 8 Type and ammount of EG or FG doping per ml of 1:5 dyluted TiO_2 Dyesol paste in ethanol

We have to take into consideration that EG is in a water solution with a concentration of 2%. For instance this means that the in the EG (I) -2mg sample, the actual amount of inserted graphene is 0.04mg. We chose this amount of doping since it was the same used by Agresti et all [52] (0.038mg in 4ml of diluted paste). The TiO_2 paste+ EG/FG samples were stirred and sonicated for 6 hours in order to obtain homogeneous dispersions.

3.2.2. Solar cells fabrication

Perovskite solar cells were fabricated following the procedure of Palma et all[51]. PSC with an active area of 0.1cm^2 were prepared on Fluorine-doped Tin Oxide (FTO) conductive glass (Pilkington, 8 Ω/□, 25mm×25mm) patterned through raster scanning laser (λ=1064nm, Nd:YVO4 pulsed at 30 kHz, average output power P=10W)[53]. A metallic mask,[54] was deposited by screen printing on the designed photo anodes measuring pads areas, in order to avoid the deposition of compact c-TiO_2 onto these areas. The c-TiO_2layer, with a thickness ~100nm was deposited by Spray Pyrolysis technique onto the FTO surface, as reported elsewhere[53].

Table 9 List of the fabricated and tested devices. We decided to analyse different levels of deposition in order to assess the influence and effect of each layer on the final device

Name	c-TiO_2	nc-TiO_2	nc-TiO_2+G(n°)	Peroskite	Spiro	Au
R-TiO_2	X	X				
R-P	X	X		X		
R-C	X	X		X	X	X
S-FG (I)-2mg	X		X			
S-P-FG(I)-2mg	X		X	X		
S-C-FG(I)-2mg	X		X	X	X	X
S-FG (II)-10mg	X		X			
S-P-FG(II)-10mg	X		X	X		
S-C-FG(II)-10mg	X		X	X	X	X
S-EG (I)-2mg	X		X			
S-P-EG(I)-2mg	X		X	X		
S-C-EG(I)-2mg	X		X	X	X	X
S-EG (II)-10mg	X		X			
S-P-EG(II)-10mg	X		X	X		
S-C-EG(II)-10mg	X		X	X	X	X

After the removal of the metallic mask, a layer of TiO_2nanoparticles-based paste (18NR-T paste, Dyesol) was screen-printed over the c-TiO_2/FTO substrates and subsequently exposed to a sintering process with a final step carried out at 480°C for 30 min. The outlined procedure brings to the formation of a nano-crystalline (nc) mesoporous TiO_2 layer. The final thickness of the nc-TiO_2 film (300 nm) The perovskite active layer deposition was carried out by a double step method. The lead iodide solution (PbI2 in DMF, 460 mg/ml heated at 60°C) was spin coated at 3000 rpm for 40 s with an air flow (Speed: 10 m3 s−1, Temperature: 25°C, Distance: 6 cm);[55] then, the samples were sintered for 20 min. in air at 70°C. The CH3NH3PbI3 crystallization was achieved by dip coating of the samples in a methylammonium iodide solution (CH_3NH_3I in anhydrous isopropanol, 10 mg/ml) for 30 min in air, with a subsequent annealing for 30 min carried out at 100 °C in air. A solution of Spiro-OMeTAD (61.4 mM) doped with 4-tert-butylpyridine (TBP, 26 mM) and Lithium Bis(Trifluoromethanesulfonyl)Imide (Li-TFSI, 55 mM) was deposited on the perovskite layer by spin-coating at 2000 rpm for 60 s in air and exploited as hole-transporting layer. The as

produced PSCs were then left in air overnight in a closed box containing silica desiccant[56]. The excess of perovskite and Spiro-OMeTAD, which during the spin coating deposition over the nc-TiO_2 have covered the photo-anodes FTO measuring pads, were removed using a CO_2 laser (λ=10.6 μm).Finally, an Au layer (100 nm), acting as counter electrode, was evaporated on the cells, in a high vacuum chamber (10−6mbar). The assembled PSCs were, then, sealed in air pressing square cut glass and thermoplastic over the devices at a pressure of 0.2 bar and a temperature of 95° C. Table 9 reports the list of the fabricated and tested devices. We decided to analyse different levels of deposition in order to assess the influence and effect of each layer on the final device.

3.2.3. Photophisical characterization:

3.2.3.1. Aborption spectra

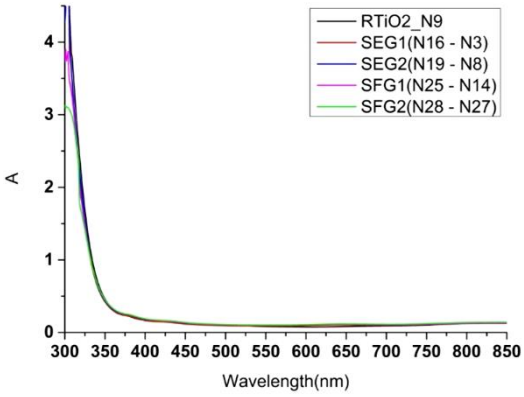

Figure. 20. Average absorbance of TiO_2 or TiO_2 Gr deposited layers. The absorbance of the substrates c-TiO_2c / nc-TiO_2, do not show significant differences in the absorption spectrum following the addition of a graphene doping in nc-TiO_2 layer.

The absorbance spectra of the substrates c-TiO_2 / nc-TiO_2, do not show significant differences in the absorption spectrum following the addition of a graphene doping in nc-TiO_2 layer Figure 20. This means that at this deposition layer, the graphene does not interfere with the processes of absorption of the device. The minimum reliably wavelength for the reported spectrum is 350nm as to shorter wavelengths of the substrate glass begins to absorb UV radiation. The reported spectra are the result of the average of the absorption spectra of the samples sent in duplicate.

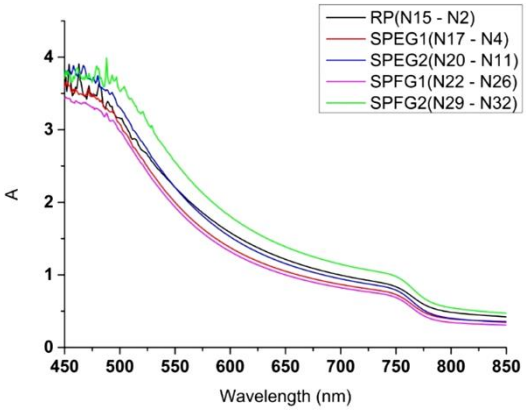

Figure. 21 Average absorbance of Perovskite-TiO_2 or TiO_2-Gr deposited layers. The absorbance of the substrates show that Graphene can Interact with the Perovskite layer. This can be seen from an increment in the absorption spectra of the samples that was not noted in the nc-TiO_2-Gr layer.

The absorption spectra of the samples containing the perovskite layer (right Figure) show the typical bands of the material. In particular, due to the high content of graphene samples (SPEG2 and SPFG2), it is possible to see: 1)an increment of the absorption band with decreasing wavelength, 2)a more abrupt sigmoid in correspondence with the characteristic peak of the perovskite at 750nm. Since the substrates containing doped titanium showed no abnormalities (Figure18), further insights are needed to understand the nature of this electronic interaction.

3.2.3.2. Photoluminescence (PL) measurements

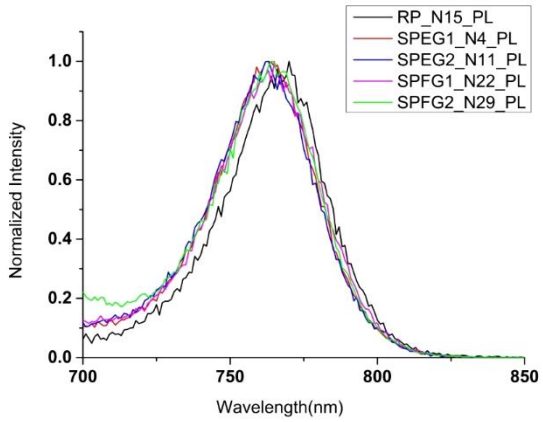

Figure. 22 The PL spectra of the samples and references

The photoluminescence spectra were normalized to compare the spectral shape. **The presence of graphene, in all analyzed samples, bring a blue-shift in the PL of the perovskite.** This certainly means that the presence of graphene leads to a recombination between

electron and the hole which are located at higher energies. The mechanism by which this phenomenon occurs is to be checked.

3.2.3.3. Time Resolved Emission Spectra (TRES): PL lifetime

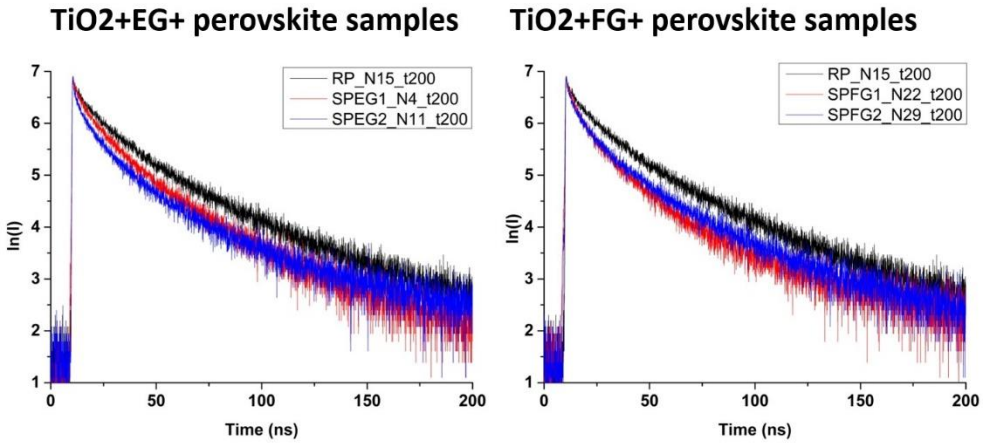

Figure. 23 Photoluminescence lifetime in the nanoseconds time scale

Time resolved Photoluminescence decays showed that the presence of graphene (both EG that FG) leads to a decrease in the average life time of the charge carriers, favoring the migration to the device electrodes. The processing of life times, on a scale of 200 ns, can be identified as a tri-exponential trend. The decays showed in Figure 23 can be fitted with a multi-exponential decay in order to calculate the kinetic constant responsible of the each decay pathway. The fitting equation is (Eq.22):

$$Fit = A + B_1 e^{(-t/\tau_1)} + B_2 e^{(-t/\tau_2)} + B_3 e^{(-t/\tau_3)}$$

As can be seen from Table 10, the time of the three processes (τi) considered remains more or less equal, but what changes is the weight (Bi) of such decays on the overall process. This last parameter gives an idea of the preferential relaxation pathway of the composite. Table 10 reports also the fitting parameters χ^2. This parameter show the accurancy of the mathematical fit; closer is its value to 1 better is the mathematical fit.

3.2.3.4. Average PL lifetime

The average decay time <τ> is the final evaluation parameter of the analysis (Eq.23):

$$\langle \tau \rangle = \sum_{i=3}^{i=0} B_i \tau_i$$

A lower average lifetime may imply an increase in the performance of the PV cell because of an electron transfer. The SPFG1 and SPEG2 samples show a decrease in mean life time of about 10 ns with respect of R-P, see Table 10, which results in an increase in performance + 30% in charge extraction/transport of the device.

Table 10 Results of the fitting of the PL lifetime, following Eq.22. from the first to the last column: lifetimes of the multi exponential decay, pre-exponential parameters(Bi,A), accuracy parameter, and average lifetime(following Eq 23)

Sample	τ_i	B_i	A	X^2	<τ>
R-P	4.1477	245.3140	1.7340	1.1230	**29.9**
	25.3316	474.9340			
	74.8168	187.9430			
SPEG1	5.1184	278.4730	1.5380	1.1040	**21.9**
	20.9157	488.2100			
	62.4583	126.2940			
SPEG2	3.3924	353.7420	4.8210	1.1370	**20.8**
	18.9579	373.7280			
	90.0400	98.9490			
SPFG1	6.0112	373.9180	1.7680	1.1580	**20.2**
	23.8371	417.722			
	72.2826	72.1370			
SPFG2	5.1113	388.1520	1.6700	1.1130	**21.7**
	24.1448	403.6460			
	79.9865	93.1270			

3.2.3.5. Time Resolved Emission Spectroscopy (TRES) mapping

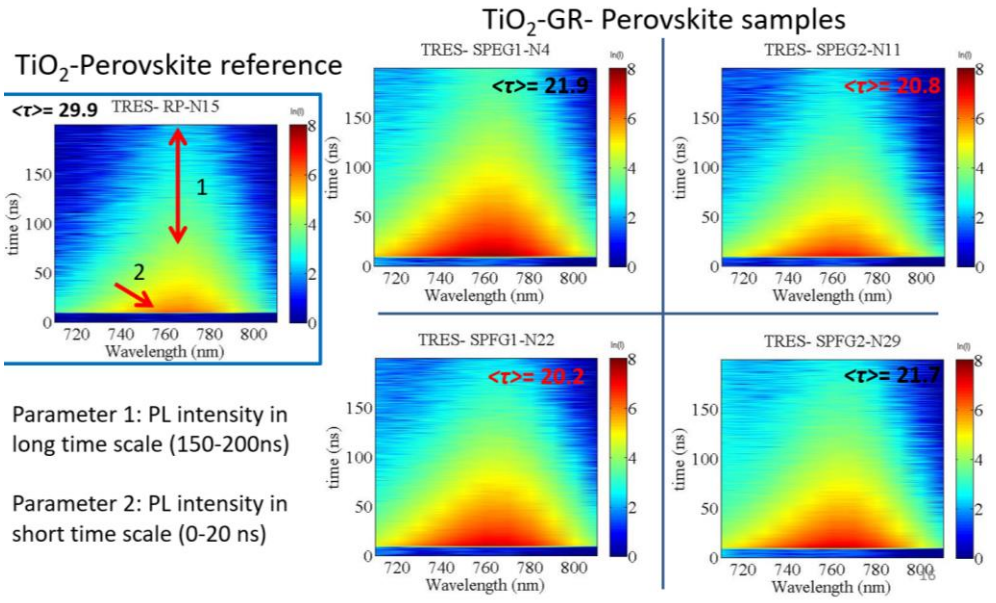

Figure. 24 Time Resolved Emission Spectroscopy (PL lifetime on multiple wavelength) for all the samples.

In order to have a precise behavior of the substrate in the range between700 and 850 nm, we did a study of photoluminescence decay on multiple wavelength. The parameters that revealed the efficiency in electron extraction are the ones marked with the red arrows in figure 24: 1) PL intensity in long time scale (150-200ns), 2) PL intensity in short time scale (0-20 ns). Those parameters allow to understand how fast is the process of electron transfer from the perovskite to TiO_2-GR layer. As it is possible to see, the maps in Figure 24 reveals that for the reference sample we have a low intensity in the region 2, but high intensity in longer time scale. For the Gr doped sample, considering both effects on region 1 and 2, the most promising samples are the one already detected with the single wavelength analysis.

3.2.4. Characterization of the final PV device

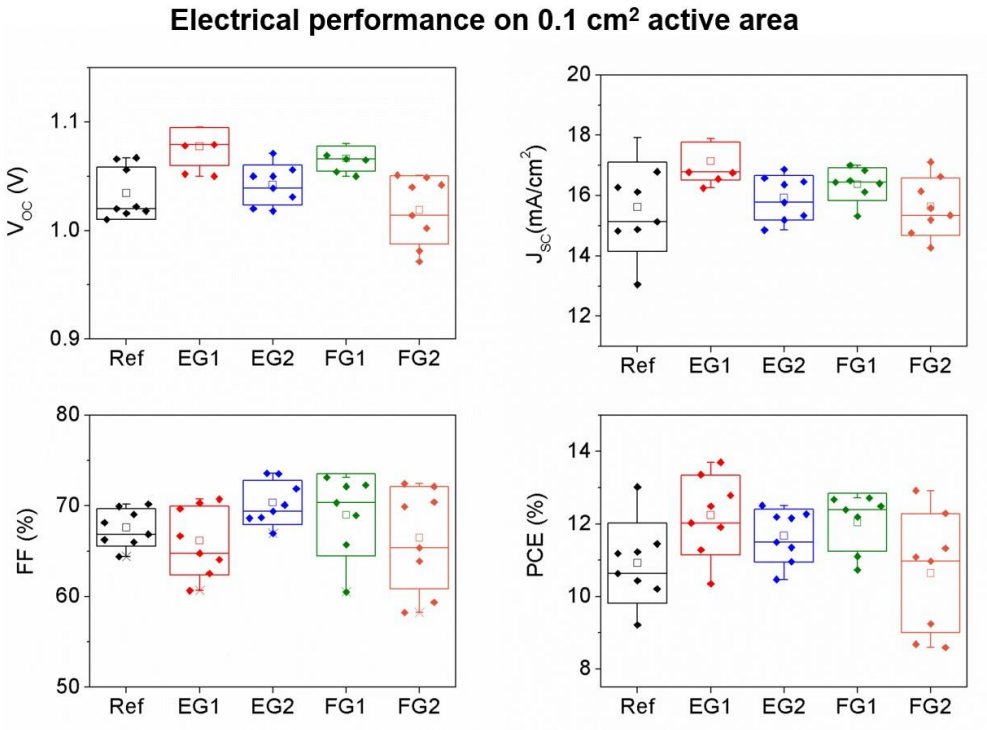

Figure. 25 open circuit voltage (Voc), short circuit current density (Jsc), fill factor (FF) and PCE of all the devices EG and FG based with different doping amounts.

Figure25 reports the statistics on the PV performances of the as-produced PSCs exploiting the different graphene dopings. The PV performances: open circuit voltage (Voc), short circuit current density (Jsc), fill factor (FF) and PCE, clearly indicate that **electrochemically exfoliated graphene seems most promising in term of device's PCE**. Is it possible to notice that the PCE increase with respect to the graphite exfoliation and a **lower graphene concentration (1% in vol.) is preferred** to higher concentration (10% in vol.).

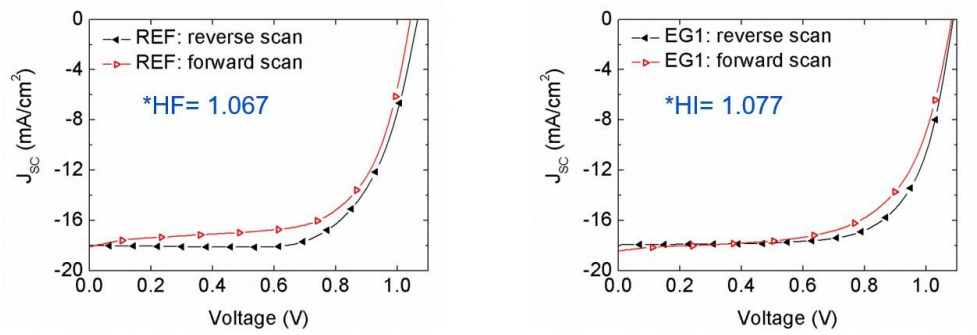

Figure. 26 I/V curves of solar cells selected for the 1987 h endurance test.

The I/V curves and PV figures of merit for the PSCs, as prepared and after the 1987 h endurance test, are reported in Figure 26. The Hysteresis Factor (HF) is calculated ad PCE(rev.scan)/PCE(forw.scan). HF with and without EG1 TiO_2 doping did not undergo significant change.

3.2.4.1. Parameters for: Solar cells endurance test, Electrical characterization and Open circuit voltage decay

Solar cells endurance test tests were carried out in two different conditions and timeframes. The first test was based on 138 h ISOS-D-1 shelf life ageing test protocol carried out on unsealed PSCs [57]. For the test, the PSCs were left in dark, at ambient temperature and Relative Humidity (R.H.), in open circuit load conditions. After the sealing procedure, reported in Section Solar cells encapsulation, the cells were tested in ISOS-D-1 shelf life ageing protocol conditions for a total of 1987 h. Moreover, the cells were subjected to ISOS-L-2 Laboratory weathering [57]light soaking endurance test under continuous 1 Sun (C class, Sunirad C-65, Solaronix) at 65°C, at ambient R.H. for 120 h. **Electrical characterization**. The PSCs substrates were masked using black scotch tape with 5mm × 2mm windows to avoid the overestimation of the performance due to the diffused light irradiation entering the sides of the cell through the surrounding glass. In this configuration, only the direct light contributed to the measured PV performance. The latter were determined by reverse voltage scan in air under a solar simulator (ABET Sun 2000, class A) at AM 1.5 and 100mW/cm2 illumination conditions, calibrated with a certified

reference Si Cell (RERA Solutions RR-1002). Incident power was measured with a Skye SKS 1110 sensor. The class of the sun simulator was measured with a BLACK-Comet UV–vis Spectrometer. **Open circuit voltage decay measurements** were performed with a white led (3 W-4200K luxeon star) supplied from a constant current driver (Newport mod. 505b). The voltage of the sample was acquired with a high speed digitizer (PXI 5922 National Instruments).

3.2.5. Concluding remarks on Secion 3.2: Pervskite solar cells (PSC) with TiO_2:graphene nanocomposites

What we manage to see is that the versatility of pristine graphene was especially exploited for charge extraction. The presence of graphene leads to a decrease in the average life time of the charge carriers, promoting their migration to the electrodes of the device. Show the photoluminescence life-time decay of Ref (reference without graphene), SPFG1 and SPEG2 samples (which contains two different graphene doping level). **The presence of a graphitic honeycomb structure produces a decrease in the average life time of about 10 ns, which is an increment of +30%, that means a faster the charge transfer in the system.** The significant enhancement of device performance are evidenced, attributed to the natural ability of graphene for charge transport and/or to favourable interfacial charge transfer with the involved materials.

To sum up:

1. Graphene doping of mTiO_2 layer lead to an improved charge injection at the PE.
2. Electrochemically exfoliated graphene seems most promising in term of device's PCE increase with respect to the graphite exfoliation;
3. A lower graphene concentration (1% in vol.) is preferred to higher concentration (10% in vol.);
4. mTiO_2 graphene doping can be further optimized by slightly change the doping concentration.

3.3. Bibliography chapter 3

[1] B. R. 2015 P. T. and G. Markets, "BCC Research 2015 Photocatalysts: Technologies and Global Markets http://www.bccresearch.com/market-research/advanced-materials/photocatalyststechnologies-markets-report-avm069b.html (accessed 4 Apr 2016)," *http//www.bccresearch.com/market-research/advanced-materials/photocatalyststechnologies-markets-report-avm069b.html (accessed 4 Apr 2016)*.

[2] M. Chen and J. W. Chu, "NOx photocatalytic degradation on active concrete road surface - from experiment to real-scale application," *J. Clean. Prod.*, vol. 19, no. 11, pp. 1266–1272, 2011.

[3] M. Delnavaz, B. Ayati, H. Ganjidoust, and S. Sanjabi, "Kinetics study of photocatalytic process for treatment of phenolic wastewater by TiO2 nano powder immobilized on concrete surfaces," *Toxicol. Environ. Chem.*, vol. 94, no. 6, pp. 1086–1098, 2012.

[4] H. Dylla, M. M. Hassan, M. Schmitt, T. Rupnow, and L. N. Mohammad, "Laboratory Investigation of the Effect of Mixed Nitrogen Dioxide and Nitrogen Oxide Gases on Titanium Dioxide Photocatalytic Efficiency in Concrete Pavements," *J. Mater. Civ. Eng.*, vol. 23, no. 7, pp. 1087–1093, 2011.

[5] M. Fleisch and D. Bahnemann, "Photocatalitically Active Concrete: How Innovative Construction Materials Can Contribute to the Degradation of Dangerous Air Pollutants," *Beton- Und Stahlbetonbau*, vol. 112, pp. 47–53, 2017.

[6] M. M. Hassan, "Quantification of the Environmental Benefits of Ultrafine/Nanotitanium Dioxide Photocatalyst Coatings for Concrete Pavement Using Hybrid Life-Cycle Assessment," *J. Infrastruct. Syst.*, vol. 16, no. 2, pp. 160–166, 2010.

[7] http://www.italcementigroup.com/ITA/Ricerca+e+Innovazione/Prodotti+Innovativi/TX+Active/, "No Title."

[8] M. Janus, J. Zatorska, K. Zajac, E. Kusiak-Nejman, A. Czyzewski, and A. W. Morawski, "Study of nitric oxide degradation properties of photoactive concrete containing nitrogen and/or carbon co-modified titanium dioxide - preliminary findings," *Micro Nano Lett.*, vol. 11, no. 5, pp. 231–235, 2016.

[9] P. Kovar, Z. Lacny, J. Prikryl, and V. Matejka, "The Route for the Decreasing of Air Pollutants Using Photocatalysis over Titanium Dioxide Incorporated in to Different Kinds of Concrete Surfaces," *Iv Czech-Slovak Sci. Conf. Transp. Heal. Environ.*, pp. 133–138, 2010.

[10] R. K. Nath, M. F. M. Zain, A. A. H. Kadhum, and R. Alam, "Mixed Photocatalyst for

Sustainable Concrete Construction," in *Advanced Materials Engineering and Technology*, vol. 626, M. M. A. Abdullah, L. Jamaludin, R. A. Razak, Z. Yahya, and K. Hussin, Eds. 2012, p. 39–+.

[11] D. Osborn, M. Hassan, S. Asadi, and J. R. White, "Durability Quantification of TiO2 Surface Coating on Concrete and Asphalt Pavements," *J. Mater. Civ. Eng.*, vol. 26, no. 2, pp. 331–337, 2014.

[12] F. Pacheco-Torgal and S. Jalali, "Nanotechnology: Advantages and drawbacks in the field of construction and building materials," *Constr. Build. Mater.*, vol. 25, no. 2, pp. 582–590, 2011.

[13] C. S. Poon and E. Cheung, "NO removal efficiency of photocatalytic paving blocks prepared with recycled materials," *Constr. Build. Mater.*, vol. 21, no. 8, pp. 1746–1753, 2007.

[14] A. M. Ramirez, K. Demeestere, N. De Belie, T. Mantyla, and E. Levanen, "Titanium dioxide coated cementitious materials for air purifying purposes: Preparation, characterization and toluene removal potential," *Build. Environ.*, vol. 45, no. 4, pp. 832–838, 2010.

[15] R. Zouzelka and o Chemagazin s r, "THE PHOTOCATALYTIC ABATEMENT OF NOX IMISSIONS USING COMMERCIAL FUNCTIONAL COATING WITH POROUS MORPHOLOGY," *Ix. Konf. Pigment. a Pojiva*, pp. 19–21, 2016.

[16] A. Folli, U. H. Jakobsen, G. L. Guerrini, and D. E. Macphee, "Rhodamine B Discolouration on TiO2 in the Cement Environment: A Look at Fundamental Aspects of the Self-cleaning Effect in Concretes," *J. Adv. Oxid. Technol.*, vol. 12, no. 1, pp. 126–133, 2009.

[17] A. Folli, C. Pade, T. B. Hansen, T. De Marco, and D. E. Macphee, "TiO2 photocatalysis in cementitious systems: Insights into self-cleaning and depollution chemistry," *Cem. Concr. Res.*, vol. 42, no. 3, pp. 539–548, 2012.

[18] Y. Lai *et al.*, "Recent Advances in TiO2-Based Nanostructured Surfaces with Controllable Wettability and Adhesion," *Small*, vol. 12, no. 16, pp. 2203–2224, 2016.

[19] S. N. Zailan, N. Mahmed, M. M. A. Abdullah, A. Victor Sandu, and N. F. Shahedan, "Review on Characterization and Mechanical Performance of Self-cleaning Concrete," in *Engineering Technology International Conference 2016*, vol. 97, M. A. B. Abdullah, S. Z. AbdRahim, M. E. M. Suandi, M. N. M. Saad, and M. F. Ghazali, Eds. 2017.

[20] G. Husken, M. Hunger, and H. J. H. Brouwers, "Experimental study of photocatalytic concrete products for air purification," *Build. Environ.*, vol. 44, no. 12, pp. 2463–2474, 2009.

[21] H. S. Müller, E. Bohner, and M. Vogel, "Repair of architectural concrete and related modelling of carbonation-induced corrosion," 2009.

[22] C. Yu, W. Zhou, H. Liu, Y. Liu, and D. D. Dionysiou, “Design and fabrication of microsphere photocatalysts for environmental purification and energy conversion,” *Chem. Eng. J.*, vol. 287, pp. 117–129, 2016.

[23] A. H. Mamaghani, F. Haghighat, and C.-S. Lee, “Photocatalytic oxidation technology for indoor environment air purification: The state-of-the-art,” *Appl. Catal. B Environ.*, vol. 203, pp. 247–269, 2017.

[24] J. S. Dalton, P. A. Janes, N. G. Jones, J. A. Nicholson, K. R. Hallam, and G. C. Allen, “Photocatalytic oxidation of NOx gases using TiO2: a surface spectroscopic approach,” *Environ. Pollut.*, vol. 120, no. 2, pp. 415–422, 2002.

[25] T. Xia *et al.*, “Comparison of the abilities of ambient and manufactured nanoparticles to induce cellular toxicity according to an oxidative stress paradigm,” *Nano Lett.*, vol. 6, no. 8, pp. 1794–1807, 2006.

[26] M. R. Hoffmann, S. T. Martin, W. Choi, and D. W. Bahnemann, “Environmental applications of semiconductor photocatalysis,” *Chem. Rev.*, vol. 95, no. 1, pp. 69–96, 1995.

[27] http://www.cnchemicals.com/Press/88893-CCM:%20TiO2%20price%20in%20China%20still%20booming%20in%20December%202016.html., “No Title.”

[28] A. L. Linsebigler, G. Lu, and J. T. Yates Jr, “Photocatalysis on TiO2 surfaces: principles, mechanisms, and selected results,” *Chem. Rev.*, vol. 95, no. 3, pp. 735–758, 1995.

[29] C. Tuchinda, S. Srivannaboon, and H. W. Lim, “Photoprotection by window glass, automobile glass, and sunglasses,” *J. Am. Acad. Dermatol.*, vol. 54, no. 5, pp. 845–854, 2006.

[30] X. Chen and S. S. Mao, “Titanium dioxide nanomaterials: synthesis, properties, modifications, and applications,” *Chem. Rev*, vol. 107, no. 7, pp. 2891–2959, 2007.

[31] A. Fujishima, X. Zhang, and D. A. Tryk, “TiO2 photocatalysis and related surface phenomena,” *Surf. Sci. Rep.*, vol. 63, no. 12, pp. 515–582, 2008.

[32] N. Serpone, D. Lawless, and R. Khairutdinov, “Size effects on the photophysical properties of colloidal anatase TiO2 particles: size quantization versus direct transitions in this indirect semiconductor?,” *J. Phys. Chem.*, vol. 99, no. 45, pp. 16646–16654, 1995.

[33] C. Walgraeve, K. Demeestere, J. Dewulf, K. Van Huffel, and H. Van Langenhove, “Diffusive sampling of 25 volatile organic compounds in indoor air: Uptake rate determination and application in Flemish homes for the elderly,” *Atmos. Environ.*, vol. 45, no. 32, pp. 5828–5836, 2011.

[34] J. V Gómez, F. E. Sandnes, and B. Fernández, “Sunlight intensity based global

positioning system for near-surface underwater sensors," *Sensors*, vol. 12, no. 2, pp. 1930–1949, 2012.

[35] C. Pepe and G. L. Guerrini, "Cement compositions with a high photocatalytic power and an improved rheology." Google Patents, 29-Jan-2009.

[36] R. Ancora, M. Borsa, and L. Cassar, "Titanium dioxide based photocatalytic composites and derived products on a metakaolin support." Google Patents, 02-Jul-2009.

[37] M. Rastogi and R. Vaish, "Visible light induced water detoxification through Portland cement composites reinforced with photocatalytic filler: A leap away from TiO2," *Constr. Build. Mater.*, vol. 120, no. Supplement C, pp. 364–372, 2016.

[38] B. C. Pokroy A; Capone, C; De Notarpietro, G; Goisis, M; Molfetta, M; Zerbetto, F; Falini, G; Calvaresi, M; Motalti, M; Guidetti, G., "Compositions with increased photocatalytic activity," vol. EP3216771. Patent , 2017.

[39] Y. ; Z. Zhu Z., "Patent Application CN104446594 ," *Patent*, vol. CN10444659, 2015.

[40] I. Q. and answers on photocatalytic Products, "No Title," *http://www.italcementigroup.com/NR/rdonlyres/6E200E8B-19FA-4986-BA3C-51938F166822/0/Q_A_TX_xBiennale_UK.pdf*.

[41] A. C. Ferrari *et al.*, "Science and technology roadmap for graphene{,} related two-dimensional crystals{,} and hybrid systems," *Nanoscale*, vol. 7, no. 11, pp. 4598–4810, 2015.

[42] F. Bonaccorso, A. Lombardo, T. Hasan, Z. Sun, L. Colombo, and A. C. Ferrari, "Production and processing of graphene and 2d crystals," *Mater. Today*, vol. 15, no. 12, pp. 564–589, 2012.

[43] Y. Hernandez *et al.*, "High-yield production of graphene by liquid-phase exfoliation of graphite.," *Nat. Nanotechnol.*, vol. 3, no. 9, pp. 563–8, Sep. 2008.

[44] V. Leon *et al.*, "Few-layer graphenes from ball-milling of graphite with melamine," *Chem. Commun.*, vol. 47, no. 39, pp. 10936–10938, 2011.

[45] M. Quintana, E. Vazquez, and M. Prato, "Organic Functionalization of Graphene in Dispersions," *Acc. Chem. Res.*, vol. 46, no. 1, SI, pp. 138–148, 2013.

[46] V. Leon, A. M. Rodriguez, P. Prieto, M. Prato, and E. Vazquez, "Exfoliation of Graphite with Triazine Derivatives under Ball-Milling Conditions: Preparation of Few-Layer Graphene via Selective Noncovalent Interactions," *ACS Nano*, vol. 8, no. 1, pp. 563–571, 2014.

[47] M. Yi and Z. Shen, "A review on mechanical exfoliation for the scalable production of graphene," *J. Mater. Chem. A*, vol. 3, no. 22, pp. 11700–11715, 2015.

[48] K. R. Paton *et al.*, "Scalable production of large quantities of defect-free few-layer

graphene by shear exfoliation in liquids," *Nat. Mater.*, vol. 13, no. 6, pp. 624–630, 2014.

[49] G. Guidetti, A. Cantelli, R. Mazzaro, L. Ortolani, V. Morandi, and M. Montalti, "Tracking graphene by fluorescence imaging: a tool for detecting multiple populations of graphene in solution," *Nanoscale*, vol. 8, no. 16, pp. 8505–8511, 2016.

[50] L. Guardia, J. I. Paredes, R. Rozada, S. Villar-Rodil, A. Martínez-Alonso, and J. M. D. Tascón, "Production of aqueous dispersions of inorganic graphene analogues by exfoliation and stabilization with non-ionic surfactants," *Rsc Adv.*, vol. 4, no. 27, pp. 14115–14127, 2014.

[51] A. L. Palma *et al.*, "Reduced graphene oxide as efficient and stable hole transporting material in mesoscopic perovskite solar cells," *Nano Energy*, vol. 22, no. Supplement C, pp. 349–360, 2016.

[52] A. Agresti *et al.*, "Graphene–Perovskite Solar Cells Exceed 18 % Efficiency: A Stability Study," *ChemSusChem*, vol. 9, no. 18, pp. 2609–2619, 2016.

[53] F. Matteocci *et al.*, "Blocking layer optimisation of poly(3-hexylthiopene) based Solid State Dye Sensitized Solar Cells," *Org. Electron.*, vol. 14, no. 7, pp. 1882–1890, 2013.

[54] M. Abd-Ellah *et al.*, "Hierarchical Tin Oxide Nanostructures for Dye-Sensitized Solar Cell Application," *Adv. Electron. Mater.*, vol. 1, no. 9, 2015.

[55] K. Wojciechowski, M. Saliba, T. Leijtens, A. Abate, and H. J. Snaith, "Sub-150 C processed meso-superstructured perovskite solar cells with enhanced efficiency," *Energy Environ. Sci.*, vol. 7, no. 3, pp. 1142–1147, 2014.

[56] F. Di Giacomo *et al.*, "High efficiency CH3NH3PbI(3−x)Clx perovskite solar cells with poly(3-hexylthiophene) hole transport layer," *J. Power Sources*, vol. 251, no. Supplement C, pp. 152–156, 2014.

[57] M. O. Reese *et al.*, "Consensus stability testing protocols for organic photovoltaic materials and devices," *Sol. Energy Mater. Sol. Cells*, vol. 95, no. 5, pp. 1253–1267, 2011.

4.FUNDAMENTAL STUDY ON GRAPHENE

Production of graphene via exfoliation of graphite flakes is one of the easiest and cheapest way to get it. Surfactants can be exploited to obtain “green” dispersions of graphene (G) in water media, and in particular non-ionic surfactants, like Pluronics, were demonstrated to yield particularly high fraction of exfoliated material[1] However presence of the surfactants strongly affect the surface properties of graphene and this kind of chemical production is often associated to the uncertainty above exfoliation quality. Unfortunately there are very few techniques to characterize directly size and thickness in solution, like liquid-state Raman spectroscopy, but they can’t assess the presence of surfactant on the top of graphene as far as describe the dynamic behaviour carbon materials of the solution. Furthermore, most methods used for the characterization of graphene produced by liquid phase exfoliation require the deposition of the liquid sample on a substrate and subsequent drying. Because of this or other post-synthetic treatments, becomes questionable the reliability of the data in describing the actual features of the graphene particles in the pristine solution. Henceforth there is a need for new methods that permit the study of graphene directly in solution. Based on new designed fluorescent surfactants, in this chapter it is reported an easy, quick, innovative method to understand what’s really happens inside of the solution and the real dynamic interaction between G-sheet/surfactants and G-sheet/G-sheets. Exploiting the characteristics of the designed system, G-sheet/fluorescent surfactants we coupled Wide field Fluorescence Microscopy with a CCD camera to track graphene flakes motions and dynamics, going beyond the information provided by the study of the static system with fluorescence quenching microscopy (FQM) previously proposed by other authors[2]. Probe graphene Brownian motion permits to estimate some useful parameters like its velocity and hydrodynamic volume to understand: the dimension, motions and aggregation state of 2D sheets. Our present results demonstrate that those fluorescent surfactants can be exploited to bring enormous advantage for both characterization and design of new exfoliation pathways.

4.1. Liquid exfoliated graphene characterization tools

Graphene is a very versatile building block for the design of complex supramolecular system and nanostructured materials. To take advantage of its properties (eg conductivity, strength and surface area…) in luminescent systems, it is fundamental to study the interactions between graphene and photoactive molecules and materials. This first part of my research report is dedicated to the study that I carried on involving graphene and fluorescent dyes in liquid solution. At the beginning I started with the production of graphene (G) via exfoliation of graphite flakes. Ultrasound assisted exfoliation of graphite in liquid media is a convenient method for producing graphene[1], [3], [4]. Nevertheless, few experimental techniques are currently available to directly characterize the solution produced by liquid phase exfoliation [5]–[9], see Table 8. In this chapter is reported a new method for characterizing liquid phase exfoliated graphene based on fluorescence imaging and graphene particles tracking. This technique will permit to perform the simultaneous detection of a large number of particles directly on the sample produced (avoiding any post-treatment, e.g. dilution)[10].

Table 1 Pros and Cons of the currently available techniques to characterize exfoliated graphene suspensions.

Technique	Pros	Cons	Ref
Optical absorption spectroscopy	• Can be performed on solution. • Information on the concentration of suspended graphitic material	• no direct information about the dimensions of the carbon particles	[11]
TEM	• Number and dimensions of graphene layers	• It is expensive and not suitable for industrial routine characterization since it requires the manual counting of the edges of the flakes. • Samples need to be dried and treated, and hence potentially altered, before observation	[12], [13]

Atomic force microscopy (AFM)	• Estimation of the height of the deposited flakes: number and dimensions of graphene layers	• Samples need to be dried and treated. •	[14]
Elastic light scattering (Rayleigh) spectroscopy	• Determination of the number of graphene layers	• deposition of the samples on optimized substrates	[15]
Raman spectroscopy	• Can be applied to all graphene samples	• Detection of a Raman signal for individual carbon objects requires their immobilization by either substrate deposition or optical trapping.	[12], [16], [17]
Dynamic light scattering (DLS) analysis	• Can be performed directly on graphene suspensions	• No details of the features of the individual flakes. • Results for poly-dispersed or light absorbing samples can be ambiguous or unreliable	[18]
Optical microscopy	• Can be performed directly on graphene suspensions • Use of a conventional fluorescence microscopy set-up.	• Is not suitable for detecting and simultaneously tracking a large population of particles since there is no sufficient optical contrast objects/background.	[2]
Fluorescence microscopy	• Can be performed directly on graphene suspensions • Use of a conventional fluorescence microscopy set-up.	• Graphene sheets and platelets have not been reported to be photoluminescent, hence they cannot be directly observed by fluorescence microscopy	[19]
Fluorescence microscopy(This work)	• Possibility of using this method to identify two different populations of graphene particles with different sizes and levels of aggregation • Visualizing and tracking liquid phase exfoliated graphene directly in solution in an "as prepared" sample.	• More sophisticated parameters such as the particle aspect ratio and thickness needs to be developed	[10]

	• Use of a conventional fluorescence microscopy set-up.		

4.2. Production of Liquid Exfoliated Graphene

Differently from carbon dots[20]–[23] and graphene oxide[24], [25] that show relevant fluorescence, large graphene sheets and platelets have not reported to be photoluminescent, hence they cannot directly be observed by fluorescence microscopy[19]. On the other hand stable aqueous dispersions of graphene are typically prepared in the presence of surfactants[26]–[28]and the interaction with the exfoliating moieties has been exploited to functionalize graphene[29].

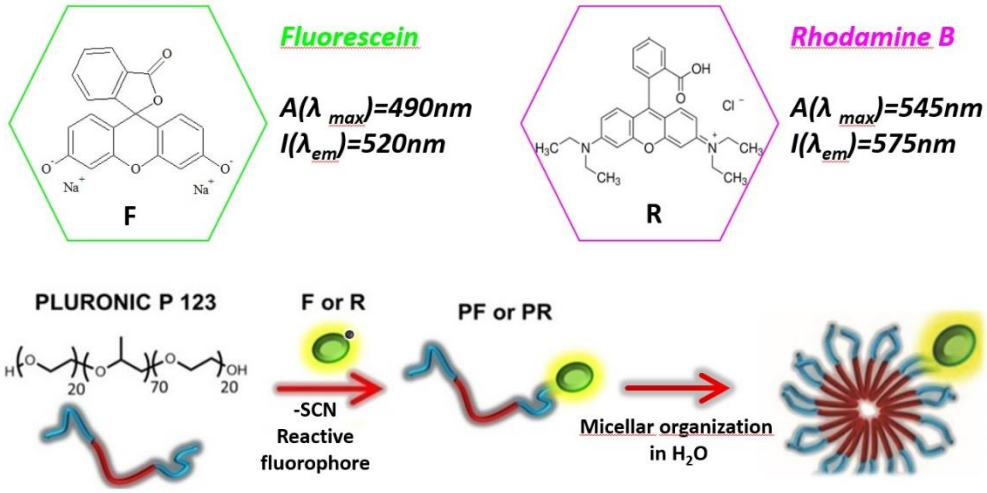

Figure. 1 Up, fluorophore used for the production of Pluronic fluorescent surfactant, and their photophysical characteristics. Scheme of the reaction of the functionalization.

Fluorescent graphene suspensions can be obtained by the functionalization of a small fraction (~0.5% mol mol^{-1}) of the neutral surfactant Pluronic P123 (P)[30], [31] with organic fluorophores: fluorescein isothiocyanate (F) or rhodamine isothiocyanate (R) to give PF and PR respectively, see Figure 1. Then we used PR or PF to exfoliate graphite[27], see Figure 2,obtaining G-PR and G-PF respectively. Besides, we prepared three reference graphene

samples obtained by exfoliating graphite with P in the presence of: (i) no fluorophores (G-P), (ii) fluorescein F (4.4 µM) (G-P + F) or (iii) rhodamine R (4.4 µM) (G-P + R), see Figure 2.

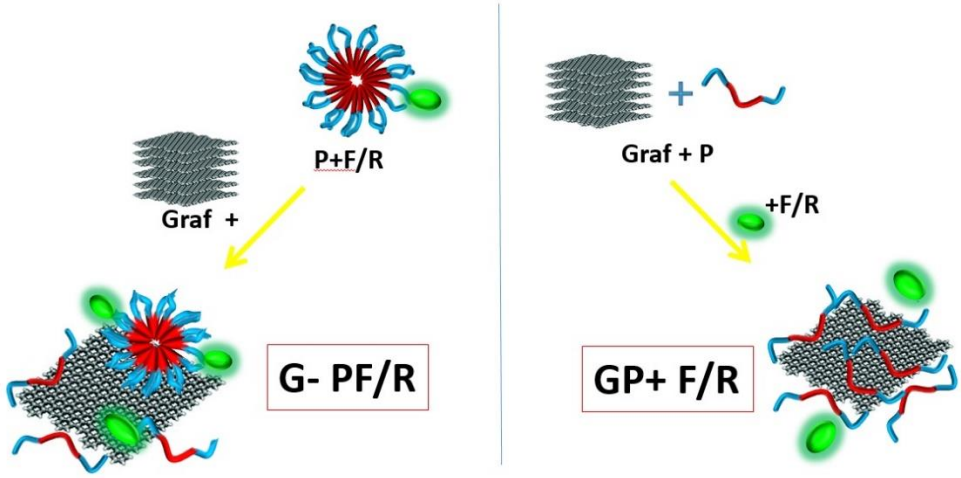

Figure. 2 Scheme of the systems produced and studied in this work.

In order to perform the synthesis all the reagents were purchased from Sigma-Aldrich and used as received. In particular exfoliation was performed in Millipore water using graphite flakes G (332461 ALDRICH) and Pluronic® P-123 (P) surfactant purchased from Sigma–Aldrich (product code: 435465 ALDRICH). To obtain fluorescent surfactants the fluorophores: tetraethyl rhodamine-5-(and 6) Isothiocyanate (R; RBITC; Product: 283924 Aldrich) and fluorescein isothiocyanate isomer I (F; FITC; Product: F7250 Sigma) were purchased from Sigma–Aldrich. Going into detail in the synthetic step, fluorescent surfactants PF an PR prepared using a solvent free approach. In particular for synthesizing PF the surfactant P (2000 mg, 0.35 mmol) was mixed with F (0.7 mg, 0.002 mmol) in a mortar for 10 minutes. Mixture was then introduced in a hoven at 120 °C for 1 hour. The product was purified by size-exclusion chromatography to remove the unreacted fluorophores. PR was synthesized following the same procedure reported above for PF starting from P (2000 mg, 0.35 mmol) and R (0.9 mg, 0.002 mol). Furthermore, graphene water dispersions (10 mL sample volume in cylindrical vials) were prepared according to the method proposed by Guardia et al[27]. In particular 10 mg of graphite G were suspended in 10 ml ultrapure water in the presence of the surfactant (0.5%w/v). The mixture was first vortexed at 500 rpm for 30 minutes and then sonicated for 4 hours (ELMA TRANSSONIC T 460/H – 35 KHz

frequency Elma GmbH & Co KG) at 40 °C. Additionally, the mixture was handy stirred every hour. After settling overnight (15 hours) the upper 70% of the suspension were collected and analysed. After investigating in detail the interactions between the fluorescent surfactants and graphene we demonstrated the possibility of detecting, tracking and characterizing graphene in the suspensions produced.

4.3. Characterization

4.3.1. Absorption measurements

We investigated the photophysical properties of these samples just to study the interaction between the fluorescent moieties and the carbon structures.

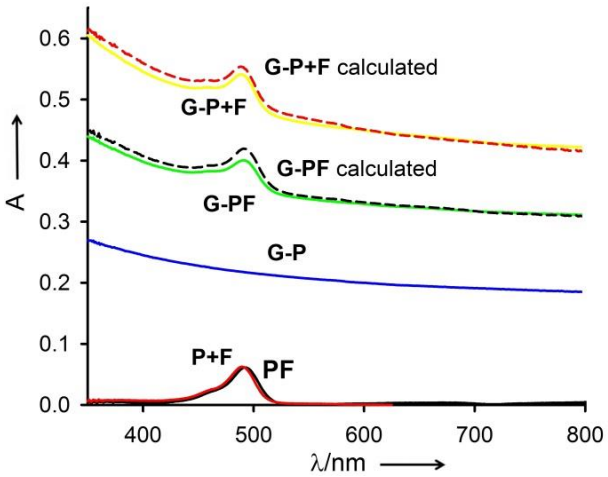

*Figure. 3 Absorption spectra of the fluorescent surfactant **PF** 0.5% w/w in water and of a solution of Pluronic P 123 0.5% w/w and fluorescein 4.4 µM (**P+F**). Absorption spectra of the graphene dispersions (**G-P**, **G-PF**, **G-P+F**) compared with the spectra calculated in the case of no ground state interaction between the components.*

UV-VIS absorption spectra were recorded at 25°C by means of Cary 300 UV-Vis spectrophotometer (Agilent Technologies). Figure 3 reports the reference sample G-P together with the samples containing fluorescein. The absorption spectra of the starting solutions PF and P+F adding the spectrum of exfoliated graphene G-P (Figure 3, calculated spectra). match those of G-PF and G-P + F. Because of this spectral matching, it is possible to say that **the interaction of fluorescein chromophore with graphene is weak in the ground state**[20].

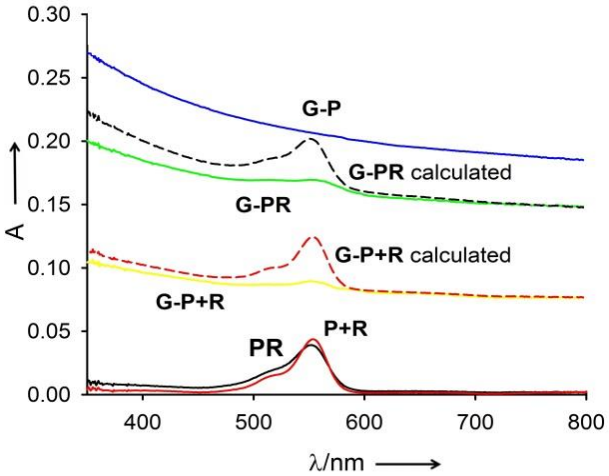

*Figure. 4 Absorption spectra of the fluorescent surfactant **PR** 0.5% w/w in water and of a solution of Pluronic P 123 0.5% w/w and rhodamine 0.5 µM (**P+R**). Absorption spectra of the graphene dispersions (**G-P**, **G-PF**, **G-P+F**) compared with the spectra calculated in the case of no ground state interaction between the components.*

In the case of the rhodamine samples a different comportment was observed. The contribution from the rhodamine band to the absorption spectra of the graphene containing samples G-PR and G-P + R is much lower than that expected from the combination of the spectra of the reference samples PR, P+R and P-G. this means that **the interaction between the rhodamine and graphene is a strong ground state interaction**. A possible explanation of this phenomenon can be the direct adsorption of the dye onto the carbon surface.

4.3.2. Emission measurements

With a Horiba Fluoromax-4 spectrofluorimeter the fluorescence spectra were recorded in disposable polystyrene cuvettes with optical path length of 1 cm (used for both absorbance and emission measurements).

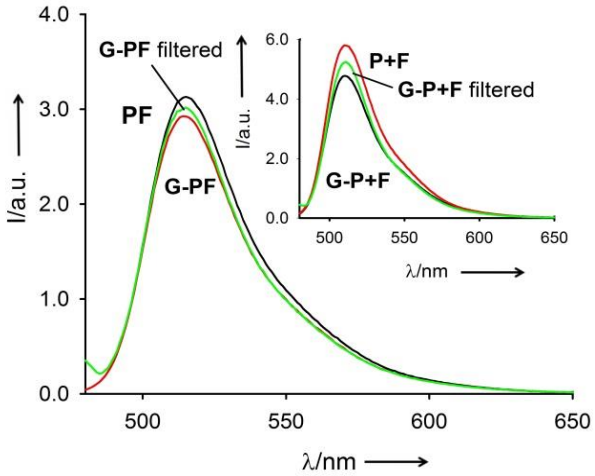

Figure. 5 Fluorescence spectra of the fluorescent surfactant PF 0.5% w/w in water and of sample G-PF before and after filtration (λexc=490 nm). Inset) Fluorescence spectra of Pluronic P 123 0.5% w/w and fluorescein 4.4 μM (P+F) in water and of sample G-P+F before and after filtration (λexc=490 nm).

Fluorescein can be excited at the wavelength of λexc = 490 nm. Though the excitation of F based samples at the above mentioned wavelength it was possible to collect the fluorescence spectra, Figure 5.The graphene-containing samples G-PF and G-P + F showed a fluorescence intensities that are very close to those of the reference solutions PF and P+F respectively. This effect can be addressed to **two different phenomena**:

- the **G and F have a physical interaction**, by means of an adsorption phenomenon, **but no electronic interaction** between the excited chromophore and the carbon structure occurs;
- There is a **very small and negligible fraction of the dye adsorbed and quenched from G**, so that the solution keep on emit.

The filtration experiments confirms the second hypothesis since after graphene was removed from the samples G-PF and G-P + F, no significant decrease of the absorbance and fluorescence of fluorescein was detected (Fig. 5, filtered). Rhodamine can be efficiently excited at the wavelength λexc = 545 nm.

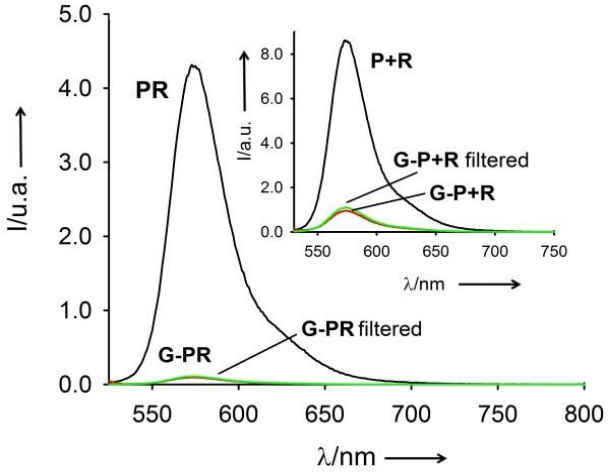

Figure. 6 Fluorescence spectra of the fluorescent surfactant PR 0.5% w/w in water and (in the inset) of a solution of Pluronic P 123 0.5% w/w and rhodamine 0.5 µM (P+R).

From fluorescent spectra of R based samples it is possible to notice that **R emission is strongly quenched (>90%) by graphene** in the case of both PR and P+R and no relevant decrease of the fluorescence was observed upon removal of the graphene by filtration. On the contrary to previous observations for fluorescein derivatives, the residual emission of rhodamine is due to a minor fraction of molecules that do not bind to graphene.

4.3.3. Fluorescence anisotropy measurements

The fluorescence anisotropy spectra were recorded with an Edinburgh FLS920 fluorimeter equipped with a photomultiplier Hamamatsu R928P.This measurement permit the investigation of the rotational mobility of fluorescent species dispersed in a viscous environment. The fluorescence anisotropy value (r) is a measure of the degree of polarization of the light emitted by a fluorophore upon polarized excitation. An higher r value with respect of the free dye means that the rotational diffusion of the emitter is slowed down. For instance when a fluorescent unit binds to a heavy structure with a large moment of inertia r value rise up[32].We found that a similar values of r (approximately 0.15) were measured for fluorescein in all the samples. This can be due to a predominant fraction of unbound fluorophores or a high local mobility of the chromophore due to the presence of Pluronic chain. However from the evidences noted wit absorption/emission spectra it

is possible to conclude that there is a very small and negligible fraction of the dye adsorbed and quenched from graphene. In the case of R it was not possible to perform this measurement since the solution was quenched.

4.3.4. Wide field Fluorescence microscopy

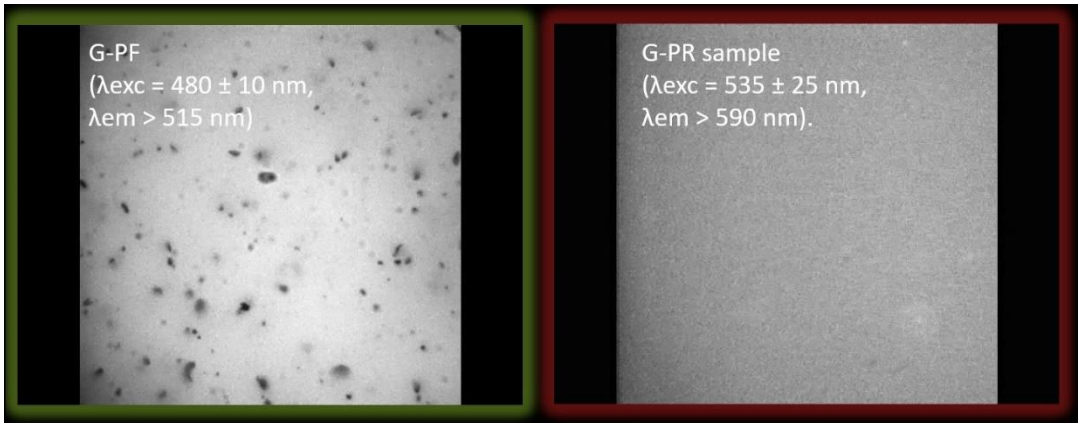

Figure. 7 Fluorescence microscopy images of samples G-PF (left) and G-PR (right). Inset the experimental parameters used for each image collection.

The average macroscopic behaviour of the surfactant–graphene system can be obtained from an optical microscopy measurement. A conventional optical microscope at high magnification (100×, using an Electron Multiplying charge-coupled device (EMCCD) camera Princeton Instruments, Photon Max 512 at 33 frames per second) can acquire images from few to several hundred nanometres carbon structures since they are expected to diffuse in an aqueous environment slowly enough to be observable. This is strictly dependent from the intensity of the signal of the particles (S) with respect to the background noise (N). A S/N ratio higher than 5 guarantees reliable tracking and image processing[33]. Just to investigate the actual performance of PF or PR as contrast agents for the optical tracking of graphene, we performed fluorescence imaging experiments [33]. Samples in the form of thin layers (0.11 ± 0.01 mm) of solutions are observed them with a wide-field fluorescence microscope an inverted microscope (Olympus IX71) equipped with a Xenon lamp for excitation. This set-up was equipped with an EMCCD camera. Electron Multiplying Charge Coupled Device EMCCD Camera. The

fluorescence images were obtained with dichroic and emission filters purchased from Chroma and Thorlabs. Acquisition time was 30 ms per frame at the maximum amplification gain using a 100x oil immersion objective for fluorescence (Olympus UPLFLN100XO2). In the case of G-PF sample (λexc = 480 ± 10 nm, λem > 515 nm) it was possible to track individual carbon particles as dark spots against the intense background of the fluorescent solution, see figure. A similar situation was detected for the sample G-P + F. On the other hand in the G-PR sample (λexc = 535 ± 25 nm, λem > 590 nm) graphene particles could hardly be detected. In order to have an enhancement of the S/N ratio as well as a better image contrast a background subtraction and image inversion was performed with the software ImageJ[34].

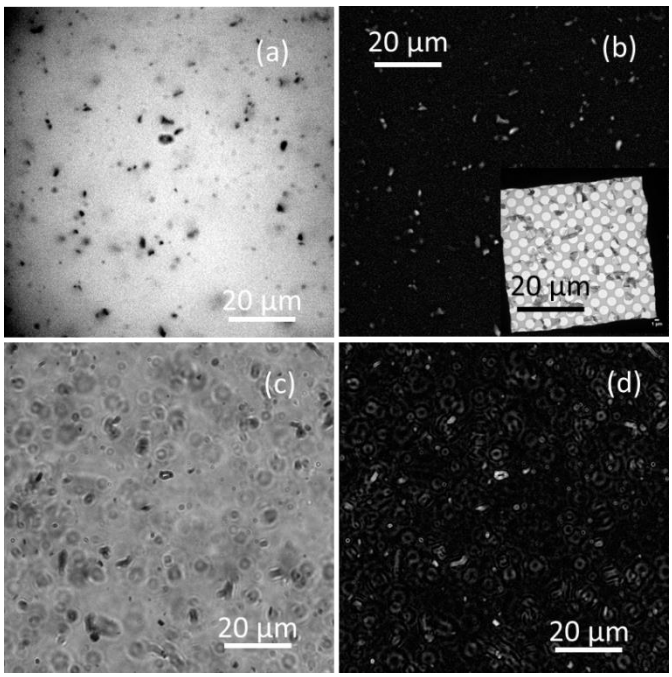

Figure. 8(a) Representative fluorescence image a 0.11±0.01 mm liquid film of G-PF (magnification 100x). Graphene particles can be detected as dark spots. Image contrast can be improved by inversion and background subtraction as in (b). The inset of (b) shows, in the same scale, the TEM image of the same G-PF after deposition. (c) Representative optical image a 0.11±0.01 mm liquid film of G-PF (magnification 100x) in transmission mode (white light). Image quality does not improve after inversion and back-ground subtraction (d).

Transmission mode images can be processed in the same way, but even with this processing, there is a strong presence of unfocussed material, and it is not possible to detect individual particles (Figure 8, d). Result of the fluorescence and transmission processed images are shown in Figure 8.Figure 8, a, clearly shows the graphene flakes dispersed in a fluorescent medium, that is the fluorescent surfactant. This difference in intensity can be seen with

an intensity profile plot, that corresponds to the typical image of an individual graphene particle (30 ms acquisition, 100× magnification) is shown in Fig 9.

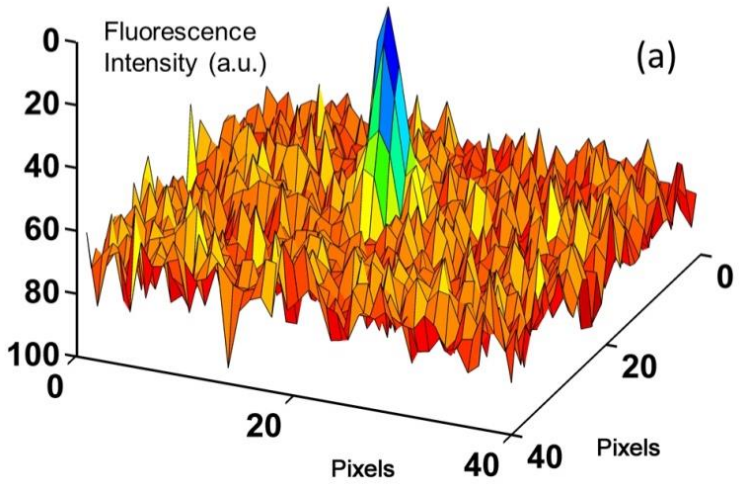

*Figure. 9 Fluorescence wide field image (magnification 100x) of an individual graphene particle observed in a 0.11±0.01 mm liquid film of **G-PF**. Each pixel corresponds to 160 nm and the lateral size is 40x40 pixels.*

These data were used to calculate a S/R that was typically higher than 6, demonstrating that graphene particles can be tracked by fluorescence imaging with the aid of PF for the exfoliation of graphene. Trajectories were tracked by analysing sequences of images acquired with an integration time τ of 30 ms per frame with a set of 500 frames corresponding to 15 seconds of acquisition. From the inverted images it is possible to follow the graphene sheets motions in subsequent frames as they appear as white spots on dark background, Figure 10

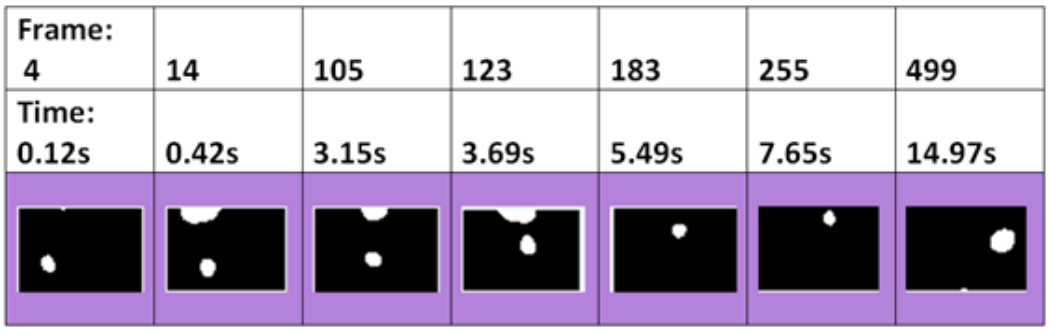

Figure. 10 Motion of a graphene particle, enhanced with optical contrast into subsequent frames.

This can be done for all the graphene object detectable in the focal plane of the solution, and as a consequence, it is possible to track their trajectories.

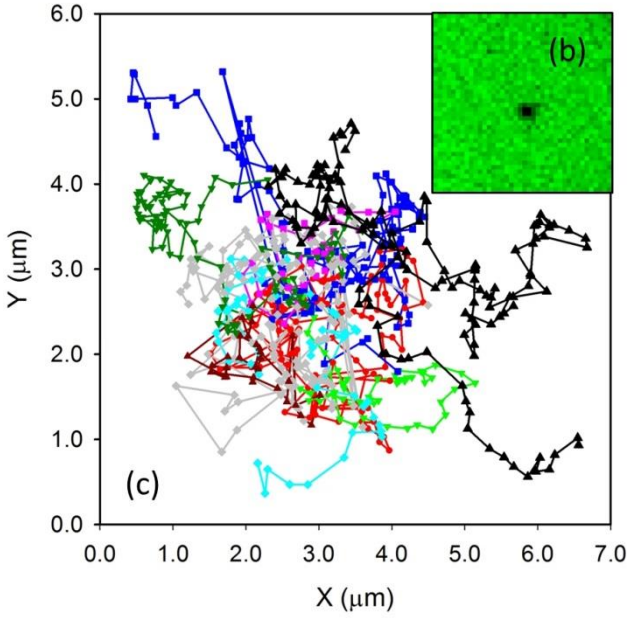

Figure. 11(b) Intensity profile of image a. (c) Nine representative trajectories of graphene particles in the film. Coordinates are taken at 30 ms intervals

For multiple G sheet Brownian movements we used for quantitative analysis, the ImageJ plug-in Mosaic[35] to measure the average displacement of the graphene particles in the 30 ms acquisition time of each frame. Result of a multiple tracking are reported in Figure 11. The displacement distribution for 13300 particles is plotted and is processed with the software Sigmaplot. The measured displacement were collected in histograms that were fitted with Gaussian peaks. Figure 12 clearly shows two peaks corresponding to two different populations of particles. For simplicity, we used a spherical model for the particles and fitted the two peaks with a Gaussian profile. The average square displacement $\langle \Delta x^2 \rangle + \langle \Delta y^2 \rangle$ in the x, y dimensions, can be correlate to the time interval t and the diffusion coefficient D of the particle D with the following equation (Eq 24):

$$\langle \Delta x^2 \rangle + \langle \Delta y^2 \rangle = 4Dt$$

Consequently, the D coefficient is used to obtain the particle diameter d with the Einstein-Smoluchowski equation (Eq 25):

$$D = \frac{k_B T}{6\pi\eta R}$$

where kB is Boltzmann's constant, T is temperature, η is the medium viscosity and R is the hydrodynamic radius of the particle.

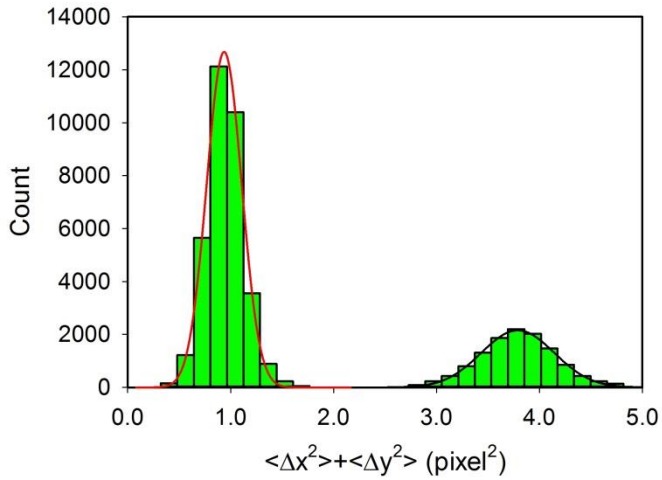

Figure. 12 Distribution of the displacement of the carbon particles tracked by fluorescence microscopy (green bars). One pixel corresponds to 160 nm. Data are relative to 13300 particles tracked with the Image J plug-in Mosaic.39 The data were fitted with Gaussian peaks to give average values of 3.79±0.35 and 0.93±0.17 pixels corresponding to hydrodynamic diameters of 265±25 and 1100±200 nm respectively.

The histogram's Gaussian fitting, Figure 12, gave peaks at 3.79 ± 0.35 and 0.93 ± 0.17 pixels, taking into account that each pixel corresponds to 160 nm. Then, the Eq 25 was used to calculate **from the particle tracking, the average hydrodynamic diameter of the particles (265 ± 25 and 1100 ± 200 nm respectively).**

4.3.5. Dynamic Light Scattering (DLS)

Just to compare the obtained diameter of the graphite flakes with the one obtained with other type of measurements and assess the reliability of the technique, we performed a Dynamic Light Scattering measurement with a Malvern Nano ZS instrument equipped with a 633 nm laser diode. The samples were analysed in a disposable polystyrene cuvettes of 1 cm optical path length, with water as solvent. The result was a correlogram corresponding to the presence of a single broad population with an average size of 720 nm and a PdI as high as 0.697. As said in the introduction the drawback of this technique in the analysis of a graphene solution is the fact that it is a strongly light absorbing sample and it is not suitable for accurate distribution analysis, even if the general reliability of this kind of approach is still debated [36], [37].

4.3.6. High Resolution Transmission Electron Microscopy (HR-TEM)

In order to find a comparative technique to assess the reliability of the particle tracking method for size detection and characterization of graphene suspensions, and to investigate the effect of the deposition process on the properties of our graphene suspensions we analysed them by TEM and to and Bright-field TEM. Images were taken at the Electron Microscopy Laboratory of the CNR-IMM Institute of Bologna, with a FEI Tecnai F20T HR-TEM instrument. Samples were prepared to be analysed by casting 3 drops of 1 µL of sample onto holey carbon grids (400 mesh), or lacy carbon grids. After a washing step with a few drops of water and isopropyl alcohol, the grids are then dried at 150 °C to allow : i) the evaporation of the solvent, ii) to avoid contamination from other organics, iii) promote the adhesion of the sample to the grid.

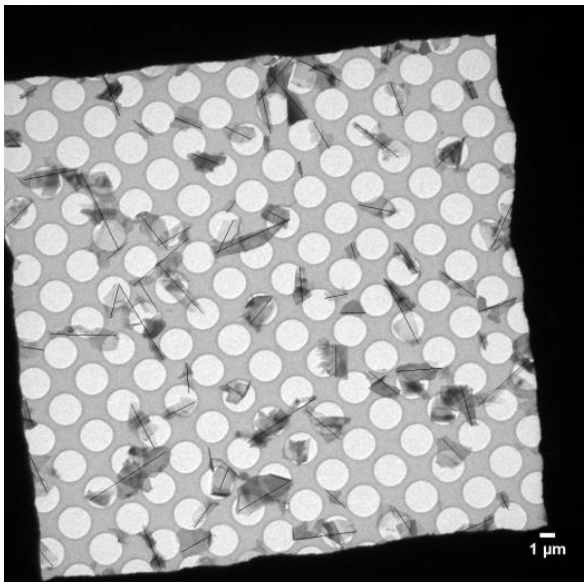

Figure. 13 TEM grid covered with G-PF. The reported lines highlight the measurements performed on each flake.

Even if TEM technique requires sample deposition and drying, this is still the most informative technique used for characterizing graphene. In general, graphene sheets have a rectangular shape, therefore with a long side and a short one, as shown in Figure 13. From TEM images, collected on G-PF, it is possible to discriminate between these two dimensions of the aggregates. Inside of the pictures, 190 different flakes were measured and data were processed by using Image J and Sigma Plot software. The data were plotted through the use of a histogram plot where each bar represents the number of flake between 50nm 1-dimension size.

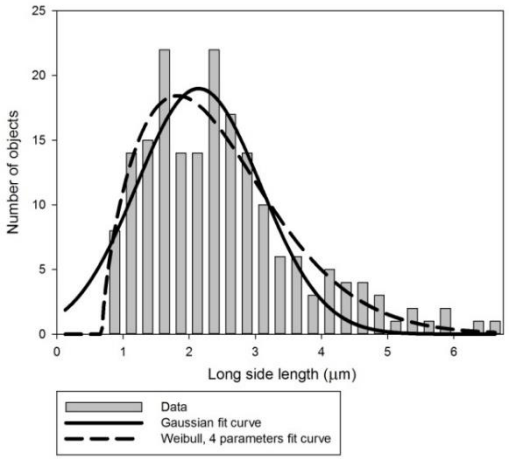

Figure. 14 Calculation of the average value of the long side. The different fits performed are reported. Solid line is the Gaussian fit, while the dashed line is the Weibull fit. Results on 190 measurements different measurements

As we performed for the average displacement, even in this case the histogram plot at first was fitted using a Gaussian Fit curve, see Figure 14. Since the accuracy of this fitting was not the most representative one, a Sigma Plot Weibull, 4 Parameter function was used to fit the curve of data. This fitting with Weibull equation displayed a regression coefficient R =0.90 with respect of the R=0.83 obtained with the Gaussian one, and, therefore, is it possible to say that this curve fits histogram trend. The average value for the long side of 2140 ±70 nm, see Figure 14. From the same images, we measured then the short dimension of the flakes, obtaining an average value of 720 ±20 nm.

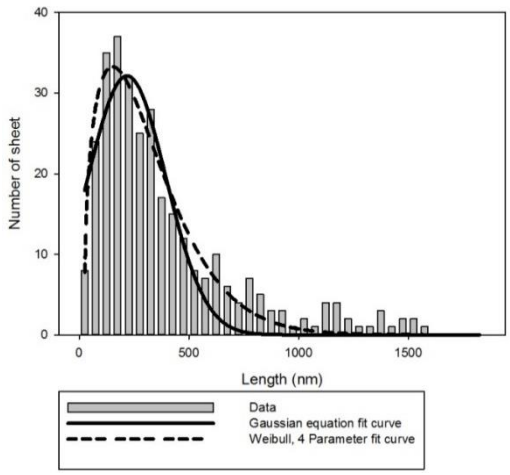

Figure. 15 Calculation of the average side size of G-PF. Two curves show the different fits performed. Continuous line is Gaussian Equation fit. Dashed line is Weibull Equation fit.

So TEM at low magnification reveals the presence of aggregates of 2000–3000 nm, considerably larger than the biggest particles detected in solution (1100 ± 200 nm). Observation at higher magnification demonstrates that indeed these large particles are aggregates of small graphene sheets with a lateral size of a few hundreds of nanometres.

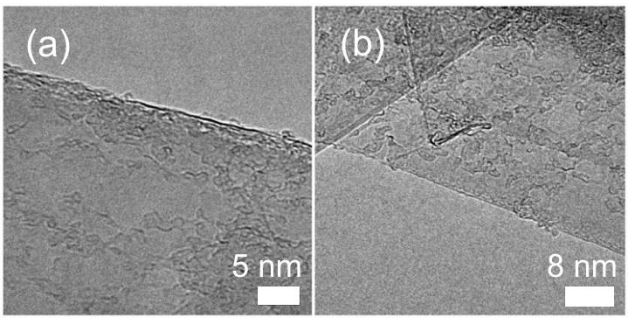

Figure. 16 HR-TEM images of samples G-PF (left) and G-PR (right).

A new detailed analysis of (HR-TEM) images demonstrated that the sheets have an average lateral size of 220± 10 nm, and that the aggregates have a width of 720 ± 20 nm, a length of 2140 ± 70 µm and an average surface area of 1,4 µm^2. Then, 86 TEM images were collected and analysed in order to have a value of the flakes thickness, and assess the exfoliation degree of the produced graphene flakes solution with Pluronic. Sigma Plot Log Normal-3 Parameter equation was used to fit the curve with a regression coefficient R equal to 0.99. HR-TEM images of the samples G-PF and G-PR are shown in Figure 16.

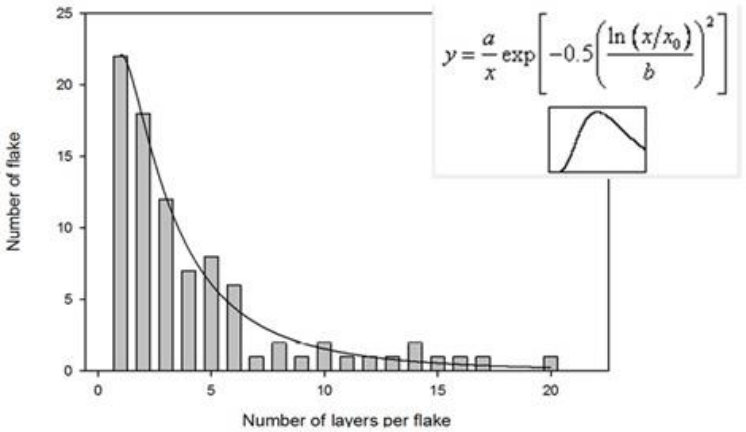

Figure. 17 Number of layers detected for the flakes present in the 86 images analysed. In the inset, the Sigma Plot Log Normal-3Parameter equation is reported.

TEM measurements on the samples G-P, G-PR and G-PF reveal an **average number of layers per flake of N =2 –3**, which is constant, within experimental error, for the three samples (Figure 17). It has to be noticed that the hydrodynamic diameter of the smallest of the two populations of diffusing objects observed by fluorescence imaging tracking matches with the size of the individual graphene sheets observed by TEM. However, an aspect that is

extremely important from the applicative point of view is that it is not possible to state from TEM images analysis whether the small graphene sheets are indeed present in the pristine solution as individual objects or only as aggregates. Hence fluorescence imaging allowed us to observe and confirm the presence in solution of small individual graphene sheets as well as the presence of larger aggregates. The same result could not be achieved using DLS.

4.4. Concluding remarks on chapter 4: fundamental study on graphene

Based on low cost: surfactants, chromophores and instruments; the technique showed in this chapter is a tool that can be exploited for characterization of liquid graphene suspension both for industrial and laboratory production. **The synthesized fluorophores, as far as the synthesized systems, allowed to understand:**

1. **the interaction between graphene and fluorescent molecules:** while PF does not bind to graphene and maintains its fluorescence unchanged in the exfoliated graphene samples, and PR binds almost quantitatively to graphene leading to its fluorescence being strongly quenched;
2. **understand the actual function and distribution of surfactants during the exfoliation process;**
3. **exploit that results to to track the graphene** particles produced during ultrasound-assisted liquid phase exfoliation and **solve the problem of graphene nanomaterials direct-imaging that those fluorescent surfactants;**
4. demonstrated that **fluorescence imaging can be used to identify different populations of graphene in "as-prepared"** exfoliated graphite samples using a conventional fluorescence microscope.

In addiction this technique has the potential for acquisition of more detailed structural information such as the aspect ratio and thickness of graphene particles using a more sophisticated set-up and in particular increasing the frame acquisition rate.

4.4. Bibliography chapter 4

1 A. Ciesielski and P. Samori, Chem. Soc. Rev., 2014, 43, 381– 398.

2 A. C. Ferrari, et al., Nanoscale, 2015, 7, 4598–4810.

3 S. Yang, S. Bruller, Z. S. Wu, Z. Y. Liu, K. Parvez, R. H. Dong, F. Richard, P. Samori, X. L. Feng and K. Mullen, J. Am. Chem. Soc., 2015, 137, 13927–13932.

4 S. Eigler and A. Hirsch, Angew. Chem., Int. Ed., 2014, 53, 7720–7738.

5 M. Quintana, J. I. Tapia and M. Prato, Beilstein J. Nanotechnol., 2014, 5, 2328–2338.

6 M. Lotya, A. Rakovich, J. F. Donegan and J. N. Coleman, Nanotechnology, 2013, 24, 6.

7 C. Backes, R. J. Smith, N. McEvoy, N. C. Berner, D. McCloskey, H. C. Nerl, A. O'Neill, P. J. King, T. Higgins, D. Hanlon, N. Scheuschner, J. Maultzsch, L. Houben, G. S. Duesberg, J. F. Donegan, V. Nicolosi and J. N. Coleman, Nat. Commun., 2014, 5, 10.

8 A. Pénicaud and C. Drummond, Acc. Chem. Res., 2013, 46, 129–137.

9 Y. Hernandez, V. Nicolosi, M. Lotya, F. M. Blighe, Z. Sun, S. De, I. T. McGovern, B. Holland, M. Byrne, Y. K. Gun'Ko, J. J. Boland, P. Niraj, G. Duesberg, S. Krishnamurthy, R. Goodhue, J. Hutchison, V. Scardaci, A. C. Ferrari and J. N. Coleman, Nat. Nanotechnol., 2008, 3, 563–568.

10 A. C. Ferrari, J. C. Meyer, V. Scardaci, C. Casiraghi, M. Lazzeri, F. Mauri, S. Piscanec, D. Jiang, K. S. Novoselov, S. Roth and A. K. Geim, Phys. Rev. Lett., 2006, 97, 187401.

11 I. H. Son, J. Hwan Park, S. Kwon, S. Park, M. H. Rummeli, A. Bachmatiuk, H. J. Song, J. Ku, J. W. Choi, J.-m. Choi, S.-G. Doo and H. Chang, Nat. Commun., 2015, 6, 7393.

12 C. Vallés, C. Drummond, H. Saadaoui, C. A. Furtado, M. He, O. Roubeau, L. Ortolani, M. Monthioux and A. Pénicaud, J. Am. Chem. Soc., 2008, 130, 15802–15804.

13 C. Casiraghi, A. Hartschuh, E. Lidorikis, H. Qian, H. Harutyunyan, T. Gokus, K. S. Novoselov and A. C. Ferrari, Nano Lett., 2007, 7, 2711–2717.

14 A. C. Ferrari and D. M. Basko, Nat. Nanotechnol., 2013, 8, 235–246.

15 O. M. Maragó, F. Bonaccorso, R. Saija, G. Privitera, P. G. Gucciardi, M. A. Iatì, G. Calogero, P. H. Jones, F. Borghese, P. Denti, V. Nicolosi and A. C. Ferrari, ACS Nano, 2010, 4, 7515–7523.

16 N. Fakhri, F. C. MacKintosh, B. Lounis, L. Cognet and M. Pasquali, Science, 2010, 330, 1804–1807.

17 C. W. Twombly, J. S. Evans and I. I. Smalyukh, Opt. Express, 2013, 21, 1324–1334.

18 V. Filipe, A. Hawe and W. Jiskoot, Pharm. Res., 2010, 27, 796–810.

19 M. Montalti, G. Battistelli, A. Cantelli and D. Genovese, Chem. Commun., 2014, 50, 5326–5329.

20 L. Li, G. Wu, G. Yang, J. Peng, J. Zhao and J.-J. Zhu, Nanoscale, 2013, 5, 4015–4039.

21 S. Y. Lim, W. Shen and Z. Q. Gao, Chem. Soc. Rev., 2015, 44, 362–381.

22 M. Montalti, A. Cantelli and G. Battistelli, Chem. Soc. Rev., 2015, 44, 4853–4921.

23 J. Z. Shang, L. Ma, J. W. Li, W. Ai, T. Yu and G. G. Gurzadyan, Sci. Rep., 2012, 2, 8.

5.FUNDAMENTAL STUDY ON PERYLENE AND GOLD FLUORESCENT NANOPARTICLES

5.1. Ultra-bright Nanoparticles and Perylene

Perylenes were found to be a promising candidates in DSSC as sensitizers as well as in bioimaging applications due to their: thermal and chemical stability, low cost and good light-harvesting ability [1]. As explained in Chapter 2, perylene has a fast electron injection in TiO_2 , ~ 190-210 fs [2], [3], and a slower back electron transfer of the electron injected into the semiconductor NP with the dye radical cation(e.g. recombination time for perylenes: 14 µs - 30 ms[3]) compared to other dye sensitizers (e.g. recombination time for squaraine dye : 2.7 ns[4]) . In addition, the high absorbance in the visible ($\varepsilon \sim 10^5$ M^{-1} cm^{-1}) range (absorption at 450–750 nm) and emission from a singlet state with high quantum yield. One particular feature of great interest in designing perylenes is the ability to impart charge transfer absorption characteristics by inducing perturbation of HOMO and LUMO distribution with electron-donating group on the perylene core[1]. Furthermore the aggregation degree as well as the aggregates type(J or H) strictly influence Perylenes absorption as well as their emission, Figure 1.

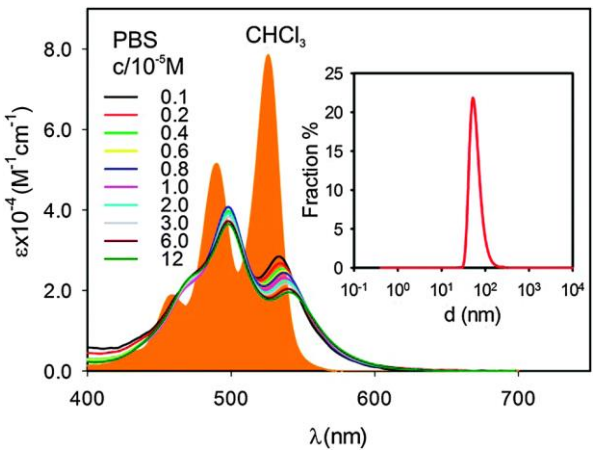

Figure. 1 Molar absorption coefficient of P monomer in CHCl3 (filled orange curve) and in its form of aggregates in water based solution at concentrations ranging from 1 × 10−6 M to 1.2 ×10−4 M. Inset: size distribution of the P NPs in water based solution measured by DLS.[5]

For these reason the use of perylene it is not only in the sensitization of titania, as explained in the chapter 2, but also it has a wide range of applications in contrast agents for bioimaging. In particular they are used in fluorescent nanoparticles (NPs) since in this form, perylenes have a brightness similar or superior to semiconductor quantum dots[6]. In general these ultra-bright NPs consist of a silica or polymeric matrix that incorporate the emitting dyes as individual moieties or aggregates and promise to be more biocompatible than semiconductor quantum dots. High doping of nanoparticles with dyes in general can bring sides effects such as: aggregation-caused quenching (ACQ) and proximity-caused quenching (PCQ) due to the ground state and excited state interactions between the molecular emitters. These effects can become even more severe because of Föster resonance energy transfer (FRET), specially for dyes in multichromophoric systems studied for bioimaging. Figure 2 reports a general scheme of ACQ and PCQ mechanisms. PCQ and ACQ involve different electronic processes. The former happens when , dyes in close proximity (indicated as B in Figure 2, right) interact only after excitation, producing quenched excimers, the latter occurs when dye molecules aggregate at the ground state in the NPs. In case of ACQ processes both absorption and emission properties of the involved chromophores (indicated as B in Figure 2, left) are altered with respect to the non-aggregated molecules (indicated as A). This is effect on booth absorption and emission is the one exemplified in Figure 1. In order to avoid ACQ and PCQ a possible way can be the design of systems based on aggregation-induced emission (AIE). Otherwise, this ACQ and PCQ can be exploited in the opposite way, designing stimuli-responsive fluorogenic probes through disaggregation-induced emission (DIE) in alternative to AIE. Both AIE and DIE can be designed with the aid of molecules like perylenes, since, as said, they have a tuneable aggregation and emission dependent from the modifications on the molecular structure.

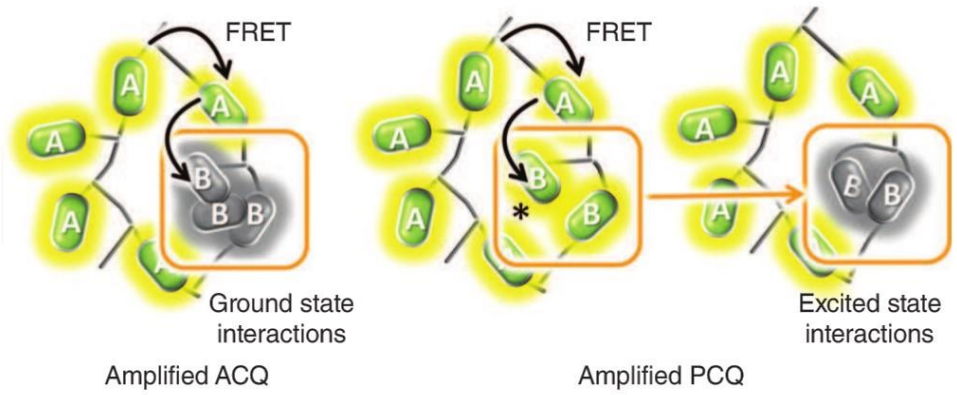

Figure. 2 Amplification of aggregation-caused quenching (ACQ, left) and proximity-caused quenching (PCQ) in NPs. The former process involve Föster resonance energy transfer (FRET) from 'isolated' excited dyes (A molecules) to nonluminescent aggregates already present before excitation because of the action of ground state interaction between B molecules. Amplified PCQ is analogous but takes place also in the absence of aggregates: FRET leads to excitation of molecule which are not aggregated (weak ground state interaction) but are close enough to bind after excitation to give quenched species.[6]

The achievement of ultra-bright NPs requires the capability of producing heavily doped materials where ACQ and PCQ and their amplification through FRET are prevented[6]. It is possible to avoid these drawbacks by controlling the organization of the emitters in the nanostructure otherwise a pristine dye moiety has to be developed that, when excited, deactivate via a radiative pathway even if densely packed in a network. This has to be done in order to avoid bimolecular or collective quenching processes. Otherwise, as said, ACQ and PCQ can be exploited for the design of stimuli-responsive fluorogenic probes according to a general mechanistic scheme that we recently proposed as disaggregation-induced emission (DIE)[5]. In this case, an external stimulus is responsible for the disaggregation of the highly concentrated and packed dye in NPS. This process induces a robust signal switching on. DIE is more convenient with respect of AIE in the case of processes that produce bond cleavage, as in the case of enzymatic action.

5.1.1. **Perylene Nanoparticles**

Ultra-bright NPs based on the use of molecular or polymeric emitters in general does not suffer severe ACQ or PCQ [7]–[9]. Another option can be the design of J type of nanoaggregates[10], [11], therefore it has to be taken into account that the Photoluminescence of these aggregates is strictly dependent on the molecular structure as well as molecular organization. Wuerthner et all investigated these aggregates/molecular parameters and reported that the emission quantum yield of aggregates of the same perylene diimide (PDI)[12]molecules increase relevantly going from nanorods to nanoribbons structures[10], [12]. This was reported that the presence of local environmental perturbations in the structure of similar PDI molecules to create localized excited states that act as excitation energy traps and show a peculiar red shifted emission[13].Zhou et all reported, in apparent contrast with the excitonic coupling theory, a strong emission from H-type aggregates [14]. ACQ and PCQ can become powerful tool to develop stimuli-responsive NPs, taking into consideration that these phenomena severe drawbacks in the use of multichromophoric systems as environmental nanoprobes. Here is proposed a mechanism of DIE in correlation to the specular phenomenon of AIE often exploited to design fluorogenic probes[5], since up to now only the AIE has been systematically studied[8]. **Figure 3 shows the system that we reported regarding the use of NPs as fluorogenic probes for bioimaging** (Figure 3)[5]. These NPs were obtained by the self-assembly of a PDI functionalized with amino terminated PPG (Poly Propylene Glycol), and the absorption as well as the emission of these molecules is strictly dependent from the degree of aggregation, Figure 1. **These NPs become strongly luminescent when internalized by cells, even if they have are very weak fluorescence in aqueous environment.** Furthermore, after direct incubation with the cells, from the fluorescence images it is possible to notice that there is almost no background signal although the biological sample underwent no washing[6]. The particularity of this PDI based NPs system is that, depending on the incubation conditions, it is possible to achieve either green or red fluorescent labelling of the cells as shown in Figure 3(a)–(b). **In addiction by irradiating incubated perylene based NPs with blue light the fluorescence colour of the red emitting cells could be tuned**, as shown in the image sequence (c–e) in Figure 3.

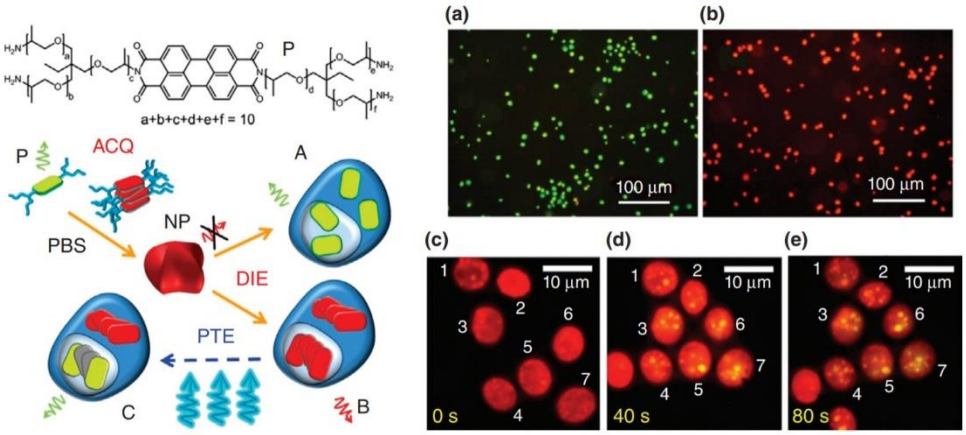

Figure. 3 Scheme of the mechanism of response of the fluorogenic nanoparticles (NPs) formed by P in phosphate buffered saline (PBS). NPs are not fluorescent due to aggregation-caused quenching (ACQ). Adsorption by cells leads to disaggregation of the NPs and to fluorescence recovery of disaggregation-induced emission (DIE). The cells become green fluorescent (case A, picture a) or red fluorescent (case B, picture a), respectively, at low and high NPs dosage. Exposure to strong visible light allows the photo tuning of the emission (PTE) of specific cellular compartments (C).Fluorescence images during irradiation are shown in the sequence c–e.[6].

Figure 3 reports the scheme of colour tuning. photo treatment increases the contrast in imaging application and it allows the identification of specific cellular compartments that after irradiation emits yellow or green fluorescence. Another way to achieve the same result is by tuning the interaction between the chromophores. This can be done by controlling their organization in the volume of the NPs. As said in the introduction one particular feature of great interest in designing PDI is the ability to impart charge transfer absorption characteristics by inducing perturbation of HOMO and LUMO distribution with electron-donating group on the perylene core[1]. This outcome of molecular changing has also consequence on aggregation of the dyes. **Aggregation in fact can be prevented by introducing bulky substituent in Perylenes structures**. Klymchenko et all recently demonstrated that ACQ and PCQ can be prevented in the case of modified PDIs [11] encapsulated into biodegradable PLGA NPs. The PDIs tested were: one bearing bulky hydrophobic groups at the imides, while the other was substituted in both imide and bay regions (Lumogen Red, Figure 4). Lumogen Red showed nearly no aggregation inside the polymer NPs and maintained high quantum yield and photostability. PLGA NPs loaded with 1% (w/w)

Lumogen Red were >10-fold brighter than quantum dots (QD-585), were stable in biological media. Furthermore they entered spontaneously into HeLa cells by endocytosis, as shown in Figure 4, showing no sign of cytotoxicity.

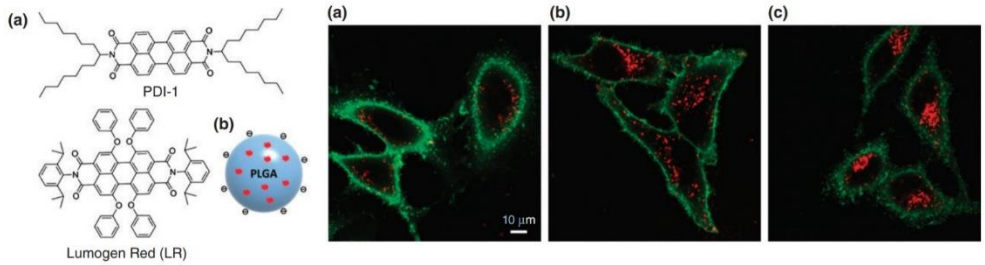

Figure. 4 Left: chemical structure of PDI-1 and LR dyes (a) and schematic presentation of dye-doped poly(DL-lactide-co-glycolide) PLGA) nanoparticles (b). Right: confocal fluorescence imaging of HeLa cells cultured for 1 (a), 2 (b), and 6 (c) h in the presence of 1wt% LR nanoparticles (NPs) and for 10 min in the presence of wheat germ agglutinin-Alexa488 for labelling cell membranes.[11] Reproduced with permission from ref. [11]; Copyright (2014) Royal Society of Chemistry

5.2. Ultra-Bright Gold Nanoclusters

In order to avoid ACQ and PCQ effects, as alternatives to organic Dyes in aggregates or NPs, is the use of quantum dots or metal nanoparticles[15], [16]. For instance, techniques based on gold nanoclusters (GNCs) can be developed, since a size quantum confinement in gold nanostructure bring them to be luminescent. If compared to diagnostic approach, GNCs are poorly invasive and highly sensitive. As said, GNCs emission is tuneable from the visible (VIS) to the near infrared region (NIR), as shown in Figure 5.

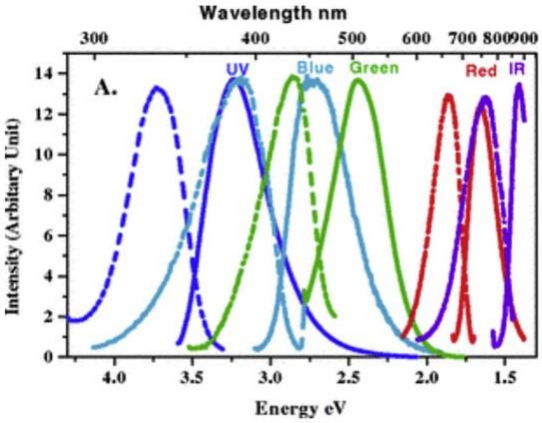

Figure. 5 UV-VIS emission and excitation profiles of different sized GNCs[17]

This spectral VIS-NIR region is ideal for photo-activation and detection in-vivo. Because of their high economic and social impacts as materials in life sciences, GNCs can also be inserted in stimuli-responsive nanostructured systems.
The comparison between GNCs and common organic fluorophores enlighten the advantages in the use of GNCs: superior photochemical stability[18]–[20], tuneable emission wavelength (Figure 5)[17], satisfying luminescence quantum yield (QY) in the NIR and luminescence lifetimes in the microseconds range [17], [18]. Even though GNCs present big advantages, some general principles governing the phenomenon have been clarified since the photophysical properties have not been completely interpreted.
The contribution that can be addressed to the emission features of GNCs are three:

- the size confinement effect of the core, that generates discrete electronic states with shapes and energies affected by the core structure [17];
- superficial phenomena and to the nature of the ligands [21],
- the aggregation of gold species and aurophilic interactions [22].

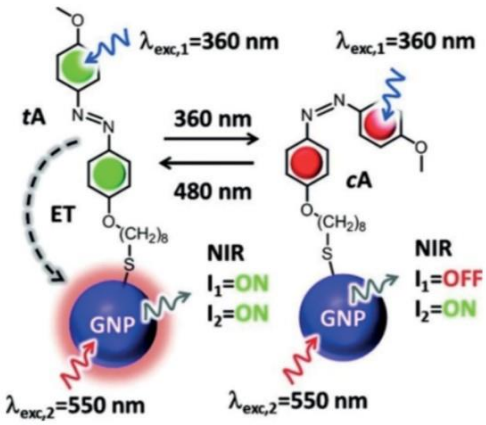

Figure. 6 Chemical formula of the trans azobenzene tA and of its cisisomer cA bound to gold NP (GNP). When the ligands are in the trans form (left, tAGNP, ON state) ET from tA to the GNP produces NIR-sensitized emission upon ligand excitation. Such contributions, owing to sensitization, are lost upon PI in cA covered NPs (right, cA-GNP, OFF state). [23]

The only drawback in the use of GNPc is the fact that they have a molar absorption coefficient ($\varepsilon \approx 10^4\ M^{-1}\ cm^{-1}$) which is about one order of

magnitude lower than organic chromophores. This is extremely important since the brightness of nanoprobes depends on the efficiency of absorption of the excitation light (ε). Au NCs present and on the PL quantum yield but. **In order to improve the efficiency of absorption of the excitation light (ε), our and other groups proposed the design of hybrid structures that combine the PL properties of Au NCs with the optical properties of organic dyes in order to enhance the brightness of the inorganic emitters**. In an analogous way with respect of the one explained for the sensitization of TiO_2 with organics in Chapter 2, it is possible to transfer the excitation energy from an organic ligand able to efficiently adsorb light (chromophores) to the emitting gold core. With this should in principle improve the brightness of GNPs[22].**Figure 6 reports the system that we developed. It consists in a different strategy to turn on/off the PL of Au144 NCs using as organic sensitizer a photoswitchable azobenzene derivative [23]**. Upon irradiation at 360 nm, the conversion of the trans form(tA-GNP) of the ligand into the cis one(cA-GNP) took place almost quantitatively (> 95 %) with a quantum yield identical to the one measured for the same molecule free in solution. Then, irradiation of cA-GNP at 480 nm the regeneration of 70 % of trans was achieved. The produced Au NCs are proofed to be sensitized from the ligands by means of photophysical measurements. The results confirmed the occurrence of an excitation **energy transfer process from the ligands to the Au NCs that produced sensitized NIR emission, furthermore PL brightness of the Au NCs is enhanced upon excitation of the ligands.** The comparison between the tA-GNP and cA-GNP reveals that this energy transfer is higher in the case of the trans form. We also noticed that another advantage of this successfully synthesized system is that azobenzene functionalized Au NCs, the photo-isomerization rate of the ligands was not affected by the interaction with the gold NCs. This last result that there is no competition between the energy transfer to gold and the photo-isomerization of the ligand. In conclusion this system can be exploited in order to enhance GNPc PL in NIR region.

5.3. Concluding remarks on chapter 5: ultra-bright Perylene and Gold NPs

In the first part of this chapter we showed that it is not a trivial to obtain high brightness feature of heavily dye-doped nanomaterials. In particular ACQ and PCQ can be exploited in the opposite way, designing stimuli-responsive fluorogenic probes through disaggregation-induced emission (DIE) in alternative to AIE. For this reason Perylene based NPs can be exploited as fluorogenic probes for bioimaging. These NPs become strongly luminescent when internalized by cells, even if they have are very weak fluorescence in aqueous environment, in addiction by irradiating incubated perylene based NPs with blue light the fluorescence colour of the red emitting cells could be tuned. In order to avoid ACQ and PCQ effects, as alternatives to organic Dyes in aggregates or NPs our results demonstrate that gold nanoparticles can be used. In particular we developed a different strategy to turn on/off the PL of Au144 NCs using as organic sensitizer a photoswitchable azobenzene derivative, and we also successfully found that PL brightness of the Au NCs is enhanced upon excitation of the ligands.

5.4. Bibliography chapter 5

[1] S. Mathew and H. Imahori, "Tunable, strongly-donating perylene photosensitizers for dye-sensitized solar cells," *J. Mater. Chem.*, vol. 21, no. 20, pp. 7166–7174, 2011.

[2] B. Burfeindt, T. Hannappel, W. Storck, and F. Willig, "Measurement of Temperature-Independent Femtosecond Interfacial Electron Transfer from an Anchored Molecular Electron Donor to a Semiconductor as Acceptor," *J. Phys. Chem.*, vol. 100, no. 41, pp. 16463–16465, Jan. 1996.

[3] L. I. Hernández *et al.*, "Spectral Characteristics and Photosensitization of TiO2 Nanoparticles in Reverse Micelles by Perylenes," *J. Phys. Chem. B*, vol. 117, no. 16, pp. 4568–4581, Apr. 2013.

[4] P. V Kamat, S. Das, K. George Thomas, and M. V George, "Ultrafast photochemical events associated with the photosensitization properties of a squaraine dye," *Chem. Phys. Lett.*, vol. 178, no. 1, pp. 75–79, 1991.

[5] M. Montalti, G. Battistelli, A. Cantelli, and D. Genovese, "Photo-tunable multicolour fluorescence imaging based on self-assembled fluorogenic nanoparticles," *Chem. Commun.*, vol. 50, no. 40, pp. 5326–5329, 2014.

[6] G. Battistelli, A. Cantelli, G. Guidetti, J. Manzi, and M. Montalti, "Ultra-bright and stimuli-responsive fluorescent nanoparticles for bioimaging," *WILEY Interdiscip. Rev. NANOBIOTECHNOLOGY*, vol. 8, no. 1, pp. 139–150, 2016.

[7] S. P. Anthony, "Organic Solid-State Fluorescence: Strategies for Generating Switchable and Tunable Fluorescent Materials," *Chempluschem*, vol. 77, no. 7, pp. 518–531, 2012.

[8] M. Shimizu and T. Hiyama, "Organic Fluorophores Exhibiting Highly Efficient Photoluminescence in the Solid State," *Chem. ASIAN J.*, vol. 5, no. 7, pp. 1516–1531, 2010.

[9] S. Fery-Forgues, "Fluorescent organic nanocrystals and non-doped nanoparticles for biological applications," *Nanoscale*, vol. 5, no. 18, pp. 8428–8442, 2013.

[10] F. Wuerthner, T. E. Kaiser, and C. R. Saha-Moeller, "J-Aggregates: From Serendipitous Discovery to Supramolecular Engineering of Functional Dye Materials," *Angew. CHEMIE-INTERNATIONAL Ed.*, vol. 50, no. 15, pp. 3376–3410, 2011.

[11] Z. Xu *et al.*, "Water-miscible organic J-aggregate nanoparticles as efficient two-photon fluorescent nano-probes for bio-imaging," *J. Mater. Chem.*, vol. 22, no. 34, pp. 17737–17743, 2012.

[12] D. Goerl, X. Zhang, and F. Wuerthner, “Molecular Assemblies of Perylene Bisimide Dyes in Water,” *Angew. CHEMIE-INTERNATIONAL Ed.*, vol. 51, no. 26, pp. 6328–6348, 2012.

[13] A. Merdasa, A. J. Jimenez, R. Camacho, M. Meyer, F. Wuerthner, and I. G. Scheblykin, “Single Levy States-Disorder Induced Energy Funnels in Molecular Aggregates,” *NANO Lett.*, vol. 14, no. 12, pp. 6774–6781, 2014.

[14] L. Wang *et al.*, “Novel highly emissive H-aggregates with aggregate fluorescence change in a phenylbenzoxazole-based system,” *Chem. Commun.*, vol. 50, no. 63, pp. 8723–8726, 2014.

[15] A. Cantelli, G. Battistelli, G. Guidetti, J. Manzi, M. Di Giosia, and M. Montalti, “Luminescent gold nanoclusters as biocompatible probes for optical imaging and theranostics,” *Dye. Pigment.*, vol. 135, no. SI, pp. 64–79, 2016.

[16] A. Cantelli, G. Guidetti, J. Manzi, V. Caponetti, and M. Montalti, “Towards Ultra-Bright Gold Nanoclusters,” *Eur. J. Inorg. Chem.*, vol. 2017, no. 44, pp. 5068–5084, 2017.

[17] J. Zheng, C. W. Zhang, and R. M. Dickson, “Highly fluorescent, water-soluble, size-tunable gold quantum dots,” *Phys. Rev. Lett.*, vol. 93, no. 7, 2004.

[18] S. Xu, P. Liu, Q. Song, L. Wang, and X. Luo, “One-pot synthesis of biofunctional and near-infrared fluorescent gold nanodots and their application in Pb2+ sensing and tumor cell imaging,” *RSC Adv.*, vol. 5, no. 5, pp. 3152–3156, 2015.

[19] Q. Zheng *et al.*, “Ultra-stable organic fluorophores for single-molecule research,” *Chem. Soc. Rev.*, vol. 43, no. 4, pp. 1044–1056, 2014.

[20] E. Rampazzo *et al.*, “Energy Transfer from Silica Core-Surfactant Shell Nanoparticles to Hosted Molecular Fluorophores,” *J .Phys. Chem. B*, vol. 114, no. 45, pp. 14605–14613, 2010.

[21] G. Wang, R. Guo, G. Kalyuzhny, J.-P. Choi, and R. W. Murray, “NIR luminescence intensities increase linearly with proportion of polar thiolate ligands in protecting monolayers of Au-38 and Au-140 quantum dots,” *J. Phys. Chem. B*, vol. 110, no. 41, pp. 20282–20289, 2006.

[22] S. H. Yau, O. Varnavski, J. D. Gilbertson, B. Chandler, G. Ramakrishna, and T. Goodson III, “Ultrafast Optical Study of Small Gold Monolayer Protected Clusters: A Closer Look at Emission,” *J. Phys. Chem. C*, vol. 114, no. 38, pp. 15979–15985, 2010.

[23] S. Bonacchi *et al.*, “Photoswitchable NIR-Emitting Gold Nanoparticles,” *Angew. CHEMIE-INTERNATIONAL Ed.*, vol. 55, no. 37, SI, pp. 11064–11068, 2016.